

# Building models and searching for signals: pulsar glitches, solar flares, and continuous gravitational waves

Julian Brian Carlin

ORCID: 0000-0001-5694-0809 

MAY, 2023

A THESIS SUBMITTED IN COMPLETE FULFILLMENT  
OF THE REQUIREMENTS FOR THE DEGREE OF

DOCTOR OF PHILOSOPHY  
PHYSICS  
THE UNIVERSITY OF MELBOURNE

“ALL MODELS ARE WRONG, BUT SOME ARE USEFUL” — GEORGE BOX

---

## Abstract

---

Building a model is the only way to search for a signal in noisy data. Many systems governed by stress accumulating steadily and releasing abruptly are difficult to model from the microphysical interactions all the way up to the macroscopic observables. Instead, one can build phenomenological models which encompass the underlying mechanics, and falsify them with data. When the signal is weak compared to the noise, signal models must balance the flexibility required to encompass the stochastic generative process, while maintaining the specificity required to find particular markers of the physics in the data. This thesis explores these ideas in three different contexts.

Pulsar glitches are sudden, unpredictable jumps in the spin frequencies of some pulsars. The state-dependent Poisson (SDP) process is a framework which models the globally averaged stress in a system as a function of time. The stress accumulates deterministically between events. The instantaneous rate of a stress-release event is a monotonic function of the stress, i.e. as the stress increases, an event becomes more likely. Once a stress-release event is triggered, some fraction of the stress is released instantaneously. Previous work has shown that for individual glitching pulsars the observed distributions of waiting times between glitches, and the distributions of their sizes, are consistent with the SDP process. The cross-correlation between sizes and the subsequent (or preceding) waiting time are also consistent with the process, and falsifiable predictions are made regarding which pulsars may exhibit such a cross-correlation in the future, as more glitches are discovered. Considering the autocorrelation between consecutive waiting times, or sizes, provides an additional constraint. Even when combining all the above statistical measures, there exists a configuration of the SDP framework which adequately describes the observed sequence of glitch waiting times and sizes, for pulsars with more than 15 recorded glitches. However, as this configuration must vary pulsar-to-pulsar, there is tentative evidence that the underlying mechanism triggering glitches may also vary pulsar-to-pulsar.

If the stress instead accumulates between glitches via a random walk, until a stress threshold is reached, the statistical predictions regarding waiting times and sizes are less permissive than within the SDP framework. This alternative stress-accumulation and relax “meta-model” is motivated by glitch trigger mechanisms involving hydrodynamic instabilities, as well as pulse-to-pulse observations of the Vela pulsar showing evidence for a negative fluctuation in spin frequency immediately prior to its 2016 glitch. One key prediction of the Brownian stress accumulation meta-model is that the cross-correlation between the size and subsequent waiting time should be greater than zero in all pulsars, as well as predicting an excess of short waiting times if the cross-correlation is low. The observed sequence of sizes and waiting times for at least two pulsars can only be explained as arising from this meta-model if many small glitches are missing from glitch catalogs.

A key phenomenological degree of freedom in the SDP framework is the conditional

distribution of stress-release event sizes. This degree of freedom is necessary to encompass the variety of possible glitch trigger mechanisms in the literature. However, if one specializes the meta-model, it is possible to (provisionally) falsify individual microphysical mechanisms, for example the idea that glitches are the result of a coherent stress process which triggers superfluid vortex avalanches. The SDP meta-model is augmented such that the amount of stress released at each event is no longer a random variable, however the probability of a glitch is still a monotonic function of the stress in the system. The amount of stress released is calculated endogenously, by tracking the distribution of pinning strengths of occupied vortex pinning sites. Tracking this distribution over time allows for a long-term memory of the past history of stress-release events. This alternative meta-model predicts distinctive statistical observables. For example, there should be a peak and cut-off in both the waiting time and size distributions, corresponding to events that completely reset the system by unpinning all vortices. We do not see this in any glitching pulsar, although we need to observe more glitches to concretely falsify this mechanism.

Pulsar glitches are not the only physical system which is governed by a stress accumulation and relaxation process. There is broad agreement that solar flares are a sudden release of magnetic energy from the sun's corona. The energy accumulates via sub-photospheric motion, and a flare is more likely to trigger as the energy density increases. The SDP framework is mapped to the context of solar flares, and the hypothesis that solar flares are triggered when the stress reaches a static-in-time threshold is interrogated. If it were true, one should see a cross-correlation between flare sizes and subsequent waiting times, alongside similarly shaped distributions for flare sizes and waiting times. Across  $\sim 2 \times 10^3$  active regions and  $\sim 5 \times 10^4$  flares, there is no strong evidence for this association in the *Geostationary Operational Environmental Satellite* (GOES) historic soft X-ray flare database. If the database is complete, i.e. not missing many flares, this implies that perhaps flares are triggered before the stress nears the threshold, perhaps the threshold varies in time, or perhaps the rate at which stress accumulates in the system varies in time.

Detecting continuously-emitted quasi-monochromatic gravitational waves is a key goal of the Laser Interferometer Gravitational-Wave Observatory (LIGO), Virgo, and KAGRA collaborations. One such search from accreting millisecond X-ray pulsars is performed using data from the latest LIGO observing run. These targets are promising due to accretion possibly building surface asymmetries (“mountains”) or exciting  $r$ -mode superfluid oscillations in the neutron star interior. However, direct integration of the data over long time spans is hindered by the varying accretion torque, which causes the spin frequency of the star to wander stochastically. The signal model, in the source frame of the target, is that of a piecewise-constant frequency, which is allowed to randomly wander up to  $\sim 5 \times 10^{-7}$  Hz every ten days. This is implemented via the  $\mathcal{J}$ -statistic, which performs the coherent matched filter over ten-day chunks. These statistics are combined with a hidden Markov model to stitch together the most-likely path of the signal, given the data. However, the loudest candidates from the search are consistent with arising from noise. Upper limits are placed on the detectable wave strain amplitude at 95% confidence, and thus the neutron star ellipticity and  $r$ -mode amplitude. The strictest of these constraints are from IGR J00291+5934, and are  $\epsilon^{95\%} = 3.1 \times 10^{-7}$  and  $\alpha^{95\%} = 1.8 \times 10^{-5}$  respectively.

---

## Declaration

---

This page certifies that:

- This thesis contains only original work towards a Doctor of Philosophy, except where indicated in the preface.
- Due acknowledgement has been made in the text to all other material used.
- This thesis is fewer than 100 000 words in length, exclusive of tables, figures, bibliographies, and appendices.

Julian Brian Carlin

---

## Preface

---

Here and henceforth “the author” refers to the author of this thesis, Julian Brian Carlin. This thesis is an original work of the author reporting research done alone or in collaboration with other authors. This section provides a chapter-by-chapter summary of the author’s contributions and the publication status of all material.

**Chapter 1** is a comprehensive literature review for the work in Chapters 2–6 written by the author for this thesis. It is an original work of the author, with editing from A. Melatos, and has not been submitted for publication.

**Chapter 2** is published as *J. B. Carlin and A. Melatos*, Monthly Notices of the Royal Astronomical Society, 488, 4, 4890 (2019) [1]. This work was written primarily by the author, with scientific input and editing from A. Melatos. The calculation of glitch waiting time and size autocorrelations originally appeared in the thesis submitted for the degree of Master of Science (Physics) awarded to the author in 2018. Figure 2.2 originally appeared as Figure 4.5 in the above-mentioned Master’s thesis. All figures and tables are the work of the author.

**Chapter 3** is published as *J. B. Carlin, and A. Melatos*, Monthly Notices of the Royal Astronomical Society, 494, 3, 3383 (2020) [2]. It was written primarily by the author, with scientific input and editing from A. Melatos. All figures and tables are the work of the author.

**Chapter 4** is published as *J. B. Carlin, and A. Melatos*, The Astrophysical Journal, 917, 1 (2021) [3]. It was written primarily by the author, with scientific input and editing from A. Melatos. All figures are the work of the author.

**Chapter 5** is published as *J. B. Carlin, A. Melatos, and M. S. Wheatland*, The Astrophysical Journal, 948, 2 (2023) [4]. It was written primarily by the author, with scientific input and editing from A. Melatos and M. Wheatland. Appendix 5.A1 was written primarily by A. Melatos, but is included in this thesis for completeness. All figures and tables are the work of the author. An erratum is published as *J. B. Carlin, A. Melatos, and M. S. Wheatland*, The Astrophysical Journal, 953, 1 (2023) [5]. It is incorporated into the text of this chapter.

**Chapter 6** is published as *R. Abbott et al. (LIGO Scientific Collaboration, Virgo Collaboration, and KAGRA Collaboration)*, Physical Review D, 105, 2, 022002 (2022) [6]. It was written primarily by the author, with scientific input and editing from A. Melatos, and other members of the LVK collaboration. According to LVK policies, all members of the collaboration are listed as authors on the publication, in alphabetical order. The author was responsible for selecting the targets for the search, developing the scripts to run the search pipeline, running the search,

constructing and testing validation procedures for outliers, and calculating upper limits on detectable strain. The core search algorithms were first coded by Sofia Suvorova, Patrick Clearwater, and Lilli Sun [7, 8]. An interface to facilitate interacting with the underlying code was developed by Pat Meyers, Meg Millhouse, Hannah Middleton, and the author. The search is structured similarly to the search performed by Hannah Middleton in earlier LIGO data [9]. The analysis was reviewed within the collaboration by Pat Meyers and Evan Goetz. The followup search described in the final two paragraphs of Appendix 6.A3 was performed by Rodrigo Tenorio and David Keitel using the PyFSTAT pipeline [10], thus those paragraphs were written by them, not the author. All figures and tables are the work of the author.

**Chapter 7** summarizes the work in Chapters 2–6. It includes some exploratory future directions for the work in this thesis. It was written by the author, with editing from A. Melatos. All figures and tables are the work of the author.

The author also contributed to two other publications during their PhD candidature, which are not included for examination in this thesis, but are listed here for completeness.

- Millhouse et al. [11] studies how observed glitch rates scale with the spin frequency, spin frequency derivative (and combinations thereof). The author contributed edits to the manuscript, and scientific input regarding treatment of the likelihood function and related statistics.
- Jones et al. [12] presents a guide for two follow-up procedures for continuous gravitational wave candidates. The author contributed edits to the manuscript, and scientific input regarding the effective point spread function of the matched filtering statistic.

The author acknowledges funding support through the Australian Research Council (ARC) Centre of Excellence for Gravitational Wave Discovery (OzGrav) (project number CE170100004) and ARC Discovery Project DP170103625. The author is supported by an Australian Government Research Training Program Scholarship.

---

## Acknowledgments

---

It has been a long time coming. Over the last four-and-a-bit years I was at times excited, challenged, joyful, depressed, relieved, and more. With the support of many, I am at the finish line. My supervisor Andrew Melatos was correct in warning me when I started that it would not be all sunshine and roses. The “second-year blues” coincided neatly with the arrival of COVID-19, and the necessary mental, physical, and social readjustments to work out how to work from home in a vaguely productive manner. If I at all succeeded, it was due to the support of everyone below.

Foremost, I must thank Andrew. His curiosity, intellect, and broad interests have steered me and the projects I have worked on in many varied directions. Despite mostly finding results that seemed like dead-ends, there was always a nugget of knowledge or understanding to explore. His rigour and candour (some might un-generously add persnicketyness) has inspired me to see physics, models, and the world in a new light.

I am also grateful to my supervisory panel, Rob Evans, Andy Martin, and David Simpson. Their excellent advice helped me reign in some of the potential excesses of this thesis. I am also thankful for the research opportunities and mentorship that Rachel Webster and Michele Trenti offered me before I had even started my Masters degree. Their training allowed me to hit the ground running.

Thanks also to the Viterbi, NS/GW, and Astro groups at the University of Melbourne. It was missing the friendly and stimulating environment of the David Caro building’s third floor that made the shunting to working from home over 2020 and 2021 so hard.

Finally, I need to thank my family, friends, and partner for keeping me sane (mostly), work-life-balanced (sometimes), and not-*too*-distracted.

---

## Contents

---

ABSTRACT	i
DECLARATION	iii
PREFACE	iii
ACKNOWLEDGMENTS	vi
LIST OF FIGURES	xviii
LIST OF TABLES	xxi
1 INTRODUCTION	1
1.1 WHAT MODELS AND WHAT SIGNALS?	1
1.2 OBSERVATIONAL TAXONOMY OF NEUTRON STARS	2
1.3 PULSAR TIMING	5
1.3.1 Timing noise	6
1.3.2 Glitch detection	7
1.4 NEUTRON STAR STRUCTURE	7
1.5 PULSAR GLITCHES	8
1.5.1 Phenomenology and statistics	8
1.5.2 Glitch trigger mechanisms	11
Superfluid vortex avalanches	12
Crustquakes	12
Superfluid instabilities and other possibilities	12
1.6 STRESS ACCUMULATION AND RELAXATION	13
1.6.1 Solar flares	14
1.6.2 State-dependent Poisson process	14
1.7 CONTINUOUS GRAVITATIONAL WAVES	16
1.7.1 General relativity	16
1.7.2 Ground-based gravitational wave detectors	17
1.7.3 Continuous gravitational wave emission mechanisms	18
1.7.4 Standard signal model	19
1.7.5 Hidden Markov Models and wandering signals	21
1.7.6 Accreting millisecond X-ray pulsars	24
1.8 THESIS OUTLINE	28
2 AUTOCORRELATIONS IN PULSAR GLITCH WAITING TIMES AND SIZES	29
2.1 ABSTRACT	29

2.2	INTRODUCTION . . . . .	30
2.3	TIMING OBSERVATIONS . . . . .	30
2.3.1	Data . . . . .	30
2.3.2	Autocorrelations . . . . .	31
2.4	STATE-DEPENDENT POISSON PROCESS . . . . .	33
2.4.1	Meta-model . . . . .	33
2.4.2	Autocorrelations: qualitative predictions . . . . .	34
2.4.3	Autocorrelations: quantitative predictions . . . . .	35
2.5	WHAT DO AUTOCORRELATIONS TEACH US? . . . . .	38
2.5.1	Existing data . . . . .	38
2.5.2	Future data . . . . .	38
2.5.3	Combining auto- and cross-correlations . . . . .	39
2.5.4	Size and waiting time PDFs . . . . .	42
2.5.5	Physical implications . . . . .	42
2.6	CONCLUSIONS . . . . .	43
3	LONG-TERM STATISTICS OF PULSAR GLITCHES TRIGGERED BY A BROWNIAN STRESS ACCUMULATION PROCESS	44
3.1	ABSTRACT . . . . .	44
3.2	INTRODUCTION . . . . .	45
3.3	BROWNIAN STRESS ACCUMULATION . . . . .	46
3.3.1	Equation of motion . . . . .	46
3.3.2	Waiting time and size distributions . . . . .	47
3.3.3	Average waiting time . . . . .	48
3.3.4	Comparison with the SDP meta-model . . . . .	49
3.3.5	Inter-glitch spin wandering . . . . .	50
3.4	OBSERVABLE LONG-TERM STATISTICS . . . . .	50
3.4.1	Waiting time distribution . . . . .	52
3.4.2	Correlations and memory . . . . .	54
3.5	FALSIFYING THE BROWNIAN META-MODEL . . . . .	55
3.5.1	PSR J0537-6910 . . . . .	56
3.5.2	PSR J1740-3015 . . . . .	56
3.5.3	PSR J0534+2200 . . . . .	57
3.5.4	PSR J1341-6220 . . . . .	57
3.5.5	PSR J0835-4510 . . . . .	58
3.5.6	PSR J0631+1036 . . . . .	58
3.6	POPULATION TRENDS . . . . .	58
3.7	CONCLUSIONS . . . . .	59
	APPENDIX 3.A1 ANALYTIC SOLUTION OF THE FOKKER-PLANCK EQUATION FOR THE INTER-GLITCH STRESS DISTRIBUTION . . . . .	61
	APPENDIX 3.A2 CONDITIONAL WAITING TIME PDF WITHOUT THE REFLECTING BOUNDARY . . . . .	62
4	LONG-TERM STATISTICS OF PULSAR GLITCHES DUE TO HISTORY-DEPENDENT AVALANCHES	63
4.1	ABSTRACT . . . . .	63
4.2	INTRODUCTION . . . . .	64

4.3	PINNING THRESHOLD DISTRIBUTION . . . . .	66
4.3.1	Standard picture . . . . .	66
4.3.2	Available versus occupied sites . . . . .	67
4.3.3	Unpinning and repinning . . . . .	68
4.3.4	Equation of motion for the distribution of occupied pinning sites . . . . .	70
4.4	STATE-DEPENDENT POISSON PROCESS . . . . .	71
4.4.1	Equation of motion for the stress . . . . .	72
4.4.2	Monte Carlo simulations . . . . .	72
4.4.3	Qualitative results . . . . .	73
4.4.4	Differences from previous meta-models . . . . .	75
4.4.5	Mutual friction . . . . .	77
4.5	OBSERVABLE LONG-TERM STATISTICS . . . . .	77
4.5.1	Waiting time and size PDFs . . . . .	78
4.5.2	Cross- and autocorrelations . . . . .	78
4.5.3	Aftershocks and precursors . . . . .	81
4.6	ASTRONOMICAL OBSERVATIONS . . . . .	83
4.7	CONCLUSION . . . . .	84
APPENDIX 4.A1 NON-MAXIMAL STRESS-CRUST COUPLING . . . . .		85
APPENDIX 4.A2 ENSEMBLE-AVERAGED STRESS THRESHOLD DISTRIBUTION AT OC- UPIED PINNING SITES . . . . .		86
APPENDIX 4.A3 RELATION TO POINT PROCESSES AND TIME SERIES MODELING . . .		87
5	A STATISTICAL SEARCH FOR A UNIFORM TRIGGER THRESHOLD IN SOLAR FLARES FROM INDIVIDUAL ACTIVE REGIONS . . . . .	89
5.1	ABSTRACT . . . . .	89
5.2	INTRODUCTION . . . . .	90
5.3	STATE-DEPENDENT POISSON PROCESS . . . . .	91
5.3.1	Equation of motion . . . . .	91
5.3.2	Monte Carlo automaton . . . . .	92
5.3.3	Mapping to solar flares . . . . .	92
5.4	OBSERVABLE SIGNATURES OF A RAPIDLY-DRIVEN PROCESS . . . . .	94
5.4.1	Slow driver . . . . .	94
5.4.2	Fast driver . . . . .	95
5.4.3	Heuristic test for a threshold-driven process . . . . .	95
5.5	GOES SOFT X-RAY OBSERVATIONS . . . . .	96
5.5.1	Flare data . . . . .	96
5.5.2	Obscuration and flare size bias of subsequent flares after a large flare . . . . .	97
5.5.3	Aggregate size and waiting time statistics . . . . .	98
5.6	DISAGGREGATED DATA IN INDIVIDUAL ACTIVE REGIONS . . . . .	99
5.6.1	Waiting time and size PDFs versus flare rate . . . . .	99
5.6.2	Size-waiting-time cross-correlations . . . . .	102
5.6.3	Matching the shapes of $p(\Delta t)$ and $p(\Delta s)$ . . . . .	104
5.6.4	Autocorrelations and longer term memory . . . . .	106
5.7	CONCLUSION . . . . .	106

APPENDIX 5.A1 MAGNETIC ENERGY DENSITY AS A STRESS VARIABLE IN AN ACTIVE REGION . . . . .	108
APPENDIX 5.A2 HIERARCHICAL BAYESIAN FRAMEWORK . . . . .	109
5.A2.1 Likelihood and Bayes' theorem . . . . .	110
5.A2.2 Population-level parameter estimation . . . . .	110
5.A2.3 Validation with synthetic data . . . . .	111
5.A2.4 Likelihood based on the average waiting time . . . . .	112
APPENDIX 5.A3 CLEANING GOES FLARE SUMMARY DATA . . . . .	112
APPENDIX 5.A4 LOG-NORMAL WAITING TIME DISTRIBUTIONS . . . . .	113
APPENDIX 5.A5 EXAMPLE FITS FOR INDIVIDUAL ACTIVE REGIONS . . . . .	113
 6 SEARCH FOR CONTINUOUS GRAVITATIONAL WAVES FROM 20 ACCRETING MILISECOND X-RAY PULSARS IN O3 LIGO DATA . . . . .	<b>116</b>
6.1 ABSTRACT . . . . .	116
6.2 INTRODUCTION . . . . .	117
6.3 SEARCH ALGORITHM . . . . .	118
6.3.1 HMM . . . . .	118
6.3.2 $\mathcal{J}$ -statistic . . . . .	119
6.4 TARGETS . . . . .	120
6.5 SEARCH PARAMETERS . . . . .	122
6.5.1 Coherence time and frequency binning . . . . .	122
6.5.2 Number of orbital templates . . . . .	123
6.5.3 Thresholds . . . . .	126
6.5.4 Computing resources . . . . .	126
6.6 O3 DATA . . . . .	127
6.7 VETOES . . . . .	127
6.7.1 Known line veto . . . . .	127
6.7.2 Single interferometer veto . . . . .	128
6.7.3 Off-target veto . . . . .	128
6.8 O3 SEARCH RESULTS . . . . .	128
6.8.1 IGR J18245–2452 . . . . .	130
6.8.2 IGR J00291+5934 . . . . .	130
6.8.3 MAXI J0911–655 . . . . .	131
6.8.4 XTE J0929–314 . . . . .	131
6.8.5 IGR J16597–3704 . . . . .	131
6.8.6 IGR J17062–6143 . . . . .	131
6.8.7 IGR J17379–3747 . . . . .	131
6.8.8 SAX J1748.9–2021 . . . . .	132
6.8.9 NGC 6440 X–2 . . . . .	132
6.8.10 IGR J17494–3030 . . . . .	132
6.8.11 Swift J1749.4–2807 . . . . .	132
6.8.12 IGR J17498–2921 . . . . .	132
6.8.13 IGR J17511–3057 . . . . .	132
6.8.14 XTE J1751–305 . . . . .	133
6.8.15 Swift J1756.9–2508 . . . . .	133
6.8.16 IGR J17591–2342 . . . . .	133

6.8.17	XTE J1807–294 . . . . .	133
6.8.18	SAX J1808.4–3658 . . . . .	133
6.8.19	XTE J1814–338 . . . . .	134
6.8.20	HETE J1900.1–2455 . . . . .	134
6.9	TARGET-OF-OPPORTUNITY SEARCH: SAX J1808.4–3658 IN OUTBURST . . .	134
6.9.1	Search parameters . . . . .	135
6.9.2	Search results . . . . .	135
6.10	FREQUENTIST UPPER LIMITS . . . . .	135
6.10.1	Upper limit procedure in a sub-band . . . . .	136
6.10.2	Upper limits . . . . .	137
6.10.3	Comparison to expected strain from AMXPs . . . . .	138
6.10.4	Astrophysical implications . . . . .	141
6.11	CONCLUSIONS . . . . .	142
APPENDIX 6.A1	THRESHOLD SETTING . . . . .	144
6.A1.1	Exponential tail method . . . . .	144
6.A1.2	Percentile method . . . . .	145
6.A1.3	Comparison of methods . . . . .	145
6.A1.4	Off-target thresholds . . . . .	146
6.A1.5	Probability that a candidate arises due to noise . . . . .	146
APPENDIX 6.A2	FULL SEARCH RESULTS AND SURVIVOR FOLLOW-UP . . . . .	147
6.A2.1	Additional follow-up for survivors . . . . .	148
APPENDIX 6.A3	SURVIVOR FOLLOW-UP FOR TARGET-OF-OPPORTUNITY SEARCH CANDIDATE . . . . .	155
7	CONCLUSIONS AND FUTURE DIRECTIONS	157
7.1	UNDERSTANDING PULSAR GLITCHES THROUGH THE LENS OF STRESS-ACCUMULATION AND RELAXATION META-MODELS . . . . .	157
7.2	ARE SOLAR FLARES THE RESULT OF STRESS APPROACHING A THRESHOLD BEFORE EACH EVENT? . . . . .	160
7.3	SEARCHING FOR CONTINUOUS GRAVITATIONAL WAVES FROM ACCRETING MILLISECOND X-RAY PULSARS . . . . .	161
REFERENCES		166

---

## List of Figures

---

1.1	Schematic showing the three major topics of this thesis in red, while the overarching theme that links all the topics is in blue. Pulsar glitches and continuous gravitational waves are connected in yellow by both having to do with neutron star timing; glitches are seen as sudden deviations from a steady timing solution, while a sensitive continuous gravitational wave search is enabled by pulsar timing providing reference ephemerides. A continuous wave detection would result in an independent timing solution. Pulsar glitches and solar flares are connected in green via the underlying mechanism with which they operate, namely that stress builds up steadily over time, and is released suddenly. Long-term sequences of waiting times between events, and event sizes, allow for falsification of these stress-relax models. . . . .	2
1.2	Period $P$ and period derivative $\dot{P}$ diagram for over 3300 objects retrieved from the ATNF Pulsar Catalog. Black crosses sitting at the bottom of the figure are pulsars which do not have a recorded $\dot{P}$ . Orange boxes indicate pulsars with at least one recorded glitch, and are the objects of interest for Chapters 2–4 of this thesis. Purple stars mark the known AMXPs, which are the objects of interest for Chapter 6 of this thesis. Dotted and dashed lines show lines of constant magnetic field at the poles and characteristic age respectively. . . . .	4
1.3	Representative ASDs for the Livingston (L1) LIGO detector in S5 (purple curve) and O3b (orange curve). The ASDs are representative in that they are calculated from $\sim 5$ min of data for a period of time in which the detectors are operating within their modal binary neutron star detection range for that observing run, see Weinstein and Privitera [13] and Goetz [14] for details. . . . .	18
1.4	Illustration demonstrating the Viterbi algorithm finding a wandering signal in noise. The color for each state and time represents the likelihood $L_{o_i q_j}$ , with purple and yellow corresponding to low and high relative $L_{o_i q_j}$ respectively. In panel (a) we have injected a wandering signal into noise. In panel (b) we see the Viterbi algorithm dynamically pruning the possible trajectories of the signal in white. In panel (c) we highlight the maximum <i>a posteriori</i> trajectory in green, i.e. the trajectory that maximizes Equation (1.21). Finally, in panel (d) we reveal the trajectory of the injected signal in blue, and show that the trajectory recovered by the Viterbi algorithm overlaps with it. . . . .	23

2.1	Measured autocorrelation coefficient between consecutive waiting times, $\rho_{\Delta t}$ (top row, orange vertical lines), and consecutive sizes, $\rho_{\Delta X}$ (bottom row, purple vertical lines), for the five most active glitching pulsars. The null distribution (colored histogram in each panel) is estimated using a bootstrap permutation method, as described in the text. See Table 2.1 for numerical values of $\rho_{\Delta t}$ and $\rho_{\Delta X}$ . . . . .	32
2.2	Autocorrelations between consecutive waiting times ( $\rho_{\Delta t}$ , orange curves) and sizes ( $\rho_{\Delta X}$ , purple curves) for glitches generated using the state-dependent Poisson process outlined in Section 2.4.1. Simulation parameters: 100 logarithmically spaced $\alpha$ values, $10^5$ glitches per $\alpha$ value, rate function as given by (2.4), $\beta = 10^{-2}$ for power-law $\eta$ (top-left panel), $\mu_G = 0.5$ and $\sigma_G = 0.125$ for fixed and stretchable Gaussian $\eta$ (bottom-left and bottom-right panels respectively). The uniform $\eta$ (top right panel) has no free parameters. Explicit functional forms for each $\eta(\Delta X   X_p)$ are presented by Carlin and Melatos [15, Table 1]. . . . .	36
2.3	Autocorrelations generated by the state-dependent Poisson process. Top panel: $\rho_{\Delta t}$ when $\eta(\Delta X   X_p)$ is a power law and $\beta$ is changed from $10^{-2}$ (solid curve) to $10^{-3}$ (dashed curve) to $10^{-4}$ (dotted curve). Bottom panel: $\rho_{\Delta X}$ when $\eta(\Delta X   X_p)$ is a stretchable Gaussian and $\mu_G$ is changed from 0.2 (dashed curve) to 0.5 (solid curve) to 0.8 (dotted curve). Simulation parameters: 100 logarithmically spaced $\alpha$ values, $10^5$ glitches per $\alpha$ value, rate function as given by (2.4), power-law index fixed at $-1.5$ (top panel), $\sigma_G = 0.125$ (bottom panel). Explicit functional forms for $\eta(\Delta X   X_p)$ are presented by Carlin and Melatos [15, Table 1]. . . . .	37
2.4	Theoretical (solid curves) and measured (dashed lines and shaded bands) correlations for PSR J0534+2200. Top panel: Size-forward waiting time cross-correlation ( $\rho_+$ , green curves), and size-backward waiting time cross-correlation ( $\rho_-$ , pink curves). Bottom panel: Waiting time autocorrelation ( $\rho_{\Delta t}$ , orange curves), and size autocorrelation ( $\rho_{\Delta X}$ , purple curves). The shaded bands indicate the 95% confidence interval for each observed correlation. Model parameters common to both panels: power law $\eta$ , $\beta = 10^{-2}$ , power-law index of $-1.5$ . . . . .	40
2.5	As in Figure 2.4, except for PSR J0537–6910, and with a stretchable Gaussian $\eta$ in both panels. Model parameters common to both panels: $\mu_G = 0.5$ , $\sigma_G = 0.125$ . . . . .	41
3.1	Visual comparison of the evolution of the internal, unobservable stress, $X(t)$ , for four different values of $\xi/\sigma^2$ . The red dashed line indicates the stress threshold, set to $X_c = 1$ , where glitches are triggered. The same sequence of glitch sizes, drawn from a power-law $\eta(\Delta X)$ distribution, is used in each panel. The small black tick marks indicate the epoch of each glitch. . . . .	48

3.2	Comparison between two representative time series of stress (top panels) and crust angular velocity (bottom panels) from the SDP meta-model (left) and the Brownian meta-model (right). A deterministic, secular torque drives the stress between glitches in the SDP meta-model, whereas a stochastic Langevin torque drives the stress between glitches in the Brownian meta-model. Black tick marks in the top panels indicate the glitch epochs. Parameters for SDP meta-model: $\alpha = 1$ , power law conditional jump distribution, as described in equations (17) and (19) of Fulgenzi et al. [16] respectively. Parameters for Brownian meta-model: $\mu = 50$ , power law stress-release distribution, as in (3.15). Parameters shared between meta-models: $\delta = -1.5$ , $\beta = 10^{-2}$ in (3.15). . . . .	51
3.3	Waiting time PDF, $p(\Delta t)$ , for four values of $\mu$ on log-linear (left panel) and log-log (right panel) scales. The stress release distribution, $\eta(\Delta X)$ , is a power law, as in (3.15), with $\delta = -1.5$ and $\beta = 10^{-2}$ . . . . .	52
3.4	As for Figure 3.3 but with a Gaussian $\eta(\Delta X)$ , as in (3.16), with $\mu_G = 0.5$ and $\sigma_G = 0.125$ . . . . .	53
3.5	As for Figure 3.3 but with a log-normal $\eta(\Delta X)$ , as in (3.17), with $\mu_{LN} = -1$ and $\sigma_{LN} = 0.5$ . . . . .	53
3.6	Spearman cross-correlation between the size of a glitch and the waiting time until the next glitch versus $\mu$ . At 200 logarithmically spaced values of $\mu$ , $10^5$ waiting times and sizes are drawn from (3.8) and (3.15) respectively, using each generated size to determine the starting point for the next inter-glitch interval and hence waiting time. . . . .	54
4.1	A toy example illustrating schematically the evolution of $g(X_{th}, t)$ during a sequence of four glitches, with $X(t_1^+) < X(t_3^+) < X(t_2^+) < X_{th,max} < X(t_4^-)$ , where $g(X_{th}, t_1^-) = \phi(X_{th})$ is the uniform distribution between $0 \leq X_{th} \leq X_{th,max}$ . The colors correspond to how many glitches occur in the time elapsed since vortices unpin from pinning sites with a certain threshold. Darker colors indicate that the vortices have stayed pinned during more events. . . . .	70
4.2	Evolution of $X$ (main panel) and $g(X_{th}, t)$ (sub-panels) across four glitches at $t_1, \dots, t_4$ , generated via the automaton outlined in Section 4.4.2. Parameters: $\alpha = 0.2$ , $X_{th,max} = 0.95$ (indicated in both the main panel and sub-panels with a red dashed line), $K = X_{th,max}$ . $X$ and $X_{th}$ are in units of $X_c$ and $t$ is in units of $X_c I_C / N_{em}$ . . . . .	74
4.3	As in Figure 4.2 but with $\alpha = 1$ . . . . .	74
4.4	As in Figure 4.2 but with $\alpha = 10$ . . . . .	75
4.5	Long-term qualitative behavior of $X$ for three different values of $\alpha = 0.2$ , 1, and 10 in the top, middle and bottom panel respectively. Parameters: $X_{th,max} = 0.95$ (indicated with a red dashed line in each panel), $K = X_{th,max}$ . . . . .	76
4.6	Fraction of glitches that reset the system as a function of $\alpha$ for three different values of $X_{th,max}$ . Parameters: $N = 10^5$ glitches generated at 50 logarithmically spaced values of $\alpha$ for each value of $X_{th,max}$ , with $K = X_{th,max}$ . . . . .	77

4.7	Waiting time, $\Delta t$ , and size, $\Delta X$ , PDFs on the top and bottom panel respectively. Parameters: $N = 10^7$ simulated glitches for each value of $\alpha$ , $X_{\text{th},\text{max}} = 0.95$ (indicated with a red dashed line in each panel), $K = X_{\text{th},\text{max}}$ . . . . .	79
4.8	Top panel: Forward cross-correlation, $\rho_+$ , and backward cross-correlation, $\rho_-$ , as a function of $\alpha$ (orange and purple curves respectively). Bottom panel: Auto-correlation between waiting times, $\rho_{\Delta t}$ , and sizes, $\rho_{\Delta X}$ , as a function of $\alpha$ (red and blue curves respectively). Parameters: $N = 10^5$ glitches generated at 100 logarithmically spaced values of $\alpha$ , $X_{\text{th},\text{max}} = 0.95$ , $K = X_{\text{th},\text{max}}$ . . . . .	80
4.9	Top panel: PDFs of all waiting times, $\Delta t$ , waiting times just prior to a system-resetting glitch, $\Delta t_{\text{pre}}$ , and waiting times just after a system-resetting glitch, $\Delta t_{\text{post}}$ . Bottom panel: Corresponding PDFs for sizes. Parameters: $\alpha = 10$ , $N = 10^8$ total glitches, $\sim 10^5$ of which reset the system completely, $X_{\text{th},\text{max}} = 0.95$ , $K = X_{\text{th},\text{max}}$ . . . . .	82
4.10	Waiting time PDFs for $K = 0.6$ (left panel) and $K = 0.01$ (right panel). Parameters: $N = 10^7$ simulated glitches for each value of $\alpha$ , with $X_{\text{th},\text{max}} = 0.95$ . The black dashed vertical line indicates $\Delta t = K$ in each panel. . . . .	86
4.11	Ensemble averaged PDF of occupied pinning sites $g_s(X_{\text{th}}) = \langle g(X_{\text{th}}, t) \rangle$ calculated empirically for three values of $\alpha$ . Parameters: $10^7$ samples of $g(X_{\text{th}})$ for each value of $\alpha$ , $X_{\text{th},\text{max}} = 0.95$ , with $K = X_{\text{th},\text{max}}$ . . . . .	87
5.1	Top panels: qualitative behavior of the evolution of the stress, $X(t)$ , in the SDP process in the two main regimes, slowly driven (left panel, $\alpha = 10$ ), and rapidly driven (right panel, $\alpha = 0.1$ ). Bottom panels: predicted waiting time and size PDFs $p(\Delta t)$ and $p(\Delta X)$ respectively in the above regimes. For all panels we fix $\eta[\Delta X_i   X(t_i^-)] \propto (\Delta X_i)^{-3/2} H[\Delta X_i - 10^{-2} X(t_i^-)]$ , where the Heaviside function $H(\dots)$ enforces a minimum stress-release size of 1% of the stress in the system, ensuring integrability. The histograms in the bottom panels each include $N = 10^7$ events. . . . .	92
5.2	Forward, $\rho_+$ (solid curve), and backward, $\rho_-$ (dashed curve), cross-correlations between event sizes and waiting times for $10^2$ values of $10^{-2} \leq \alpha \leq 10^2$ , with $N = 10^5$ events generated per value of $\alpha$ . We fix $\eta[\Delta X_i   X(t_i^-)]$ to the same functional form as in Figure 5.1. A version of this figure first appeared as figure 13 in Fulgenzi et al. [16]. . . . .	94
5.3	Top panel: Probability mass function of the number of flares per active region, $N_k$ , for all active regions with $N_k \geq 5$ . Regions with $0 \leq N_k \leq 4$ are excluded, as the number of samples per region is too small for the statistical tests in this paper. Bottom panel: PDF of the flare rate, $\lambda_k$ , for all active regions with $N_k \geq 5$ , binned into 50 uniformly spaced bins between $0 \text{ hours}^{-1}$ and $0.5 \text{ hours}^{-1}$ . . . . .	97

5.4	Top panel: PDF $p(\Delta t)$ of waiting times (thick black stepped curve), $\Delta t$ , aggregated over all active regions with $N_k \geq 5$ , binned into 50 linearly spaced bins between the minimum and maximum $\Delta t$ in the full, unmasked catalog. Overlaid are the best fit estimates of an exponential (blue dashed curve), power law (orange dotted curve), and log-normal (green dot-dashed curve) PDF. Bottom panel: As for top panel, but for sizes $\Delta s$ , and the data is binned into 50 logarithmically spaced bins. The grey region in the bottom panel shows the difference between the size PDFs from the masked and full catalogs (see Section 5.5.2). . . . .	100
5.5	Top panel: Proportion of active regions with waiting time PDF fitted best by three possible shapes (a power law, an exponential, and a log-normal) as determined by the AICc, as a function of the region's flare rate, $\lambda_k$ . The CDF of $\lambda_k$ is overlaid in black. Bottom panel: As in the top panel, but for size PDFs. . . . .	101
5.6	Top panel: PDF of forward cross-correlation, $\rho_{+,k}$ (black stepped curve), and backward cross-correlation, $\rho_{-,k}$ (black dashed curve), for all active regions with $N_k \geq 5$ . Data binned into 30 uniformly spaced bins between $\rho_{\pm,k} = -1$ and $\rho_{\pm,k} = 1$ . Bottom panel: Scatter plot of the forward cross-correlation, $\rho_{+,k}$ , and flare rate, $\lambda_k$ , for all regions with $N_k \geq 10$ . The dashed grey line corresponds to $\rho_{+,k} = 0$ . . . . .	103
5.8	Posterior predictive check demonstrating the recovery of injected population-level parameters. The weakly informative priors set on the hyper-parameters $\tau$ , $\xi$ , and $\beta$ are shown in green, histograms of samples from the injected population parameters are shown in red, while histograms of samples from the posterior distributions are shown in blue. See text in Appendix 5.A2.3 for details on the procedure. . . . .	112
5.9	Complementary cumulative distribution functions (CCDFs) for four arbitrary but representative active regions with $N_k \geq 20$ . The distribution that best describes the data in each panel (black stepped curve), according to the AICc, is in bold type-face in the legend for each panel. The grey regions in the bottom panels indicate $\Delta s \leq 10^{-3} \text{Jm}^{-2}$ , i.e. where the masking described in Section 5.5.2 is applied. . . . .	115
6.1	Summary of search results across all targets and sub-bands with $\mathcal{L} > \mathcal{L}_{\text{th}}$ . The different symbols correspond to candidates from different targets. The ordinate shows $p_{\text{noise}}$ for each candidate, the probability that a search of that candidate's sub-band in pure noise would return at least one candidate at least as loud as the one seen. The color of each candidate indicates $\mathcal{L}$ (see color bar at right). Candidates that are eliminated by the vetoes outlined in Sec. 6.7 are not shown for clarity. Details on the search results are in Sec. 6.8 and Appendix 6.A2. . . . .	129

6.2	Search results for IGR J18245–2452. Black crosses indicate the terminating frequency and $\mathcal{L}$ for the most likely path through the sub-band for each binary template. The vertical blue dashed (green dot-dashed) lines correspond to the threshold set via Gaussian (off-target) noise realizations, $\mathcal{L}_{\text{th},G}$ ( $\mathcal{L}_{\text{th},\text{OT}}$ ), in each sub-band. Solid red lines in the right panel indicate the peak frequency of known instrumental lines in the Hanford detector; the orange band indicates the width of the line in the detector frame and the yellow band indicates the increased effective width due to Doppler broadening, as described in Sec. 6.7.1. Multiple overlapping orange bands creates the red bands. The sub-band around 508.8 Hz is especially noisy due to test mass suspension violin mode resonances [524]. The transparency of crosses in sub-bands with many templates, is adjusted relative to the maximum $\mathcal{L}$ in that sub-band for clarity. . . . .	130
6.3	Kernel density estimate of the PDF of the constraints on ellipticity $\epsilon^{95\%}$ (left panel) and dimensionless $r$ -mode amplitude $\alpha^{95\%}$ (right panel) via Eqs. (6.14) and (6.15) respectively. Both PDFs are normalized to a height of one. The black dashes in both panels correspond to the individual estimates of $\epsilon^{95\%}$ or $\alpha^{95\%}$ from each target. . . . .	141
6.4	Search results for each target and sub-band, laid out as in Fig 6.2. Black crosses indicate the frequency and $\mathcal{L}$ for the most likely path through the sub-band for each binary template. The vertical blue dashed (green dot-dashed) lines correspond to the threshold set via Gaussian (off-target) noise realizations, $\mathcal{L}_{\text{th},G}$ ( $\mathcal{L}_{\text{th},\text{OT}}$ ), in each sub-band. Solid red lines indicate the peak frequency of known instrumental lines in the detectors; the red band indicates the width of the line and the yellow band indicates the increased effective width due to Doppler broadening, as described in Sec. 6.7.1. The transparency of crosses in sub-bands with many templates, e.g. the sub-bands of IGR J16597–3704, is adjusted relative to the maximum $\mathcal{L}$ in that sub-band for clarity. . . . .	153
6.5	Top panels: frequency paths, $f(t)$ , for candidates with $p_{\text{noise}} \leq 0.1$ . The terminating frequency bin, $f(N_T)$ , is subtracted and displayed in the title of each figure for clarity. Faint horizontal grey lines demarcate frequency bins of size $\Delta f = 5.787037 \times 10^{-7}$ Hz, while faint vertical grey lines demarcate chunks of length $T_{\text{drift}} = 10$ d. Bottom panels: the cumulative log-likelihood along the frequency path relative to the average sum log-likelihood needed to reach $\mathcal{L}_{\text{th}}$ , $C\mathcal{L} \equiv \sum_{i=0}^{i=t} [\mathcal{L}(i) - \mathcal{L}_{\text{th}}/N_T]$ , where $\sum_{i=0}^{i=t} \mathcal{L}(i)$ is $\ln P(Q^* O)$ from Eq. (6.2) truncated after the $t$ -th segment. The horizontal blue dashed line corresponds to $\sum_{i=0}^{i=t} \mathcal{L}(i) = t\mathcal{L}_{\text{th}}/N_T$ . The grey shaded regions in both top and bottom panels correspond to the segments which have no SFTs and are therefore filled with a uniform log-likelihood, as described in Sec. 6.6. . . . .	154
6.6	$\mathcal{L}$ , as represented by the color of each pixel, calculated at 3721 regularly spaced sky locations in a $100 \text{ arcmin}^2$ patch of sky, centered on IGR J16597–3704. See text in Appendix 6.A2.1 for details. . . . .	155

- 7.1 Template placement in the  $P$ - $T_{\text{asc}}$  space for the  $2f_\star$  subband of Swift J1756.9–2508. Black dots correspond to the templates in the O3 search present in Chapter 6. The purple ellipse is the true  $3\sigma$  joint prior on these parameters, and the green crosses indicate which templates lie within this prior.  $P_{\text{central}}$  and  $T_{\text{asc},\text{central}}$  refer to the central  $P$  and propagated  $T_{\text{asc}}$  values for this target, as recorded in Table 6.1. . . . . 163
- 7.2 Detectable strain  $h_0^{95\%}$  as a function of the threshold  $\mathcal{L}_{\text{th}}$  for the  $2f_\star$  subband of Swift J1756.9–2508. The original  $\mathcal{L}_{\text{th}}$  used in the O3 search, and corresponding  $h_0^{95\%}$ , is marked with a red dashed line. The updated  $\mathcal{L}_{\text{th}}$  obtained by restricting the search space in  $P$ - $T_{\text{asc}}$  to only the templates contained within the true joint prior, as shown in Figure 7.1, results in an updated  $h_0^{95\%}$ , and is marked with a green dashed line. . . . . 164

---

## List of Tables

---

1.1	Pulsar name, number of recorded glitches $N$ , best-fitting waiting time PDF $p(\Delta t)$ , size PDF $p(\Delta\nu/\nu)$ , forward cross-correlation $\rho_+$ , backward cross-correlation $\rho_-$ , waiting time autocorrelation $\rho_{\Delta t}$ , and size autocorrelation $\rho_{\Delta\nu/\nu}$ for the eight pulsars with $N \geq 10$ . The distribution that fits the waiting time and size PDFs best is determined via the AICc. The 95% confidence intervals for the Spearman cross-correlation coefficients are calculated via Equation (2.6). The top four pulsars are “Poisson-like”, while the bottom four are “quasiperiodic”, see the text for details. Abbreviations are E, PL, LN, and G for exponential, power-law, log-normal and Gaussian respectively. . . . .	9
1.2	Non-exhaustive list of algorithms and/or detection statistics used to search for continuous gravitational wave signals from neutron stars in binary orbits. “TD” refers to a search performed in the time (rather than frequency) domain. “Sco X-1” refers to Scorpius X-1, a LMXB discussed further in Section 1.7.6. Directed searches have a fixed sky position (i.e. the target is known from electromagnetic observations), but search a wide frequency band. Targeted searches have a fixed sky position, and fix the gravitational wave phase evolution to an exact harmonic of the electromagnetically observed phase evolution. Blind searches are not targeting a known system, but instead search the whole sky and a wide frequency band. Narrowband searches have a fixed sky position, but search a narrow frequency band around harmonics of the electromagnetically observed spin frequency. O1, O2, and O3 refer to Observing Runs 1, 2, and 3 respectively of the LVK. S5 and S6 refer to Science Runs 5 and 6 respectively of the LIGO detectors. Only searches using the latest data searched (fourth column) are listed in the sixth column. . . . .	22
2.1	Pulsar name, number of glitches ( $N$ ), Spearman autocorrelation coefficient ( $\rho$ ), and associated p-value for waiting times (subscript $\Delta t$ ) and sizes (subscript $\Delta X$ ) for the five pulsars with the most recorded glitches. The p-value is estimated using a bootstrap permutation method, as described in the text. . . . .	33
2.2	Acceptable values of $\alpha$ , given a functional form of $\eta$ , for which the state-dependent Poisson process automaton produces cross-correlations and autocorrelations that all lie within the 95% confidence interval of the correlations observed in five pulsars. See text for details. . . . .	41

3.1	Pulsar name, number of glitches ( $N$ ), Spearman correlation coefficient between glitch size and subsequent waiting time ( $\rho_+$ ), associated p-value, and the 95% confidence interval (CI). The last two columns indicate the functional form of the best-fitting distribution for glitch sizes, $p(\Delta X)$ , and waiting times, $p(\Delta t)$ [17–19]. . . . .	56
5.1	Anomalous active region numbers found in the <i>GOES</i> flare summary data by checking whether one has $\Delta t_{i,k} < 14$ days for $1 \leq i \leq N_k - 1$ for each active region. Corrected values are determined manually, by considering the context of what active regions are present at the time of the anomalous flare at a similar latitude. Corrected values of “–” indicate that we cannot identify a reasonable active region to associate with the anomalous flare. . . . .	114
6.1	Target list: position (RA and Dec), orbital period ( $P$ ), projected semi-major axis in light-seconds ( $a_0$ ), time of passage through the ascending node as measured near the time of the most recent outburst ( $T_{\text{asc}}$ ), the time of passage through the ascending node as propagated to the start of O3 ( $T_{\text{asc}, \text{O3}}$ ), as described in Sec. 6.5.2, and frequency of observed pulsations ( $f_\star$ ). Numbers in parentheses indicate reported $1\sigma$ errors (68% confidence level), unless otherwise noted. All objects have positional uncertainty $\leq 1$ s in RA and $\leq 0.5''$ in Dec. . . . .	121
6.2	Starting frequencies, $f_s$ , for each $\sim 0.61$ Hz-wide sub-band, number of templates needed to cover the $P$ and $T_{\text{asc}}$ domains in that sub-band, $N_P$ and $N_{T_{\text{asc}}}$ respectively, and the total number of templates for each sub-band, $N_{\text{tot}} = N_P N_{T_{\text{asc}}}$ . The projected semi-major axis $a_0$ is known precisely enough that we have $N_{a_0} = 1$ for each sub-band. . . . .	125
6.3	Upper limits on the detectable gravitational wave strain at a 95% confidence level, $h_0^{95\%}$ , in each of the sub-bands for each target. See Sec. 6.10.1 for details on how they are estimated, and the precision to which they are known. Upper limits are not estimated in sub-bands marked with a “–” as these sub-bands are highly contaminated with known noise lines. . . . .	137
6.4	Full caption on previous page. . . . .	140
6.5	Target, starting frequency, $f_s$ , for each $\sim 0.61$ Hz-wide sub-band, threshold calculated using Gaussian noise realizations and the exponential tail method, $\mathcal{L}_{\text{th}, \text{G}}^e$ , and threshold calculated using off-target noise realizations and the percentile method, $\mathcal{L}_{\text{th}, \text{OT}}^p$ . All thresholds are calculated with $\alpha_{N_{\text{tot}}} = 0.3$ . . . . .	147
6.6	Orbital template, $(P, a_0, T_{\text{asc}})$ , terminating frequency bin, $f(N_T)$ , log-likelihood, $\mathcal{L}$ , and the probability that a search of the candidate’s sub-band in pure noise would return a candidate just as loud, $p_{\text{noise}}$ , for the 16 candidates with $\mathcal{L} > \mathcal{L}_{\text{th}}$ that cannot be eliminated by any of the vetoes detailed in Sec. 6.7. . . . .	148

- 6.7 Orbital template, ( $P$ ,  $a_0$ ,  $T_{\text{asc}}$ ), frequency,  $f$ , log-likelihood,  $\mathcal{L}$ , and the probability of seeing a candidate at least this loud in pure noise,  $p_{\text{noise}}$ , for the remaining candidate from the target-of-opportunity, 24 d coherent search when SAX J1808.4–3658 was in outburst. The candidate cannot be eliminated by any of the vetoes detailed in Sec. 6.7. . . . . 156

# CHAPTER 1

---

## Introduction

---

### 1.1. WHAT MODELS AND WHAT SIGNALS?

Modern physics involves a constant iteration between theoretical model-building, new data collection, and the attempted falsification of models with that data. This thesis is concerned with pulsar glitches, solar flares, and continuously-emitted gravitational waves from neutron stars in accreting binary systems. While these topics are disparate, there is overlap in the methodology with which specific, bespoke statistical models are built to test and explore the underlying physics.

The connections are outlined diagrammatically in Figure 1.1. Rapidly-rotating neutron stars are often seen as pulsars, with remarkably regular pulsed radio emission. These radio pulsations are timed using phase-connected models. The predictable spin of some pulsars is sporadically interrupted by timing irregularities known as “glitches”. These glitches are suspected to arise from the sudden relaxation of steadily-built-up stress in the interior. An analogous phenomenon of stress build-up and release is believed to drive solar flares. Stress-relax models are falsifiable using long-term statistics calculated from the observed sequences of waiting times between and sizes of events. The spin of neutron stars in binary systems is modulated due to accretion from a companion star, and possibly gravitational wave emission if such accretion builds a time-varying mass quadrupole. Precision timing using pulsations observed in the X-ray emission from the neutron star in these systems enables highly-sensitive searches for continuous gravitational waves.

The remainder of this chapter serves as an introduction and literature review of the underlying theoretical physics and observational evidence of the above phenomena. In Section 1.2 we present a taxonomical overview of neutron stars from an observational perspective. In Section 1.3 we discuss pulsar timing and glitch detection. In Section 1.4 we review what is known about the structure of neutron stars. In Section 1.5 we discuss the phenomenology and statistics of glitches, and how they are triggered. We shift focus to general statistical models built to understand complex systems, including solar flares, which undergo stress-accumulation and release in Section 1.6. In Section 1.7 we introduce gravitational wave emission in general, the specific case of continuous gravitational waves, and discuss accreting millisecond X-ray pulsars (AMXPs) as potential continuous gravitational waves sources. Finally, we provide an outline for the structure of the remainder of the thesis in Section 1.8.

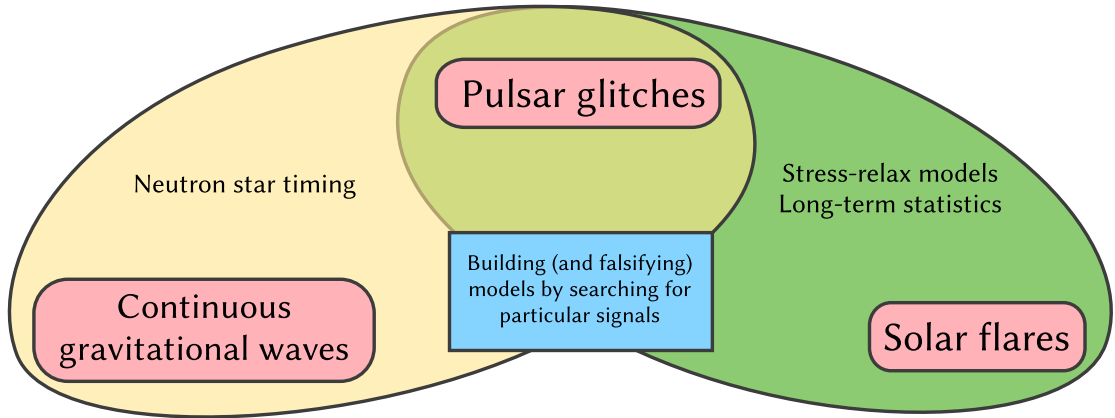


Figure 1.1: Schematic showing the three major topics of this thesis in red, while the overarching theme that links all the topics is in blue. Pulsar glitches and continuous gravitational waves are connected in yellow by both having to do with neutron star timing; glitches are seen as sudden deviations from a steady timing solution, while a sensitive continuous gravitational wave search is enabled by pulsar timing providing reference ephemerides. A continuous wave detection would result in an independent timing solution. Pulsar glitches and solar flares are connected in green via the underlying mechanism with which they operate, namely that stress builds up steadily over time, and is released suddenly. Long-term sequences of waiting times between events, and event sizes, allow for falsification of these stress-relax models.

## 1.2. OBSERVATIONAL TAXONOMY OF NEUTRON STARS

A neutron star is the dense remnant of a massive star (with mass  $9 \lesssim M/M_{\odot} \lesssim 25$ , where  $M_{\odot}$  is the mass of the Sun), after it has undergone a core collapse supernova [20]. First theorized to exist by Baade and Zwicky [21], direct observational evidence came over 30 years later with the discovery of a steadily pulsating radio source by then-PhD candidate Jocelyn Bell-Burnell and her supervisor Antony Hewish [22]. This object, the pulsar now known as PSR J1921+2153, was quickly designated as a rotating neutron star [23, 24], and many more pulsars were discovered soon after [25–29].

After 55 years of new discoveries, the variety of neutron stars with differing properties allows us to form a taxonomy broadly divided into two categories:

- **Isolated neutron stars** are seen most commonly as radio pulsars, but are also detected across the electromagnetic spectrum, e.g. optical, infrared, gamma-ray, and X-ray. Isolated pulsars are typically further classified into two main groups, so-called “rotation-powered” and “magnetars”. The former have spin periods of  $0.01 \lesssim P/\text{s} \lesssim 10$ , and time-derivative of their period of  $10^{-16} \lesssim \dot{P} \lesssim 10^{-12}$ . The latter are generally slower but spin down faster, with  $P \gtrsim 1 \text{ s}$  and  $\dot{P} \gtrsim 10^{-13}$  [30]. Some pulsars do not fit in the above two groups, for example if they only pulse intermittently, so-called “rotating radio transients” (RRATs) [31]. Some isolated neutron stars do not exhibit pulsations at any wavelength, e.g. central compact objects (CCO, also called supernova remnants), which often have a black-body spectrum peaked in the X-rays [32, 33]. We discuss in Section 1.3 how pulsar

timing is performed, and the timing irregularities, such as glitches, that are found in the process.

The mechanism generating pulsed radio emission is an unsolved problem in the field (see Cerutti and Beloborodov [34], Harding [35] and references therein). A recent critique by Melrose et al. [36] dismisses many of the currently favored models; the authors propose an alternative mechanism in Melrose et al. [37] (see also the work of Philippov et al. [38]). Whatever the emission mechanism, as the pulsed emission is coherent, the emission region must be small and offset from the rotation axis of the neutron star – leading to a “lighthouse effect” where the emission region periodically enters our line-of-sight. Thermal black-body emission peaked at shorter wavelengths (e.g. X-ray) is attributed to the residual heat in the neutron star crust which is slowly dissipating after the supernova that formed the object (typically observable for  $\sim 10^5$  yr) [39].

- **Binary neutron stars** are also sometimes seen as radio pulsars, but are more often detected due to their X-ray emission (so-called “X-ray binaries”). This emission is thought to arise due to accretion from their companion star forming hot-spots on the surface of the star. The mass of the companion further categorizes X-ray binaries as either low-mass (LMXB, companion mass  $M_c \lesssim M_\odot$ ), intermediate mass (IMXB, companion mass  $1 \lesssim M_c/M_\odot \lesssim 10$ ), or high mass (HMXB, companion mass  $M_c \gtrsim 10M_\odot$ ) [40]. Typically, the accretion in LMXBs is fed from an accretion disk, while in HMXBs it is fed via stellar winds from the companion [41, 42].

Some binary neutron stars are observed to have millisecond periods, and are thus called millisecond pulsars (MSPs). MSPs usually have quite small period derivatives,  $\dot{P} \lesssim 10^{-18}$ , compared to standard rotation-powered pulsars. However, most X-ray binaries are not seen as pulsars, for example neither Scorpius X-1 nor Cygnus X-2 have detectable pulsations [43]. A small fraction of compact (projected semi-major axis  $a_0 \lesssim 2$  lt-s) LMXBs intermittently go into outburst, where the X-ray flux is enhanced by roughly two orders of magnitude for days to months (depending on the object and outburst) [44]. During these periods of outburst pulsations are sometimes detectable, which puts these objects in a separate class of “accreting millisecond X-ray pulsars” (AMXPs). We return to AMXPs in Section 1.7.6.

The small spin period of MSPs is explained via a recycling mechanism, in which the magnetocentrifugal torque exerted by accretion spins up the neutron star [45–47]. Some MSPs are not seen in binaries, which is explained via a few pathways: either the neutron star could have fully ablated their companion (as seen in progress in so-called “black widow” pulsars), or dynamical effects resulting from a dense stellar environment could have disrupted the binary.

The above distinctions are driven by observations, and there are many systems that straddle the border between the outlined categories, or even move between categories [48]. For example, transitional millisecond pulsars, also known as redbacks, are sometimes observed as accretion-powered X-ray binaries, and then as rotation-powered radio pulsars [49]. Magnetars and CCOs are likely newly born neutron stars with strong birth magnetic fields [50]. The orientation of the emission region with respect to our line-of-sight could explain why some objects pulsate and some do not.

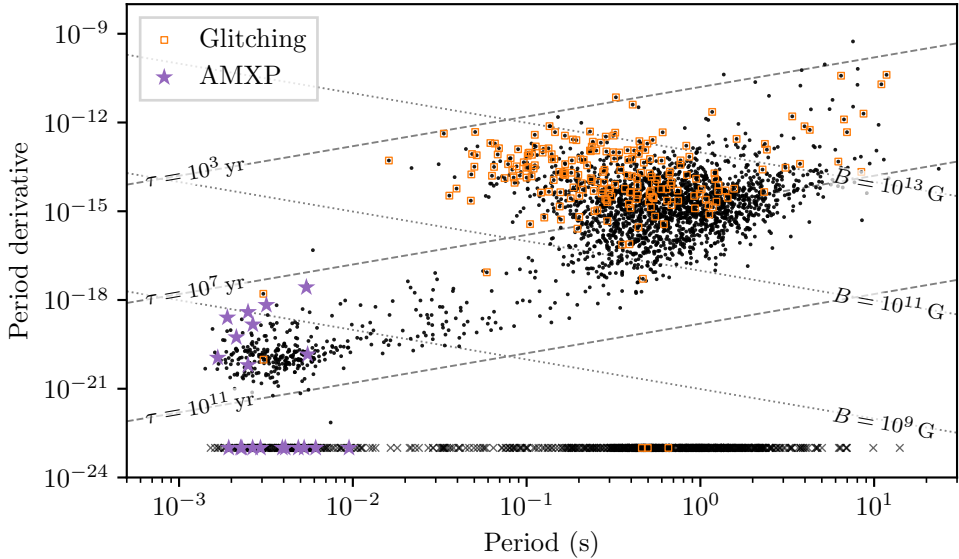


Figure 1.2: Period  $P$  and period derivative  $\dot{P}$  diagram for over 3300 objects retrieved from the ATNF Pulsar Catalog. Black crosses sitting at the bottom of the figure are pulsars which do not have a recorded  $\dot{P}$ . Orange boxes indicate pulsars with at least one recorded glitch, and are the objects of interest for Chapters 2–4 of this thesis. Purple stars mark the known AMXPs, which are the objects of interest for Chapter 6 of this thesis. Dotted and dashed lines show lines of constant magnetic field at the poles  $B$  and characteristic age respectively.

Typically, the pulsar population is visualized in a  $P - \dot{P}$  diagram, such as Figure 1.2. Each black dot is a pulsar recorded in the Australian Telescope National Facility (ATNF) Pulsar Catalog [51]<sup>1</sup>. Black crosses near the abscissa mark pulsars without a recorded period derivative, constituting nearly 23% of pulsars in the catalog. Objects marked with an orange square indicate that at least one glitch is recorded for that pulsar (see Section 1.4 for more on glitches). AMXPs are marked with a purple star. Lines of constant characteristic age  $\tau$  and magnetic field strength at the poles  $B$  are shown as dashed and dotted lines respectively. These two quantities are calculated by modeling the pulsar as a simple rotating magnetic dipole [24, 52, 53] for which the electromagnetic power emitted is

$$\dot{E}_{\text{dipole}} = \frac{-4\pi^4 B^2 R^6 \sin^2 \alpha}{3c^3 P^4}, \quad (1.1)$$

where  $R$  is the neutron star radius,  $\alpha$  is the angle between the rotation and magnetic axes, and  $c$  is the speed of light. Combining Equation (1.1) with the rate of change of the rotational kinetic energy

$$\dot{E}_{\text{rot.}} = \frac{-4\pi^2 I \dot{P}}{P^3}, \quad (1.2)$$

where  $I$  is the moment of inertia of the neutron star, gives

$$B \approx 3.2 \times 10^{19} \text{ G} \left( \frac{I}{10^{45} \text{ g cm}^2} \right)^{1/2} \left( \frac{R}{10^6 \text{ cm}} \right)^{-3} \sqrt{\dot{P}P}, \quad (1.3)$$

<sup>1</sup>Accessed via <https://www.atnf.csiro.au/research/pulsar/psrcat/>.

where we have included fiducial values for  $I$  and  $R$ , and set  $\sin \alpha = 1$ . The characteristic age is calculated by assuming that none of the parameters in Equation (1.3) vary in time from birth at  $t = 0$  to the current age  $\tau$  (besides  $P$ ), and integrating  $\dot{P} \propto 1/P$  to find

$$\tau = \frac{P^2 - P_0^2}{2\dot{P}P} \approx \frac{P}{2\dot{P}}, \quad (1.4)$$

where we assume the birth period  $P_0 \ll P$ .

Pulsars are almost certainly not perfectly rotating magnetic dipoles in a vacuum, and thus the above calculations are true only to zeroth order. They do apply remarkably well in some individual circumstances, e.g. the Crab pulsar (PSR J0537+2200) which is associated with a supernova remnant that was observed in 1054 AD by contemporary Chinese astronomers [54]. The current measurements of  $P \approx 0.033$  s and  $\dot{P} \approx 4.2 \times 10^{-13}$  [55] give  $\tau \approx 1258$  yr, only off from the true age by  $\sim 300$  yr. The power implied by Equation (1.2) of  $\dot{E}_{\text{rot.}} \approx -4.5 \times 10^{38}$  erg s $^{-1}$  (assuming  $I = 10^{45}$  g cm $^2$ ) is comparable to the total energy requirements of the Crab nebula,  $5 \times 10^{38}$  erg s $^{-1}$  [56], implying that the energy lost due to rotation is likely absorbed and re-emitted by the nebula surrounding the pulsar.

### 1.3. PULSAR TIMING

There is a multi-stage process to “time” a pulsar, i.e. model and track the rotation over time. Most pulsars are not bright enough to resolve individual pulses, so the first stage is “folding” 5 – 30 minutes (depending on the pulsar and observatory) of radio intensity time-series data, i.e. averaging the data modulo the fiducial rotation period of the pulsar [57].

In the second stage the folded data is correlated with a pulse shape template to generate a highly precise reference time for the observation, known as a time of arrival (TOA). The TOA for an observation is defined as the time at which we have zero rotational phase, i.e.  $\phi = 0$ . A correction is applied to each TOA to subtract the effect of the motion of the observatory around the solar system barycentre (SSB).

In the third and final stage, a model is fit to a series of TOAs to model the phase as a function of time, noting that  $\phi(t)$  must be an integer at each TOA. Traditionally, the phase is modelled as a simple Taylor series

$$\phi(t) = \phi(t_0) + \nu(t - t_0) + \frac{\dot{\nu}}{2}(t - t_0)^2 + \frac{\ddot{\nu}}{6}(t - t_0)^3 + \delta\phi(t), \quad (1.5)$$

where  $t_0$  is an arbitrary reference time,  $\nu = \frac{d\phi}{dt}\big|_{t=t_0}$ ,  $\dot{\nu} = \frac{d^2\phi}{dt^2}\big|_{t=t_0}$ , and  $\ddot{\nu} = \frac{d^3\phi}{dt^3}\big|_{t=t_0}$ . The phase residuals  $\delta\phi(t)$  are studied for features of non-Gaussian noise, i.e. signatures that the Taylor series phase model does not adequately explain the data. Software such as TEMPO2 [58, 59] performs an iterated weighted-least-squares [60] procedure to calculate the values of various pulsar parameters which minimize  $|\delta\phi(t)|^2$ . These parameters include but are not limited to:  $\nu$ ,  $\dot{\nu}$ ,  $\ddot{\nu}$ , right ascension and declination (henceforth RA and Dec. respectively), proper motion, and any relevant binary orbital elements.

Recent advances in modelling stochastic variations in  $\delta\phi(t)$  have led to extensions to TEMPO2, such as the software TEMPONEST [61] and the Hidden Markov Model (HMM)

tracking described by Melatos et al. [62]. We discuss these approaches further in Sections 1.3.1 and 1.3.2 respectively.

### 1.3.1. Timing noise

The residuals  $\delta\phi(t)$  often have a time-correlated stochastic structure that is not expected from measurement errors alone. The structure is also not attributable to incorrectly modelled (deterministic) pulsar parameters such as position or proper motion on the sky [63, 64]. The power spectrum of such residuals is red, with a mixture of random walks in  $\nu$  and  $\dot{\nu}$ , alongside discrete jumps in  $\phi$ . These residuals are typically called “timing noise” [65, 66]. Timing noise makes precision timing experiments such as pulsar timing arrays (PTAs) difficult [67–70]. The Bayesian inference software TEMPONEST performs parameter inference on not just the deterministic pulsar parameters, but also estimates the amplitude and spectral index of the power spectral density (PSD) of the residuals by simultaneously modelling a red noise process and the deterministic phase evolution in the frequency domain.

However, while such an approach can model the aggregate statistical properties of the residuals, it explicitly does not model the observed instantiation of the stochastic process. That is, it does not fit the specific time-ordered sequence of residuals to a particular stochastic process, only their time-averaged statistical properties. On the other hand, one may treat  $\phi$ ,  $\nu$ , and potentially  $\dot{\nu}$ , as hidden random variables that are estimated via a hidden Markov model (HMM) [62]. We summarize the work of Melatos et al. [62] in the context of glitch detection in the following subsection, and discuss the mathematical formulation of a HMM in the context of searches for gravitational waves in Section 1.7.

The mechanism causing timing noise is uncertain. What follows is a non-exhaustive list of the various mechanisms posited in the literature: i) free precession [71–73], ii) undetected debris or planetary companions [74, 75], iii) unmodelled pulse shape changes [76, 77], iv) magnetospheric state switching [78, 79], v) superposition of small rotational glitches [17, 80], vi) superfluid turbulence [81–83], vii) variations in external torques [84, 85], or viii) variations in the coupling between internal components and the crust [86].

In some contexts, including continuous gravitational wave searches (discussed in more detail in Section 1.7), timing noise is referred to as “spin-wandering” [7, 87–89]. Spin-wandering is typically, but not always, attributed to stochastic variations in the mass accretion rate  $\dot{M}$ . We remind the reader that only binary systems will have appreciable accretion; we must appeal to an alternative mechanism to explain spin-wandering in isolated pulsars. Coincident measurements of the instantaneous spin frequency of a pulsar from both a continuous gravitational wave detection and electromagnetic observations would allow estimates of various coupling parameters between the crust (to which the electromagnetic frequency is bound) and core (to which the gravitational wave frequency may be bound) [90, 91]. The degree of spin-wandering in Scorpius X-1 is estimated by Mukherjee et al. [89] to limit the coherence time for a continuous gravitational wave search to  $\lesssim 10$  d. Spin-wandering has not been estimated quantitatively in other accreting systems, although recent advances in the state-space formulation of the problem could enable these estimates in the future [92].

### 1.3.2. Glitch detection

A sudden discontinuity in the gradient of the phase residuals points to the occurrence of a rotational glitch. For example, if a glitch involves only a jump in spin frequency, the magnitude of the phase residuals will show a linear increase with time, while a change in the spin frequency time derivative would result in parabolic phase residuals. We discuss the broad phenomenology of glitches further in Section 1.5.1. Traditionally, these phase gradient discontinuities are discovered by eye, and two glitchless phase models, i.e. Equation (1.5), are fit to TOAs before and after the glitch epoch to define the parameters of the glitch. Both timing noise and long, irregular gaps between TOAs can lead to imprecise or degenerate estimates of glitch parameters [93, 94].

Recent advances in Bayesian model selection techniques, i.e. TEMPONEST, may help, but are not yet mature enough to deploy without human supervision [95]. An automated pipeline that fits phase residuals within a sliding window, and flags deviations from a polynomial regression, is implemented at the Ooty Radio Telescope [96]. The HMM-based method outlined by Melatos et al. [62] simultaneously models the secular and stochastic behavior of the phase. It determines if a glitch is present in the data by comparing the Bayesian evidence for models that do and do not include a glitch. Due to the computational efficiency of the method, and its automated nature, it is possible to quantitatively assess the upper limit of the smallest detectable glitch, at a given confidence level. For the set of 282 pulsars timed in the UTMOST [97] pulsar timing programme the mean upper limit on the glitch size, as a fraction of the spin frequency, is  $1.9 \times 10^{-8}$ , at 90% confidence. Historic datasets for the Crab and Vela pulsars were analyzed by Espinoza et al. [98] and Espinoza et al. [99] respectively, who found that there exists a minimum glitch size in both pulsars. However, this analysis uses a semi-automated technique, for which the discriminating power between timing noise and glitch is unclear.

## 1.4. NEUTRON STAR STRUCTURE

A supernova explosion will release some fraction of the original star’s mass as heat, light, and via a mass outflow. However, much ( $1\text{--}2M_{\odot}$ ) will collapse into a small radius (9–14 km) and form a neutron star [20]. The possible values of mass and radius for a neutron star are highly dependent on the so-called “equation of state” of matter at extreme densities. The equation of state gives the pressure-density relation, allowing one to solve the equations of hydrostatic equilibrium for mass and radius, along with other physical parameters. The behavior of matter under extreme pressures and densities cannot be studied in terrestrial laboratories, however theoretical nuclear physics studies produce tabulated repositories of plausible equations of state [100, 101].

Recent measurements from the Neutron Star Interior Composition Explorer (NICER) X-ray telescope have constrained both the mass and radius for two millisecond pulsars, PSR J0030+0451 [102, 103], and PSR J0740+6620 [104, 105]. Combining these measurements with constraints derived from gravitational wave data of the coalescence of two neutron stars in GW170817 and GW190425 places observational limits on the equation of state [106–109].

Almost all equations of state lead to a layered structure for a neutron star. The out-

ermost layer is a crystalline crust of iron, nickel, and other metals. As one descends deeper into the “outer crust” the pressure increases, and inverse beta decay increases the fraction of neutrons. Once the density is larger than  $\rho_{\text{drip}} \approx 4 \times 10^{11} \text{ g cm}^{-3}$ , neutrons begin to “drip” out of nuclei, which may condense into a superfluid phase [110]. In this “inner crust” the nuclei form clusters or defects, to which superfluid vortices may pin, a scenario we discuss further in Section 1.5.2. The nuclei at the bottom of the inner crust, are sometimes referred to as “nuclear pasta” [111–113] due to the variety of shapes and structures displayed in proton density isosurfaces in three-dimensional molecular dynamics simulations. Eventually, there is a transition to a region where a superfluid neutron fluid, and a (potentially superconducting) proton-electron plasma, are co-threading [20, 110]. This region is called the “outer core”. Below this we arrive at the inner core, where the dominant physics is much more uncertain, but a condensate of deconfined quarks are one possibility [114].

Observational evidence for the superfluid nature of (at least) the outer core comes from the cooling rate of Cassiopeia A [115–118]. Note, however, that Posselt et al. [119] and Posselt and Pavlov [120] question whether this evidence is biased by the model used to screen noise artifacts from the Chandra X-ray detectors. Glitches provide independent evidence for superfluidity, as explained further in Section 1.5.

## 1.5. PULSAR GLITCHES

As discussed in Section 1.3.2, glitches are abrupt changes in the spin frequency, and sometimes frequency derivative, of the pulsar. We discuss the broad phenomenology of glitches in Section 1.5.1, and move on to the physical models that may explain these events in Section 1.5.2.

### 1.5.1. *Phenomenology and statistics*

Not all glitches share the same observational characteristics. For example, while the vast majority of recorded glitches involve an increase in the spin frequency (i.e.  $\Delta\nu > 0$ ), some glitches in magnetars and accreting systems have  $\Delta\nu < 0$  [121, 122]. While glitches in accreting systems appear to have similar properties to glitches seen in rotation-powered pulsars [123], we do not discuss them further in this thesis. Glitches in magnetars are also not discussed further; they are occasionally accompanied by changes in the pulse shape, hinting that they may be due to a reconfiguration of the magnetic field, rather than any of the mechanisms discussed in Section 1.5.2 [124–127]. Most standard spin-down glitches in rotation-powered pulsars do not change the pulse or emission profile [30, 128].

The time-scale over which the change in spin frequency occurs (“rise time”) has never been resolved. The most stringent constraint is that it occurs in less than 12.6 s, at 90% confidence, for a glitch from the Vela pulsar in 2016 [129, 130]. The Vela pulsar is the only glitching pulsar that is constantly monitored, and is bright enough to allow measurements of individual pulses. These properties allowed detailed analysis of the pulse timing immediately before and after the aforementioned glitch, revealing evidence for an “overshoot” (“undershoot”) of the spin frequency after (before) the glitch [130]. Regardless of whether there is an overshoot, an exponential decay of the spin frequency

Table 1.1: Pulsar name, number of recorded glitches  $N$ , best-fitting waiting time PDF  $p(\Delta t)$ , size PDF  $p(\Delta\nu/\nu)$ , forward cross-correlation  $\rho_+$ , backward cross-correlation  $\rho_-$ , waiting time autocorrelation  $\rho_{\Delta t}$ , and size autocorrelation  $\rho_{\Delta\nu/\nu}$  for the eight pulsars with  $N \geq 10$ . The distribution that fits the waiting time and size PDFs best is determined via the AICc. The 95% confidence intervals for the Spearman cross-correlation coefficients are calculated via Equation (2.6). The top four pulsars are “Poisson-like”, while the bottom four are “quasiperiodic”, see the text for details. Abbreviations are E, PL, LN, and G for exponential, power-law, log-normal and Gaussian respectively.

Name (J2000)	$N$	$p(\Delta t)$	$p(\Delta\nu/\nu)$	$\rho_+$	$\rho_-$	$\rho_{\Delta t}$	$\rho_{\Delta\nu/\nu}$
PSR J1740–3015	36	LN/E	PL	$0.29^{+0.29}_{-0.35}$	$-0.11^{+0.34}_{-0.32}$	$0.17^{+0.31}_{-0.35}$	$0.02^{+0.33}_{-0.34}$
PSR J0534+2200	29	E/LN	PL	$0.10^{+0.36}_{-0.39}$	$0.13^{+0.36}_{-0.40}$	$0.19^{+0.35}_{-0.41}$	$-0.35^{+0.40}_{-0.30}$
PSR J0631+1036	17	E	PL	$0.21^{+0.44}_{-0.54}$	$-0.19^{+0.54}_{-0.44}$	$-0.20^{+0.56}_{-0.45}$	$0.32^{+0.40}_{-0.56}$
PSR J1413–6141	14	PL	E/LN	$0.82^{+0.14}_{-0.50}$	$-0.31^{+0.63}_{-0.44}$	$0.01^{+0.57}_{-0.58}$	$-0.27^{+0.62}_{-0.45}$
PSR J0537–6910	53	G/LN	G	$0.91^{+0.05}_{-0.10}$	$-0.21^{+0.29}_{-0.25}$	$-0.13^{+0.29}_{-0.27}$	$-0.23^{+0.28}_{-0.25}$
PSR J1341–6220	33	LN	LN	$0.62^{+0.20}_{-0.34}$	$-0.13^{+0.36}_{-0.33}$	$-0.00^{+0.35}_{-0.35}$	$-0.08^{+0.36}_{-0.34}$
PSR J0835–4510	24	G	G	$0.19^{+0.37}_{-0.44}$	$0.19^{+0.37}_{-0.44}$	$-0.29^{+0.46}_{-0.36}$	$-0.29^{+0.45}_{-0.35}$
PSR J1801–2304	15	LN/G	E/LN	$0.71^{+0.21}_{-0.56}$	$-0.29^{+0.60}_{-0.43}$	$-0.02^{+0.56}_{-0.55}$	$-0.13^{+0.57}_{-0.49}$

is often seen, on timescales ranging from seconds to months after the glitch [130, 131]. This decay is not always “complete”, i.e. in many glitches there remains a permanent increase in both the spin frequency and/or the time derivative thereof [128, 132, 133]. Interpretations of these features with respect to possible physical models is presented in Section 1.5.2.

As discussed in Section 1.3.2, the detection of glitches has historically been performed via visual inspection of timing residuals. As such, the completeness of historical catalogs is not well established. In this context a “complete” catalog would include all glitches that have occurred in each pulsar down to a selected size. Completeness is hindered by infrequent observations of many pulsars, and by the minimum detectable glitch size. It is not possible to differentiate whether one large or many smaller glitches occur between two observation epochs [134, 135]. Small glitches, with  $\Delta\nu/\nu \lesssim 10^{-9}$ , may also be hard to distinguish from timing noise, or so-called “micro-glitches” [134, 136]. Howitt et al. [137] estimates that roughly 100–200 glitches are missing from glitch catalogs by comparing the rate at which new glitching pulsars are detected, and the rate at which the total number of glitches in the catalog grows, ascribing the shortfall as due to insufficient monitoring of known glitching pulsars.

As of 2023 March 21 there are 670 glitches from 208 pulsars recorded in the Jodrell Bank Centre for Astrophysics online catalog<sup>2</sup>. While much can be learnt from aggregated

<sup>2</sup> Accessible via <http://www.jb.man.ac.uk/pulsar/glitches.html> [128, 138].

statistics [128, 131, 138–142], in what follows we focus on the pulsars that have glitched the most, to enable a disaggregation of the data. Only eight pulsars have more than 10 recorded glitches. The names of these pulsars and the number of recorded glitches,  $N$ , are listed in the first two columns of Table 1.1. Given a set of  $N$  events, we construct a set of  $N - 1$  waiting times<sup>3</sup>  $\Delta t$ , i.e. the set of differences between consecutive glitch epochs.

In the third and fourth columns of Table 1.1 we list the probability density function (PDF) that fits best the set of waiting times, and the fractional glitch sizes,  $\Delta\nu/\nu$ , respectively. These best-fitting distributions are determined via the corrected Akaike Information Criterion (AICc) [144, 145]. The AICc computes the relative evidence of the data being described by one model out of a set of models, while correcting for the bias introduced by the models potentially having a different number of parameters. The AICc value of a model is calculated as

$$\text{AICc}/2 = k - \ln(\hat{\mathcal{L}}) + \frac{k^2 + k}{N - k - 1}, \quad (1.6)$$

where  $k$  is the number of model parameters,  $N$  is the number of data points that contribute to  $\hat{\mathcal{L}}$ , the likelihood of the data given the model, maximized over the model parameters. The model with the smallest AICc value minimizes the information lost in having a model that does not perfectly describe the data. For Table 1.1 the possible models we compare between are an exponential, a Gaussian, a power-law, and a log-normal (E, G, PL, and LN in Table 1.1 respectively). When the relative probability between the top two models is within 50% we list both, separated with a slash<sup>4</sup>.

Waiting time distributions are best described with an exponential or log-normal for PSR J0534+2200, PSR J0631+1036, PSR J1341–6220, and PSR J1740–3015. They are best described with a Gaussian or log-normal for PSR J0537–6910, PSR J0835–4510, and PSR J1801–2304. PSR J1413–6141 has its waiting time PDF best described with a power law. Size distributions are best described by a power law for PSR J0534+2200, PSR J0631+1036, and PSR J1740–3015. They are best described by an exponential or log-normal for PSR J1341–6220, PSR J1413–6141, and PSR J1801–2304. Both PSR J0537–6910 and PSR J0835–4510 have size PDFs best described with a Gaussian. These results are consistent with previous analyses of glitches from individual pulsars [17–19, 140]. Typically, glitching pulsars are separated into two distinct groups: “Poisson-like” with exponentially distributed waiting times and power-law distributed sizes, or “quasiperiodic” with unimodal (i.e. Gaussian or log-normal) waiting times and sizes [17, 18]. We find that some pulsars, namely PSR J0534+2200, PSR J0631+1036, and PSR J1740–3015, can be adequately described as Poisson-like. Some are quasiperiodic, namely PSR J0537–6910, PSR J0835–4510, PSR J1341–6220, and PSR J1801–2304. One pulsar, PSR J1413–6141 does not cleanly fall into either group. We caution that with such small sample sizes, it may be the case that neither the demarcation into these two groupings nor the assignations above will persist in the future, as more glitches are observed from these and other pulsars.

---

<sup>3</sup>Due to a 3-yr (5-yr) gap in monitoring between 1979 and 1982 (2012 and 2017) the waiting time between the fourth and fifth (45-th and 46-th) glitch is not included in the analysis for PSR J0534+2200 (PSR J0537–6910) [98, 143].

<sup>4</sup>Whether a given model fits the data “well” is a subtle point, especially with few data points. The AICc is a reasonable tool, among many, which can quantitatively compare plausible phenomenological models [146].

The cross-correlation between the glitch size and the following (preceding) waiting time is denoted as the forward (backward) cross-correlation  $\rho_+$  ( $\rho_-$ ), and is listed in the fifth (sixth) column of Table 1.1. The forward cross-correlations are consistent with zero, at the 95% confidence level, for PSR J0534+2200, PSR J0631+1036, PSR J0835–4510, PSR J1740–3015, while the other four pulsars have  $\rho_+$  greater than zero. That PSR J0537–6910 has a strong forward cross-correlation is well-known in the literature, allowing confident prediction of the time until the next glitch [143, 147–149]. As Fuentes et al. [19] noted, while some pulsars have a forward cross-correlation that is consistent with zero at the 95% confidence level, it would be an unlikely coincidence that we would measure  $\rho_+ > 0$  in all pulsars just by chance, assuming the null hypothesis of  $\rho_+ = 0$ . No pulsar has a backward cross-correlation that is different from zero, at the 95% confidence level.

The autocorrelation between subsequent waiting times  $\rho_{\Delta t}$  (sizes  $\rho_{\Delta\nu/\nu}$ ) is listed in the seventh (eighth) column of Table 1.1. They are all consistent with zero, at the 95% confidence level.

We return to what long-term statistical measures of waiting time and size PDFs, cross-correlations, and autocorrelations can tell us about the physics of pulsar glitches in Chapters 2–4.

### 1.5.2. Glitch trigger mechanisms

The mechanism causing pulsar glitches is uncertain. Since the discovery of glitches shortly after the discovery of the first pulsar, models have proliferated. In this subsection we review the mechanisms that remain popular in the literature to this day, summarizing the reviews of Haskell and Melatos [150], Antonopoulou et al. [151], Antonelli et al. [152], and Zhou et al. [153].

As discussed in Section 1.4 the interior of a neutron star is likely to contain both a charged plasma (predominantly electrons and protons), as well as a superfluid component (composed of neutrons). The charged plasma will couple tightly to the crust via the electromagnetic interactions, however a superfluid is irrotational in the bulk. The circulation of a superfluid is carried by quantised vortices, the areal density of which corresponds to a local rotation rate of the superfluid [154, 155]. These vortices are regions with zero superfluid density. However, they act as quasiparticles which exert an effective drag force that couples the superfluid and normal components of the fluid on long timescales, due to the scattering of electrons off the vortex cores [156, 157].

A lag between the rotation rate of the normal and superfluid components gives rise to a hydrodynamic Magnus force on the vortices, pushing them radially outwards [158]. If vortices can flow without restriction an equilibrium will quickly be reached, where the time derivative of the angular speed of the superfluid and normal components is equal. However, vortices are likely “pinned” in at least some regions. In the inner crust, lattice defects or nuclei clusters could create energetically favorable locations for vortices [159–167]. The pinning potential in each site will likely vary due to the balance between the self-energy required to bend a vortex, and the interaction strength of the vortex and pinning site, as well as the structure of the lattice nearby [168]. In the core, vortices could pin to superconducting flux tubes [155, 158, 169, 170]. Whatever the mechanism, pinning will frustrate the free motion of vortices, leading to an increasing Magnus force over time, as the lag between the fluid components grows.

Differential rotation of fluid components and/or the crust provides a reservoir of angular momentum with which we can explain glitches [171]. The mechanism by which the angular momentum is transferred is likely the mass transport of  $\sim 10^{10-13}$  vortices (the exact number of vortices needed depends on the size of the glitch, among other factors) [159, 172]. What could trigger the simultaneous unpinning of such a large number of vortices?

### *Superfluid vortex avalanches*

As the Magnus force on a vortex is proportional to the lag between the fluid components, the stress will eventually accumulate until it is enough to unpin the vortex from its pinning site. While details of the motion of superfluid vortices is complex [168], two-dimensional point-vortex simulations [137], as well as full quantum dynamical simulations [173–175] exhibit “avalanches”, where the unpinning of a small subset of vortices can trigger a mass unpinning event through “knock-on” interactions with their neighbors. Such stick-slip cascade dynamics are emblematic of systems in a state of self-organized criticality, which we discuss further in Section 1.6.

### *Crustquakes*

The crystalline crust of a neutron star is naturally oblate when born, due to the balance of gravitational and centrifugal forces. As the neutron star spins down, this balance changes, and so does the shape of the star [176]. However, while the interior is an incompressible fluid, the crust can support some mechanical strain. This strain will build up over time until failure occurs: a crustquake. Ruderman [177] proposed that crustquakes would be able to adjust the moment of inertia sufficiently to explain all glitches, however too much strain would need to build up too quickly to explain the glitching history of some pulsars [178]. For example, large glitches ( $\Delta\nu/\nu \sim 10^{-6}$ ) would release  $\sim 10^5$  yrs of built-up strain, however the Vela pulsar (PSR J0835–4510) experiences glitches that large every 2–3 years. The superfluid nature of the interior could assist in building crustal strain, via the elastic stress attributable to vortices pinned to the crust [179, 180]. Molecular dynamics simulations give maximal breaking strains that are large (of order  $\sim 0.1$ ), which would likely not be reached before the vortices unpin naturally [181]. Despite the above concerns, crustquakes remain a viable mechanism to trigger at least some glitches, a rearrangement of the crust would likely adjust the pinning potentials near the fault-line, in which many vortices may sit, leading to a mass unpinning event [182].

Unrelated to glitches, crustquakes may play an important role in building “mountains” (i.e. mass asymmetries) on the surfaces of some neutron stars, perhaps enabling the generation of continuous gravitational waves [183–185]. We return to mountains on neutron stars in Section 1.7.

### *Superfluid instabilities and other possibilities*

The onset of an instability in the fluid flow may also precipitate a mass unpinning of vortices. While superfluid flow is typically considered smooth, the interaction between the superfluid and normal components could lead to, for example, a Kelvin-Helmoltz

[186] or two-stream instability [187, 188]. The excitation of an instability may create a vortex tangle, i.e. a disruption of the vortex array, which reduces the coupling between the crust and the superfluid [189]. The exact mechanism with which superfluid turbulence triggers a glitch is unclear, but it is likely an important ingredient in understanding glitch recoveries [190–192].

Mass unpinning of vortices may also occur through so-called “vortex creep”, where thermal activation continually unpins vortices, allowing an average vortex current and creating an avenue for collective unpinning without avalanche dynamics [170, 172, 193, 194].

## 1.6. STRESS ACCUMULATION AND RELAXATION

In light of the complexities of the mechanisms discussed in Section 1.5.2, it is helpful to summarize the major, phenomenological commonalities. Glitches are (broadly) unpredictable events that become more likely to occur as stress (e.g. lag in rotation rate between fluid components) accumulates. The amount of stress released after an event is triggered varies over many orders of magnitude. Unpredictable events of varying sizes are hallmarks of a system in a state of self-organized criticality, but are not unique to such systems [195, 196].

The canonical example of a system exhibiting self-organized criticality are the sand-piles of Bak et al. [197, 198]. This mathematical system describes a grid, upon which grains of sand are dropped at a steady rate. If the local gradient of the sandpile height exceeds a threshold, a toppling event is triggered, reallocating some sand to neighboring grid points. This toppling results in avalanches across all length-scales, the size-invariant statistics thereof are widely studied (e.g. by Hwa and Kardar [199], Rosendahl et al. [200], De Menech and Stella [201], and Lippiello et al. [202], among many others). Models with a stochastic driving force (“coherent noise”) also exhibit avalanche-like behavior [193, 203–205].

Mathematically modelling the repeated accumulation and depletion of stress in a system is complicated by the “doubly stochastic” nature of the process. By doubly stochastic we refer to the fact that both the time between events, and the amount of stress released at each event is a random variable. If one assumes various limits, such as the full depletion of the stress reservoir after each event [206], or that an event is only triggered when a stress threshold is reached [207], the problem becomes analytically tractable. We call such phenomenological descriptions of stress accumulation and relaxation “meta-models”, as they typically encompass a broad array of more specific micro-physical models.

In the following Section 1.6.1 we shift our attention to the phenomenon of solar flares, and describe how current thinking positions flares as arising from a stress-relax process. In Section 1.6.2 we introduce the state-dependent Poisson (SDP) process, a mathematical framework for understanding a broad range of stress-relax systems. In this thesis we use the SDP framework, or stress-relax meta-model variants thereof, to help understand pulsar glitches.

### 1.6.1. Solar flares

Our sun is a main sequence star about halfway through its life, at the end of which it will become a red giant, and then a white dwarf. It is not massive enough to become a neutron star, and thus will never be seen to glitch like a pulsar. However, it does exhibit flares. Solar flares are eruptive emissions of electromagnetic radiation [208, 209]. Flares are often, but not always, emitted from sunspots, active regions with magnetic fields an order of magnitude larger than the rest of the star [210]. These magnetic fields are visible via magnetograms [211], which show flares often occurring on the boundary between differing magnetic polarity regions. Across these so-called “neutral lines” we observe loops, prominences, and arcades of plasma following the field lines. A shift in the footpoints of these features results in an abrupt reconfiguration of the magnetic field, releasing stored magnetic energy [208]. Arcade shearing is not the only possible physical mechanism that involves the release of stored energy, see Table 1 of Green et al. [212] for more. A key concept in most is that when anti-parallel magnetic field lines become close a magnetic reconnection event occurs, dissipating energy into the surrounding plasma [213]. Flare prediction is not possible in general, despite much effort [214–220].

While solar flares exhibit a rich phenomenology across the electromagnetic spectrum, the peak flux  $f_p$  is typically emitted in the X-ray wavelength [208, 209]. For consistency with historical records, modern flare catalogs encode the peak flux of a flare between 1–8 Å into flare classes: “A”, “B”, “C”, “M”, or “X”. A class A flare has  $f_p < 10^{-7} \text{ Wm}^{-2}$ , a class B flare has  $10^{-7} \leq f_p/(\text{Wm}^{-2}) < 10^{-6}$ , a class C flare has  $10^{-6} \leq f_p/(\text{Wm}^{-2}) < 10^{-5}$ , a class M flare has  $10^{-5} \leq f_p/(\text{Wm}^{-2}) < 10^{-4}$ , and class X flares have  $f_p \geq 10^{-4} \text{ Wm}^{-2}$ . These classes are further subdivided via a subsequent number, such that, for example, a class M7.3 flare has  $f_p = 7.3 \times 10^{-5} \text{ Wm}^{-2}$ .

Interpreting the sequences of flares from individual active regions through the lens of stress-relax models enables detailed interrogation of the broad underlying mechanism [221–226]. In these models, magnetic energy accumulates secularly, and is released abruptly via flares. The long-term statistical consequences of such a model are somewhat different to the complementary phenomenological description of flares as occurring as a result of an avalanche or self-organized critical system [220, 227–230]. In particular, while waiting time and size PDFs may or may not differ between models, the avalanche model predicts no long-term memory, e.g. no cross-correlations between flare waiting times and sizes. We connect solar flare observations with the machinery of the SDP process in Chapter 5, where we search for these cross-correlations and other tell-tale signs of a stress-relax process that is driven towards a static-in-time threshold before each event.

### 1.6.2. State-dependent Poisson process

We can approach modelling a stress-relax process many ways. For example, cellular automata capture local knock-on effects, and the dynamics therein [185, 198, 231]. An alternative is to track a globally averaged stress,  $X$ , as it accumulates gradually between events, and depletes suddenly at events. Early work simplified this approach by either assuming the stress reservoir is depleted at each event [206, 221] or that the stress reaching a static-in-time threshold triggers an event [207, 226, 232]. These simplifications natu-

rally result in a prediction of a large backward or forward cross-correlation respectively. In the former case this is because the size of a stress release event is purely determined by the waiting time since the last event (which reset the stress to zero). In the latter case the system must accumulate the stress it lost at the previous event, before the threshold is breached again. Broadly speaking, these cross-correlations are not observed in the natural phenomena these models represent, with a few notable exceptions [147, 233].

Mathematically, globally averaged stress-accumulation and release is governed as a function of time  $t$  by the stochastic differential equation

$$\frac{dX}{dt} = f(X, t) + g(X, t) + J(X, t), \quad (1.7)$$

where we have separated the stress evolution into three parts. The function  $f(X, t)$  is the deterministic driver of stress into the system, i.e.  $f(X, t) \geq 0$ . The function  $g(X, t)$  models the continuous but stochastic variations in the stress (e.g. Brownian motion), while  $J(X, t)$  models the stochastic jumps that occur at epochs  $t_1, \dots, t_i$ , i.e.

$$J(X, t) = \sum_{i=1}^{N(t)} \Delta X_i [X(t_i^-)] \delta(t - t_i), \quad (1.8)$$

where  $N(t)$  is the number of jumps that have occurred up until time  $t$ , and  $\delta(\dots)$  corresponds to the Dirac-delta function [206, 207, 234]. The size of each stress-release event  $\Delta X[X(t_i^-)]$  typically depends on the stress in the system immediately prior to the event, as otherwise one may have  $X < 0$ , which is non-physical.

When do stress-release events occur? For the state-dependent Poisson process, this is governed by the instantaneous rate  $\lambda[X(t)]$ . The PDF of waiting times drawn from a time-dependent Poisson distribution is [235]

$$p(\Delta t | t) = \lambda(t + \Delta t) \exp \left[ - \int_{t'}^{t' + \Delta t} dt' \lambda(t') \right]. \quad (1.9)$$

Given a prescription for i)  $f(X, t)$ , ii)  $g(X, t)$ , iii)  $\lambda[X(t)]$ , and iv) a method for picking  $\Delta X[X(t_i^-)]$ , one may evolve Equation (1.7) forward in time. As noted by Fulgenzi et al. [16] and Wheatland [234], directly solving Equation (1.7) is often intractable, except for a restricted set of choices i)–iv). Instead, one may simulate the system via a Monte Carlo automaton, which iteratively picks waiting times and sizes [15, 16, 234].

A wide variety of physics is encoded in the choices i)–iv). A simple example is if one has  $f(X, t) = f$ , and  $g(X, t) = 0$  the system accumulates stress deterministically between jumps, and is driven at a constant rate  $f$ . This is the choice made by Carlin and Melatos [1, 3], Carlin et al. [4], Carlin and Melatos [15], Fulgenzi et al. [16], and Wheatland [224, 234], in both solar flare and pulsar glitch contexts. We explore some of the statistical long-term observables of this “standard” configuration of the SDP process in Chapter 2. We search for signatures of a SDP process underlying solar flares in Chapter 5.

On the other hand, if  $g(X, t) \neq 0$  the stress driver has some stochasticity [2, 206, 207]. In Chapter 3 we investigate what a stochastic stress driver implies for the long-term statistical observables of the meta-model, again in the context of pulsar glitches. The choice of iv), i.e. how event sizes are decided, is another key place where physics

is encoded in the model. Fulgenzi et al. [16] and Wheatland [234] both have  $\Delta X$  as a random variable, drawn from a power law PDF, as the underlying stress-release mechanism assumes scale-free avalanche dynamics [195]. As noted by Carlin and Melatos [15] the functional form of this PDF has a large impact on all of the long-term observables, not just the PDF of observed event sizes, due to the coupled nature of the equation of motion. In Chapter 4 we specialize the SDP process to a particular choice of iv) which makes  $\Delta X$  no longer a random variable, but instead a complex function of the stress-release history. This choice allows for a detailed interrogation of the superfluid vortex avalanche model of pulsar glitches.

## 1.7. CONTINUOUS GRAVITATIONAL WAVES

We turn our attention now to the final topic of this thesis, a search for continuous gravitational waves from AMXPs. In Section 1.7.1 we briefly review the necessary background to understand gravitational waves. In Section 1.7.2 we introduce the active ground-based gravitational wave detectors. In Section 1.7.3 we discuss plausible emission mechanisms for continuous gravitational waves. In Section 1.7.4 we discuss the standard signal model, while in Section 1.7.5 we discuss how considerations of spin-wandering modify it. Finally, in Section 1.7.6 we describe why AMXPs are plausible sources for continuous gravitational waves.

### 1.7.1. General relativity

In the weak-field limit, Einstein's field equations of general relativity admit wave-like solutions as perturbations  $h_{\mu\nu}$  to a flat spacetime metric. In the transverse-traceless gauge a plane wave travelling in the  $z$ -direction is given by

$$h_{\mu\nu}(t, z) = \begin{pmatrix} 0 & 0 & 0 & 0 \\ 0 & h_+ & h_\times & 0 \\ 0 & h_\times & -h_+ & 0 \\ 0 & 0 & 0 & 0 \end{pmatrix} \exp\left[i\omega\left(\frac{z}{c} - t\right)\right], \quad (1.10)$$

where  $\omega$  is the gravitational wave angular frequency,  $h_+$  is the + polarization amplitude,  $h_\times$  is the  $\times$  polarization amplitude, and the tensor components of  $h_{\mu\nu}$  are given by the matrix elements. The dominant contribution for a non-relativistic source at a distance  $D$  is,

$$h_{\mu\nu}(t, x^i) = -\frac{2G}{Dc^4} \frac{d^2}{dt^2} \left[ I_{\mu\nu}\left(t - \frac{D}{c}\right)\right], \quad (1.11)$$

where  $G$  is the gravitational constant,  $c$  is the speed of light, and  $I_{\mu\nu}$  is the mass quadrupole moment tensor, calculated viz.

$$I^{\mu\nu} = \int d^3x T^{00} x^\mu x^\nu, \quad (1.12)$$

where  $T^{00}$  is the time-time component of the stress-energy tensor [236]. The monopole and dipole contributions to gravitational radiation vanish due to conservation of energy and momentum respectively. A time varying mass-current multipole also generates

gravitational waves. Adopting the notation of Thorne [237], a mass-current multipole produces a wave with components

$$h_{\mu\nu}(t, x^i) = \frac{2G}{Dc^4} \sum_{l=2}^{\infty} \sum_{m=-l}^{m=l} \frac{\partial^l S^{lm}(t - D/c)}{\partial t^l} T_{\mu\nu}^{B2,lm}, \quad (1.13)$$

where  $S^{lm}$  is the  $(l, m)$ -th current multiple moment, and  $T_{\mu\nu}^{B2,lm}$  are components of the tensor spherical harmonic, not the stress-energy tensor [237, 238]. We return to both time-varying mass quadrupole and mass-current sources in Section 1.7.3.

Equations (1.11) and (1.13) result in wave amplitudes too small to detect, unless the gravitational wave source is a compact object with a large, rapidly varying moment of inertia or current. We restrict our attention to single sources of gravitational radiation, i.e. we do not discuss the stochastic gravitational wave background (see Renzini et al. [239] for a comprehensive review of modern stochastic gravitational wave searches).

The one confirmed gravitational wave source to date are coalescing binaries composed of black holes or neutron stars, as detected routinely by the LIGO-Virgo-KAGRA Collaboration (LVK) since 2015 [240, 241], and detected indirectly via orbital shrinkage in pulsar binaries [242]. Other, short-duration ( $\lesssim 100$  s) so-called “burst” gravitational wave sources include core-collapse supernovae [243, 244], cosmic strings [245, 246], and pulsar glitches [247–249], but are yet to be detected [250, 251]. In this thesis we do not consider binary coalescence or burst gravitational wave sources further. Rapidly rotating non-axisymmetric neutron stars are a plausible source of continuous gravitational waves, and are discussed further in Sections 1.7.3–1.7.5.

### 1.7.2. *Ground-based gravitational wave detectors*

The most sensitive gravitational wave detectors to a broad range of frequencies are laser interferometers [252]. Currently, there are five large interferometers around the world: the two LIGO detectors in the United States of America (in Livingston Louisiana, “L1”, and Hanford Washington, “H1”), Virgo in Italy, KAGRA in Japan, and GEO 600 in Germany. As the work in Chapter 6 uses only data from the LIGO detectors, we will focus our attention there.

The LIGO detectors are power-recycled Fabry-Pérot Michelson interferometers with 4 km arms. As a gravitational wave passes through a detector, the length difference  $\Delta L(t)$  between the arms varies as a function of time. Measuring the dimensionless strain  $h(t) = \Delta L(t)/L$ , where  $L$  is the arm length, allows one to infer the polarization amplitudes  $h_+$  and  $h_\times$  of the gravitational wave, given adequate information about the source direction and inclination. The sensitivity of the detectors to a given strain is typically quantified in the frequency domain, by calculating the amplitude spectral density (ASD)  $S^{1/2}(f)$  of the noise in units of  $\text{Hz}^{-1/2}$ . Figure 1.3 shows the improvement in the typical ASD for the L1 detector between the fifth Science Run (S5), which ran from November 2005 to September 2007, and the second half of the third Observing Run (O3b), which ran from November 2019 to March 2020. The roughly order-of-magnitude improvement in ASD allows one to detect an order-of-magnitude smaller amplitude gravitational wave, at a fixed signal-to-noise ratio (SNR), when using matched filtering method such as the ones discussed in Section 1.7.4.

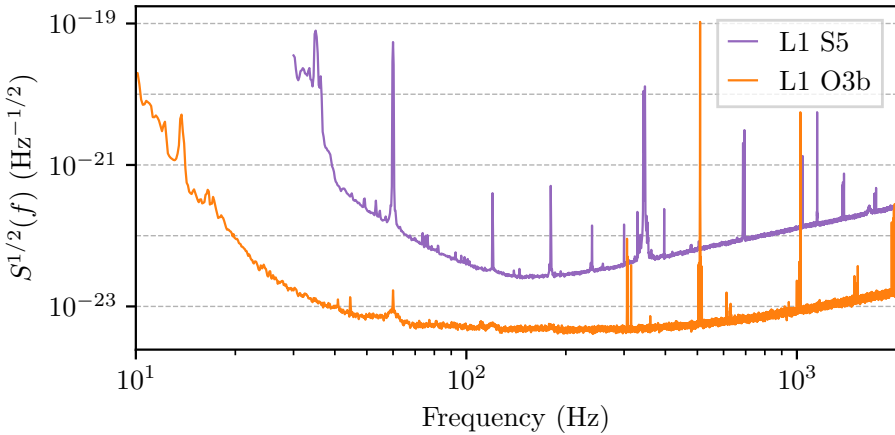


Figure 1.3: Representative ASDs for the Livingston (L1) LIGO detector in S5 (purple curve) and O3b (orange curve). The ASDs are representative in that they are calculated from  $\sim 5$  min of data for a period of time in which the detectors are operating within their modal binary neutron star detection range for that observing run, see Weinstein and Privitera [13] and Goetz [14] for details.

### 1.7.3. Continuous gravitational wave emission mechanisms

Continuous gravitational waves are both persistent, with durations  $\gtrsim 1$  yr, and “quasi-monochromatic”. In this context, quasi-monochromatic corresponds to the frequency of the gravitational wave  $f_{\text{GW}}$  in the frame of the gravitational wave detector varying by  $\lesssim 0.01$  Hz over the course of a year. These small variations in frequency are due to different factors, depending on the source of the continuous gravitational wave, which we explain further in Section 1.7.4. The prototypical continuous gravitational wave source is a rapidly rotating non-axisymmetric neutron star, which may or may not be in a binary system.

There are many physical processes that may lead to the asymmetry of the source. For example “mountains” (either on the surface or in the interior of the star) which lead to a time-varying mass quadrupole could be supported via thermoelastic [178, 183, 253], magnetic [254–256], or tectonic processes [147, 185, 257, 258]. A perpendicular biaxial rotor (e.g. a rigid star with a mountain symmetrically straddling the equator) will emit GW at a frequency  $f_{\text{GW}} = 2f_{\star}$ , where  $f_{\star}$  is the underlying neutron star rotation frequency. If the principal axis of the moment of inertia and the rotation axis are offset by a “wobble” angle  $0 < \theta < \pi/2$ , the system freely precesses and will emit gravitational waves at both  $f_{\star}$  and  $2f_{\star}$ , and potentially other harmonics [259–261].

For the simplest case of a perpendicular biaxial rotor rotating around its  $z$  axis, the strain is [262]

$$h_0 = \frac{4\pi^2 G}{c^4} \frac{\epsilon I_{zz} f_{\text{GW}}^2}{D} \quad (1.14)$$

where  $h_0 \equiv |h_{+/\times}|$  (if the system is inclined edge-on to the detector), and  $\epsilon = |I_{xx} - I_{yy}|/I_{zz}$ .

Oscillation modes in the interior of a neutron star may lead to gravitational wave emission via a time-vary mass-current multipole, see Equation (1.13). Rotation-dominated axial modes (so-called  $r$ -modes, in analogy to Rossby modes on Earth) are unstable under gravitational wave emission [263–265]. By unstable, we refer to the mode amplitude

growing exponentially with time, due the current moving retrograde in the frame of reference rotating with the neutron star, but prograde in an external frame; thus gravitational radiation removes positive angular momentum from a mode that has negative angular momentum, increases the strength of the current [264]. The oscillation mode grows until a saturation amplitude  $\alpha$  is reached, when non-linear hydrodynamic and viscous effects damp the growth [266]. Once the mode saturates, it may be active for years or decades [267]. The gravitational wave frequency, in the slow-rotation Newtonian limit, is

$$f_{\text{GW}} = m \left[ 1 - \frac{2}{l(l+1)} \right] f_\star , \quad (1.15)$$

where  $l$  and  $m$  are the standard orders of a multipolar expansion [268]. The  $l = m = 2$  mode is most susceptible to the above instability, and is the least likely to be damped by viscous effects [269, 270], leading to  $f_{\text{GW}} = 4f_\star/3$ . Accounting for the impact of rapid rotation, a realistic equation of state, and corrections due to general relativity is complex. These considerations lead to suggestions that searches for gravitational waves from  $r$ -modes should allow for  $1.39 - 0.195(f_\star/f_K)^2 \lesssim f_{\text{GW}}/f_\star \lesssim 1.57$ , where  $f_K$  is the Keplerian frequency at which a neutron star breaks up [271, 272].

An  $r$ -mode generates gravitational waves with strain

$$h_0 = \sqrt{\frac{512\pi^7}{5}} MR^3 \tilde{J} \frac{\alpha f_{\text{GW}}^3}{D} , \quad (1.16)$$

where  $M$  and  $R$  are the mass and radius of the neutron star respectively, and  $\tilde{J}$  is an equation-of-state-dependent dimensionless quantity, typically taken as  $\tilde{J} \approx 0.0164$  [265, 273].

A pinned superfluid also results in a mass-current quadrupole, leading to a gravitational wave signal similar to that of a precessing star, i.e. at  $f_\star$  and/or  $2f_\star$  [189, 274–277].

#### 1.7.4. Standard signal model

While the many processes discussed in Section 1.7.3 are quite different in nature, the signal processing techniques needed to detect a continuous gravitational wave are broadly independent of the generation mechanism [273, 278]. In the global Lorentz frame of reference of an observer not moving relative to the center of mass of the neutron star, the phase of the gravitational wave is typically modelled as a Taylor series, as in Equation (1.5). By the time the gravitational wave reaches the detectors on Earth there are modulations to this phase. For concreteness (and simplicity), in what follows we consider a perpendicular biaxial rotor, i.e. we have  $\theta = \pi/2$  and only consider emission at  $f_{\text{GW}} = 2f_\star$ . The data  $x(t)$  in a single detector is

$$x(t) = F_+(t)h_+(t) + F_\times(t)h_\times(t) + n(t) , \quad (1.17)$$

where  $F_{+/\times}(t)$  are beam-pattern functions given as equations (10)–(14) in Jaranowski et al. [262], and  $n(t)$  is the time-dependent noise. The beam-pattern functions describe the response of the detector to a given gravitational wave strain. They depend on the orientation, longitude, latitude, and opening angle of the detector, as well as the RA,

Dec., and polarization angle  $\psi$  of the source (see Figure 1 of Wette [279] for a visual representation of this angle). The other components of Equation (1.17) are given by

$$h_+(t) = \frac{1}{2}h_0(1 + \cos^2\iota)\cos\Phi(t), \quad (1.18)$$

$$h_\times(t) = h_0\cos\iota\sin\Phi(t), \quad (1.19)$$

where  $\iota$  is the inclination angle of the source's total angular momentum vector with respect to our line of sight, and  $\Phi(t)$  is given by Equation (1.5) with the addition of time-dependent terms to account for the diurnal and annual motions of the Earth. For a source at a given sky location the signal has  $5 + s$  unknown parameters:  $h_0, \psi, \iota, \Phi_0, f_{\text{GW}}, f_{\text{GW}}^{(s)}$ , where  $\psi$  is the polarization angle,  $\Phi_0$  is an arbitrary phase offset,  $s$  is the number of frequency-derivatives included in Equation (1.5), with  $f_{\text{GW}}^{(s)}$  denoting the  $s$ -th time derivative of the frequency. For a source in a binary system there is an additional Doppler modulation, which introduces three additional parameters, the semimajor axis  $a$  projected on the sky  $a_0 = a\sin\iota$ , the orbital period  $P$ , and an additional phase offset, typically defined at the time of passage through the ascending node  $T_{\text{asc}}$ . Explicitly, the binary orbit introduces a Rømer delay  $\Delta_R(t)$ , which shifts the time at which a given gravitational wave phase reaches the SSB by

$$\Delta_R(t) = a_0 \sin \frac{2\pi(t - T_{\text{asc}})}{P}, \quad (1.20)$$

see Section 2.2 of Wette [279] for details. The above assumes circular orbits for both the Earth, and the object in its binary system. It is possible to account for non-circular orbits in general [88], however LMXBs typically have negligible measured eccentricity [280].

One approach to search for the above signal is to construct the optimal maximum-likelihood matched filter called the  $\mathcal{F}$ -statistic [262]. The matched filter analytically maximizes the log-likelihood of the data over a subset of the (typically unknown *a priori*) parameters, i.e.  $h_0$ ,  $\psi$ ,  $\iota$ , and  $\Phi_0$ . Due to the numerical efficiency of the fast Fourier transform, the  $\mathcal{F}$ -statistic is typically computed in the frequency domain [262, 281].

A  $\mathcal{F}$ -statistic-based search typically iterates over a template bank of the remaining unknown parameters, recording which parameter combinations result in detection statistic values that exceed a threshold. The requisite spacing of the templates is determined by the “metric” of the detection statistic, i.e. one calculates the maximum distance with which templates can be placed without diminishing the SNR overmuch [88]. Precise knowledge of the unknown parameters reduces the volume of this search space, and thus increases the probability of detection at a fixed probability of false alarm, due to a reduced effective trials factor.

While the  $\mathcal{F}$ -statistic can account for the additional Doppler modulation due to binary motion [282], there are numerous alternatives or augmentations which trade off between numerical and detection efficiencies. By numerical efficiency we refer to the ability of a search algorithm to save and re-use intermediate data products, reducing the total computational cost of searching a template bank. By detection efficiency we refer to the ability of a search algorithm to detect a given signal strength in noise, typically estimated empirically through a campaign of software injections and recoveries.

A circular binary orbit causes the gravitational wave phase to vary harmonically, c.f. Equation (1.20). If unaccounted for, this harmonic modulation creates so-called “orbital sidebands” [283, 284], i.e. periodic peaks in the power spectrum with spacing  $2\pi/P$ .

The  $\mathcal{C}$ -statistic incoherently sums the power dispersed into these sidebands [284]. The  $\mathcal{J}$ -statistic uses a Jacobi-Anger expansion of the phase to construct a coherent matched filter, allowing for increased detection efficiency at the expense of requiring knowledge of (or a search over)  $T_{\text{asc}}$  [8]. See Section 3 of Suvorova et al. [8] for mathematical and implementation details of the  $\mathcal{J}$ -statistic.

To demonstrate the breadth of signal processing techniques applied to search for continuous gravitational wave signals from neutron stars in binary orbits, we present a non-exhaustive list of search algorithms and/or detection statistics in Table 1.2. For detailed, modern reviews, see Wette [279], Piccinni [285], and Riles [286].

Despite differing approaches to the numerical and computational challenges of a continuous gravitational wave search, the algorithms and/or detection statistics in Table 1.2 have the same inherent signal model. They assume the signal phase varies deterministically, according to Equation (1.5), plus the requisite Doppler corrections. Coherent searches track the phase over the entire data span  $T_{\text{obs}} \sim 1 \text{ yr}$  (for a typical observing run of the LVK), but are prohibitively expensive unless many of the unknown spin parameters, including  $f_{\text{GW}}$  and  $\dot{f}_{\text{GW}}$  are fixed at values inferred via electromagnetic observations. However, if the template bank is large, a semi-coherent technique which splits the data span into  $N_T$  segments of length  $T_{\text{drift}}$  is employed. Semi-coherent pipelines do not require phase continuity between blocks. Often, semi-coherent pipelines follow up candidates above the initial search threshold by increasing the coherence time  $T_{\text{drift}}$ , which will increase the SNR if the signal conforms to the deterministic phase model discussed above [10, 295].

For continuous gravitational wave searches targeting known pulsars, i.e. targets with an electromagnetically measured  $f_\star$ , so-called “targeted” or “narrowband” searches are typically conducted. A targeted search assumes a strict signal model that the  $\Phi(t)$  in Equations (1.18) and (1.19) is an exact harmonic of the electromagnetically measured phase, i.e.  $f_{\text{GW}}$  (and time-derivatives thereof) are assumed to be known exactly [289, 305]. On the other hand, a narrowband search allows a slight mismatch between  $f_\star$  ( $\dot{f}_\star$ ) and the harmonics at which  $f_{\text{GW}}$  ( $\dot{f}_{\text{GW}}$ ) may exist. The degree of allowed mismatch varies, but recent searches allow for  $1 - \delta < f_{\text{GW}}/(2f_\star) < 1 + \delta$ , with  $\delta \sim 10^{-3}$  [305, 306]. The rationale for allowing such a mismatch is that the gravitationally emitting mass or current quadrupole may not co-rotate exactly with the electromagnetically emitting component of the star. For example, there may exist differential rotation between the crust and core, as discussed in Sections 1.4 and 1.5.2.

### 1.7.5. Hidden Markov Models and wandering signals

Timing noise, or spin-wandering as it is often called in continuous gravitational wave contexts, is ubiquitous in pulsars, as discussed in Section 1.3.1. The effect that spin wandering has on the standard signal model discussed in Section 1.7.4 depends on both the continuous gravitational wave emission mechanism, and the mechanism underlying spin wandering. Most emission mechanisms predict  $f_{\text{GW}} \propto f_\star$ , as discussed in Section 1.7.3, so if  $f_\star$  fluctuates stochastically, so will  $f_{\text{GW}}$ . This stochastic fluctuation limits the coherence time over which the deterministic signal model discussed above is valid.

One method of incorporating a stochastically fluctuating frequency into the signal model is by treating  $f_{\text{GW}}$  as a hidden random variable. This hidden random variable is

Table 1.2: Non-exhaustive list of algorithms and/or detection statistics used to search for continuous gravitational wave signals from neutron stars in binary orbits. “TD” refers to a search performed in the time (rather than frequency) domain. “Sco X-1” refers to Scorpius X-1, a LMXB discussed further in Section 1.7.6. Directed searches have a fixed sky position (i.e. the target is known from electromagnetic observations), but search a wide frequency band. Targeted searches have a fixed sky position, and fix the gravitational wave phase evolution to an exact harmonic of the electromagnetically observed phase evolution. Blind searches are not targeting a known system, but instead search the whole sky and a wide frequency band. Narrowband searches have a fixed sky position, but search a narrow frequency band around harmonics of the electromagnetically observed spin frequency. O1, O2, and O3 refer to Observing Runs 1, 2, and 3 respectively of the LVK. S5 and S6 refer to Science Runs 5 and 6 respectively of the LIGO detectors. Only searches using the latest data searched (fourth column) are listed in the sixth column.

Algorithm	Target(s)	Search type	Latest data searched	Method reference(s)	Search reference(s)
5n-vector	Sco X-1	Directed	O2	[287, 288]	[288]
	Known MSPs	Targeted	O3	[287]	[289]
BinarySkyHough	Unknown MSPs	Blind	O3	[290]	[291, 292]
$\mathcal{C}$ -statistic	Sco X-1	Directed	O1	[284]	[293] <sup>a</sup>
CrossCorr	Sco X-1	Directed	O3	[294, 295]	[296, 297]
$\mathcal{J}$ -statistic	Sco X-1	Directed	O3	[8]	[298] <sup>a</sup>
	Known MSP	Directed	O3	[8]	[299] <sup>a</sup>
	AMXPs	Narrowband	O3	[8]	[6] <sup>a</sup>
TD $\mathcal{F}/\mathcal{G}$ -statistic	Known MSPs	Targeted	O3	[262, 300]	[289]
TD Bayesian	Known MSPs	Targeted	O3	[301]	[289]
TwoSpect	Sco X-1	Directed	S6	[302]	[303]
	AMXP	Narrowband	S6	[302]	[303]
	Unknown MSPs	Blind	S6	[302]	[304]

<sup>a</sup> Uses a hidden Markov model framework to track spin-wandering, see Section 1.7.5.

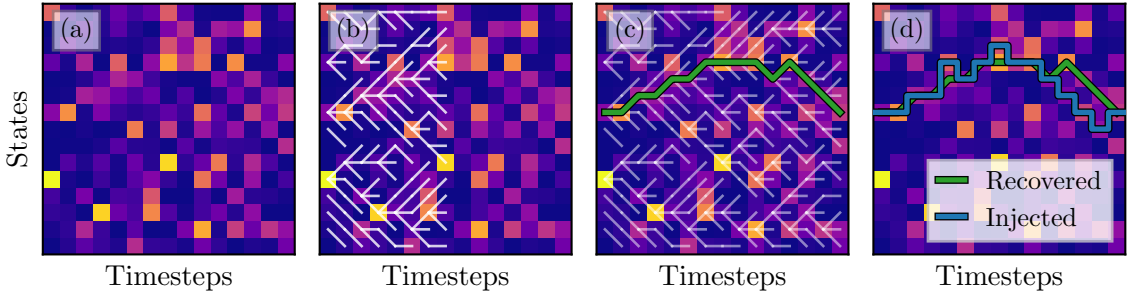


Figure 1.4: Illustration demonstrating the Viterbi algorithm finding a wandering signal in noise. The color for each state and time represents the likelihood  $L_{o_i q_j}$ , with purple and yellow corresponding to low and high relative  $L_{o_i q_j}$  respectively. In panel (a) we have injected a wandering signal into noise. In panel (b) we see the Viterbi algorithm dynamically pruning the possible trajectories of the signal in white. In panel (c) we highlight the maximum *a posteriori* trajectory in green, i.e. the trajectory that maximizes Equation (1.21). Finally, in panel (d) we reveal the trajectory of the injected signal in blue, and show that the trajectory recovered by the Viterbi algorithm overlaps with it.

observable through noisy measurements, i.e. matched filters with a deterministic signal model applied to segments of data  $T_{\text{drift}}$  in length. To search for such a hidden random variable, a standard signal processing technique is to frame the problem in terms of a hidden Markov model (HMM) [307]. Concretely, a HMM describes a Markovian random process that moves between a finite set of discrete states  $\{q_1, \dots, q_{N_Q}\}$  over a finite set of discrete time steps  $\{t_1, \dots, t_{N_T}\}$ . The possible trajectories of the process are determined probabilistically via the transition matrix  $A_{q_i q_j}$ , which gives the probability of moving to state  $q_i$  from state  $q_j$ . This transition matrix is combined at each timestep with the emission probability  $L_{o_i q_j}$ , which gives the probability of observing the noisy measurement  $o_i$  if the process is in the state  $q_j$ . The probability of a trajectory through the set of states  $Q = \{q(t_1), \dots, q(t_{N_T})\}$  given a set of observations  $O = \{o(t_1), \dots, o(t_{N_T})\}$  is

$$\Pr(Q|O) = \Pi_{q(t_1)} \prod_{i=2}^{i=N_T} L_{o(t_i)q(t_i)} A_{q(t_i)q(t_{i-1})}, \quad (1.21)$$

where  $\Pi_{q(t_1)}$  is the prior probability of starting in each state. The Viterbi algorithm [308] efficiently solves the problem of finding the most probable trajectory  $Q^*$  through the state–time trellis, given a set of observations and a prescribed transition matrix. It does so in a dynamic, recursive manner; at every timestep the algorithm only retains most-likely trajectories ending in each of the  $N_Q$  states. Once the final timestep is reached, the most probable trajectory is reconstructed via backtracking. See equations (14)–(19) of Suvorova et al. [7] for a pseudocode implementation of the Viterbi algorithm. We show a toy illustration of the Viterbi algorithm recovering an injected signal in noise in Figure 1.4.

Mapping the physics of spin-wandering onto a HMM-based search for continuous gravitational waves requires us to choose: i) a method of estimating  $L_{o_i q_j}$  for a given time chunk of length, ii) the duration  $T_{\text{drift}}$  over which  $f_{\text{GW}}$  stays within one frequency bin, and iii) the transition matrix  $A_{q_i q_j}$  [7]. For i) we assign the hidden discrete states

of the HMM to  $f_{\text{GW}}$ , and thus use a frequency-domain estimator for  $L_{o_i q_j}$ . Typically, for searches targeting isolated sources the  $\mathcal{F}$ -statistic is used [309–313], while the  $\mathcal{J}$ -statistic is used for targets in binary systems [6, 298, 314], however other choices exist [293, 315, 316]. For ii) and iii), the most common choice is to assume that spin-wandering amounts to an unbiased random walk in  $f_{\text{GW}}$ . One way to approximate an unbiased random walk in a HMM is to choose

$$A_{q_{i+1}q_i} = A_{q_iq_i} = A_{q_{i-1}q_i} = \frac{1}{3}, \quad (1.22)$$

with all other elements zero, such that at each timestep the process may move one state up or down, or stay in the same state, with each option having equal probability. We limit  $T_{\text{drift}}$  such that  $f_{\text{GW}}$  moves at most one frequency bin  $\Delta f$  over  $T_{\text{drift}}$ . We set  $\Delta f = 1/(2T_{\text{drift}})$ , i.e. we over-sample the Nyquist frequency by a factor of two. For LMXBs, fluctuations in  $f_{\star}$  are inferred from X-ray flux fluctuations [87], which then map to fluctuations in  $f_{\text{GW}}$  via the mechanisms discussed in Section 1.7.3. X-ray flux fluctuations indicate auto-correlation time-scales of order  $\sim 10$  days [89], informing our choice of  $T_{\text{drift}}$ .

### 1.7.6. Accreting millisecond X-ray pulsars

First discovered in 1998, AMXPs provide concrete evidence for the so-called “recycling scenario” of radio millisecond pulsars. In this scenario, a no-longer-pulsating neutron star (having spun down into the so-called “death valley”, the bottom-right corner of the  $P-\dot{P}$  diagram, see Figure 1.2 [317]) has a stellar-mass binary companion. The companion eventually overflows its Roche lobe due to standard binary evolution, creating an accretion disk around the neutron star. The matter in this accretion disk is funneled onto the magnetic poles of the neutron star, providing a torque that can spin it up, “reviving” the neutron star as a millisecond pulsar [318, 319].

There is an abrupt cut-off in the spin frequency distribution of millisecond pulsars, with none observed spinning faster than  $f_{\star} \approx 716$  Hz [320]. Millisecond oscillations in the tails of thermonuclear X-ray bursts also provide evidence for an upper limit in spin frequency for neutron stars that do not persistently pulsate [321]. The fastest spinning AMXP has  $f_{\star} \approx 599$  Hz [322]. The distribution of spin frequencies for AMXPs is statistically consistent with a uniform distribution between 100 and 600 Hz, as assessed via a Kolmogorov-Smirnov test (p-value of 0.91). The frequency at which a neutron star is disrupted via centrifugal effects is uncertain, however most estimates put it at higher than 1 kHz [323]. This implies that either the torque due to accretion must switch off at a certain frequency, or there is an opposing, balancing torque that stops the neutron star in these systems from spinning up to the break-up frequency.

The microphysical details of accretion onto a magnetized neutron star are complex, so we summarize only the pertinent details here, and refer the interested reader to modern reviews in Di Salvo and Sanna [44] and Patruno and Watts [324], and references therein. Adopting the simplistic model of steady accretion from a geometrically thin disk onto a star with dipolar magnetic field with magnetic moment  $\mu$ , the radius  $r_m$  at which the freely-falling gas has comparable kinetic and magnetic energy density in the

magnetosphere is

$$r_m = \xi \left( \frac{\mu^4}{2GM\dot{M}^2} \right)^{1/7}, \quad (1.23)$$

$$\approx 18 \text{ km} \left( \frac{\xi}{0.5} \right) \left( \frac{\mu}{10^{26} \text{ G cm}^3} \right)^{4/7} \left( \frac{\dot{M}}{10^{-10} M_{\odot} \text{ yr}^{-1}} \right)^{-2/7} \left( \frac{M}{1.4 M_{\odot}} \right)^{-1/7}, \quad (1.24)$$

where  $\dot{M}$  is the mass accretion rate at the inner boundary of the disk, and  $\xi \approx 0.3 - 1.0$  corrects for the non-spherical geometry, non-dipolar magnetic field, and more, see D'Angelo and Spruit [325] for details. Without the correction factor  $\xi$ ,  $r_m$  is more commonly known as the Alfvén radius,  $r_A$ . The distance  $r_m$  is where the gas transfers angular momentum to the neutron star, applying a torque. This torque spins up the star, if we have  $r_m < r_{\text{co}}$ , where  $r_{\text{co}}$  is the radius at which the gas is co-rotating in a Keplerian orbit, with the same angular frequency as the surface of the star, i.e.

$$r_{\text{co}} = \left( \frac{GM}{4\pi^2 f_{\star}^2} \right)^{1/3} \quad (1.25)$$

$$\approx 18 \text{ km} \left( \frac{M}{1.4 M_{\odot}} \right)^{1/3} \left( \frac{f_{\star}}{900 \text{ Hz}} \right)^{-2/3}. \quad (1.26)$$

On the other hand, if  $r_m > r_{\text{co}}$ , the accretion torque will have the opposite sign, i.e. it will spin down the star. This implies that, under the assumptions of the above simple model, accretion will only spin up the neutron star until  $r_m \sim r_{\text{co}}$ , which occurs at  $f_{\star} \approx 9 \times 10^2 \text{ Hz}$  for the fiducial values inserted into Equations (1.24) and (1.26) above [46, 326]. This equilibrium frequency depends on  $\mu$  and  $\dot{M}$ , which can in principle be estimated from X-ray data [92]. In the above argument we have obviated the complexity of the magnetic field interacting not just with the inner boundary, but the entire accretion disk [327, 328], among other considerations.

An alternative explanation for the lack of observed spin frequencies above 716 Hz is that gravitational wave emission balances the torque provided via accretion [87]. The torque produced by gravitational waves  $N_{\text{GW}}$  depends on the degree of asymmetry, as well as the rotation frequency, viz. [87]

$$N_{\text{GW}} = -\frac{32G\epsilon^2 I_{zz}(4\pi f_{\star})^5}{5c^5}, \quad (1.27)$$

where we have assumed the simple ‘‘mountain’’ emission mechanism discussed in Section 1.7.3. If we also assume the simple model for the accretion torque above (i.e. neglecting the additional torque induced by the interaction of the magnetic field with the accretion disk), we have [46]

$$N_{\text{acc}} = \dot{M} \sqrt{GM r_m}. \quad (1.28)$$

When we let Equation (1.27) balance Equation (1.28), we rearrange to find

$$\begin{aligned} f_{\star} \approx 767 \text{ Hz} & \left( \frac{M}{1.4 M_{\odot}} \right)^{-3/70} \left( \frac{I_{zz}}{10^{45} \text{ g cm}^2} \right)^{1/5} \left( \frac{\xi}{0.5} \right)^{1/10} \left( \frac{\mu}{10^{26} \text{ G cm}^3} \right)^{4/70} \\ & \times \left( \frac{\epsilon}{10^{-7}} \right)^{-2/5} \left( \frac{\dot{M}}{10^{-10} M_{\odot} \text{ yr}^{-1}} \right)^{-3/35}, \end{aligned} \quad (1.29)$$

where we have inserted Equation (1.24) for  $r_m$ . That is, for reasonable values of  $\epsilon \sim 10^{-7}$  [183, 329, 330], the gravitational wave back-reaction torque will balance the torque from accretion at a spin frequency for which  $r_m < r_{\text{co}}$ , i.e. before the magnetospheric radius increases to the point where accretion begins to spin down the star.

Typically,  $\dot{M}$  is assumed to be proportional to the X-ray flux  $F_X$ , as the maximum possible accretion luminosity is  $L = (GMM)/R$ , and  $F_X = L/(4\pi D^2)$ . Thus, at fixed  $f_{\text{GW}}$  and  $\epsilon$ , sources with the highest  $F_X$  will produce the largest  $h_0$  (see Equation (1.14)) [87, 331]. This torque-balance argument motivates continuous gravitational wave searches for Scorpius X-1, the brightest extra-solar X-ray source in the sky, and is a LMXB which likely hosts a neutron star [293, 296–298, 303, 314, 332, 333]. No detection of continuous gravitational wave emission is claimed. There are multiple reasons why searches for continuous gravitational waves from this target are challenging: i) no pulsations have been seen, thus the rotation frequency of the neutron star is unknown [43]; ii) relatedly, the binary orbital elements are poorly constrained [334]; and iii) flux variations indicate the timescale of spin-wandering is  $T_{\text{drift}} \sim 10$  days [89]. Items i) and ii) require search algorithms iterate through not only the plausible frequency range, but also a large template bank of orbital elements. The impact of item iii) is ameliorated with a HMM-based search method, as introduced in Section 1.7.5, but still limits the chunk of time  $T_{\text{drift}}$  over which coherent integration is feasible.

AMXPs are alternative LMXB targets for continuous gravitational wave searches. They are a heterogeneous class of objects, with few features that are shared among all known AMXPs, hence the conditional statements below. For detailed reviews, see Di Salvo and Sanna [44], Patruno and Watts [324], and Marino et al. [335]. Most AMXPs are in a quiescent state most of the time, with no X-ray pulsations visible. The typical X-ray flux in this state is three to four orders of magnitude smaller than that for Scorpius X-1 (c.f. Table 6.4 and references therein). Sporadically, AMXPs go into “outburst”, where their X-ray flux is enhanced by roughly two orders of magnitude, and X-ray pulsations are usually detectable. The durations of and waiting times between outburst phases are usually unpredictable, with durations ranging from minutes to months, and some AMXPs going decades between outbursts. The enhanced X-ray flux is interpreted as a temporary increase in the mass accretion rate. Coherent timing, as discussed in Section 1.3, is performed whenever pulsations are visible. These timing solutions reveal both positive and negative spin-frequency derivatives, which are small in magnitude, typically  $\dot{f}_\star \sim \pm 10^{-14} \text{ Hz s}^{-1}$ . There is little concrete evidence of spin-wandering in AMXPs, however timing noise is found in some [336], and accretion torques are observed to vary on timescales of weeks in others [49]. By connecting timing solutions from different outbursts, a long-term negative spin-frequency derivative ( $\dot{f}_\star \sim -10^{-15} \text{ Hz s}^{-1}$ ) is found in some AMXPs [337–339].

What is the motivation behind searching for continuous gravitational waves from AMXPs specifically? Variable accretion rates, and evidence that these systems are not in spin equilibrium (i.e.  $\dot{f}_\star \neq 0$ ), limit the direct application of the classic torque-balance argument [87]. However, it is unclear whether the sharp cut-off in spin frequency is adequately explained from accretion theory alone [321, 340], especially given transient accretion episodes can spin up AMXPs to higher spin frequency compared to persistent accretors [341]. Active accretion events can plausibly deposit sufficient material to form mountains [87, 254, 329, 342], or ring-up  $r$ -modes [343–345]. A search in modula-

tions of X-ray spectra tentatively reveals *r*-mode oscillations may exist in some AMXPs [346, 347]. Detection of continuous gravitational waves is likely difficult, given the suspected small strains, and the current sensitivity of the detectors [348, 349]. However, searches are computationally inexpensive as both the spin frequency and orbital elements of AMXPs are well known from electromagnetic timing solutions provided from X-ray pulsations. The timescale of spin-wandering in AMXPs is not well understood. We use  $T_{\text{drift}} = 10 \text{ d}$  for consistency with previous analyses of Scorpius X-1 [284, 293, 298, 314], where the timescale of spin-wandering is constrained via studies of the X-ray flux variability [89].

Searches were performed in both S6 [303] and O2 LIGO data [9] for one and five AMXPs respectively. In Chapter 6 we perform a HMM-based search for continuous gravitational waves from 20 AMXPs using O3 LIGO data.

## 1.8. THESIS OUTLINE

We structure the remainder of the thesis as follows.

- Chapter 2 investigates how autocorrelations between glitch waiting times or sizes provide an additional statistical tool for falsifying the SDP process, as the underlying meta-model governing how glitches are triggered. We show that the SDP process cannot currently be falsified in any individual pulsar, but the diversity of statistical classes of glitching pulsars necessitates that the distribution of stress-release sizes must vary pulsar-to-pulsar. This tentatively indicates that different physical mechanisms are triggering glitches in different pulsars.
- Chapter 3 introduces a new stress-accumulation and relaxation meta-model wherein the stress accumulates via a biased Brownian random walk, until a stress threshold is reached. The long-term statistical predictions of this meta-model are compared to data, and we show that the model cannot adequately explain the sequences of glitches in all pulsars, unless we are not detecting many small glitches.
- In Chapter 4 we augment the SDP framework by explicitly tracking the pinning strength of pinning sites that are occupied by vortices over sequences of glitches. Doing so specializes the meta-model to interrogate the superfluid vortex avalanche micophysical model for pulsar glitches. We find that the predictions of such a meta-model are incongruent with the long-term statistical observables from glitching pulsars.
- Chapter 5 adapts the SDP framework to the context of solar flares. We search for evidence that solar flares are triggered when an underlying stress variable reaches a static-in-time threshold before each event. We find no strong evidence for this in the historical catalog of flares.
- Chapter 6 presents a search for continuous gravitational waves from 20 AMXPs in LIGO O3 data. The search uses a HMM pipeline that explicitly accommodates a stochastically wandering signal model. We find no strong evidence of any signals, and thus set upper limits on the maximum possible asymmetry in these objects.
- Chapter 7 concludes the thesis with a summary of the above work, and some directions for future work.

# CHAPTER 2

---

## Autocorrelations in pulsar glitch waiting times and sizes

---

This chapter is a reproduction of [1]

*J. B. Carlin, and A. Melatos,*

Monthly Notices of the Royal Astronomical Society, 488, 4, 4890 (2019)

reformatted with the following changes only:

- **Footnote 2 in Section 2.4.1 is included in response to a suggestion of the thesis examiner.**
- **A minor typo in Section 2.6 is corrected.**
- **The text is styled to match the rest of this thesis.**
- **Notation is updated to match the rest of this thesis, this necessitates a minor update to the legends in Figures 2.4 and 2.5.**
- **Where necessary, bibliographic records are updated.**

### 2.1. ABSTRACT

Among the five pulsars with the most recorded rotational glitches, only PSR J0534+2200 is found to have an autocorrelation between consecutive glitch sizes which differs significantly from zero (Spearman correlation coefficient  $\rho = -0.46$ , p-value = 0.046). No statistically compelling autocorrelations between consecutive waiting times are found. The autocorrelation observations are interpreted within the framework of a predictive meta-model describing stress-release in terms of a state-dependent Poisson process. Specific combinations of size and waiting time autocorrelations are identified, alongside combinations of cross-correlations and size and waiting time distributions, that are allowed or excluded within the meta-model. For example, future observations of any “quasiperiodic” glitching pulsar, such as PSR J0537–6910, should not reveal a positive waiting time autocorrelation. The implications for microphysical models of the stress-release process driving pulsar glitches are discussed briefly.

## 2.2. INTRODUCTION

The secular electromagnetic spin down of some rotation-powered pulsars is interrupted stochastically by spin-up events called “glitches”. The statistical properties of glitches have been studied across the whole pulsar population (see [139, 140, 350]; among others), and more recently in individual pulsars as the number of recorded glitches has grown [17, 18, 128, 141, 351]; see Table 2.1 for a list of the main objects studied by previous authors. The latter analyses reveal that there are two main statistical classes of glitching pulsar: “Poisson-like” objects, with exponentially distributed waiting times and power-law distributed sizes; and “quasi-periodic” objects, which have non-monotonic waiting time and size distributions [17, 18, 128]. What physically triggers glitches, and why two classes of activity exist, are open questions. In general terms, most models posit that glitches occur when the elastic stress and/or differential rotation in the star exceed a threshold, triggering some sort of scale-invariant avalanche process such as a starquake or superfluid vortex avalanche; see the recent review by Haskell and Melatos [150] and references therein.

Pulsar glitches are events that are naturally ordered in time. It is therefore profitable to ask whether their order of occurrence contains statistical information about the underlying physics. The ordered set of glitch epochs shows some evidence of clustering, or equivalently a variable rate, in PSR J0534+2200 (also known as B0531+21) [55, 352]. Analysis of time-ordered stochastic events is a rich field of study. For example, Omori’s law describes the observed sequence of aftershocks following a large terrestrial earthquake [353]. Autocorrelations between waiting times of stochastic events have been studied in the context of numerical sandpile simulations [201, 354], solar flares [355], and other self-organized critical systems [356].

Melatos et al. [351] studied the forward and backward cross-correlations between glitch sizes and waiting times in the context of a state-dependent Poisson process [16, 207, 224] and made falsifiable predictions regarding the cross-correlation coefficients as functions of the spin-down rate and mean waiting time. In this paper we ask whether falsifiable predictions can also be made regarding sizes and waiting time autocorrelations. In Section 2.3 we outline the current observational situation on this front and calculate autocorrelation coefficients for the five pulsars with the most recorded glitches. Section 2.4 sets up the state-dependent Poisson process model for glitches and predicts the autocorrelation coefficient as a function of key inputs to the model, e.g. the spin-down rate. In Section 2.5 we directly compare the theory and existing observations and make falsifiable predictions regarding future observations.

## 2.3. TIMING OBSERVATIONS

### 2.3.1. *Data*

Large-scale, multi-object radio timing campaigns devoted to systematic searches for pulsar glitches are currently carried out at the Jodrell Bank [128] and Parkes [131, 135] Observatories. These campaigns are supplemented by additional current programs such as CHIME [357] and UTMOST [97] that take place at the Dominion Radio Astrophysical Observatory and Molonglo Synthesis Telescope respectively. The analysis in this pa-

per combines the above observations with historical data sets from the Hartebeesthoek Radio Astronomy Observatory [358], Mount Pleasant Radio Observatory [359], Arecibo Observatory [360], and Jet Propulsion Laboratory [361]. The completeness of the Parkes data set, i.e. whether all detectable glitches have been identified, was discussed by Yu and Liu [135]. Espinoza et al. [98] claimed that the data set for PSR J0534+2200 is complete, and that the minimum physically allowed glitch size is resolved. However, for most pulsars the cadence of observations is variable [134, 135]. It is still uncertain whether the data sets we analyze in this paper are complete.

According to the Jodrell Bank online catalogue<sup>1</sup>, the five most prolific glitchers as of 2019 February 11 are PSR J0537–6910 ( $N = 42$  recorded glitches<sup>2</sup>), PSR J1740–3015 ( $N = 36$ ), PSR J0534+2200 ( $N = 23$  or  $27^3$ ), PSR J1341–6220 ( $N = 23$ ), and PSR J0835–4510 ( $N = 20$ ). The mean number of glitches per year are 3.2, 1.1, 0.64, 1.1, and 0.38 for the five objects respectively; they have been monitored for different lengths of time.

### 2.3.2. Autocorrelations

We can arrange the epochs,  $t_i$ , and fractional sizes,  $s_i = \Delta\nu_i/\nu_i$ , in any given pulsar as a sequence of time-ordered waiting times between glitches,  $\{\Delta t_1, \Delta t_2, \dots, \Delta t_{N-1}\}$ , with  $\Delta t_i = t_{i+1} - t_i$ , and a sequence of time-ordered sizes,  $\{s_1, s_2, \dots, s_N\}$ . Note that, if  $N$  glitches are observed, there are  $N - 1$  observed waiting times. The autocorrelation of an ordered data set of  $N$  discrete points,  $\{x_i\}$ , is calculated by constructing  $N - k$  pairs of points,  $(x_1, x_{1+k}), (x_2, x_{2+k}), \dots, (x_{N-k}, x_N)$ , i.e. pairs of points separated by lag  $k$ . The first and second entries in each pair constitute the two variates to be correlated. The Spearman rank correlation coefficient,  $\rho$ , is calculated as [362]

$$1 - \rho = 6 \left\{ (N - k) \left[ (N - k)^2 - 1 \right] \right\}^{-1} \sum_{i=1}^{N-k} d_i^2 , \quad (2.1)$$

where  $d_i$  is the difference between the ordinal ranks of the  $i$ -th pair of observations. While it is possible to calculate autocorrelations at an arbitrary lag  $k$ , we restrict our subsequent analysis to  $k = 1$ , i.e. autocorrelations between consecutive events. A partial check of lags  $1 < k \leq 5$  does not reveal any autocorrelations significantly different from zero. We use the Spearman rank correlation coefficient, which looks for monotonic relationships, instead of the standard Pearson correlation coefficient, as the former is less sensitive to outliers and does not assume a parametric (e.g. linear) form for the relationship.

Table 2.1 contains the calculated Spearman correlation coefficients for autocorrelations in consecutive waiting times,  $\rho_{\Delta t}$ , and consecutive sizes,  $\rho_{\Delta X}$ , for the five most

---

<sup>1</sup>Found through the Jodrell Bank Centre for Astrophysics at <http://www.jb.man.ac.uk/pulsar/glitches.html> [128].

<sup>2</sup>The number and parameters of glitches recorded for this pulsar vary between Middleditch et al. [147], Ferdman et al. [148], and Antonopoulou et al. [149]. We opt to include in our analysis events that occur in two out of three sources.

<sup>3</sup>The first four glitches in the Jodrell Bank catalogue occurred before high-cadence monitoring of PSR J0534+2200 began, and there is a known gap in observations between the fourth and fifth recorded glitches [55]. Henceforth we denote the full data set with an asterisk (i.e. PSR J0534+2200\*), and the 23 events since 1982 without an asterisk.

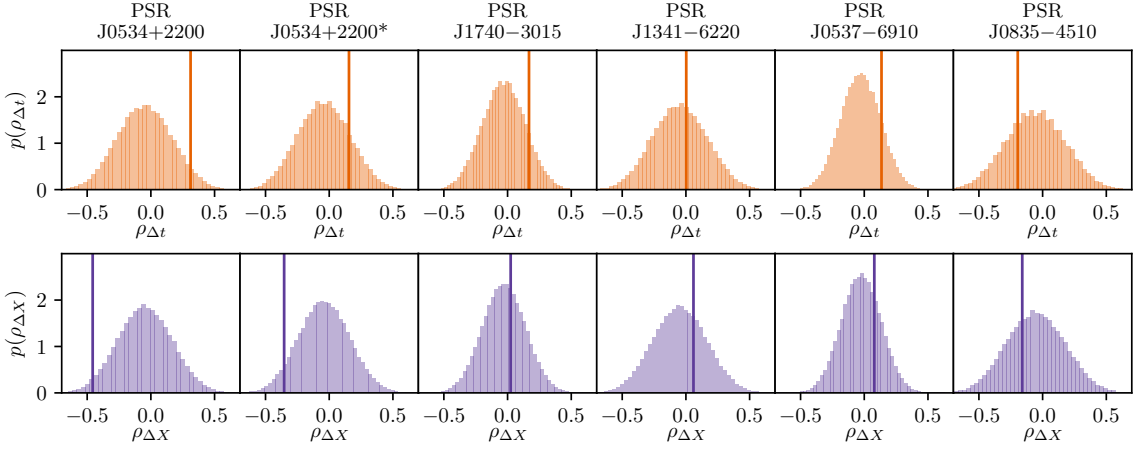


Figure 2.1: Measured autocorrelation coefficient between consecutive waiting times,  $\rho_{\Delta t}$  (top row, orange vertical lines), and consecutive sizes,  $\rho_{\Delta X}$  (bottom row, purple vertical lines), for the five most active glitching pulsars. The null distribution (colored histogram in each panel) is estimated using a bootstrap permutation method, as described in the text. See Table 2.1 for numerical values of  $\rho_{\Delta t}$  and  $\rho_{\Delta X}$ .

active glitching pulsars. The autocorrelations for PSR J0534+2200\* (see footnote 3) are calculated by ignoring the comparison between  $s_4$  and  $s_5$ , and between  $\Delta t_3$  and  $\Delta t_5$ , in (2.1) due to the known gap in observations between the fourth and fifth glitch [55]. The significance of the calculated Spearman correlation coefficients is estimated using a bootstrap permutation method. This nonparametric method uses permutations of the ordered data set to estimate the null distribution (i.e. the distribution of  $\rho$ , if there is no autocorrelation in the data). We use this estimate of the null distribution to calculate a p-value: the probability that we would see  $|\rho|$  greater than the calculated value, if the null hypothesis is true. This method is robust when compared to the asymptotic (i.e. large  $N$ ) or parametric assumptions of other significance tests [363, 364]. None of the six data sets in Table 2.1 have autocorrelations in waiting times or sizes that are significantly different from zero (p-value  $> 0.05$ ), barring perhaps the size autocorrelations in PSR J0534+2200 ( $\rho_{\Delta X} = -0.46$ , p-value = 0.046). As we are in effect carrying out 12 independent significance tests it should not be surprising that at least one of the 12 has a p-value of less than 0.05, if the null hypothesis (that there is no autocorrelation) is true for all data sets.

Figure 2.1 shows the estimated null distributions (shaded histograms) and calculated Spearman correlation coefficients (vertical lines) for the autocorrelation between consecutive waiting times (top row) and sizes (bottom row) in the five most active glitching pulsars. The null distributions are quite broad due to the small number of glitches observed in each pulsar. We do not show the confidence intervals for the measured values of  $\rho$  in Figure 2.1 for clarity. However they are consistent with the p-values, i.e. the 95% confidence interval includes the value of  $\rho = 0$  for all coefficients except the size autocorrelation in PSR J0534+2200.

Table 2.1: Pulsar name, number of glitches ( $N$ ), Spearman autocorrelation coefficient ( $\rho$ ), and associated p-value for waiting times (subscript  $\Delta t$ ) and sizes (subscript  $\Delta X$ ) for the five pulsars with the most recorded glitches. The p-value is estimated using a bootstrap permutation method, as described in the text.

Name (J2000)	$N$	Waiting times		Sizes	
		$\rho_{\Delta t}$	p-value	$\rho_{\Delta X}$	p-value
PSR J0534+2200	23	0.31	0.094	-0.46	0.046
PSR J0534+2200*	27	0.16	0.35	-0.35	0.11
PSR J1740–3015	36	0.17	0.25	0.024	0.75
PSR J1341–6220	23	0.0026	0.81	0.059	0.62
PSR J0537–6910	42	0.14	0.31	0.079	0.51
PSR J0835–4510	20	-0.20	0.56	-0.16	0.64

## 2.4. STATE-DEPENDENT POISSON PROCESS

### 2.4.1. Meta-model

Long-term glitch activity can be meta-modelled as a state-dependent Poisson process without specializing to a particular glitch mechanism [15, 16, 351]. The meta-model assumes that the instantaneous glitch rate at time  $t$ ,  $\lambda(t)$ , is governed by a single variable: the mean-field stress in the star,  $X(t)$ . The exact nature of  $X(t)$  depends on the physical mechanism causing glitches. For example it could be the spatially averaged lag between the angular velocities of the rigid crust and the superfluid interior in the vortex avalanche picture [159, 173], or the crustal strain in the starquake picture [147, 365]. It is assumed that  $\lambda[X(t)]$  grows monotonically with time, as the stress builds due to spin down, until  $\lambda[X(t)]$  diverges at some critical stress  $X_{\text{cr}}$ , and some fraction of the stress is released. Although we present the meta-model henceforth in terms of the vortex avalanche picture we emphasize that it applies equally to any stick-slip stress-release process [351].

The equation of motion for the system is

$$X(t) = X(0) + t - \sum_{i=1}^{N(t)} \Delta X^{(i)} , \quad (2.2)$$

where  $X$  and  $t$  are expressed in dimensionless units of  $X_{\text{cr}}$  and  $X_{\text{cr}} I_c / N_{\text{em}}$  respectively,  $I_c$  is the moment of inertia of the crust,  $N_{\text{em}}$  is the electromagnetic torque acting on the crust, and  $X(0)$  is an arbitrary initial condition. Both  $N(t)$ , the number of glitches up to and including time  $t$ , and the size of each stress-release event,  $\Delta X^{(i)}$ , are random variables, making the process an example of a doubly stochastic Poisson process [235, 366].

The sizes,  $\Delta X^1, \dots, \Delta X^{N(t)}$ , are drawn from a conditional jump distribution,  $\eta(\Delta X | X_p)$ , with  $\int d(\Delta X) \eta(\Delta X | X_p) = 1$ . The function  $\eta$  depends explicitly on the stress in the system just prior to the glitch,  $X_p$ , because we stipulate that no glitch reduces the stress in the system below zero [16]. The exact functional form of  $\eta$  is unobservable; it depends on the glitch microphysics. Fulgenzi et al. [16] and Melatos et al. [351] used a

power law with exponent  $-1.5$  and fractional lower cutoff  $\beta$ , but in this paper we allow  $\eta$  to vary, following the framework in Section 3 of Carlin and Melatos [15].

The counting function  $N(t)$  is implicitly determined by repeated draws from the standard probability density function (PDF) for waiting times,  $\Delta t$ , from a variable rate Poisson process [235],

$$p[\Delta t | X(t)] = \lambda[X(t) + \Delta t] \exp\left\{-\int_t^{t+\Delta t} dt' \lambda[X(t')]\right\}. \quad (2.3)$$

The exact form of the rate function  $\lambda[X(t)]$  does not significantly impact the long-term dynamics of the system [15, 16], so long as there is a divergence at the critical lag  $X_{\text{cr}}$ . Following previous work, we use

$$\lambda[X(t)] = \frac{\alpha}{1 - X(t)}, \quad (2.4)$$

where

$$\alpha = \frac{I_c X_{\text{cr}} \lambda_0}{N_{\text{em}}} \quad (2.5)$$

is a dimensionless control parameter and  $\lambda_0$  is a reference rate, i.e.  $\lambda_0 = \lambda(1/2)/2$ .

Long-term glitch statistics are generated by running a Monte-Carlo automaton which alternates drawing  $\Delta t$  from (2.3) and  $\Delta X$  from  $\eta(\Delta X | X_p)$  while tracking the stress  $X(t)$  and hence  $\lambda[X(t)]$ . We find that the automaton output falls into two regimes: “fast” spin-down ( $\alpha \lesssim 1$ ), which generates power-law distributed sizes and exponentially distributed waiting times, and “slow” spin-down ( $\alpha \gtrsim 1$ ), which generates sizes and waiting times distributed with the same functional form as  $\eta$  [15, 16]<sup>2</sup>.

Melatos et al. [351] studied the size–waiting-time cross-correlations predicted by the above meta-model. When  $\eta$  is a power law, the state-dependent Poisson process predicts large positive cross-correlations between sizes and forward waiting times, when  $\alpha$  is small, and small positive cross-correlations between sizes and backward waiting times, when  $\alpha$  is large; see Figure 4 in Melatos et al. [351]. When  $\eta(\Delta X | X_p)$  is not a power law, the large positive cross-correlation between sizes and forward waiting times at small  $\alpha$  remains, while the small positive cross-correlation between sizes and backward waiting times at large  $\alpha$  increases, depending on which functional form is used, see Appendix A and Table 1 in Carlin and Melatos [15] for details. These falsifiable theoretical trends open the door to a number of interesting observational tests.

#### 2.4.2. Autocorrelations: qualitative predictions

Does the meta-model outlined in Section 2.4.1 predict analogous trends for size and waiting time autocorrelations? We first argue qualitatively that the answer is yes before confirming the result with simulations in Section 2.4.3. For example, in the fast spin-down regime ( $\alpha \lesssim 1$ ), we have  $\eta(\Delta X | X_p) \approx \eta(\Delta X | 1)$ , as the stress in the system quickly recovers to  $X \approx 1$  after each glitch. Hence the system does not remember the size of the

---

<sup>2</sup>The parameter  $\alpha/\lambda_0$  determines the time for the system to reach  $X = X_{\text{cr}}$  from  $X = 0$  in the absence of any stress-release events. Mapping  $\alpha$  directly to physical properties is stymied by our uncertainty regarding  $X_{\text{cr}}$  and  $\lambda_0$  in individual systems.

previous glitch, nor the waiting time between the previous two glitches. There are no size or waiting time autocorrelations in this regime, regardless of the choice of  $\eta$ . On the other hand, in the slow spin-down regime ( $\alpha \gtrsim 1$ ), we expect different behavior. If  $\eta$  is peaked around a fraction,  $\mu_G$ , of  $X_p$ , a positive autocorrelation between consecutive sizes (but not waiting times) should arise. In this scenario,  $p[\Delta t | X(t)]$  does not change much with time, as  $X(t)$  remains small, when  $\alpha$  is high. Hence, we expect no waiting time autocorrelation, as the waiting times are effectively independent draws from the same PDF. However consecutive glitch sizes are correlated, because a fraction of the current stress is released at each glitch; if the stress is higher than average to begin with, one observes a sequence of larger than average glitches, before the stress resets back to its mean value.

#### 2.4.3. Autocorrelations: quantitative predictions

To quantify the trends identified in Section 2.4.2, we run a Monte Carlo automaton to simulate sequences of glitches from the model defined in Section 2.4.1, given  $\eta$  and  $\alpha$ . Pseudocode for the automaton is presented in Section 2.5 in Carlin and Melatos [15]. The functional forms of  $\eta$  used in our simulations are the same ones used by Carlin and Melatos [15] to study size–waiting-time cross-correlations. Figure 2.2 shows  $\rho_{\Delta t}$  (orange curves) and  $\rho_{\Delta X}$  (purple curves) for four different functional forms of  $\eta(\Delta X | X_p)$ . When  $\eta(\Delta X | X_p)$  is a power law (top left panel), both  $\rho_{\Delta t}$  and  $\rho_{\Delta X}$  are small for all values of  $\alpha$ . There is a slight rise to  $\rho_{\Delta t} \approx 0.15$  around  $\alpha \approx 1$ , which coincides with a slight dip to  $\rho_{\Delta X} \approx -0.05$ . When  $\eta(\Delta X | X_p)$  is uniform (top right panel),  $\rho_{\Delta t} \ll 1$  and  $\rho_{\Delta X} \ll 1$  are identical at all  $\alpha$ , with a trough of  $\rho \approx -0.1$  at  $\alpha \approx 1$ . When  $\eta(\Delta X | X_p)$  is Gaussian, the behavior changes. The lower two panels of Figure 2.2 correspond to two types of Gaussian: “fixed” (bottom left panel) and “stretchable” (bottom right panel). These correspond to a Gaussian that is peaked at a fixed value of  $X$ , regardless of  $X_p$ , and a Gaussian that is peaked at a fraction of  $X_p$ , respectively; see Section 3.1 in Carlin and Melatos [15] for details. For both fixed and stretchable Gaussians we find  $\rho_{\Delta t} < 0$  for  $5 \times 10^{-2} \lesssim \alpha \lesssim 1$ . On the other hand,  $\rho_{\Delta X}$  differs between the two functional forms. When the Gaussian is fixed,  $\rho_{\Delta X}$  peaks at  $\approx 0.15$  at  $\alpha \approx 1$ , with  $\rho_{\Delta X} \ll 1$  otherwise. When the Gaussian is stretchable,  $\rho_{\Delta X}$  grows monotonically with  $\alpha$ , asymptotizing to  $\rho_{\Delta X} \approx 0.45$  at  $\alpha \geq 10^3$ .

When  $\eta(\Delta X | X_p)$  is a power law, the automaton output depends on  $\beta$ , the fractional minimum size of a glitch. When  $\beta$  is adjusted from  $10^{-2}$  to  $10^{-3}$  to  $10^{-4}$ , the peak in  $\rho_{\Delta t}$  shifts from  $\rho_{\Delta t} \approx 0.15$  around  $\alpha \approx 1$  to  $\rho_{\Delta t} \approx 0.35$  around  $\alpha \approx 2$  to  $\rho_{\Delta t} \approx 0.50$  around  $\alpha \approx 3$ , as we see in the top panel of Figure 2.3. On the other hand,  $\rho_{\Delta X}$  does not change appreciably with  $\beta$ . The index of the power law also affects  $\rho_{\Delta t}$ . A shallower power law with index  $-0.5$  shifts the slight rise at  $\alpha \approx 1$  to a slight dip at the same  $\alpha$ , i.e. the output approaches the case when  $\eta$  is uniform. Interestingly, steeper power law indices of  $-2$  and  $-3$  also produce a small trough in  $\rho_{\Delta t}$  at  $\alpha \approx 0.2$  of  $\rho_{\Delta t} \approx -0.05$  and  $\rho_{\Delta t} \approx -0.15$  respectively.

When  $\eta(\Delta X | X_p)$  is a Gaussian, the automaton output depends on both the standard deviation of  $\eta$ , denoted by  $\sigma_G$ , and the mean, denoted as  $\mu_G$ . For both the fixed and stretchable Gaussian  $\eta$ , as  $\sigma_G$  increases, the system again approaches the case where  $\eta$  is uniform. For the fixed Gaussian the rise in  $\rho_{\Delta X}$  and the dip in  $\rho_{\Delta t}$  shifts  $\approx 0.3$  dex

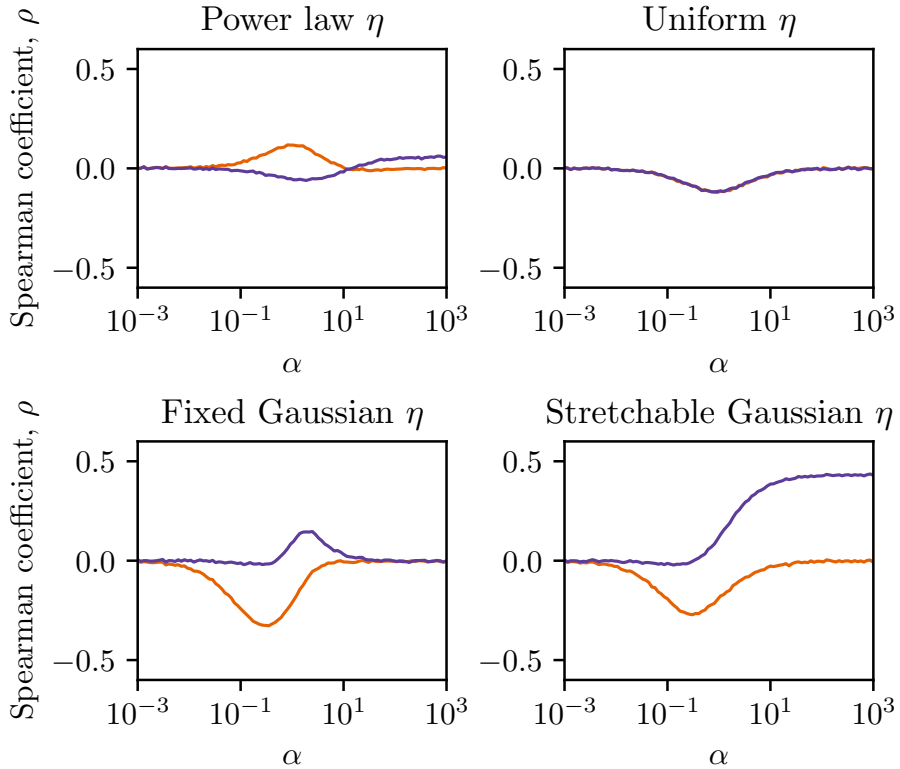


Figure 2.2: Autocorrelations between consecutive waiting times ( $\rho_{\Delta t}$ , orange curves) and sizes ( $\rho_{\Delta X}$ , purple curves) for glitches generated using the state-dependent Poisson process outlined in Section 2.4.1. Simulation parameters: 100 logarithmically spaced  $\alpha$  values,  $10^5$  glitches per  $\alpha$  value, rate function as given by (2.4),  $\beta = 10^{-2}$  for power-law  $\eta$  (top-left panel),  $\mu_G = 0.5$  and  $\sigma_G = 0.125$  for fixed and stretchable Gaussian  $\eta$  (bottom-left and bottom-right panels respectively). The uniform  $\eta$  (top right panel) has no free parameters. Explicit functional forms for each  $\eta(\Delta X \mid X_p)$  are presented by Carlin and Melatos [15, Table 1].

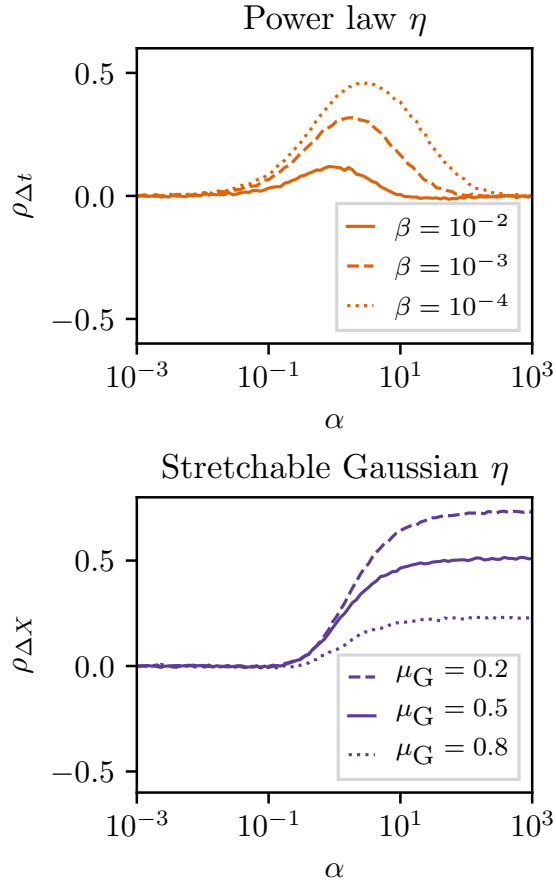


Figure 2.3: Autocorrelations generated by the state-dependent Poisson process. Top panel:  $\rho_{\Delta t}$  when  $\eta(\Delta X | X_p)$  is a power law and  $\beta$  is changed from  $10^{-2}$  (solid curve) to  $10^{-3}$  (dashed curve) to  $10^{-4}$  (dotted curve). Bottom panel:  $\rho_{\Delta X}$  when  $\eta(\Delta X | X_p)$  is a stretchable Gaussian and  $\mu_G$  is changed from 0.2 (dashed curve) to 0.5 (solid curve) to 0.8 (dotted curve). Simulation parameters: 100 logarithmically spaced  $\alpha$  values,  $10^5$  glitches per  $\alpha$  value, rate function as given by (2.4), power-law index fixed at  $-1.5$  (top panel),  $\sigma_G = 0.125$  (bottom panel). Explicit functional forms for  $\eta(\Delta X | X_p)$  are presented by Carlin and Melatos [15, Table 1].

down (up) in  $\alpha$  for  $\mu_G = 0.8$  (0.2) as compared to  $\mu_G = 0.5$ . For the stretchable Gaussian,  $\mu_G$  is inversely proportional to  $|\rho_{\Delta X}|$  and  $|\rho_{\Delta t}|$  at a given  $\alpha$ . We show the behavior of  $\rho_{\Delta X}$  with changing  $\mu_G$  in the bottom panel of Figure 2.3. With  $\mu_G = 0.2$  the peak  $\rho_{\Delta X}$  increases to  $\approx 0.7$  and the trough in  $\rho_{\Delta t}$  decreases to  $\approx -0.4$ . For  $\mu_G = 0.8$   $\rho_{\Delta X}$  decreases and  $\rho_{\Delta t}$  increases. The behavior of  $\rho_{\Delta X}$  is anticipated qualitatively at high values of  $\alpha$ , because when  $\mu_G$  is low,  $X(t)$  spends more time being higher (or lower) than average, at fixed  $\alpha$ , compared to when  $\mu_G$  is high.

## 2.5. WHAT DO AUTOCORRELATIONS TEACH US?

The state-dependent Poisson meta-model is agnostic regarding the exact mechanism underlying glitches. It describes any process that hovers around a point of marginal stability, with events triggered at some threshold, e.g. superfluid vortex avalanches, crustquakes, and many other models commonly proposed in the literature [150]. It is therefore profitable to compare its autocorrelation predictions with data, knowing that the conclusions are unlikely to depend on the specific microphysics.

### 2.5.1. Existing data

No significant autocorrelations in sizes or waiting times have been measured to date in the five objects in Section 2.3. What does this tell us about glitch physics when combined with the results in Section 2.4? It is hard to make firm statements without more data. However the large negative size autocorrelation seen in PSR J0534+2200 ( $\rho_{\Delta X} = -0.46$ , p-value = 0.046) is incongruous with most models in the literature. That is to say, there is no combination of  $\alpha$  and  $\eta$  that generates  $\rho_{\Delta X} = -0.46$ . Moreover, we see no evidence in any pulsar for a strong, positive size autocorrelation in existing data, as expected if  $\eta$  is a stretchable Gaussian and we have  $\alpha \gg 1$ , (see the bottom-right panel of Figure 2.2). Finally, existing data disfavor models that predict sizable negative waiting time autocorrelations, as seen if  $\eta$  is Gaussian with  $0.1 \lesssim \alpha \lesssim 1$ .

### 2.5.2. Future data

As the number of recorded glitches grows, the variance of the null distributions displayed in Figure 2.1 shrinks. Armed with accurate measurements of both  $\rho_{\Delta t}$  and  $\rho_{\Delta X}$ , it will eventually be feasible to rule out sections of the parameter space of the state-dependent Poisson process model for individual pulsars. For example,  $\alpha \lesssim 0.1$  is disallowed, if either  $\rho_{\Delta t}$  or  $\rho_{\Delta X}$  differ significantly from zero. Similarly,  $\alpha \gtrsim 10$  is disallowed, if  $\rho_{\Delta t}$  is positive. Uniform  $\eta$  is ruled out, if either autocorrelation differs significantly from zero, e.g.  $|\rho| \geq 0.1$ . A positive  $\rho_{\Delta t}$  is only possible if  $\eta$  is a power law. The magnitude of a positive  $\rho_{\Delta t}$  places constraints on  $\alpha$  and  $\beta$ . Any observed positive  $\rho_{\Delta t}$  (which implies that  $\eta$  is a power law) should come along with a negligible  $\rho_{\Delta X}$ , otherwise the model is not self-consistent.

### 2.5.3. Combining auto- and cross-correlations

To test the state-dependent meta-model further, we can con-currently consider size auto-correlations, waiting time autocorrelations, cross-correlations between sizes and backwards waiting times ( $\rho_-$ ), and cross-correlations between sizes and forwards waiting times ( $\rho_+$ ). Melatos et al. [351] found that, when  $\eta$  is a power law, we should see a large  $\rho_+$  alongside  $\rho_- \ll 1$  in the low- $\alpha$  regime, and low  $\rho_+$  and  $\rho_-$  in the high- $\alpha$  regime. Similar predictions are made for numerous choices of  $\eta$  [15].

An example of the above, four-way comparison is presented in Figures 2.4 and 2.5 for PSR J0534+2200 and PSR J0537–6910 respectively. The 95% confidence intervals for the observed correlations are estimated via the standard error for the Spearman correlation coefficient [367],

$$\rho_{\text{CI}\pm} \simeq \tanh^{-1} \left[ \tanh \rho \pm 1.96 \left( \frac{1 + \rho^2/2}{\sqrt{N - 3}} \right) \right], \quad (2.6)$$

where  $\rho_{\text{CI}\pm}$  correspond to the upper and lower limits of the 95% confidence interval. In Figure 2.4, for PSR J0534+2200, the observed forward and backward cross-correlations, as well as the observed waiting time autocorrelation, are consistent with the model, if we have  $1 \lesssim \alpha \lesssim 10$  and  $\eta$  is a power law. However, the observed negative size autocorrelation contradicts this (and any other)  $\alpha$  and  $\eta$  combination. On the other hand, in Figure 2.5 we see that the observed cross- and autocorrelations for PSR J0537–6910 are consistent with the predictions of the model for  $\alpha \lesssim 10^{-2}$ . The result does not depend on  $\eta$ ; in the low- $\alpha$  regime, all choices of  $\eta$  predict the same autocorrelations and cross-correlations; cf. Figure 2.2 and Figure A1 of Carlin and Melatos [15] respectively.

To illustrate roughly what is possible using the method described above, in Table 2.2 we present “acceptable” values of  $\alpha$  and functional forms  $\eta$  for the five pulsars with the most recorded glitches. We define acceptable values of  $\alpha$  to be when, given  $\eta$ , all four of the forward cross-correlations, backward cross-correlations, size autocorrelations, and waiting time autocorrelations lie within the 95% confidence interval of the observed correlation coefficients. For PSR J1740–3015, when  $\eta$  is a power law, any value of  $\alpha \gtrsim 1$  is acceptable. For PSR J1341–6220, when  $\eta$  is a power law, only  $0.1 \lesssim \alpha \lesssim 0.5$  is acceptable; however when  $\eta$  is a Gaussian, the range shifts to  $0.01 \lesssim \alpha \lesssim 0.1$ . For PSR J0835–4510, when  $\eta$  is a power law, any  $\alpha \gtrsim 0.5$  is acceptable. When  $\eta$  is a Gaussian,  $0.05 \lesssim \alpha \lesssim 0.5$  is acceptable. We emphasize that this procedure is not equivalent to a precise parameter estimation or a systematic fit, which we leave to future work given the paucity of current data.

As explained by Melatos et al. [351], the product of the (observable) long-term average spin-down rate,  $\dot{\nu}$ , and the average waiting time between glitches for each pulsar,  $\langle \Delta t \rangle$ , is proportional to  $X_{\text{cr}}/\alpha$ , if  $\eta$  is a separable function of the form

$$\eta(\Delta X | X_p) = (\delta + 1) (X_p - \Delta X)^\delta X_p^{-(\delta+1)}. \quad (2.7)$$

The cross-correlations produced by (2.7) are similar to the standard power law  $\eta$ , i.e.  $\rho_+ \approx 1$  and  $\rho_- \ll 1$  for low  $\alpha$ ,  $\rho_+ \ll 1$  and  $\rho_- \approx 0.15$  for high  $\alpha$ . We do not use  $-\dot{\nu}\langle \Delta t \rangle$  as a proxy for  $\alpha^{-1}$  here, because (2.7) produces autocorrelations similar to those of a uniform  $\eta$ , i.e.  $\rho_{\Delta X} \ll 1$  and  $\rho_{\Delta t} \ll 1$  for all  $\alpha^{-1}$  and hence all  $-\dot{\nu}\langle \Delta t \rangle$ .

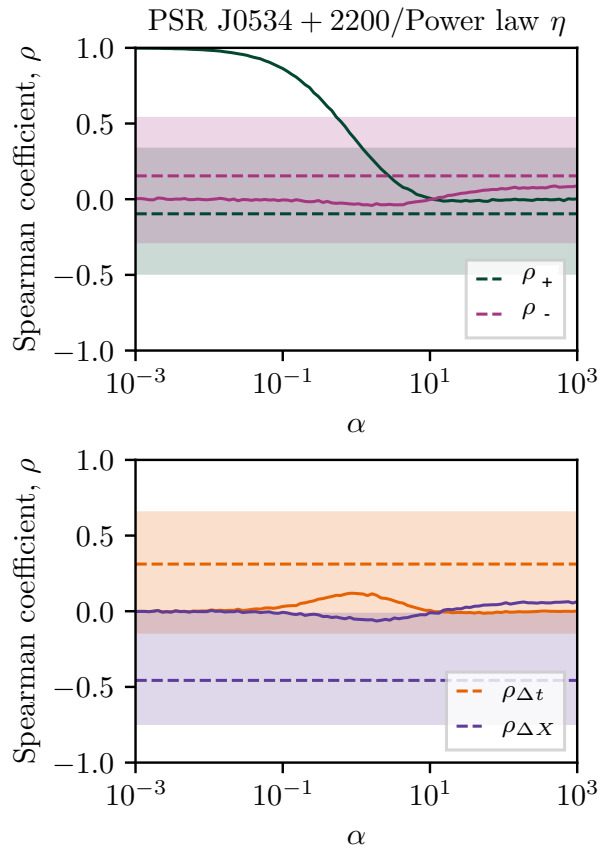


Figure 2.4: Theoretical (solid curves) and measured (dashed lines and shaded bands) correlations for PSR J0534+2200. Top panel: Size-forward waiting time cross-correlation ( $\rho_+$ , green curves), and size-backward waiting time cross-correlation ( $\rho_-$ , pink curves). Bottom panel: Waiting time autocorrelation ( $\rho_{\Delta t}$ , orange curves), and size autocorrelation ( $\rho_{\Delta X}$ , purple curves). The shaded bands indicate the 95% confidence interval for each observed correlation. Model parameters common to both panels: power law  $\eta$ ,  $\beta = 10^{-2}$ , power-law index of  $-1.5$ .

Table 2.2: Acceptable values of  $\alpha$ , given a functional form of  $\eta$ , for which the state-dependent Poisson process automaton produces cross-correlations and autocorrelations that all lie within the 95% confidence interval of the correlations observed in five pulsars. See text for details.

Name	Acceptable $\alpha$	$\eta$ functional form
PSR J0534+2200	$1 \lesssim \alpha \lesssim 10$	Power law
PSR J1740–3015	$\alpha \gtrsim 1$	Power law
PSR J1341–6220	$0.1 \lesssim \alpha \lesssim 0.5$ $0.01 \lesssim \alpha \lesssim 0.1$	Power law Gaussian
PSR J0537–6910	$\alpha \lesssim 0.01$	Any
PSR J0835–4510	$\alpha \gtrsim 0.5$ $0.05 \lesssim \alpha \lesssim 0.5$	Power law Gaussian

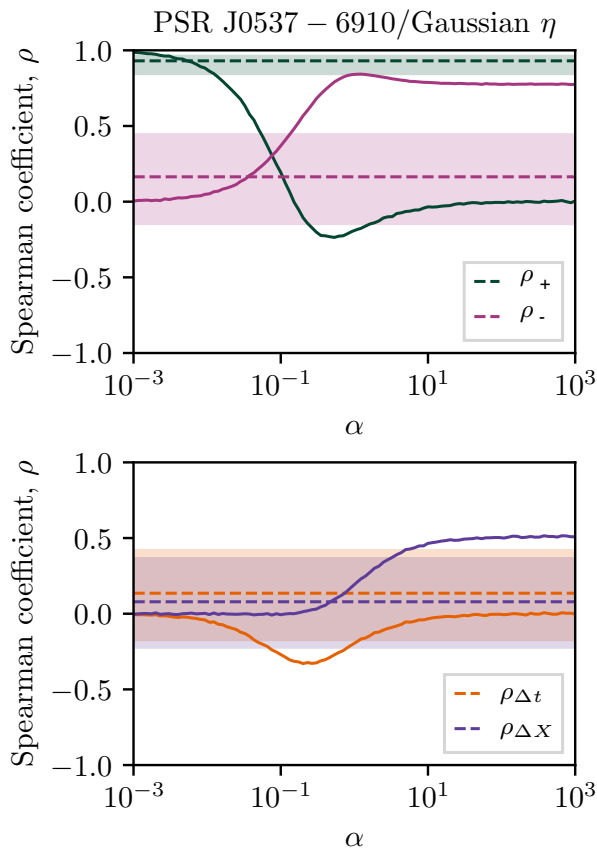


Figure 2.5: As in Figure 2.4, except for PSR J0537–6910, and with a stretchable Gaussian  $\eta$  in both panels. Model parameters common to both panels:  $\mu_G = 0.5$ ,  $\sigma_G = 0.125$ .

#### 2.5.4. Size and waiting time PDFs

The state-dependent Poisson process models more than just autocorrelations and cross-correlations. For example one can compare the shapes of the waiting time and size PDFs,  $p(\Delta t)$  and  $p(\Delta X)$ , to those observed in real pulsars [15, 18]. “Poisson-like” glitching activity, with exponential  $p(\Delta t)$  and power-law  $p(\Delta X)$ , follows from the state-dependent Poisson process if  $\eta$  is a power law, and we have  $\alpha \gtrsim 1$ . On the other hand, “quasi-periodic” glitch activity, with unimodal  $p(\Delta t)$  and  $p(\Delta X)$  [17, 18], follows from the state-dependent Poisson process if  $\eta$  is unimodal (e.g. Gaussian), and we have  $\alpha \lesssim 1$ . When  $\eta$  is unimodal, and  $\alpha \gtrsim 1$ , the model generates an exponential  $p(\Delta t)$ , and a monotonically decreasing  $p(\Delta X)$ . Whether this adequately describes what is observed for “Poisson-like” objects is an open question, given the low ( $N \leq 24$ ) number of glitches observed in these objects [15].

We now ask whether the added information from autocorrelations in waiting times and sizes helps with input selection and/or parameter estimation when loosely fitting the state-dependent Poisson process to real data as in Section 2.5.3. The answer is yes, in some cases. For example, modeling all glitching pulsars with a common, unimodal  $\eta$  such as a Gaussian is inappropriate, as a unimodal  $\eta$  does not generate positive  $\rho_{\Delta t}$  for any  $\alpha$  and only generates positive  $\rho_{\Delta X}$ . Thus the negative  $\rho_{\Delta X}$  seen in PSR J0534+2200 implies that a unimodal  $\eta$  cannot adequately model all pulsars. This conclusion cannot be reached from just the shapes of  $p(\Delta t)$  and  $p(\Delta X)$  [15], nor the cross-correlations alone [351]. In a similar vein, although the cross-correlations, waiting time and size distributions predicted by the state-dependent Poisson process with a power-law  $\eta$  are consistent with data from PSR J0534+2200, the autocorrelations complicate the picture, because the negative size autocorrelation is not predicted for any value of  $\alpha$ .

#### 2.5.5. Physical implications

If the data do not support the same  $\eta$  applying to all glitching pulsars, it may mean that different physical mechanisms cause glitches in different pulsars. Different functional forms of  $\eta$  are associated with different underlying physical processes. For example, a scale-free power law is characteristic of a spatially correlated knock-on process, such as superfluid vortex avalanches or crustquakes [147, 173]. On the other hand, a unimodal function implies a characteristic size for the stress released at each glitch, which is harder to explain microphysically but is consistent with a fluid instability triggered at a critical relative angular velocity [186, 187, 368, 369]. Improved measurements of cross-correlations and autocorrelations will improve our ability to discriminate between different functional forms of  $\eta$  and therefore different underlying physical mechanisms. Likewise if future glitch observations in PSR J0534+2200 continue to show negative size autocorrelations, it becomes hard to reconcile the observations with the state-dependent Poisson process, and the meta-model’s applicability to that pulsar should be questioned. In other words, the canonical view that glitches are the result of a marginally critical system, i.e. a process that hovers near an instability threshold, may not be valid in all pulsars.

## 2.6. CONCLUSIONS

As the number of recorded glitches grows it is profitable to disaggregate the data and study the time-ordered nature of the events in individual pulsars. One avenue is to study cross-correlations between the size of a glitch and the waiting time to the next (or previous) glitch [351]. Another is to study the autocorrelations between consecutive glitch sizes and waiting times.

We find no significant autocorrelations between waiting times or sizes in the top five most glitching pulsars, barring perhaps a negative size autocorrelation in PSR J0534+2200 ( $\rho_{\Delta X} = -0.46$ , p-value = 0.046). The absence of autocorrelations is nevertheless informative in the context of the general stress-release meta-model for glitches described by a state-dependent Poisson process [16], which predicts some small autocorrelations under certain conditions. In the fast spin-down regime ( $\alpha \lesssim 5 \times 10^{-2}$ ) the meta-model predicts  $\rho_{\Delta X} \ll 1$  and  $\rho_{\Delta t} \ll 1$ , regardless of the functional form of the conditional jump distribution  $\eta(\Delta X | X_p)$ . If  $\eta$  is a power law, as expected for spatially correlated mechanisms such as superfluid vortex avalanches or crustquakes, any nonzero autocorrelations observed become difficult to explain in the context of a state-dependent Poisson process. If on the other hand  $\eta$  is unimodal, we expect to see  $\rho_{\Delta t} < 0$  and  $\rho_{\Delta X} > 0$  in some pulsars. A unimodal  $\eta$  corresponds more closely to a trigger that produces glitches of a characteristic size, e.g. a superfluid instability.

Combining observations of cross-correlations, autocorrelations, and the shapes of the waiting time and size distributions places stronger constraints on the state-dependent Poisson process meta-model than any single statistical measurement. For PSR J0534+2200 we find that a power-law  $\eta$  and  $1 \lesssim \alpha \lesssim 10$  best describe the data, although  $\rho_{\Delta X} < 0$  complicates the picture. For PSR J0537–6910 we find that a Gaussian  $\eta$  and  $\alpha \lesssim 10^{-2}$  adequately describe the data. For PSR J1740–3015 we find a power-law  $\eta$  and  $\alpha \gtrsim 1$  are acceptable. For PSR1341–6220 we find that both a power-law  $\eta$  with  $0.1 \lesssim \alpha \lesssim 0.5$ , and a Gaussian  $\eta$  with  $0.01 \lesssim \alpha \lesssim 0.1$  adequately describe the data. Finally, for PSR J0835–4510 we find that both a power-law  $\eta$  with  $\alpha \gtrsim 0.5$ , and a Gaussian  $\eta$  with  $0.05 \lesssim \alpha \lesssim 0.5$  are acceptable.

Precise parameter estimation lies outside the scope of this paper. It involves fitting more than eight independent parameters, along with the functional form of  $\eta$ , a challenging numerical exercise attempted recently as a proof of principle by Melatos and Drummond [370] for three pulsars with  $N \geq 23$ . Larger data sets are needed for this kind of fitting to become statistically informative.

## ACKNOWLEDGEMENTS

Parts of this research are supported by the Australian Research Council (ARC) Centre of Excellence for Gravitational Wave Discovery (OzGrav) (project number CE170100004) and ARC Discovery Project DP170103625. J.B. Carlin is supported by an Australian Postgraduate Award.

# CHAPTER 3

---

## Long-term statistics of pulsar glitches triggered by a Brownian stress accumulation process

---

This chapter is a reproduction of [2]

*J. B. Carlin, and A. Melatos,*

Monthly Notices of the Royal Astronomical Society, 494, 3, 3383 (2020)

reformatted with the following changes only:

- **Footnote 1 in Section 3.3 is included in response to a suggestion of the thesis examiner.**
- **The text is styled to match the rest of this thesis.**
- **Where necessary, bibliographic records are updated.**

### 3.1. ABSTRACT

A microphysics-agnostic meta-model of rotational glitches in rotation-powered pulsars is developed, wherein the globally averaged internal stress accumulates as a Brownian process between glitches, and a glitch is triggered once a critical threshold is surmounted. Precise, falsifiable predictions are made regarding long-term event statistics in individual pulsars. For example, the Spearman cross-correlation coefficient between the size of a glitch and the waiting time until the next glitch should exceed 0.25 in all pulsars. Among the six pulsars with the most recorded glitches, PSR J0537–6910 and PSR J0835–4510 are consistent with the predictions of the meta-model, while PSR J1740–3015 and PSR J0631+1036 are not. PSR J0534+2200 and PSR J1341–6220 are only consistent with the meta-model, if there exists an undetected population of small glitches with small waiting times, which we do not resolve. The results are compared with a state-dependent Poisson process, another microphysics-agnostic meta-model in the literature. The results are also applied briefly to recent pulse-to-pulse observations of PSR J0835–4510, which appear to reveal evidence for a negative fluctuation in rotation frequency just prior to the 2016 glitch.

## 3.2. INTRODUCTION

The secular braking of rotation-powered pulsars is perturbed by two phenomena: glitches and timing noise. Timing noise, or stochastic wandering of the spin frequency, shows up in timing residuals as a red-noise process with an auto-correlation time-scale of days to weeks [63, 371, 372]. Glitches are impulsive spin-up events that recur erratically [17, 19, 128].

The microphysical mechanism that triggers glitches is an open question. Candidates include superfluid vortex avalanches [159, 173], starquakes [147, 365], hydrodynamic instabilities [186, 187, 369] and more; see Haskell and Melatos [150] for a modern review. Most of these mechanisms are predicated on the idea that the electromagnetic braking of the crust increases stress (e.g. elastic strain or differential rotation) in the system, some fraction of which is released spasmodically at each glitch. If the stress increases deterministically between glitches, the long-term glitch activity can be described by a state-dependent Poisson (SDP) process which links the instantaneous glitch rate to the stress in the system; glitches become more likely as the stress approaches a threshold [16]. The SDP process is a meta-model in the sense that it encompasses phenomenologically the stress-release idea at the core of the mechanisms listed above without specializing to the microphysics of the mechanism. It makes falsifiable statistical predictions about long-term observations of the sizes and waiting times of glitches and their correlations [1, 15, 16, 351].

Pulse-to-pulse observations of a glitch in the Vela pulsar (PSR J0835–4510) were made at the Mount Pleasant radio telescope in December 2016 [129]. Bayesian analysis finds evidence for a rotational slowdown (“precursor”) immediately prior to the glitch [130]. The slowdown is of the same order as the pulse jitter, i.e. pulse-to-pulse variations in the pulse profile, possibly caused by magnetospheric fluctuations unrelated to the internal stress. Another possibility — certainly not unique — is that the slowdown represents a random internal (e.g. hydrodynamic) fluctuation, which drives the stress above a critical threshold, triggering the glitch [130]. Stochastic fluctuations in the internal stress may be caused by superfluid turbulence, for example [83, 368, 373].

In this paper we do not seek to adjudicate on the putative link between internal stochastic fluctuations and an observed rotational slowdown prior to a glitch. Nor do we seek to model such a link directly. Instead, motivated partly by the Vela data, we investigate an alternative to the SDP meta-model, wherein glitches are the result of an internal, unobservable, globally averaged stress that evolves stochastically as a Brownian process, until a glitch is triggered at a critical stress threshold. The Brownian meta-model differs from the SDP meta-model by allowing the stress to evolve stochastically between glitches (instead of increasing deterministically), and triggering a glitch only when a critical threshold is reached (instead of at any time before the threshold is reached). Together the two meta-models encompass a large set of plausible microphysical mechanisms. Both models make falsifiable predictions about long-term statistics, a valuable feature. We describe the details of the Brownian meta-model in Section 3.3. In Section 3.4 we explore its long-term statistical predictions. In Section 3.5 we compare data from the six pulsars with the highest number of recorded glitches with the predictions of the Brownian meta-model, with an eye towards falsification. An analogous study of the SDP meta-model can be found elsewhere [1, 15, 351]. In Section 3.6 we discuss how

population trends may inform meta-model parameters.

### 3.3. BROWNIAN STRESS ACCUMULATION

#### 3.3.1. *Equation of motion*

We define  $X$  to be a stochastic variable equal to the globally averaged stress in the system. In the superfluid vortex avalanche picture  $X$  is proportional to the lag between the angular speed of the rigid crust and the superfluid interior. In the crustquake picture  $X$  is proportional to the elastic strain in the crust.

Between glitches we propose that  $X(t)$  evolves according to a Wiener process, which obeys the Langevin (Itô) equation

$$\frac{dX(t)}{dt} = \xi + \sigma B(t) , \quad (3.1)$$

with drift coefficient  $\xi$  (units: stress/time) and diffusion coefficient  $\sigma$  [units: stress/(time)<sup>1/2</sup>], and where  $B(t)$  is a white noise process of zero mean and unit variance [374, 375]. We assume both  $\xi$  and  $\sigma$  are constant with time. Practically, at each time step, the stress increments by  $\xi$  and undergoes a random step (up or down) by  $\sigma$  multiplied by a random number drawn from a Gaussian with zero mean and variance equal to the time step<sup>1</sup>. Equation (3.1) leads to the Fokker-Planck equation

$$\frac{\partial p}{\partial t} = -\xi \frac{\partial p}{\partial X} + \frac{\sigma^2}{2} \frac{\partial^2 p}{\partial X^2} , \quad (3.2)$$

where  $p dX = p(X, t | X_0) dX$  is the probability of finding the stress in the region  $(X, X + dX)$  at time  $t$ , given that it started at  $X = X_0$  after a glitch at  $t = 0$ , viz.

$$p(X, t = 0 | X_0) = \delta(X - X_0) . \quad (3.3)$$

The Brownian process terminates at  $X = X_c$ , i.e.  $X_c$  is the stress threshold where a glitch is triggered. The glitch decrements the stress by a random amount  $\Delta X$ , drawn from a stress-release distribution, discussed in Section 3.3.2. Mathematically, the termination of the Brownian process at  $X = X_c$  corresponds to an absorbing boundary condition:

$$0 = p(X = X_c, t | X_0) . \quad (3.4)$$

We also require  $X(t) \geq 0$ ; the stress is never negative<sup>2</sup>. This corresponds to a reflecting boundary condition at  $X = 0$ :

$$0 = \left. \frac{\partial p(X, t | X_0)}{\partial X} \right|_{X=0} - \frac{2\xi}{\sigma^2} p(X = 0, t | X_0) . \quad (3.5)$$

---

<sup>1</sup>This is a description of the Euler-Maruyama method for numerically approximating stochastic ordinary differential equations [376]. It is used to visualize the stochastic process in Figures 3.1 and 3.2.

<sup>2</sup>In the vortex unpinning picture, for example, a vortex avalanche cannot ever transfer so much angular momentum, that the crust rotates faster than the pinned superfluid; see Fulgenzi et al. [16] and the output of Gross-Pitaevskii simulations [173]

Equations (3.2)–(3.5) are solved analytically assuming that  $p(X, t | X_0)$  is separable in  $X$  and  $t$ . The solution is presented in Appendix 3.A1, following the approach in Sweet and Hardin [377]. Higher values of  $\xi X_c / \sigma^2$  imply drift dominates over diffusion; lower values of  $\xi X_c / \sigma^2$  imply diffusion dominates over drift. Figure 3.1 shows four representative time series of the evolution of  $X$  for four different values of  $\xi / \sigma^2$ , with  $X_c = 1$  fixed in each panel. For  $\xi / \sigma^2 = 0.1$  the process appears by eye to fluctuate randomly, with large, rapid excursions both up and down in stress. On the other hand, for  $\xi / \sigma^2 = 50$ , the stress accumulates steadily with small random excursions and large glitches are clearly demarcated from inter-glitch fluctuations.

### 3.3.2. Waiting time and size distributions

The stress is not observable. Instead, what we observe are sequences of glitch sizes and waiting times.

The conditional waiting time distribution,  $g(\Delta t | X_0)$ , gives the probability density function (PDF) of waiting times  $\Delta t$ , when the inter-glitch evolution starts at  $X_0$ , according to (3.3). It is calculated as [374]

$$g(\Delta t | X_0) = -\frac{d}{d(\Delta t)} \left[ \int_{-\infty}^{X_c} dX p(X, \Delta t | X_0) \right] . \quad (3.6)$$

The integral inside the square brackets, often called the survivor function, equals the probability density that the process stays in the interval  $-\infty < X(t) \leq X_c$  for  $0 \leq t \leq \Delta t$ .

The starting stress  $X_0$  is a random variable, related to the size of the previous glitch. To find the observable waiting time distribution,  $p(\Delta t)$ , we marginalize over the starting stress by calculating,

$$p(\Delta t) = \int_0^{X_c} dX_0 g(\Delta t | X_0) \eta(X_c - X_0) , \quad (3.7)$$

where  $\eta(\Delta X)$  equals the probability density of releasing an amount of stress  $\Delta X = X_c - X_0$  during a glitch.

We henceforth express  $t$  in units of  $2X_c^2/\sigma^2$  and  $X$  in units of  $X_c$ , unless otherwise stated. In these units, equations (3.6) and (3.26) combine to yield (see Appendix 3.A1)

$$g(\Delta t | X_0) = 2\mu \exp \left[ \mu^2 \Delta t + \mu(1 - X_0) \right] \sum_{n=1}^{\infty} \exp(-\lambda_n^2 \Delta t) \frac{\lambda_n \sin[\lambda_n(1 - X_0)]}{\mu + \cos^2 \lambda_n} , \quad (3.8)$$

where  $\lambda_n$  is the  $n$ -th positive root of the transcendental equation

$$\mu \tan \lambda_n = -\lambda_n , \quad (3.9)$$

with

$$\mu = \xi X_c / \sigma^2 . \quad (3.10)$$

In this paper, we assume for simplicity that  $\Delta X$  is proportional to the observed glitch size,  $\Delta\nu$ , i.e. the observed increment in the crust's spin frequency. Glitches represent small perturbations to an underlying equilibrium state, with  $\Delta\nu/\nu \ll 1$ , where  $\nu$  is the

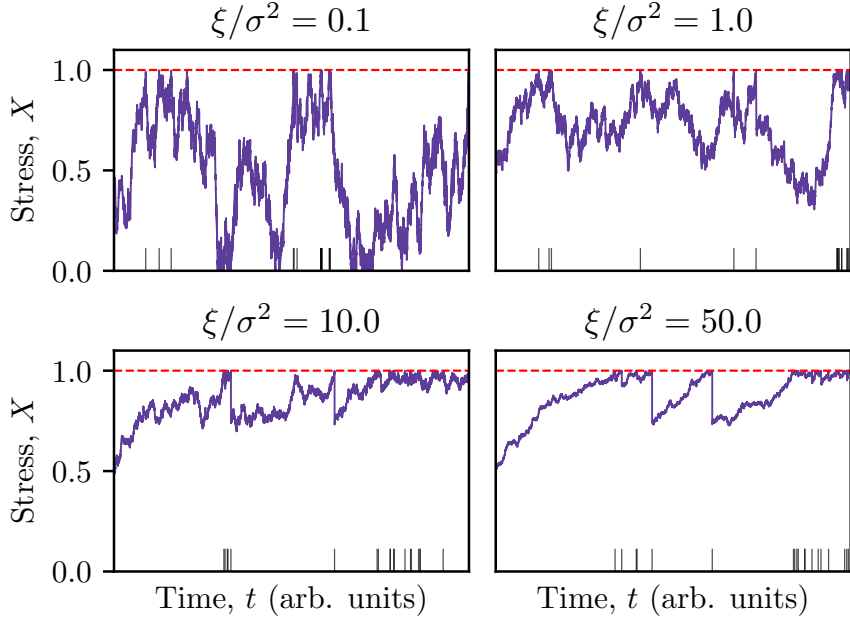


Figure 3.1: Visual comparison of the evolution of the internal, unobservable stress,  $X(t)$ , for four different values of  $\xi/\sigma^2$ . The red dashed line indicates the stress threshold, set to  $X_c = 1$ , where glitches are triggered. The same sequence of glitch sizes, drawn from a power-law  $\eta(\Delta X)$  distribution, is used in each panel. The small black tick marks indicate the epoch of each glitch.

spin frequency, so it is reasonable to model them in terms of a linear response, although nonlinear alternatives are certainly conceivable [378, 379]. In the vortex avalanche picture, for example, where  $X(t)$  equals the crust-core angular velocity lag we have [16]

$$\Delta X = -\frac{2\pi(I_c + I_s)\Delta\nu}{I_s} , \quad (3.11)$$

where  $I_c$  and  $I_s$  are the moments of inertia of the crust and superfluid interior respectively. An analogous proportionality exists in the starquake picture [147, 257]. The size distributions observed from individual pulsars are approximated by power-law, Gaussian, lognormal, and exponential distributions [17–19]. Assuming  $\Delta X \propto \Delta\nu$ , we adjust  $\eta(\Delta X)$  to match the measured size PDF  $p(\Delta\nu)$  of the pulsar under consideration.

### 3.3.3. Average waiting time

The average waiting time,  $\langle \Delta t \rangle$ , is conditional on  $X_0$ . It can be calculated from  $g(\Delta t | X_0)$  via

$$\langle \Delta t \rangle = \int_0^\infty d(\Delta t) \Delta t g(\Delta t | X_0) . \quad (3.12)$$

With the boundary conditions (3.4) and (3.5), we obtain (see Appendix 3.A1)

$$\langle \Delta t \rangle = 2\mu \exp[\mu(1 - X_0)] \sum_{n=1}^{\infty} (\lambda_n^2 + \mu^2)^{-2} \frac{\lambda_n \sin[\lambda_n(1 - X_0)]}{\mu + \cos^2(\lambda_n)} . \quad (3.13)$$

The behavior of  $\langle \Delta t \rangle$  as a function of  $\mu$  is complicated, even after marginalizing over  $X_0$ . Numerical tests indicate that for  $\mu \lesssim 1$ ,  $\langle \Delta t \rangle$  is roughly constant with  $\mu$ , while for  $\mu \gtrsim 1$  it varies inversely with  $\mu$ . The latter behavior can be understood with the help of the approximate non-reflecting solution at large  $\mu$  (see Appendix 3.A2), which has  $\langle \Delta t \rangle \propto \mu^{-1}$ , via equation (3.29) and (3.12). The behavior at low values of  $\mu$  makes sense physically, as  $\sigma$  dominates the time to reach  $X_c$  in this regime. On the other hand, at high values of  $\mu$  and fixed  $\sigma$ , a high value of the drift coefficient  $\xi$  leads the process to quickly reach  $X_c$  while a low value of  $\xi$  takes comparatively longer.

### 3.3.4. Comparison with the SDP meta-model

A key goal of this paper is to create a framework for falsifying one or both of the Brownian and SDP meta-models by making quantitative predictions about long-term glitch statistics. As the two meta-models encompass a range of plausible microphysics, falsifying one or both has significant scientific value in understanding which micophysical theories are consistent with the data.

The Brownian meta-model shares several similarities with the SDP meta-model [1, 15, 16, 351]. Both link the observed changes in  $v(t)$  to a globally averaged, unobservable stress, which fluctuates around marginal stability. Both are examples of a self-organized critical system [see Aschwanden et al. [380] for a review], where an external driver pushes the system towards criticality, until a glitch releases internal stress and transfers angular momentum from the core to the crust [195]. Neither meta-model assumes a specific micophysical trigger mechanism; together the two meta-models embrace a wide variety of plausible mechanisms of stress accumulation and threshold triggering.

The meta-models also differ in important respects. The driver in the SDP meta-model is secular; it does not vary with time. In the Brownian meta-model the driving torque is a fluctuating Langevin torque with white noise statistics, as in (3.1). The SDP process never quite reaches  $X = X_c$ , as glitches become increasingly likely for  $X \rightarrow X_c$ . In contrast, the Brownian meta-model reaches  $X = X_c$  at every glitch. This has important implications regarding the “memory” of previous events, as explored in Section 3.4.2. Finally,  $\eta(\Delta X)$  plays a different role in the two meta-models. As mentioned in Section 3.3.2, one has  $\Delta v \propto \Delta X$ , so  $\eta(\Delta X)$  and  $p(\Delta v)$  have the same shape in the Brownian meta-model. In the SDP meta-model  $\eta(\Delta X)$  is conditional on  $X(t)$  just before the glitch, so  $\eta(\Delta X)$  and  $p(\Delta v)$  have the same shape only under certain conditions; see Carlin and Melatos [15] for details.

The similarities and differences between the two meta-models are illustrated in Figure 3.2. Time series  $X(t)$  and  $v(t)$  are constructed by repeatedly evolving the stress in the system until a glitch is triggered (probabilistically at  $X < X_c$  for the SDP meta-model, deterministically at  $X = X_c$  for the Brownian meta-model), then drawing a glitch size from the stress-release PDF  $\eta(\Delta X)$ . Visually, with 20 glitches, the crust angular velocity evolves similarly for the two meta-models, despite the different stress evolution between glitches (deterministic for the SDP meta-model and stochastic for the Brownian meta-model). However, as we find in Section 3.4, the long-term statistical behavior of the two meta-models is different.

### 3.3.5. Inter-glitch spin wandering

Besides its influence on glitch statistics, the Brownian process may also drive stochastic spin wandering between glitches, unlike the SDP process. In principle, therefore, observations of inter-glitch timing noise in radio pulsars [63, 95, 371, 372] should place constraints on the meta-model parameters  $\xi$  and  $\sigma^2$  independent of the constraints derived from glitches. As an illustrative special case, if  $\xi$  and  $X_c$  are held fixed,  $\langle \Delta t \rangle$  decreases and the inter-glitch timing noise amplitude increases simultaneously, as  $\sigma^2$  increases. Hence a measured upper limit on the timing noise amplitude implies a maximum value of  $\sigma^2$  and hence a minimum value of  $\langle \Delta t \rangle$ , which provides an additional, independent opportunity to falsify the Brownian meta-model.

In practice, falsification experiments of the above kind are complicated by the unknown coupling between various components of the stellar interior. The meta-model parameters  $\xi$  and  $\sigma^2$  control the statistical behavior of the internal, i.e. unobservable, stress,  $X(t)$ . In Sections 3.3.1 and 3.3.2 we assume that changes in  $X(t)$  couple linearly to the rotational frequency of the crust,  $\nu(t)$ , only when a glitch occurs, via (3.11). If we relax this restriction and couple  $X(t)$  linearly to the crust between glitches, we have

$$\frac{d\nu}{dt} = -A \frac{dX}{dt}, \quad (3.14)$$

where  $A$  is an unknown coupling constant (units: Hz per unit stress) which depends on the physical mechanism of stress accumulation and the microphysics controlling how the star's internal angular momentum reservoir is tapped in between glitches. Equation (3.14) implies that, if the crust undergoes the same type of Brownian process with drift as described by (3.1), the observable, long-term, average spin-down rate,  $\langle \dot{\nu} \rangle$ , is proportional to  $\xi$ , while the observed spin-wandering amplitude is proportional to  $\sigma^2$ .

In the special case of  $A = A_{\max}$  (its maximum allowed value) the coupling is the same as during a glitch, e.g.  $A = I_s/[2\pi(I_c + I_s)]$  in the vortex avalanche picture. This is a problem for the Brownian meta-model, as we see from Figure 3.1. To distinguish glitches from stochastic wandering we need  $\mu \gtrsim 50$ , otherwise large Brownian fluctuations can be mistaken for glitches. For  $\mu \gtrsim 50$ , there should be a strong cross-correlation between glitch sizes and waiting times until the next glitch, as discussed in Section 3.4.2. We do not see this cross-correlation in most pulsars, so we can rule out the special case of  $A = A_{\max}$  or the Brownian meta-model (or both).

On the other hand, for  $A < A_{\max}$ , where the inter-glitch coupling is weaker than during a glitch, the problem outlined above is alleviated. Another scenario is that  $A$  is not constant, i.e. it varies with time or the stress in the system. These scenarios are motivated by the observations of the “precursor” slowdown in the Vela pulsar immediately prior to the 2016 glitch [130], and by studies of non-linear coupling mechanisms [379, 381]. A detailed study of the microphysical implications of inter-glitch spin wandering for the coupling mechanism between the stress reservoir and the crust is left for future work. For simplicity, we assume henceforth that coupling only occurs at a glitch, via (3.11).

## 3.4. OBSERVABLE LONG-TERM STATISTICS

To prepare for comparing the Brownian meta-model to data, we study how changing the input parameters affects the long-term statistical predictions.

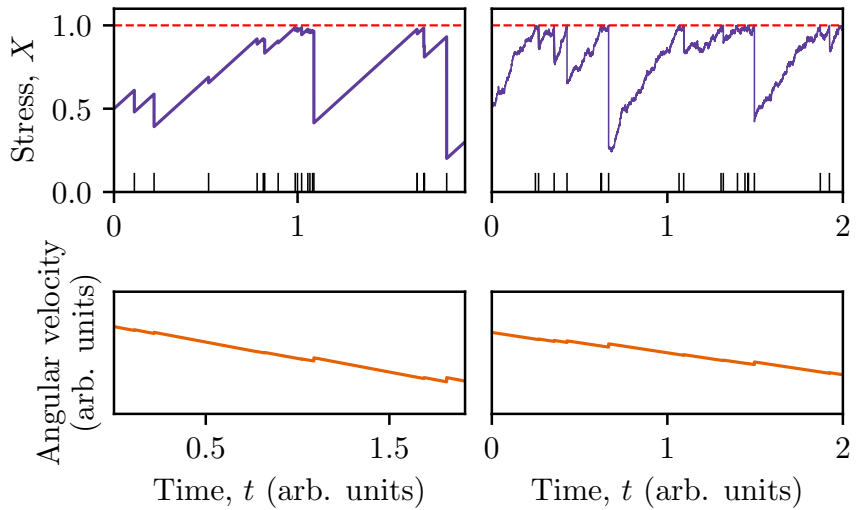


Figure 3.2: Comparison between two representative time series of stress (top panels) and crust angular velocity (bottom panels) from the SDP meta-model (left) and the Brownian meta-model (right). A deterministic, secular torque drives the stress between glitches in the SDP meta-model, whereas a stochastic Langevin torque drives the stress between glitches in the Brownian meta-model. Black tick marks in the top panels indicate the glitch epochs. Parameters for SDP meta-model:  $\alpha = 1$ , power law conditional jump distribution, as described in equations (17) and (19) of Fulgenzi et al. [16] respectively. Parameters for Brownian meta-model:  $\mu = 50$ , power law stress-release distribution, as in (3.15). Parameters shared between meta-models:  $\delta = -1.5$ ,  $\beta = 10^{-2}$  in (3.15).

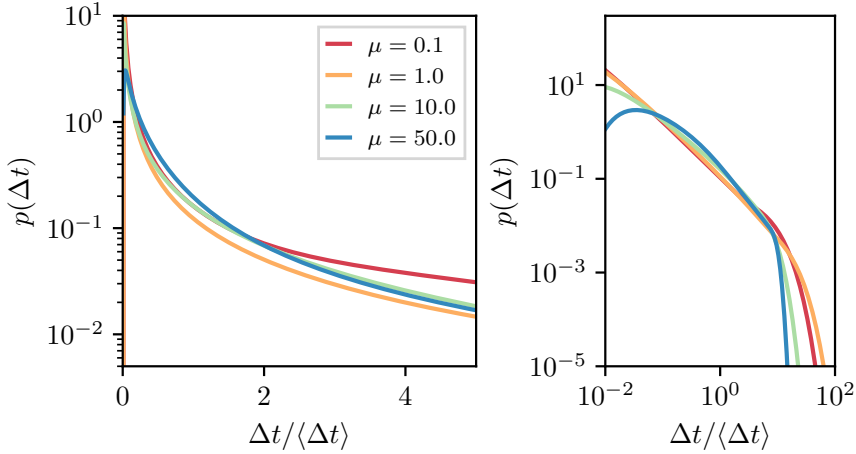


Figure 3.3: Waiting time PDF,  $p(\Delta t)$ , for four values of  $\mu$  on log-linear (left panel) and log-log (right panel) scales. The stress release distribution,  $\eta(\Delta X)$ , is a power law, as in (3.15), with  $\delta = -1.5$  and  $\beta = 10^{-2}$ .

### 3.4.1. Waiting time distribution

The long-term waiting time PDF,  $p(\Delta t)$ , constructed after many glitches are observed, is calculated from (3.7) given  $\mu$  and  $\eta(\Delta X)$ . Figure 3.3 shows  $p(\Delta t)$  for four representative values of  $\mu$  when  $\eta(\Delta X)$  is a power law of the form

$$\eta(\Delta X) \propto \Delta X^{-\delta} H(1 - \Delta X) H(\Delta X - \beta) , \quad (3.15)$$

where the proportionality constant is fixed by  $1 = \int_0^1 d(\Delta X) \eta(\Delta X)$ ,  $\delta$  is the power-law index,  $\beta$  is the lower cut-off to ensure normalisability, and  $H$  is the Heaviside function ( $\beta \leq \Delta X \leq 1$  implies  $0 \leq X \leq 1$  at all times). The abscissae are normalized by  $\langle \Delta t \rangle$  to highlight how the shape of  $p(\Delta t)$  evolves with  $\mu$ . On the log-log axes (right panel)  $p(\Delta t)$  resembles a power law over at least 3 decades, with a cut-off at  $\Delta t \approx 10\langle \Delta t \rangle$ . The cut-off steepens as  $\mu$  grows. The shape of  $p(\Delta t)$  depends weakly on  $\delta$  and  $\beta$  for  $\mu \lesssim 10$ , but depends strongly for  $\mu \gtrsim 10$ . For example, for  $\mu \gtrsim 10$  and  $\beta = 10^{-1}$ ,  $p(\Delta t)$  becomes unimodal, as small waiting times become less likely when each glitch reduces the stress by  $\Delta X \geq \beta$ .

What about other functional forms of  $\eta(\Delta X)$ ? Figure 3.4 shows  $p(\Delta t)$  for four representative values of  $\mu$ , with a Gaussian  $\eta(\Delta X)$ , viz.

$$\eta(\Delta X) \propto \exp\left[-\frac{(\Delta X - \mu_G)^2}{2\sigma_G^2}\right] H(1 - \Delta X) H(\Delta X) , \quad (3.16)$$

where the proportionality constant is fixed to normalize  $\eta(\Delta X)$ ,  $\mu_G$  is the mean, and  $\sigma_G$  is the standard deviation. For  $\mu \lesssim 1$ ,  $p(\Delta t)$  resembles an exponential distribution, if the smallest waiting times with  $\Delta t \lesssim 0.25\langle \Delta t \rangle$  are ignored. For  $\mu \gtrsim 1$ ,  $p(\Delta t)$  is unimodal. Increasing the size of the average  $\Delta X$ , via increasing  $\mu_G$ , reduces the variance in  $p(\Delta t)$  for all  $\mu$ , whereas reducing  $\mu_G$  makes  $p(\Delta t)$  resemble the results for a power law  $\eta(\Delta X)$ . Reducing the variance of each stress-release event by reducing  $\sigma_G$  also reduces the variance of  $p(\Delta t)$ , as expected.

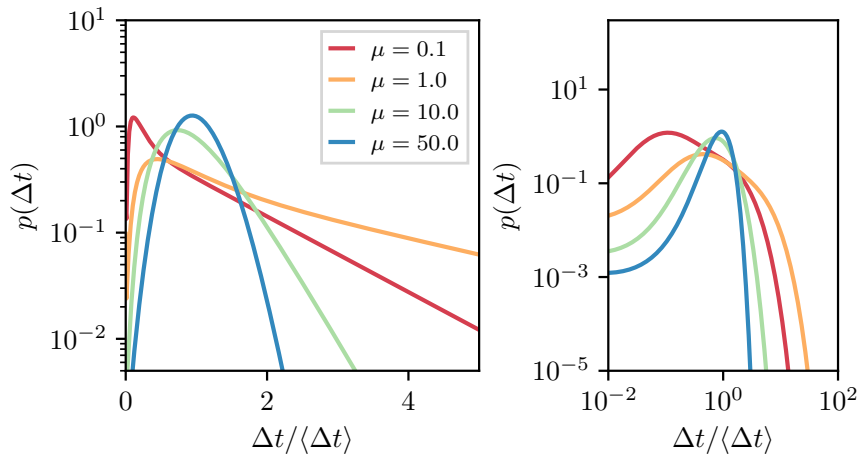


Figure 3.4: As for Figure 3.3 but with a Gaussian  $\eta(\Delta X)$ , as in (3.16), with  $\mu_G = 0.5$  and  $\sigma_G = 0.125$ .

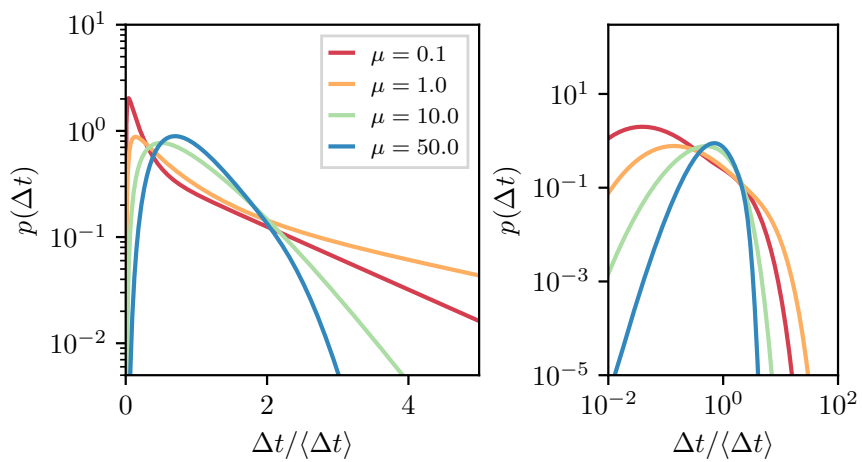


Figure 3.5: As for Figure 3.3 but with a log-normal  $\eta(\Delta X)$ , as in (3.17), with  $\mu_{LN} = -1$  and  $\sigma_{LN} = 0.5$ .

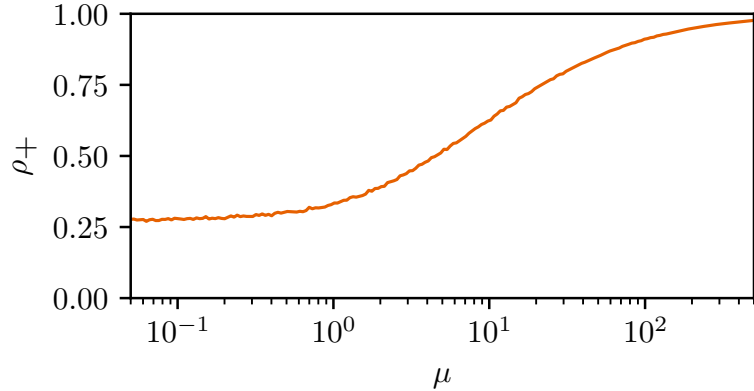


Figure 3.6: Spearman cross-correlation between the size of a glitch and the waiting time until the next glitch versus  $\mu$ . At 200 logarithmically spaced values of  $\mu$ ,  $10^5$  waiting times and sizes are drawn from (3.8) and (3.15) respectively, using each generated size to determine the starting point for the next inter-glitch interval and hence waiting time.

The third functional form of  $\eta(\Delta X)$  that we test is a log-normal distribution,

$$\eta(\Delta X) \propto \frac{1}{\Delta X} \exp\left[\frac{-(\log \Delta X - \mu_{LN})^2}{2\sigma_{LN}^2}\right] H(1 - \Delta X) H(\Delta X) , \quad (3.17)$$

where  $\mu_{LN}$  and  $\sigma_{LN}$  are the mean and standard deviation, and the proportionality constant is set by normalization. Figure 3.5 shows that the general shape of  $p(\Delta t)$  with a log-normal  $\eta(\Delta X)$  is similar to what is seen with a Gaussian  $\eta(\Delta X)$ . There are fewer small waiting times for a given  $\mu$ . If the average stress release is increased, by increasing  $\mu_{LN}$ , the same response is seen as with a Gaussian  $\eta(\Delta X)$ , i.e. the variance of  $p(\Delta t)$  drops. If we increase  $\sigma_{LN}$ ,  $p(\Delta t)$  resembles what is seen with a uniform  $\eta(\Delta X)$ .

An analogous study of  $p(\Delta t)$  for the SDP meta-model, with  $\eta(\Delta X)$  taken to be a power law, Gaussian, and a variety of other functional forms, is presented by Carlin and Melatos [15].

### 3.4.2. Correlations and memory

The meta-model in Section 3.3.1 predicts whether we should see a correlation between the size of a glitch and the subsequent waiting time, which we call a forward cross-correlation. As the glitch size is independent of the history of the stress evolution, there is no backward cross-correlation between the size of a glitch and the previous waiting time in the Brownian meta-model. Forward and backward cross-correlations have been investigated previously in the context of the SDP meta-model, and numerous falsifiable predictions are made [1, 15, 351].

Figure 3.6 shows the Spearman correlation coefficient for the forward cross-correlation,  $\rho_+$ , for  $5 \times 10^{-2} \leq \mu \leq 5 \times 10^3$ . The cross-correlation is always positive and increases from  $\rho_+ \approx 0.25$  for  $\mu \lesssim 1$  to  $\rho_+ \approx 1$  for  $\mu \gg 1$ . Figure 3.6 is generated with  $\eta(\Delta X)$  as a power law, but the result is insensitive to the form of  $\eta(\Delta X)$ . The trend in Figure 3.6 is intuitive. The size of the stress release in a glitch dictates how much stress must

be accumulated before the next glitch occurs. For  $\mu$  high, the diffusion of the Brownian process is negligible compared to the secular drift, and so the waiting time is determined almost completely by the size of the previous glitch. For  $\mu$  low, the diffusion randomizes the waiting time and decouples it from the size, while still maintaining a slight forward cross-correlation; even a process with zero drift is more likely to reach the threshold faster, if  $X_0$  is closer to  $X_c$ .

The Brownian meta-model predicts zero autocorrelations between glitch sizes, or between waiting times. The threshold at  $X = 1$  is reached before every glitch in the Brownian meta-model, removing “memory” in the system of the behavior of the stress prior to reaching that threshold. In contrast, the SDP meta-model predicts sizable auto-correlations in certain regimes [1].

### 3.5. FALSIFYING THE BROWNIAN META-MODEL

There are six pulsars with more than 15 recorded glitches<sup>3</sup>. Their names, the number of recorded glitches, the forward Spearman cross-correlation coefficient (along with associated p-value and 95% confidence interval), as well as the best-fitting size and waiting time distributions are listed in Table 3.1. The Spearman correlation coefficient minimizes the impact of outliers by testing for monotonic correlations, as opposed to the strictly linear correlations which the standard Pearson correlation coefficient describes. The confidence interval is calculated as described in Section 4 of Carlin and Melatos [1]. The best-fitting PDFs are copied from Fuentes et al. [19] and are selected based on the Akaike Information Criterion [144]. These shapes are broadly consistent with previous analyses using different techniques, although there are minor individual differences [17, 18]. We note that PDF shape fitting is uncertain when the sample size is small. Often the best one can do in the glitch context is to distinguish between a monotonic (e.g. exponential, power law) and unimodal (e.g. Gaussian) PDF, without tying down the functional form. Even then some functional forms (e.g. Weibull) straddle both categories [149]. Further shape-fitting studies should be carried out in the future, as the data sets grow.

Although not listed in Table 3.1, we note that the backward cross-correlation, the autocorrelation between glitch sizes, and the autocorrelation between waiting times are all consistent with zero, at a 95% confidence level for all six objects [1, 19, 351].

One virtue of the Brownian meta-model, like the SDP meta-model studied elsewhere [1, 15, 16, 351], is that it makes specific, quantitative predictions about PDFs and correlations. These predictions are open to falsification using existing and future data. With an eye to falsifying the meta-model presented in Sections 3.3 and 3.4 we now ask whether existing long-term observations of the pulsars in Table 3.1 can be adequately explained. In doing so, we caution that there is debate about whether the existing glitch catalogues are complete and accurate. Espinoza et al. [98] claimed that all glitches in the Crab pulsar (PSR J0534+2200) are detected. Yu and Liu [135] used a Monte Carlo study to confirm that the Yu et al. [131] analysis of 165 pulsars observed between 1990 and 2011 using the Parkes Observatory has “detected all detectable glitches in the data” (verbatim

---

<sup>3</sup>Up-to-date online catalogues of pulsar glitches are available through the Jodrell Bank Centre of Astrophysics at <http://www.jb.man.ac.uk/pulsar/glitches.html> [128], and the Australian National Telescope Facility at <https://www.atnf.csiro.au/research/pulsar/psrcat> [51]

Table 3.1: Pulsar name, number of glitches ( $N$ ), Spearman correlation coefficient between glitch size and subsequent waiting time ( $\rho_+$ ), associated p-value, and the 95% confidence interval (CI). The last two columns indicate the functional form of the best-fitting distribution for glitch sizes,  $p(\Delta X)$ , and waiting times,  $p(\Delta t)$  [17–19].

Name (PSR J)	$N$	$\rho_+$	p-value	95% CI	$p(\Delta X)$	$p(\Delta t)$
0537–6910	42*	0.93	$10^{-18}$	(0.84, 0.97)	Gaussian	Gaussian
1740–3015	36	0.29	0.091	(−0.06, 0.58)	Power law	Exponential
0534+2200	25†	−0.060	0.78	(−0.45, 0.35)	Log-normal	Exponential
1341–6220	23	0.58	0.0048	(0.13, 0.83)	Log-normal	Exponential
0835–4510	21	0.30	0.20	(−0.19, 0.67)	Gaussian	Gaussian
0631+1036	17	0.21	0.44	(−0.33, 0.65)	Power law	Exponential

\*The number and parameters of glitches in PSR J0537–6910 vary between Middleditch et al. [147], Antonopoulou et al. [149], and Ferdman et al. [148]. We include in our analysis glitches that appear in two out of three sources.

†The first four PSR J0534+2200 glitches in the Jodrell Bank catalogue occurred before daily monitoring commenced and are excluded from the analysis [55].

quote). However, as the cadence of observations for most pulsars is not constant [134], post-glitch recovery time-scales vary [172, 382], and glitch detections still rely on human intervention [135], it remains uncertain whether or not we are seeing the smallest glitches, or resolving glitches that happen in quick succession.

### 3.5.1. PSR J0537–6910

PSR J0537–6910 has the most recorded glitches and the highest forward cross-correlation amongst all the prolific glitching pulsars. In the context of the Brownian meta-model, these properties place PSR J0537–6910 in the  $\mu \gtrsim 10^2$  regime, via Figure 3.6. The glitch size distribution for PSR J0537–6910 is approximately Gaussian [19]. Looking at Figure 3.4, where  $\eta(\Delta X)$  is a Gaussian, we note that  $p(\Delta t)$  should also be a Gaussian, with  $\mu \gtrsim 10^2$ , in accord with observations. Therefore, the main features of the long-term statistics of this pulsar conform to the Brownian meta-model, if  $\eta(\Delta X)$  is a Gaussian, and one has  $\mu \gtrsim 10^2$ .

We note that the waiting time distribution for PSR J0537–6910 is also well described by a Weibull distribution [149], a more general functional form, which includes the exponential and a skewed Gaussian as special cases.

### 3.5.2. PSR J1740–3015

PSR J1740–3015 has a forward cross-correlation that is consistent with zero. However the 95% confidence interval is broad enough to encompass  $\rho_+$  up to 0.58. According to Figure 3.6 this means PSR J1740–3015 has  $\mu \lesssim 10$ , in the context of the Brownian meta-model. As PSR J1740–3015 has a power-law size PDF [19], we look to Figure 3.3, where  $\eta(\Delta X)$  is a power law. For  $\mu \lesssim 10$  the Brownian meta-model predicts that  $p(\Delta t)$  is a

power law with a cut-off at large  $\Delta t$ . Therefore, as  $p(\Delta t)$  is observed to be exponential in this object, the long-term statistics are not explained by the Brownian meta-model with any set of input parameters.

Power-law and log-normal distributions are often hard to distinguish for such small sample sizes. If  $\eta(\Delta X)$  is actually a log-normal distribution for this object, then we look at Figure 3.5. With  $\mu \lesssim 10$  we note that  $p(\Delta t)$  should be an exponential, if the smallest waiting times are not observed. Therefore, as  $p(\Delta t)$  is observed to be exponential in this object, it is consistent with the Brownian meta-model, if we are unable to observe glitches with  $\Delta t \lesssim 0.25\langle\Delta t\rangle$ . Note that  $\langle\Delta t\rangle$  refers to the true underlying average waiting time, rather than the estimate from the sample of glitches we have observed.

### 3.5.3. PSR J0534+2200

PSR J0534+2200 has a forward cross-correlation that is consistent with zero, with  $\rho_+ \leq 0.35$  at 95% confidence. This limits PSR J0534+2200 to  $\mu \lesssim 2$ , according to Figure 3.6. PSR J0534+2200 has a log-normal size distribution [19]. Taking  $\eta(\Delta X)$  to be log-normal, as in Figure 3.5, we see that  $p(\Delta t)$  should be an exponential, if the smallest waiting times are not observed. Therefore, as  $p(\Delta t)$  is observed to be exponential in this object, it is consistent with the Brownian meta-model, if we are unable to observe glitches with  $\Delta t \lesssim 0.25\langle\Delta t\rangle$ . If we do see all glitches in PSR J0534+2200, as claimed by Espinoza et al. [98], then the observations are inconsistent with the Brownian meta-model.

We note that the semi-autonomous glitch-finding algorithm of Espinoza et al. [98] may miss closely spaced glitches occasionally. For example, it missed one glitch, at epoch MJD 52146.8 with a size of  $\Delta\nu = 0.27 \mu\text{Hz}$ , which occurred  $\Delta t \approx 63\text{ d}$  after the previous glitch with Espinoza et al. [98] noting that the likely cause is “influence of the recovery from the previous glitch” (verbatim quote). If we take 63 d as the minimum resolvable waiting time, the true underlying average waiting time is  $\langle\Delta t\rangle \approx 63\text{ d}/0.25 = 252\text{ d}$ , in order for the long-term statistics to be consistent with the Brownian meta-model. The observed average waiting time is 501 d, while the median waiting time is 284 d. On the other hand, the Brownian meta-model may be ruled out, and the minimum resolvable waiting time may be shorter than 63 d. More work is needed to clarify these issues, including systematic studies of the false alarm and false dismissal probabilities of glitch-finding algorithms [77, 95, 134, 135].

### 3.5.4. PSR J1341–6220

PSR J1341–6220 has a forward cross-correlation that is significantly positive. However the 95% confidence interval is broad, allowing  $0.13 \leq \rho_+ \leq 0.83$ . According to Figure 3.6 this limits  $\mu$  to  $\mu \lesssim 10^2$ . PSR J1341–6220 has a log-normal size distribution [19], and so like PSR J0534+2200 is consistent with Brownian the meta-model, only if we do not detect glitches with  $\Delta t \lesssim 0.25\langle\Delta t\rangle$ . The observed waiting time distribution is an exponential.

### 3.5.5. PSR J0835–4510

PSR J0835–4510 has a forward cross-correlation that is consistent with zero. The 95% confidence interval encompasses  $\rho_+$  up to 0.67, consistent with  $\mu \lesssim 30$ , according to Fig-

ure 3.6. The size PDF, and hence  $\eta(\Delta X)$ , for PSR J0835–4510 is approximately Gaussian [19]. Therefore according to Figure 3.4 the meta-model predicts  $p(\Delta t)$  to be an exponential (for  $\mu \lesssim 5$ ) or a skewed Gaussian (for  $5 \lesssim \mu \lesssim 30$ ). The observed  $p(\Delta t)$  is a Gaussian, not an exponential. Therefore, the observations are currently consistent with the Brownian meta-model for  $5 \lesssim \mu \lesssim 30$ , if  $\eta(\Delta X)$  is a Gaussian.

The somewhat strict constraints on  $\mu$  imply that, with more glitches, the measured forward cross-correlation should increase to  $0.4 \lesssim \rho_+ \lesssim 0.6$ . If  $\rho_+$  stays outside this range, PSR J0835–4510 will become another counterexample to the Brownian meta-model.

### 3.5.6. PSR J0631+1036

PSR J0631+1036 has roughly half the recorded glitches of PSR J1740–3015 but is otherwise similar statistically. Hence the same conclusion holds: as long as the size distribution is a power law [19], the Brownian meta-model does not adequately explain the observations, as exponential waiting times cannot be generated if  $\eta(\Delta X)$  is a power law.

As with PSR J1740–3015, if  $\eta(\Delta X)$  is actually a log-normal distribution, instead of a power law, the conclusion is different: the observations are consistent with the predictions of the Brownian meta-model, if we do not resolve glitches with  $\Delta t \lesssim 0.25\langle\Delta t\rangle$ .

## 3.6. POPULATION TRENDS

The primary goal of this paper is to formulate rigorously and then falsify (if possible) the Brownian meta-model, rather than engage in a parameter estimation exercise. Nevertheless the results in Section 3.5 do carry some interesting preliminary implications concerning the parameters of the Brownian meta-model, in the event that it survives falsification in the future. In this section, we touch briefly on two population trends that are consistent with (albeit not guaranteed by) the results in Section 3.5: why do  $\eta(\Delta X)$  and  $\mu$  seem to vary significantly among the six pulsars in Table 3.1?

Regarding  $\eta(\Delta X)$ , laboratory studies of self-organized critical systems with avalanche dynamics, like sand piles, reveal that  $\eta(\Delta X)$  is power-law-like when the driver is “slow”, and Gaussian-like when the driver is “fast” [195]. In the former regime, avalanches occur sporadically at well-separated points within the system, so consecutive avalanches are independent and scale invariant: they can have any size, ranging from a solitary nearest-neighbor interaction to a catastrophic collapse of the whole system. In the latter regime, consecutive avalanches “trip over one another” (i.e. are correlated, not independent) and involve most of the system every time, so they all have comparable sizes, and  $\eta(\Delta X)$  is unimodal. Broadly speaking the foregoing physics may suggest a correlation between the shape of  $\eta(\Delta X)$  and  $\langle\dot{v}\rangle$ , and it will be interesting to test for such a correlation in the future, as more data are gathered. However, one must approach such a test with caution. The demarcation between “slow” and “fast” drivers is a subtle and unsolved question in idealized systems like sand piles, let alone in neutron stars where the microphysics is complicated and unknown (e.g. vortex avalanches, starquakes). Moreover observables like  $\langle\dot{v}\rangle$  cannot be related easily to the behavior of the stress reservoir, e.g. due to uncertain coupling between multiple components of the star’s interior, as discussed in Section 3.3.5.

To understand how  $\mu = \xi X_c / \sigma^2$  could vary pulsar-to-pulsar we need to unpack the various internal parameters, and relate them to potential observables. In the standard picture,  $\langle \dot{v} \rangle$  is set by the spin-down torque,  $N_{\text{ext}}$ , and moment of inertia of the crust,  $I_c$ . As discussed in Section 3.3.5, one can invoke a linear coupling between the internal stress and observed behavior of the crust. Linear coupling faces many issues, as we discuss in Section 3.3.5, but taking it to be valid for the moment, we find  $\xi \propto \langle \dot{v} \rangle \approx N_{\text{ext}}/I_c$ , where the proportionality constant controls the strength of the coupling. For the six objects discussed in this paper,  $N_{\text{ext}} \propto B^2 v^3$  (where  $B$  is the strength of the dipole magnetic field at the surface) varies across three orders of magnitude, using values of  $B$  and  $v$  from the ATNF pulsar catalogue<sup>4</sup>. The other factor is  $I_c$ . There are two popular scenarios for this quantity, as discussed in Section 3 of Melatos et al. [277]: (a) if the crust is a thin crystalline lattice and the rest of the star is composed of a superfluid we have  $I_c/I_0 \sim 10^{-2}$ , where  $I_0$  is the total moment of inertia of the star [383, 384]; (b) if the crust has most of the interior superfluid pinned and co-rotating with it (via magnetic flux tubes or charged particles), with only a bit of the inner crust superfluid decoupled, we have  $I_c/I_0 \sim 1$  [128, 139, 385]. We do not explore which of these scenarios is more likely, as both have strong support in the literature. We do note that the difference between these scenarios widens the possible range of  $\xi$  by another two orders of magnitude. The other factors in  $\mu$  are  $\sigma$  and  $X_c$ . Again, as discussed in Section 3.3.5,  $\sigma$  is proportional to the observed spin-wandering amplitude, if we assume a linear coupling. The spin-wandering amplitude in the six objects considered in this paper is not well quantified in the literature. However, Shannon and Cordes [64] found that for a general population of “canonical pulsars”, the timing noise strength,  $\sigma_{\text{TN}}$ , spans three orders of magnitude. Finally, the critical stress  $X_c$  may vary from object to object, as it is a complex combination of microphysical (e.g. pinning potential) and thermodynamic (e.g. equation of state) parameters [162]. Hence, even for linear coupling (which is already ruled out by looking at inter-glitch spin wandering, as discussed in Section 3.3.5), the possible range of  $\mu$  inferred from external observables spans more than eight orders of magnitude, comfortably encompassing the range of  $\mu$  which the meta-model considers.

### 3.7. CONCLUSIONS

The physical mechanism that triggers pulsar glitches is unknown. Phenomenological meta-models offer one way to link — and potentially falsify — broad classes of plausible microphysical mechanisms with measurements of long-term glitch statistics. The SDP meta-model [16] describes microphysical mechanisms in which glitches are triggered probabilistically, while the stress in the system rises secularly, becoming more likely as the stress increases. It makes falsifiable, quantitative predictions for size and waiting-time cross-correlations [351], autocorrelations [1], and PDFs [15]. However, the SDP meta-model does not allow the stress to fluctuate stochastically in between glitches due to random processes in the stellar interior, e.g. superfluid vortex motion [173], superfluid turbulence [83, 386], or crust cracking [181].

Motivated partly by recent observations of PSR J0835–4510 [130], we introduce an alternative meta-model, where the stress evolves between glitches according to a Brown-

---

<sup>4</sup><https://www.atnf.csiro.au/research/pulsar/psrcat/> [51]

ian process with drift and diffusion components, and where glitches are triggered deterministically once the stress surmounts a threshold. The rotational slowdown observed by Ashton et al. [130] just prior to the glitch may be a coincidentally large instance of pulse jitter, but it may also indicate a large, stochastic fluctuation in the internal stress, which briefly couples the magnetosphere to the interior and triggers the glitch. While we do not model the microphysics in detail, the Brownian meta-model encompasses such a trigger mechanism. We show in Section 3.5 and Carlin and Melatos [1] that the glitch statistics of PSR J0835–4510 are consistent with the predictions of both the Brownian and SDP meta-models.

We find that the Brownian meta-model predicts various long-term statistical fingerprints. If the glitch size distribution is not a power law, and diffusion dominates drift (i.e.  $\mu \lesssim 1$ ), the waiting time PDF is predicted to be an exponential, if glitches that occur soon after one another are not resolved. As  $\mu$  increases, the observed waiting time PDF resembles more closely the glitch size PDF. The Spearman cross-correlation coefficient between glitch size and waiting time until the next glitch is predicted to be at least 0.25 for all pulsars.

Current observations of the long-term glitch statistics in all six of the pulsars with the most recorded glitches cannot be explained adequately by the Brownian meta-model. The two “quasi-periodic” glitchers (PSR J0537–6910 and PSR J0835–4510) with Gaussian size and waiting time distributions [18, 19] can be explained with the Brownian meta-model, while PSR J1740–3015 and PSR J0631+1036 cannot (regardless of input parameters), unless their glitch sizes are distributed as a log-normal instead of a power law [19]. PSR J0534+2200 and PSR J1341–6220 are consistent with the meta-model, if there are many glitches with small waiting times that we do not resolve. More data could falsify the Brownian meta-model as it applies to individual pulsars in several ways: i) if the measured forward cross-correlation is statistically inconsistent with  $\rho_+ \geq 0.25$ ; ii) if a non-zero backward cross-correlation is measured; or iii) if the size or waiting time auto-correlations are nonzero. Additionally, measurements of the forward cross-correlation, combined with the size and waiting time PDFs, further constrain the meta-model parameters.

We note that i) the SDP meta-model is broadly consistent with the long-term statistics in the six pulsars with the most recorded glitches [1, 15], and ii) it predicts a different set of long-term statistics. Thus, over time we can distinguish between the two meta-models and falsify one, the other, or both. We remind the reader that most plausible microphysical mechanisms contemplated in the literature (e.g. superfluid vortex avalanches, starquakes, hydrodynamic instabilities and turbulence) fit broadly within one or both of the Brownian and SDP meta-models.

## ACKNOWLEDGEMENTS

Parts of this research are supported by the Australian Research Council (ARC) Centre of Excellence for Gravitational Wave Discovery (OzGrav) (project number CE170100004) and ARC Discovery Project DP170103625. JBC is supported by an Australian Postgraduate Award. We thank the anonymous referee for pointing out that inter-glitch spin wandering places independent constraints on the Brownian meta-model in principle, as discussed in Section 3.3.5.

### 3.A1. ANALYTIC SOLUTION OF THE FOKKER-PLANCK EQUATION FOR THE INTER-GLITCH STRESS DISTRIBUTION

The Fokker-Planck equation for the globally averaged stress variable,  $X$ , together with the initial and boundary conditions, (3.3)–(3.5), constitute a standard advection-diffusion problem. Namely, equation (3.2) is a parabolic partial differential equation with constant coefficients solved on the finite interval  $0 \leq X \leq X_c$ , subject to mixed Dirichlet-Neumann (also called Robin) boundary conditions. The problem can be solved analytically by expanding the solution in eigenfunctions on the interval  $0 \leq X \leq X_c$  [377].

We assume a separable ansatz

$$p(X, t) = Y(X)T(t) , \quad (3.18)$$

which converts (3.2) into two coupled ordinary differential equations,

$$\frac{2}{\sigma^2 T} \frac{dT}{dt} = -\alpha^2 , \quad (3.19)$$

$$\frac{1}{Y} \left( \frac{-2\xi}{\sigma^2} \frac{dY}{dX} + \frac{d^2Y}{dX^2} \right) = -\alpha^2 , \quad (3.20)$$

for some constant  $\alpha$ . Equation (3.20) has exponential solutions of the form

$$Y(X) \propto \exp \left[ \left( \frac{\xi}{\sigma^2} \pm \sqrt{-\lambda^2} \right) X \right] , \quad (3.21)$$

with  $\lambda^2 = \alpha^2 - \xi^2/\sigma^4$ .

As (3.2) is linear, we apply the boundary conditions to the eigenfunctions defined in (3.21) independently, then sum over the eigenvalues using the principle of superposition. For  $\lambda^2 \leq 0$ ,  $Y(X)$  becomes a linear combination of  $\sinh(\lambda X)$  and  $\cosh(\lambda X)$ . The boundary conditions imply  $\tanh(\lambda X) \propto -\lambda$ , whose only solution  $\lambda = 0$  leads to the trivial result  $Y(X) = 0$ . We therefore restrict our attention to  $\lambda^2 > 0$  and hence

$$Y(X) = \exp \left( \frac{\xi}{\sigma^2} X \right) (A \sin \lambda X + B \cos \lambda X) , \quad (3.22)$$

where  $A$  and  $B$  are constants. The reflecting boundary condition (3.5) implies

$$B = \frac{\lambda \sigma^2}{\xi} A , \quad (3.23)$$

while the absorbing boundary condition (3.4) fixes the eigenvalues,  $\lambda$ , via

$$\tan(\lambda X_c) = -\frac{\lambda \sigma^2}{\xi} . \quad (3.24)$$

Hence we write the full solution for  $P(X, t)$  as

$$P(X, t) = \exp \left( \frac{\xi}{\sigma^2} X \right) \sum_{n=1}^{\infty} A_n \exp \left[ -t \left( \frac{\lambda_n^2 \sigma^2}{2} + \frac{\xi^2}{2\sigma^2} \right) \right] \left[ \sin(\lambda_n X) + \frac{\lambda_n \sigma^2}{\xi} \cos(\lambda_n X) \right] \quad (3.25)$$

or equivalently

$$P(X, t) = \exp\left(\frac{\xi}{\sigma^2}X\right) \sum_{n=1}^{\infty} A'_n \exp\left[-t\left(\frac{\lambda_n^2 \sigma^2}{2} + \frac{\xi^2}{2\sigma^2}\right)\right] \sin[\lambda_n(X - X_c)] , \quad (3.26)$$

where  $\lambda_n$  is the  $n$ -th positive root of (3.24), and the  $A'_n$  constant coefficients are to be determined.

We find the  $A'_n$  factors by applying the initial condition (3.3) and noting that the eigenfunctions are orthogonal on  $0 \leq X \leq X_c$  (not the standard Fourier domain  $0 \leq X \leq 2\pi$ ) as a consequence of Sturm-Liouville theory [387]. Orthogonality implies

$$A'_n = \frac{\int_0^{X_c} dX \exp(-\xi X/\sigma^2) \sin[\lambda_n(X - X_c)] p(X, t=0)}{\int_0^{X_c} dX \sin^2[\lambda_n(X - X_c)]} \quad (3.27)$$

$$= 2 \exp(-\xi X_0/\sigma^2) \sin[\lambda_n(X_0 - X_c)] \frac{\xi/\sigma^2}{\xi X_c/\sigma^2 + \cos^2(\lambda_n X_c)} . \quad (3.28)$$

The full solution is given by (3.24), (3.26), and (3.28).

### 3.A2. CONDITIONAL WAITING TIME PDF WITHOUT THE REFLECTING BOUNDARY

If the reflecting boundary condition (3.5) is relaxed, such that the process operates on the semi-infinite domain  $X < X_c$ , the conditional waiting time distribution is an inverse Gaussian [374],

$$g(\Delta t | X_0) = \frac{X_c - X_0}{\sigma \sqrt{2\pi \Delta t^3}} \exp\left[\frac{-(X_c - X_0 - \xi \Delta t)^2}{2\sigma^2 \Delta t}\right] . \quad (3.29)$$

For  $\xi/\sigma^2 \gtrsim 10$ , numerical tests show that (3.29) agrees with (3.8) to within 1% for  $0 \leq \Delta t \leq 5\langle\Delta t\rangle$ . This makes intuitive sense, as the process is driven strongly away from  $X = 0$  for large  $\xi/\sigma^2 > 0$ . We use (3.29) instead of (3.8) for  $\xi/\sigma^2 \gtrsim 10$ , because (3.8) converges slowly in the latter regime.

# CHAPTER 4

---

## Long-term statistics of pulsar glitches due to history-dependent avalanches

---

This chapter is a reproduction of [3]

*J. B. Carlin, and A. Melatos,*  
The Astrophysical Journal, 917, 1 (2021)

reformatted with the following changes only:

- Footnote 3 in Section 4.3.2 is included in response to a suggestion of the thesis examiner.
- The text is styled to match the rest of this thesis.
- Where necessary, bibliographic records are updated.

### 4.1. ABSTRACT

Stress accumulation-relaxation meta-models of pulsar glitches make precise, microphysics-agnostic predictions of long-term glitch statistics, which can be falsified by existing and future timing data. Previous meta-models assume that glitches are triggered by an avalanche process, e.g. involving superfluid vortices, and that the probability density function (PDF) of the avalanche sizes is history-independent and specified exogenously. Here a recipe is proposed to generate the avalanche sizes endogenously in a history-dependent manner, by tracking the thresholds of occupied vortex pinning sites as a function of time. Vortices unpin spasmodically from sites with thresholds below a global, time-dependent stress and repin at sites with thresholds above the global stress, imbuing the system with long-term memory. The meta-model predicts PDFs, auto- and cross-correlations for glitch sizes and waiting times, which are provisionally inconsistent with current observations, unlike some previous meta-models (e.g. state dependent Poisson process), whose predictions are consistent. The theoretical implications are intriguing, albeit uncertain, because history-dependent avalanches embody faithfully the popular, idealized understanding in the literature of how vortex unpinning operates as a driven, stochastic process. The meta-model predicts aftershocks, which occur with larger than average sizes and longer than average waiting times after the largest, system-resetting glitches. This prediction will be tested, once more data are generated by the next generation of pulsar timing campaigns.

## 4.2. INTRODUCTION

More than 500 rotational glitches have been detected in radio pulsars<sup>1</sup>. The sample is large enough that it is meaningful to disaggregate the data and study the long-term statistics of glitch activity in some individual objects with enough recorded glitches. Quantities of interest include waiting time and size cross-correlations, autocorrelations, and probability density functions (PDFs) [1, 15, 17–19, 128, 351].

Given measurements of the above quantities, one can falsify popular phenomenological meta-models describing glitch activity as a stress-relax process, wherein stress accumulates between glitches and relaxes partially at a glitch. A meta-model unifies a broad class of stochastic processes under its umbrella while remaining agnostic about the specific microphysics and the physical nature of the stress. It makes concrete, falsifiable predictions about long-term glitch statistics. The pay-offs from falsifiability are considerable and have driven work in this area recently. For example, existing data have been used to discriminate between the state-dependent Poisson (SDP) and Brownian stress accumulation (BSA) meta-models in six objects with high glitch activity [2]. In the SDP meta-model, glitches are triggered stochastically via a Poisson process with a stress-dependent rate, while the stress increases deterministically between glitches [16, 174]. In the BSA meta-model, glitches are triggered deterministically when the stress reaches a threshold, while the stress evolves stochastically via a Brownian process between glitches [2]. Both meta-models are consistent with various flavors of microphysics in the literature, e.g. superfluid vortex avalanches [159, 173], starquakes [147, 365], and hydrodynamic instabilities [186, 187, 369], but they embody important physical differences in how the stress accumulates and when the relaxation events are triggered.

The roughly scale invariant glitch size PDFs observed in some pulsars suggest that the stress relaxes via an *avalanche process*, i.e. a relaxation event triggered somewhere in the star propagates to adjacent regions via some knock-on mechanism [17, 195]. “Chain reactions” of this kind are observed in Gross-Pitaevskii simulations [173–175, 388] and mean-field or N-body simulations [137, 389] of superfluid vortex avalanches. They are typical of other systems cited as analogues of pulsar glitches in the literature, e.g. self-organized critical systems like sand piles, earthquakes, and magnetic fluxoids in type II superconductors [195, 380, 390]. In the meta-models published to date, a key input is the *conditional distribution of avalanche sizes*,  $\eta[\Delta X^{(n)}|X(t_n^-)]$ , specifically the PDF of the spatially averaged stress released during the  $n$ -th avalanche,  $\Delta X^{(n)}$ , if the stress just prior to the avalanche is  $X(t_n^-)$ . There is no way to infer the functional form of  $\eta[\Delta X^{(n)}|X(t_n^-)]$  uniquely from neutron star data, although one can get a rough idea from the observed glitch size distribution. Quantities of interest, such as size and waiting time PDFs, cross-correlations, and autocorrelations all depend jointly on the form of  $\eta[\Delta X^{(n)}|X(t_n^-)]$ , however, opening the door to falsifiability [1, 2, 15].

In this paper, we generalize the successful SDP meta-model by adding a recipe to calculate  $\eta[\Delta X^{(n)}|X(t_n^-)]$  endogenously instead of stipulating it exogenously by fiat. We refer to this generalization as the endogenous- $\eta$  meta-model. The recipe makes concrete the following key idea, which underpins the traditional picture of superfluid vortex

---

<sup>1</sup>Up-to-date online catalogues are maintained at the Jodrell Bank Centre of Astrophysics, <http://www.jb.man.ac.uk/pulsar/glitches.html> [128], and the Australian National Telescope Facility, <https://www.atnf.csiro.au/research/psrcat/> [51]

avalanches in the literature: i) the vortex pinning strength varies randomly from one location to the next within the star; ii) the stress  $\Delta X^{(n)}$  released in a glitch is proportional to the number of locations where the stress  $X$  exceeds a threshold, when the glitch is triggered; and iii) the unpinned vortices are reassigned randomly to new pinning locations after the glitch. In other words, as time passes, the distribution of occupied pinning sites is continually revised in a history-dependent fashion, as the star spins down secularly and glitches occur stochastically. This idea is based on the “coherent noise” meta-model introduced by Sneppen and Newman [204] to describe sand piles [203], earthquakes [203], and biological extinctions [391]<sup>2</sup>. It has been repurposed successfully as a pulsar glitch meta-model in previous work [193].

Haskell [392] investigated a meta-model that connects the “snowplow” mechanism for hydrodynamically triggered glitches [393] to simulations of vortex unpinning and re-pinning in a two-component fluid framework [394]. It differs from the meta-model considered here in two fundamental ways: i) it unpins a random fraction of vortices at each avalanche event, independent of the past avalanche history; and ii) it assumes event waiting times are exponentially distributed (i.e. the waiting times do not depend on the stress, as in the SDP meta-model). However it does explicitly consider the mutual friction between the different fluid components, and shows that these hydrodynamic considerations produce deviations from power-law size distributions and exponential waiting time distributions.

We emphasize that we do not elect to analyze the endogenous- $\eta$  meta-model because we favor it over other options. True, it is reasonable from a physical standpoint, but so too are other options. The main motivation is that it formalizes the dominant (albeit idealized) idea in the literature about how vortex unpinning leads to glitches. We therefore quantify for the first time the long-term statistics predicted by the broad consensus behind what determines  $\eta[\Delta X^{(n)} | X(t_n^-)]$  in the superfluid vortex avalanche picture. As we show below, the long-term statistics are somewhat inconsistent with observations to date, although the conclusion is not final; more data are needed. As a matter of fact the exogenous SDP meta-model, where  $\eta[\Delta X^{(n)} | X(t_n^-)]$  is stipulated by fiat instead of being calculated self-consistently, seems to be more consistent with the data. It is unclear what this result implies more broadly, but it is intriguing and likely to inspire more investigations. It serves as a reminder of the value of falsification of physically-motivated meta-models.

The paper is structured as follows: in Section 4.3 we specify how  $\Delta X^{(n)}$  is decided at each glitch. In Section 4.4 we connect this method of determining  $\Delta X^{(n)}$  at a glitch to the SDP meta-model. In Section 4.5 we explore the long-term statistical observables predicted by the endogenous- $\eta$  meta-model, and discuss how they compare to current glitch observations in Section 4.6. We conclude in Section 4.7.

---

<sup>2</sup>The term “coherent noise” is not perfectly apt in the context of pulsar glitches, where the stress is coherent, while the noise, namely thermal creep, acts incoherently throughout the star. We retain the original terminology for consistency with previous literature [193, 204].

## 4.3. PINNING THRESHOLD DISTRIBUTION

We start by formalizing an idealized version of how the coherent stress mechanism may operate, which reflects standard ideas in the literature about stress accumulation and relaxation in pulsar glitches; see Haskell and Melatos [150] for a recent review. As argued below, there are at least three reasons why the simple version may not be what is truly occurring: i) it introduces a cross-correlation between sizes and waiting times, which is largely absent from the data; ii) it struggles to generate exponentially distributed waiting times, which are seen in some pulsars; and iii) it assumes a spatially uniform stress distribution which is qualitatively different to the spatially correlated stress distribution observed in Gross-Pitaevskii [173, 175] and N-body simulations [137] of superfluid vortex avalanches. Nonetheless it is important to study the simple version first, partly to falsify it if possible, and partly because it highlights the key idea that the stress distribution is history-dependent. As in previous papers, we develop the meta-model in the context of superfluid vortex avalanches for concreteness. Adapting it to the context of other microphysics, e.g. starquakes, is possible but outside the scope of this paper [203].

### 4.3.1. *Standard picture*

To fix ideas, suppose that the region of the stellar interior where glitch activity occurs is divided into “sites”. In the vortex avalanche picture, for example, the sites are nucleons or interstices in the nuclear lattice, where a superfluid vortex may pin [164, 165, 395]; in the starquake picture, the sites are segments of a fault or other tectonic element of the rigid crust [147, 169, 257]. At an arbitrary site located at  $\mathbf{r}$ , there is a local stress  $X(\mathbf{r}, t)$  at time  $t$ , which evolves in response to the global driver and local relaxation physics. In the vortex avalanche picture,  $X(\mathbf{r}, t)$  is proportional to the Magnus force; in the starquake picture,  $X(\mathbf{r}, t)$  is proportional to the elastic stress (or equivalently the strain in the linear regime).

Let  $X_{\text{th}}(\mathbf{r})$  denote the stress threshold at  $\mathbf{r}$ , which is assumed to be constant on the time-scales of interest (see below). Whenever the stress satisfies  $X(\mathbf{r}, t) \geq X_{\text{th}}(\mathbf{r})$ , and a glitch is triggered, the stress relaxes locally and is redistributed to nearby sites. In the vortex avalanche picture, a vortex at a site unpins when it escapes the nuclear pinning potential; in the starquake picture, the crustal lattice fails locally when the breaking strain is exceeded. On the other hand, if the stress satisfies  $X(\mathbf{r}, t) < X_{\text{th}}(\mathbf{r})$ , it remains supported stably at  $\mathbf{r}$  during a glitch. A group of contiguous sites with  $X(\mathbf{r}, t) < X_{\text{th}}(\mathbf{r})$  form a stress reservoir or capacitive domain [396]. Note that  $X(\mathbf{r}, t) > X_{\text{th}}(\mathbf{r})$  can be supported metastably for some time before a glitch is triggered.

The coarse-grained stress threshold is assumed to be spatially uniform, because the length-scale of vortex avalanches or starquakes (inferred from the size of observed glitches) is smaller than the length-scale over which the nuclear lattice is stratified (typically  $\sim 10^2$  m) [110]. However the fine-grained stress threshold varies randomly from one site to the next, due to defects and microscopic compositional gradients in the lattice.

### 4.3.2. Available versus occupied sites

When describing the pinning thresholds statistically, it is essential to distinguish between their “available” distribution (defined without reference to any vortices) and their “occupied” distribution (defined with reference only to those pinning sites where a vortex is pinned). These are not the same in general. The available distribution is governed by the physics of the nuclear lattice. The occupied distribution is governed by a combination of the available distribution and the history-dependent vortex dynamics; vortices may congregate preferentially in deeper pinning potentials, for example.

Let  $\phi(X_{\text{th}})$  denote the PDF of the thresholds at all available pinning sites. We assume that  $\phi(X_{\text{th}})$  is constant in time, because the nuclear properties of the star evolve slowly (e.g. on the cooling time-scale  $\sim 10^5$  yr) compared to the inter-glitch waiting time and the length of glitch monitoring campaigns to date. Let  $X_{\text{th},\max} = \max_{X_{\text{th}}} X_{\text{th}}$  denote the maximum pinning threshold in the star. In the superfluid vortex picture, for example,  $X_{\text{th},\max}$  corresponds to the nuclear site with the deepest pinning potential; if a uniform stress satisfying  $X \geq X_{\text{th},\max}$  is applied to the system, every vortex unpins when a glitch is triggered. The functional form of  $\phi(X_{\text{th}})$  is unknown from first principles, but theoretical calculations suggest that it is broad, with standard deviation comparable to the mean [164, 165, 395], and  $X_{\text{th},\max}$  is certain to be finite as stipulated by quantum mechanics<sup>3</sup>. In this work we assume  $\phi(X_{\text{th}})$  has compact support on the interval  $0 = X_{\text{th},\min} \leq X_{\text{th}} \leq X_{\text{th},\max}$  for simplicity, but the results carry over straightforwardly to the case  $X_{\text{th},\min} \neq 0$  without changing qualitatively. We emphasize that  $X_{\text{th},\max}$  need not equal  $X_c$ , the critical stress at which a glitch is certain in either the SDP or BSA meta-models. This subtle point is discussed further in Section 4.4.3.

What is the PDF  $g(X_{\text{th}}, t)$  of the stress thresholds at pinning sites actually occupied by vortices at time  $t$ ? In the absence of a global driver, we have  $g(X_{\text{th}}, t) = \phi(X_{\text{th}})$  in the limit  $t \rightarrow \infty$ , after initial transients die away. In the presence of a persistent global driver, however,  $g(X_{\text{th}}, t)$  depends on time and does not equal  $\phi(X_{\text{th}})$  for any  $t$  in general (except perhaps  $t = 0$ , or in the special situation where all vortices unpin at once, resetting the system back to  $g(X_{\text{th}}, t) = \phi(X_{\text{th}})$ , as described in Section 4.3.3). Whenever a glitch occurs, vortices unpin from relatively shallow pinning sites and repin randomly, changing the relative occupation of sites with lower and higher  $X_{\text{th}}$ . Thus  $g(X_{\text{th}}, t)$  is not only time- and history-dependent but also stochastic; it depends on the random sequence of glitch sizes and waiting times up to the instant  $t$ .

How  $g(X_{\text{th}}, t)$  evolves depends, among other things, on whether one treats the system as spatially uniform or nonuniform. In self-organized critical systems like sand piles, for example, long-range spatial correlations exist between the stress at different locations  $\mathbf{r}$  and  $\mathbf{r}'$ , with  $|\langle X(\mathbf{r}, t)X(\mathbf{r}', t) \rangle - \langle X(\mathbf{r}, t) \rangle \langle X(\mathbf{r}', t) \rangle| \propto |\mathbf{r} - \mathbf{r}'|^{-a}$  and  $a > 0$  typically [195, 380]. The system self-organizes through spatial gradients to produce scale-invariant dynamics (e.g. power-law avalanche size PDFs). A strong case can be made, through Gross-Pitaevskii and N-body simulations, that superfluid vortex avalanches or starquakes in a neutron star are self-organized critical systems too [17, 137, 150]. However, the theoretical treatment of a far-from-equilibrium system with correlated spatial gradients is a notoriously challenging (and unsolved) problem in statistical mechanics

---

<sup>3</sup>That is,  $X_{\text{th},\max} < \infty$  as tunneling sets an effective upper limit on the ability of a pinning site to restrict the motion of a vortex over a finite timespan [174].

[195]. In this paper, therefore, we derive an equation of motion for  $g(X_{\text{th}}, t)$  under the assumption that every pinning site in the star experiences the same, spatially-averaged stress,  $X(\mathbf{r}, t) = X(t)$ . This mean-field approximation [16, 389] has been employed successfully in the analysis of pulsar glitch observational data on size and waiting time PDFs, cross-correlations, and autocorrelations in the context of the SDP and BSA meta-models [1, 2, 15, 16, 351, 370] as well as in previous work on “coherent noise” models of pulsar glitches [see footnote 2 and Melatos and Warszawski [193]].

### 4.3.3. Unpinning and repinning

Consider two consecutive glitches that occur at times  $t_n$  and  $t_{n+1}$ . Let  $t_n^\pm$  denote the instants infinitesimally after (+) and before (−) the event at  $t = t_n$ <sup>4</sup>. During the interval  $t_n^+ \leq t \leq t_{n+1}^-$ , the vortices are pinned, so the occupied sites do not change, and neither does  $g(X_{\text{th}}, t)$ . That is, we have  $g(X_{\text{th}}, t) = g(X_{\text{th}}, t_n^+)$  for  $t_n^+ \leq t \leq t_{n+1}^-$ . We also have  $g(X_{\text{th}}, t) = 0$  for  $X_{\text{th}} \leq X(t_n^+)$ , because vortices repin exclusively at sites with  $X_{\text{th}} > X(t_n^+)$ , when the avalanche at  $t = t_n$  occurs; they cannot get stuck at sites where the stress exceeds the local threshold, while they are moving freely. Simultaneously,  $X(t)$  evolves during the interval  $t_n^+ \leq t \leq t_{n+1}^-$  (deterministically in the SDP process, stochastically in the BSA process). By the time the instant  $t = t_{n+1}$  is reached, we have  $X(t_{n+1}^-) \geq X_{\text{th}}$  at many sites; the corresponding vortices are pinned metastably and are ready to unpin when provoked by some minuscule statistical (e.g. thermal) fluctuation. When they do unpin, they are assumed to do so instantaneously at  $t = t_{n+1}$ . The instantaneous approximation is justified amply by Gross-Pitaevskii simulations, where vortex avalanches are observed to occur on a time-scale shorter than one rotation period, and by high-time-resolution radio timing observations, which reveal that the spin up during a glitch takes less than  $\sim 30$  s [129, 130, 397, 398]. Both these time-scales are much shorter than the typical inter-glitch waiting time of weeks to months.

How many vortices unpin at  $t = t_{n+1}$ ? In the mean-field approximation, the answer is all of them pinned in sites that satisfy  $X_{\text{th}} \leq X(t_{n+1}^-)$ , which represent a fraction,  $F$ , of the total, with

$$F = \int_0^{X(t_{n+1}^-)} dX'_{\text{th}} g(X'_{\text{th}}, t_{n+1}^-) \quad (4.1)$$

$$= \int_{X(t_n^+)}^{X(t_{n+1}^-)} dX'_{\text{th}} g(X'_{\text{th}}, t_n^+) . \quad (4.2)$$

The unpinned vortices move radially outward by a distance  $\Delta r$  comparable to one inter-vortex (Feynman) separation  $\lambda_F$  before repinning (as seen in Gross-Pitaevskii and N-body simulations), reducing the angular momentum of the superfluid in proportion to  $\Delta r$  and their number. By angular momentum conservation, the crust spins up, and the crust-superfluid angular velocity lag (i.e. the spatially averaged stress) decreases. That is, we have

$$X(t_{n+1}^+) - X(t_{n+1}^-) = -KF , \quad (4.3)$$

---

<sup>4</sup>It is important to distinguish  $t_n$  from  $t_n^\pm$ , because the glitch is assumed to occur instantaneously, as in previous work.

where  $K > 0$  is a constant measured in units of stress. To ensure  $X(t) \geq 0$  we require  $K \leq X_{\text{th}, \text{max}}$ .

In the vortex avalanche picture, where  $X$  is the crust-core differential angular velocity, angular momentum conservation implies [16, 277]

$$KF = \frac{2\pi(I_C + I_S)\Delta\nu}{I_S} \quad (4.4)$$

or equivalently

$$K = \frac{2\pi(I_C + I_S)}{I_C} \frac{\nu\Delta r}{R}, \quad (4.5)$$

where  $\nu$  is the rotational frequency of the rigid crust (with  $X \ll \nu$ ),  $\Delta\nu$  is the increase in  $\nu$  at the glitch,  $I_S$  and  $I_C$  are moments of inertia of the superfluid and crust respectively, and  $R$  is the neutron star radius. For  $\Delta r \sim \lambda_F = 4.1 \times 10^{-2}(\nu/10\text{Hz})^{-1/2}$  cm, we estimate

$$K \sim 10^{-7} \left( \frac{I_C + I_S}{I_C} \right) \left( \frac{\nu}{10\text{Hz}} \right)^{1/2} \left( \frac{R}{10\text{km}} \right)^{-1} \text{Hz}. \quad (4.6)$$

The factor  $(I_C + I_S)/I_C$  amounts to  $\sim 10^2$  if the crust is a thin crystalline lattice while the rest of the star is composed of a superfluid [383, 384] or  $\sim 1$  if the crust is coupled tightly to most of the neutrons and protons throughout the star, e.g. by pinning between neutron vortices and magnetic fluxoids of the superfluid [128, 139, 385, 399]. As discussed in Section 2.5 of Carlin and Melatos [2] the coupling between the rotation of the superfluid and the crust may be imperfect [400]. In light of the uncertainty, we allow  $K$  to remain a free parameter in the meta-model.

The unpinned vortices repin instantaneously. The number of pinning sites per unit area is  $\sim 10^{20}$  times the number of vortices per unit area, so there is no reason for a vortex to pin preferentially to a shallower or deeper pinning site, as it circulates freely during an avalanche. Hence the probability that a vortex repins at a site with stress threshold  $X_{\text{th}}$  is simply proportional to the number of such sites present in the crustal lattice, i.e. the fraction of the total sites with threshold  $X_{\text{th}}$ . Therefore the distribution of thresholds at which the vortices repin satisfies  $g_{\text{repin}}(X_{\text{th}}, t_{n+1}^+) \propto \phi(X_{\text{th}})$ <sup>5</sup>. Of course, freely moving vortices cannot repin at a site whose threshold is lower than the global stress, as discussed above, so we have

$$g_{\text{repin}}(X_{\text{th}}, t_{n+1}^+) = A \phi(X_{\text{th}}) H[X_{\text{th}} - X(t_{n+1}^+)], \quad (4.7)$$

where  $H(\dots)$  denotes the Heaviside function. The constant  $A$  is determined by normalization with respect to the unpinned fraction and is given by

$$A = \left[ \int_{X(t_{n+1}^+)}^{X_{\text{th}, \text{max}}} dX'_{\text{th}} \phi(X'_{\text{th}}) \right]^{-1} F. \quad (4.8)$$

---

<sup>5</sup>In other words, as there many more pinning sites than vortices, the distribution of thresholds of pinning sites at which a free vortex may repin is equal to the distribution of thresholds of pinning sites in general. A free vortex is not biased towards pinning sites with higher or lower thresholds. It pins indiscriminately to any site, whose threshold exceeds the global stress [401].

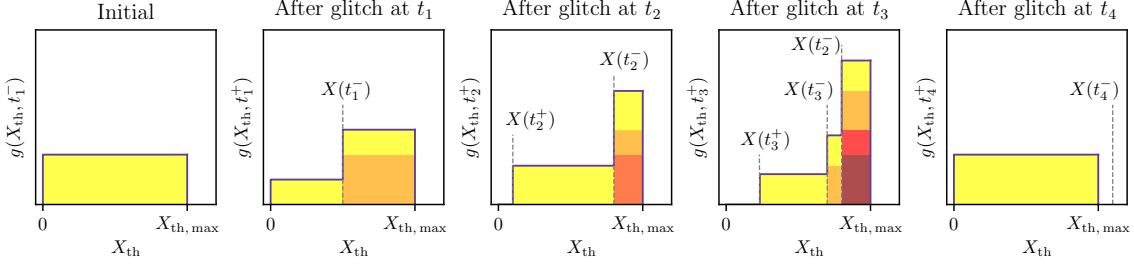


Figure 4.1: A toy example illustrating schematically the evolution of  $g(X_{\text{th}}, t)$  during a sequence of four glitches, with  $X(t_1^+) < X(t_3^+) < X(t_2^+) < X_{\text{th}, \text{max}} < X(t_4^-)$ , where  $g(X_{\text{th}}, t_1^-) = \phi(X_{\text{th}})$  is the uniform distribution between  $0 \leq X_{\text{th}} \leq X_{\text{th}, \text{max}}$ . The colors correspond to how many glitches occur in the time elapsed since vortices unpin from pinning sites with a certain threshold. Darker colors indicate that the vortices have stayed pinned during more events.

#### 4.3.4. Equation of motion for the distribution of occupied pinning sites

We are now in a position to combine the results on unpinning and repinning in Section 4.3.3 to write down the equation of motion for  $g(X_{\text{th}}, t)$ . We remind the reader that  $g(X_{\text{th}}, t)$  does not evolve at all during the inter-glitch interval  $t_n^+ \leq t \leq t_{n+1}^-$ , while vortices are pinned. Its evolution is described completely, in the above approximation, by discontinuous adjustments at each glitch. That is, at  $t = t_{n+1}$ , the following things happen to the stress threshold PDF:

- i) we start with  $g(X_{\text{th}}, t_{n+1}^-) = g(X_{\text{th}}, t_n^+)$ , which is nonzero for  $X_{\text{th}} > X(t_n^+)$ ;
- ii) we calculate the change in stress  $-KF$  in equation (4.3) by integrating  $g(X_{\text{th}}, t_n^+)$  according to equation (4.2);
- iii) we set  $g(X_{\text{th}}, t_{n+1}^-)$  to zero in the range  $X(t_n^+) \leq X_{\text{th}} \leq X(t_{n+1}^-)$ , because the vortices therein unpin;
- iv) we reassign the unpinned vortices to sites with thresholds in the range  $X(t_{n+1}^+) < X_{\text{th}} \leq X_{\text{th}, \text{max}}$  according to equations (4.7) and (4.8).

Putting steps i)–iv) together yields

$$g(X_{\text{th}}, t_{n+1}^+) = g(X_{\text{th}}, t_{n+1}^-) H[X_{\text{th}} - X(t_{n+1}^-)] + \left[ \int_{X(t_{n+1}^+)}^{X_{\text{th}, \text{max}}} dX'_{\text{th}} \phi(X'_{\text{th}}) \right]^{-1} F \phi(X_{\text{th}}) H[X_{\text{th}} - X(t_{n+1}^+)] \quad (4.9)$$

It is easy to check that this normalizes correctly with  $1 = \int_0^{X_{\text{th}, \text{max}}} dX'_{\text{th}} g(X'_{\text{th}}, t_{n+1}^+)$ . Note that  $g(X_{\text{th}}, t_{n+1}^+)$  depends on  $g(X_{\text{th}}, t_n^+)$  implicitly through  $F$ . It also depends on  $X(t_{n+1}^-)$  and  $X(t_n^+)$  independently, because the evolution of  $X(t)$  during the interval  $t_n^+ \leq t \leq t_{n+1}^-$  is controlled by the stress accumulation process, which does not depend on the unpinning and repinning physics.

Equation (4.9) resembles, but is not the same as, the equations of motion in Snepen and Newman [204] and Melatos and Warszawski [193]. The foregoing papers treat

unpinning and repinning similarly, i.e. by nullifying the unpinned portion of  $g(X_{\text{th}}, t)$  and reassigning it elsewhere  $\propto \phi(X_{\text{th}})$ <sup>6</sup>. However neither paper evolves  $g(X_{\text{th}}, t)$ . It is assumed that  $g(X_{\text{th}}, t)$  converges rapidly to its steady-state form,  $g(X_{\text{th}}, t) = g(X_{\text{th}})$ , i.e. the system establishes detailed balance between unpinning and repinning at each individual value of  $X_{\text{th}}$  [see equations (3) and (4) in Melatos and Warszawski [193]]. This approach is perfectly defensible, when the goal is to calculate the statistically stationary size and waiting time PDFs, but it does not contain enough information to study the cross- and autocorrelations we are interested in here [1, 15, 351].

To build intuition, Figure 4.1 illustrates schematically the evolution of  $g(X_{\text{th}}, t)$  over the course of four hypothetical glitches at  $t_1, t_2, t_3$ , and  $t_4$ . For simplicity we choose  $\phi(X_{\text{th}})$  to be uniform in the range  $0 \leq X_{\text{th}} \leq X_{\text{th},\text{max}}$ , with  $K = X_{\text{th},\text{max}}$ . The system starts with  $g(X_{\text{th}}, t_1^-) = \phi(X_{\text{th}})$ . In this particular realization we choose  $X(t_1^+) < X(t_3^+) < X(t_2^+) < X_{\text{th},\text{max}} < X(t_4^-)$  for illustrative purposes. The first glitch, at  $t_1$ , unpins half of the vortices, and they are reassigned according to equation (4.7). The second glitch, at  $t_2$ , unpins more than half of the vortices, but due to the previous glitch we have  $X(t_2^+) \neq 0$ , as  $g(X_{\text{th}}, t)$  is no longer uniform. The third glitch, at  $t_3$ , occurs with  $X(t_3^-) < X(t_2^+)$ , demonstrating that the memory of the previous stress in the system is imprinted on  $g(X_{\text{th}}, t)$ , i.e.  $g(X_{\text{th}}, t_3^+)$  depends on  $X(t_2^-)$ , not just  $X(t_3^\pm)$ . The fourth glitch, at  $t_4$ , resets the system back to  $\phi(X_{\text{th}})$  because we have  $X(t_4^-) > X_{\text{th},\text{max}}$ , and so all vortices unpin.

Note that there is a complex feedback loop at play which relates the glitch sizes and waiting times to  $g(X_{\text{th}}, t)$ . If chance produces a long sequence of frequent glitches, i.e. the stress does not increase much before another glitch is triggered, vortices pile up at larger values of  $X_{\text{th}}$  near  $X_{\text{th},\text{max}}$ . Then, when there is a long delay, which gives the stress time to reach  $X \approx X_{\text{th},\text{max}}$ , the vortex pile pinned at sites with  $X_{\text{th}} \approx X_{\text{th},\text{max}}$  unpins all at once to produce a relatively large glitch resetting the system. By contrast, a similarly long delay produces a smaller glitch, if it is preceded by a glitch sequence which does not pile up vortices at  $X_{\text{th}} \approx X_{\text{th},\text{max}}$ .

#### 4.4. STATE-DEPENDENT POISSON PROCESS

The above recipe for updating  $g(X_{\text{th}}, t)$  must be combined with a compatible recipe for choosing the waiting times between glitches. Two approaches have been explored previously, in the SDP [15, 16] and BSA meta-models [2]. In the BSA meta-model the stress accumulates stochastically to a fixed threshold, whereupon a glitch is triggered deterministically. In the SDP meta-model glitches are triggered probabilistically, at an instantaneous rate which depends on the stress in the system. If  $X(t_n^-) = X_c$  is identical for each glitch as in the BSA meta-model, the system does not produce glitches of different sizes, as the same fraction of vortices would unpin every time, and repopulate the same distribution of pinning sites. To avoid this trivial behavior, which is inconsistent with pulsar data, we henceforth adopt the SDP meta-model to pick waiting times, and therefore determine  $X(t_{n+1}^-)$ , given  $X(t_n^+)$ .

We position the SDP and related meta-models in the broader context of point processes and time series modeling in Appendix 4.A3.

---

<sup>6</sup>They also include an optional thermal unpinning process independent of  $X_{\text{th}}$ , which is not essential and is omitted in this paper.

#### 4.4.1. Equation of motion for the stress

The stress,  $X(t)$ , in the star evolves according to

$$X(t) = X(0) + t + \sum_{n=1}^{N(t)} \Delta X^{(n)}, \quad (4.10)$$

where  $X$  and  $t$  are here and henceforth expressed in dimensionless units of  $X_c$  (the critical stress at which a glitch becomes certain) and  $X_c I_C / N_{\text{em}}$  respectively, where  $N_{\text{em}}$  is the electromagnetic torque acting on the crust, and  $X(0)$  is an arbitrary initial condition. The number of glitches up to time  $t$ ,  $N(t)$ , is a random variable, implicitly determined by the waiting times between each glitch. The size  $\Delta X^{(n)}$  of the  $n$ -th relaxation event is a deterministic function of the fluctuating PDF  $g(X_{\text{th}}, t)$ . The recipe for determining  $\Delta X^{(n)} = -KF$  is outlined in Section 4.3.3, specifically equations (4.2) and (4.3).

One key assumption of the SDP meta-model is that the instantaneous glitch rate,  $\lambda(t)$ , is a function of the spatially-averaged stress,  $X(t)$ . We assume  $\lambda[X(t)]$  grows monotonically between glitches according to

$$\lambda[X(t)] = \frac{\alpha}{1 - X(t)}, \quad (4.11)$$

where

$$\alpha = \frac{I_C X_c \lambda_0}{N_{\text{em}}} \quad (4.12)$$

is a dimensionless control parameter, and  $\lambda_0$  is a reference rate defined as  $\lambda_0 = \lambda(1/2)/2$ . The exact functional form of  $\lambda[X(t)]$  does not significantly change the long-term dynamics, as long as the rate diverges as  $X \rightarrow X_c$  [15, 16].

The PDF of waiting times after the  $n$ -th glitch is [16, 235]

$$p[\Delta t | X(t_n^+)] = \lambda[X(t_n^+) + \Delta t] \exp \left\{ - \int_{t_n^+}^{t_n^+ + \Delta t} dt' \lambda[X(t_n^+) + t'] \right\}. \quad (4.13)$$

#### 4.4.2. Monte Carlo simulations

The evolution of  $X(t)$  and  $g(X_{\text{th}}, t)$  is jointly modeled with a simple Monte Carlo automaton.

1. Initialize the system at  $t = 0$  with  $g(X_{\text{th}}, 0) = \phi(X_{\text{th}})$ , and  $X = X(0)$ .
2. Pick a random  $\Delta t$  from equation (4.13), given the current stress  $X$ .
3. Update the stress to  $X + \Delta t$  to account for the deterministic evolution up to the glitch.
4. Evaluate  $\Delta X = -KF$  deterministically via equations (4.2) and (4.3), given  $g(X_{\text{th}}, t)$  and  $X$ .
5. Update  $g(X_{\text{th}}, t)$  according to equation (4.9).

6. Update  $X$  by adding  $\Delta X$  according to equation (4.10).

7. Repeat from step 2.

Random numbers for step 2 are picked using the standard inverse cumulative algorithm [60]. As  $\phi(X_{\text{th}})$  is chosen to be a uniform distribution between  $0 \leq X_{\text{th}} \leq X_{\text{th},\text{max}}$ ,  $g(X_{\text{th}}, t)$  is a piecewise-constant function. Hence, we efficiently update it by storing the heights at change-points  $X_{\text{th}}$  in memory, as opposed to sampling  $g(X_{\text{th}}, t)$  on a grid of  $X_{\text{th}}$  values.

#### 4.4.3. Qualitative results

There are three control parameters in the dimensionless meta-model:  $\alpha$ ,  $X_{\text{th},\text{max}}$ , and  $K$ . We fix  $\phi(X_{\text{th}})$  to be a uniform distribution between 0 and  $X_{\text{th},\text{max}}$ . For simplicity, we assume  $K = X_{\text{th},\text{max}}$  (its maximal value) for the rest of this work. Appendix 4.A1 contains a brief exploration of the impact  $K < X_{\text{th},\text{max}}$  has on long-term observables. Figures 4.2–4.4 illustrate the qualitative impact of  $\alpha$  on the evolution of  $X$  and  $g(X_{\text{th}}, t)$ , given  $X_{\text{th},\text{max}} = 0.95X_c$ . Figure 4.2 shows that at low values  $\alpha \lesssim 0.5$ , longer waiting times are more likely, and the stress often exceeds  $X_{\text{th},\text{max}}$  before each glitch, resetting the system. Therefore one finds  $g(X_{\text{th}}, t) \approx \phi(X_{\text{th}})$ , i.e. there is little long-term memory in the system. In Figure 4.4 high values  $\alpha \gtrsim 5$  produce shorter waiting times. Thus long sequences of small glitches unfold before rare, large events reset the system once the stress finally accumulates to  $X \gtrsim X_{\text{th},\text{max}}$ . Figure 4.3 shows that for intermediate values of  $\alpha$  between the above two extremes the behavior of both the stress  $X(t)$  and the evolution of  $g(X_{\text{th}}, t)$  is complex.

The qualitative long-term behavior of  $X$  is shown in Figure 4.5. In the top panel with  $\alpha = 0.2$ , the stress often exceeds  $X_{\text{th},\text{max}}$  due to the long waiting times between glitches, resetting the system and keeping the average stress around  $X \sim 0.5$ . In the middle panel with  $\alpha = 1$ , the average stress climbs stochastically until finally a longer than average waiting time allows  $X > X_{\text{th},\text{max}}$ , resetting the system. In the bottom panel with  $\alpha = 10$ , waiting times are short and the stress builds asymptotically towards  $X = X_{\text{th},\text{max}}$ . For  $\alpha \gtrsim 1$  the automaton takes some time to stabilize such that the memory of the arbitrary initial conditions  $X(t = 0) = 0$  and  $g(X_{\text{th}}, t = 0) = \phi(X_{\text{th}})$  is lost. When calculating long-term statistics predicted by the meta-model in Section 4.5 we throw away the first  $\lfloor 100\alpha \rfloor$  glitches generated.

Figures 4.2–4.4 demonstrate that how often the system completely resets is closely linked to the dynamics of how  $X$  and  $g(X_{\text{th}}, t)$  evolve, and therefore observables such as waiting times and glitch sizes. The fraction of glitches that fully reset the system, i.e. result in  $g(X_{\text{th}}, t_n^+) = \phi(X_{\text{th}})$  after a glitch at time  $t_n$ , is plotted as a function of  $\alpha$  and  $X_{\text{th},\text{max}}$  in Figure 4.6. The smallest value of  $\alpha$  where over half the glitches reset the system shifts from 0.5 to 0.3 to 0.15 as  $X_{\text{th},\text{max}}$  decreases from 0.99 to 0.95 to 0.8 respectively. This is intuitive, as lower  $\alpha$  results in longer waiting times, all else being equal, and the stress is more likely to exceed  $X_{\text{th},\text{max}}$  by the time a glitch is triggered.

For  $X_{\text{th},\text{max}} \geq 1$ ,  $X$  never exceeds  $X_{\text{th},\text{max}}$ , and the system never completely resets. That is, the repinning step in equation (4.7) assigns vortices to pinning potentials with  $X_{\text{th}} \geq 1$ , which never unpin. The system stagnates eventually, with all vortices pinned

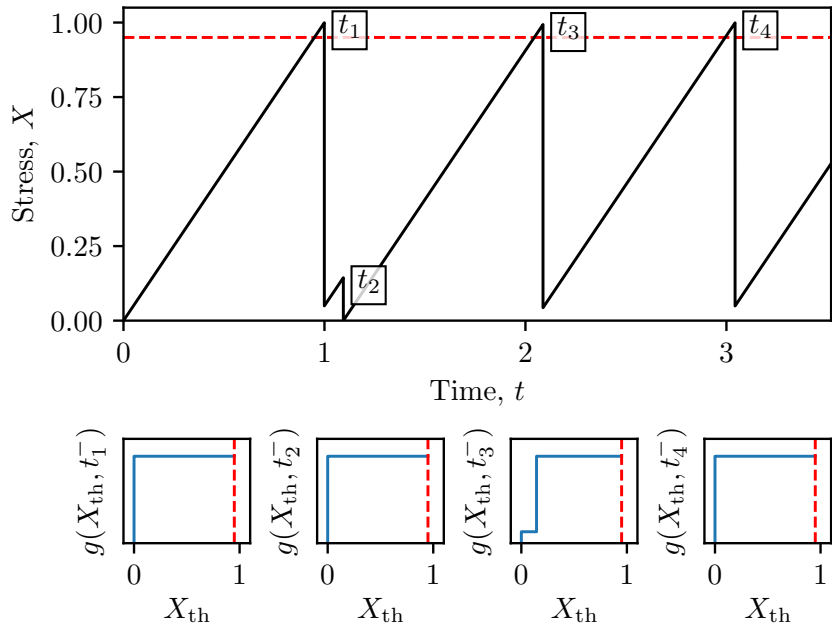


Figure 4.2: Evolution of  $X$  (main panel) and  $g(X_{\text{th}}, t)$  (sub-panels) across four glitches at  $t_1, \dots, t_4$ , generated via the automaton outlined in Section 4.4.2. Parameters:  $\alpha = 0.2$ ,  $X_{\text{th}, \text{max}} = 0.95$  (indicated in both the main panel and sub-panels with a red dashed line),  $K = X_{\text{th}, \text{max}}$ .  $X$  and  $X_{\text{th}}$  are in units of  $X_c$  and  $t$  is in units of  $X_c I_C / N_{\text{em}}$ .

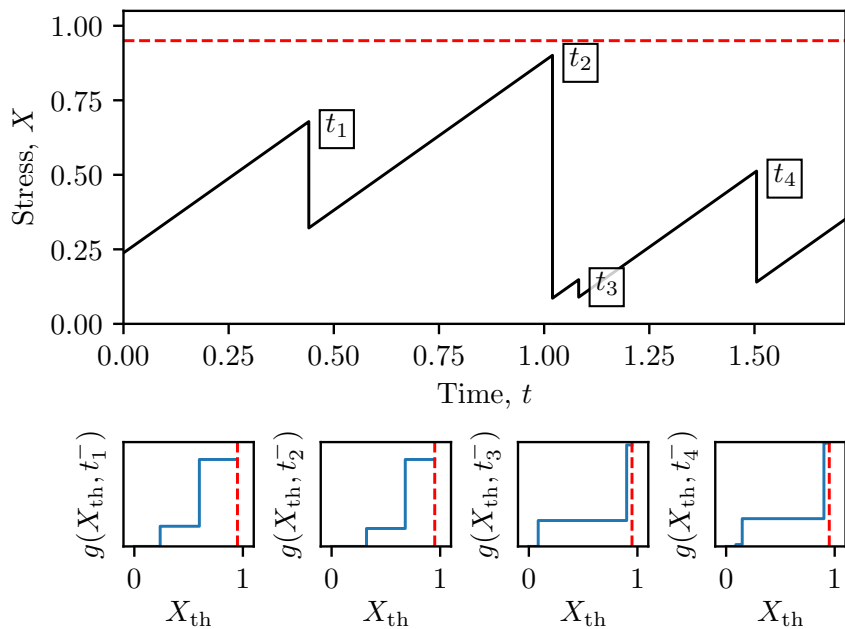


Figure 4.3: As in Figure 4.2 but with  $\alpha = 1$ .

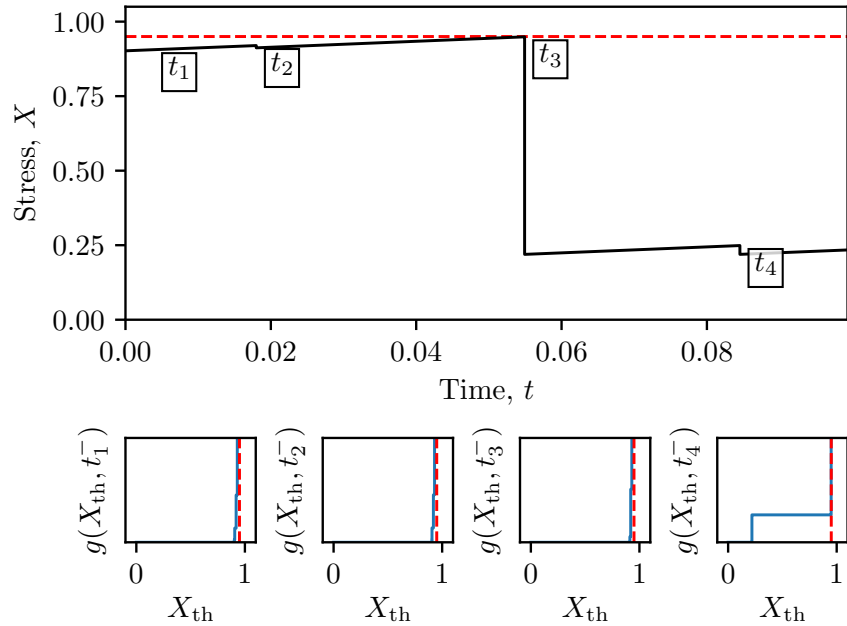


Figure 4.4: As in Figure 4.2 but with  $\alpha = 10$ .

at sites whose stress thresholds cannot be reached. Melatos and Warszawski [193] ameliorated this stagnation by allowing a “thermal creep” term, whereby a small fraction of vortices at sites with  $X_{\text{th}} > X$  unpin randomly at a glitch [204].

#### 4.4.4. Differences from previous meta-models

The recipe for updating  $g(X_{\text{th}}, t)$  and hence generating  $\Delta X^{(n)}$  differs fundamentally from the recipe in previous meta-models [2, 15, 16]. Firstly  $\Delta X^{(n)}$  is generated from  $g(X_{\text{th}}, t)$ , which is a new step. In the SDP and BSA meta-models,  $\Delta X^{(n)}$  is drawn from an exogenously defined conditional jump distribution,  $\eta[\Delta X^{(n)} | X(t_n^-)]$ , which makes no reference to which pinning sites are occupied. Secondly,  $\Delta X^{(n)}$  is generated deterministically; once  $g(X_{\text{th}}, t_n^+)$  and  $X(t_{n+1}^-)$  are known, so is  $\Delta X^{(n)}$  without rolling dice. This fundamentally alters the meta-model from a doubly stochastic process, where the waiting time  $\Delta t$  and avalanche size  $\Delta X^{(n)}$  are drawn randomly from independent PDFs (inhomogeneous Poisson and  $\eta[\Delta X^{(n)} | X(t_n^-)]$  respectively), to a singly stochastic process, where only  $\Delta t$  is drawn randomly, according to the stress accumulation process of choice.

With that said, the sequence of avalanche sizes is still unpredictable in a long-term sense in the endogenous- $\eta$  meta-model, because it is driven by stochastic draws of  $\Delta t$ . Furthermore, the ensemble average  $g_s(X_{\text{th}}) = \langle g(X_{\text{th}}, t_n^+) \rangle$ , is analogous to the statistically stationary global stress PDF  $p(X)$  discussed in Section 6 of Fulgenzi et al. [16]. From  $g_s(X_{\text{th}})$ , it is possible to calculate an effective  $\eta[\Delta X^{(n)} | X(t_n^-)]$ , which is also statistically stationary. We do so in Appendix 4.A2. If the goal of the theory is to predict the stationary glitch size and waiting time PDFs, then running the SDP meta-model as developed in previous papers and drawing randomly from  $\eta[\Delta X^{(n)} | X(t_n^-)]$  derived from  $g_s(X_{\text{th}})$  as in Appendix 4.A2 is adequate. However, if the exact temporal sequence of sizes and waiting times is of interest, e.g. to investigate cross- and autocorrelations, then the evolution of

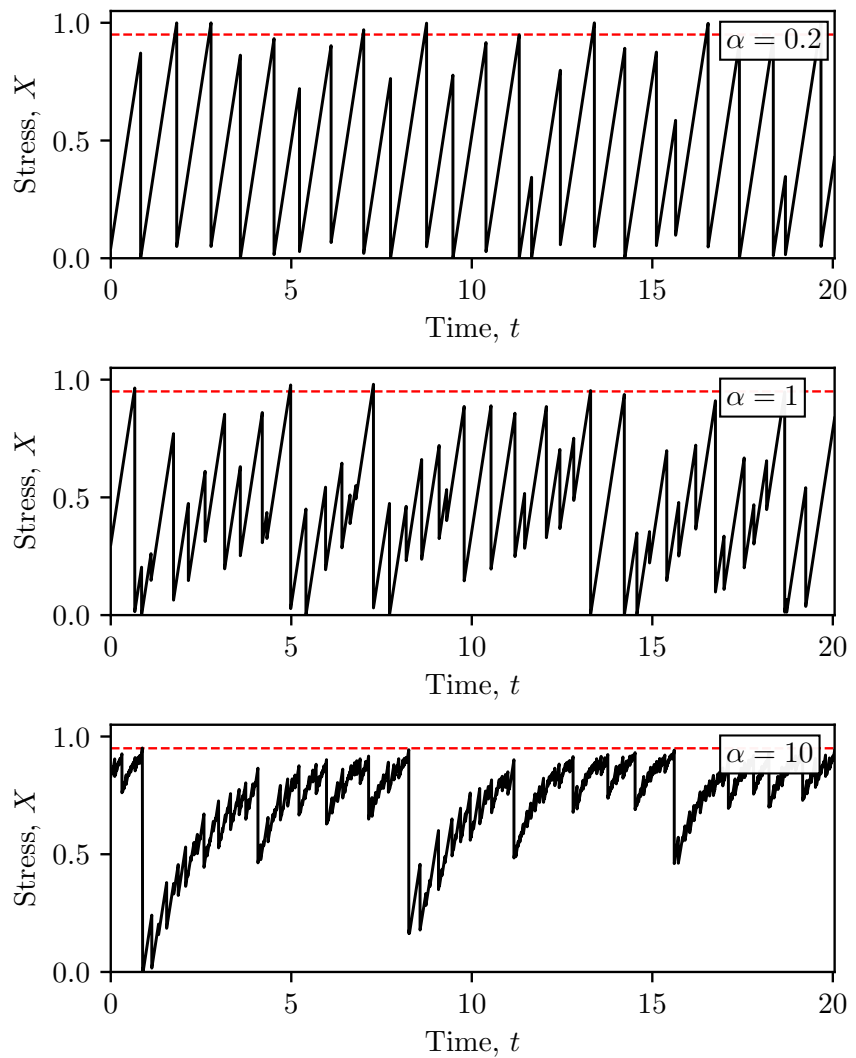


Figure 4.5: Long-term qualitative behavior of  $X$  for three different values of  $\alpha = 0.2, 1$ , and  $10$  in the top, middle and bottom panel respectively. Parameters:  $X_{\text{th}, \text{max}} = 0.95$  (indicated with a red dashed line in each panel),  $K = X_{\text{th}, \text{max}}$ .

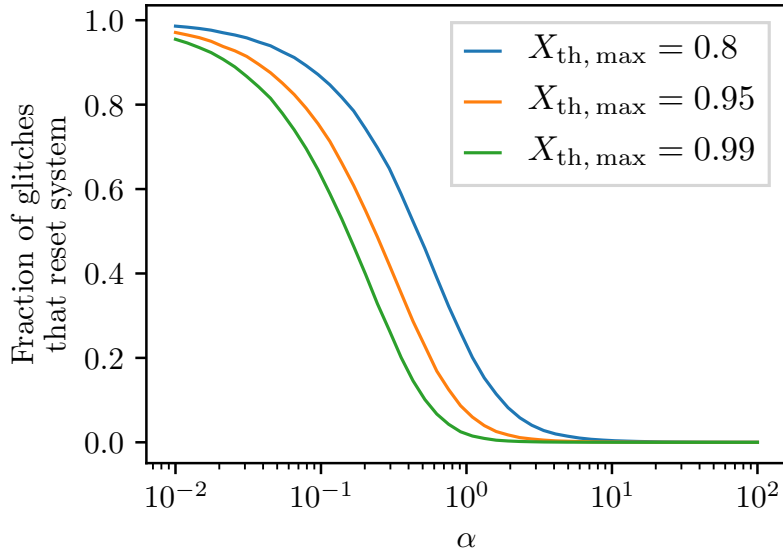


Figure 4.6: Fraction of glitches that reset the system as a function of  $\alpha$  for three different values of  $X_{\text{th},\text{max}}$ . Parameters:  $N = 10^5$  glitches generated at 50 logarithmically spaced values of  $\alpha$  for each value of  $X_{\text{th},\text{max}}$ , with  $K = X_{\text{th},\text{max}}$ .

$g(X_{\text{th}}, t)$  must be tracked according to equation (4.9) or some variant thereof.

#### 4.4.5. Mutual friction

In hydrodynamical multi-component models, the coupling between the inviscid and viscous components is called the mutual friction [156, 402, 403]. The strength and functional form of the mutual friction is fundamentally linked to how the vortices transfer angular momentum from the unobservable stress reservoir and the observable crust [381, 403, 404]. The SDP meta-model, and endogenous- $\eta$  extension considered in this paper, tacitly assume that mutual friction is weak between glitches as the stress grows linearly, irrespective of its absolute magnitude, until a glitch is triggered. These meta-models align qualitatively with phenomenological models that abruptly change the form (and usually weaken the strength) of the mutual friction when a glitch occurs, due to a phase transition between turbulent and laminar flow states [189, 191, 192]. We note that the meta-model treats glitches as impulsive events and has nothing to say in its present form about post-glitch recoveries, where hydrodynamic effects are likely to play a role.

## 4.5. OBSERVABLE LONG-TERM STATISTICS

Following the steps outlined in Section 4.4.2 one can generate sequences of waiting times and sizes of arbitrary length, given  $\alpha$ ,  $K$ , and  $X_{\text{th},\text{max}}$ . From these sequences, observable long-term statistics are predictable. They offer a baseline for falsification studies involving astronomical observations [1, 15, 351]. As stated in equation (4.4), we have  $\Delta X = -KF \propto \Delta\nu$ , implying the shape of the event size PDF  $p(\Delta X)$  is the same as the observed glitch size PDF  $p(\Delta\nu)$ .

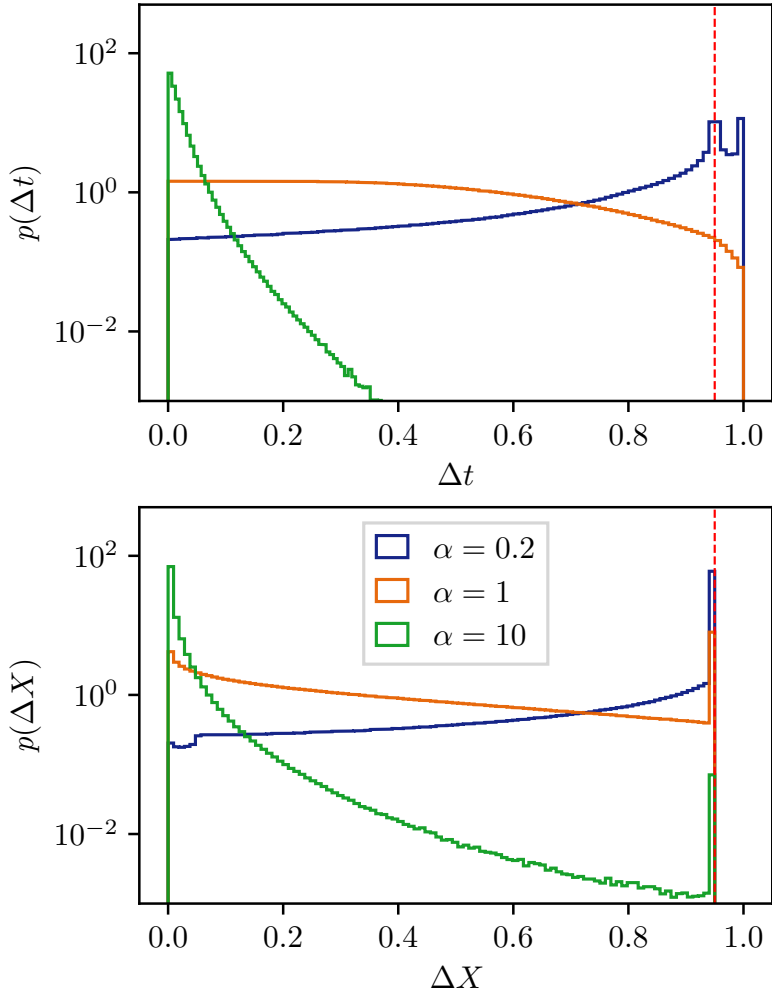


Figure 4.7: Waiting time,  $\Delta t$ , and size,  $\Delta X$ , PDFs on the top and bottom panel respectively. Parameters:  $N = 10^7$  simulated glitches for each value of  $\alpha$ ,  $X_{\text{th},\text{max}} = 0.95$  (indicated with a red dashed line in each panel),  $K = X_{\text{th},\text{max}}$ .

#### 4.5.1. Waiting time and size PDFs

Figure 4.7 shows the waiting time PDF,  $p(\Delta t)$ , and size PDF,  $p(\Delta X)$ , for three values of  $\alpha$  on a log-linear scale. For  $\alpha \lesssim 0.5$ ,  $p(\Delta t)$  has two peaks, one at  $\Delta t = X_{\text{th},\text{max}}$  and one at  $\Delta t = 1$ , and increases monotonically for  $\Delta t < X_{\text{th},\text{max}}$ . In the low- $\alpha$  regime  $X$  regularly exceeds  $X_{\text{th},\text{max}}$ , triggering a glitch of size  $\Delta X = X_{\text{th},\text{max}}$ . With  $X \approx 1$  before the glitch, and  $X \approx 1 - X_{\text{th},\text{max}}$  after, the maximum  $\Delta t$  until the next glitch is  $X_{\text{th},\text{max}}$ . As equation (4.13) increases monotonically with  $\Delta t$  for  $\alpha < 1$ , the maximum  $\Delta t$  allowed by equation (4.13) is the most likely waiting time. When plotted on a log-log scale, we see that for  $\alpha \gtrsim 3$ ,  $p(\Delta t)$  is well approximated by a power-law distribution, with a turn-off at  $\Delta t \lesssim 10^{-2}$  (in units of  $X_c I_C / N_{\text{em}}$ ). Where this turn-off occurs depends on both  $\alpha$  and  $X_{\text{th},\text{max}}$ . The slope of the power-law component of  $p(\Delta t)$  is approximately  $-3$  for  $\alpha = 10$  and decreases to  $-4$  for  $\alpha = 50$ . In the intermediate regime  $0.5 \lesssim \alpha \lesssim 3$ ,  $p(\Delta t)$  is approximately uniform.

The size PDFs also display distinctive features in the low- and high- $\alpha$  regimes. For

$\alpha \lesssim 0.5$ ,  $p(\Delta X)$  increases monotonically, with a significant fraction of the probability mass close to  $\Delta X = X_{\text{th},\max}$ . The latter events correspond to the glitches that completely reset the system, if one has  $X \geq X_{\text{th},\max}$  prior to the glitch. On a log-log scale, we see that for  $\alpha \gtrsim 3$ ,  $p(\Delta X)$  can be approximated as a broken power law distribution, with a smooth turn-over at  $\Delta X \approx 10^{-2}$  (in units of  $X_c$ ). The location of this turn-over depends on  $\alpha$  and  $X_{\text{th},\max}$ . The slope of  $p(\Delta X)$  for  $\Delta X \gtrsim 10^{-2}$  is approximately  $-2$  for  $\alpha = 10$ , and decreases to  $-2.5$  for  $\alpha = 50$ . For  $0.5 \lesssim \alpha \lesssim 3$ ,  $p(\Delta X)$  is approximately uniform, with a spike at  $\Delta X = X_{\text{th},\max}$ , again corresponding to glitches that completely reset the system.

In summary, in the low- $\alpha$  regime  $p(\Delta t)$  is bimodal with peaks at  $\Delta t = X_{\text{th},\max}$  and  $\Delta t = 1$ , while  $p(\Delta X)$  is monotonically increasing until  $\Delta X = X_{\text{th},\max}$  where there is a spike in the PDF then a sharp cut-off. In the high- $\alpha$  regime both  $p(\Delta t)$  and  $p(\Delta X)$  are approximately power-law distributed, with low-end turn-offs at  $\Delta t \approx 10^{-2}$  and  $\Delta X \approx 10^{-2}$ .

#### 4.5.2. Cross- and autocorrelations

The time-ordered nature of waiting times and relaxation events invites investigation into what relationships exist between events that happen consecutively. For example, in the SDP meta-model certain combinations of observables, such as the rate of spin-down and average waiting time, predict the cross-correlation between waiting times and the next glitch size [351]. In the SDP and BSA meta-models combinations of cross-correlations and autocorrelations restrict possible values of meta-model control parameters in individual glitching pulsars [1, 2].

Figure 4.8 shows the Spearman correlation coefficients for the forward cross-correlation,  $\rho_+$ , i.e. the correlation between the size of the previous glitch and the next waiting time; the backward cross-correlation,  $\rho_-$ , i.e. the correlation between the size of the glitch and the preceding waiting time; as well as the autocorrelations between consecutive waiting times,  $\rho_{\Delta t}$ , and sizes,  $\rho_{\Delta X}$ . It is clear that  $\rho_+$  is high for all but the smallest values of  $\alpha$ . The longer the waiting time, the larger the upper terminal in equation (4.2), and thus a greater fraction of the vortices unpin. At small values  $\alpha \lesssim 10^{-2}$  most glitches completely reset the system, and the forward cross-correlation is lower. The backward cross-correlation,  $\rho_-$ , is small and negative for  $\alpha \lesssim 0.2$ , but small and positive for  $\alpha \gtrsim 0.2$ . Size autocorrelations,  $\rho_{\Delta X}$ , are negligible for all  $\alpha$ . Waiting time autocorrelations satisfy  $\rho_{\Delta t} \sim -0.5$  for  $\alpha \lesssim 0.1$ , but are negligible for  $\alpha \gtrsim 0.2$ .

The impact of decreasing  $X_{\text{th},\max}$  on Figure 4.8 is minimal; the magnitudes of the Spearman correlation coefficients decrease marginally, and the Spearman correlation coefficients as functions of  $\alpha$  shift towards the right a small amount. As  $X_{\text{th},\max}$  decreases, Figure 4.6 shows that more glitches reset the system, at a fixed value of  $\alpha$ .

#### 4.5.3. Aftershocks and precursors

Aftershocks occur after a large event, when subsequent events are larger and more frequent than usual. They are common in spatially correlated knock-on processes such as avalanches and earthquakes [195, 353, 405]. Naively, one might expect that the endogenous- $\eta$  meta-model should not exhibit aftershocks, as it does not include spatial correlations,

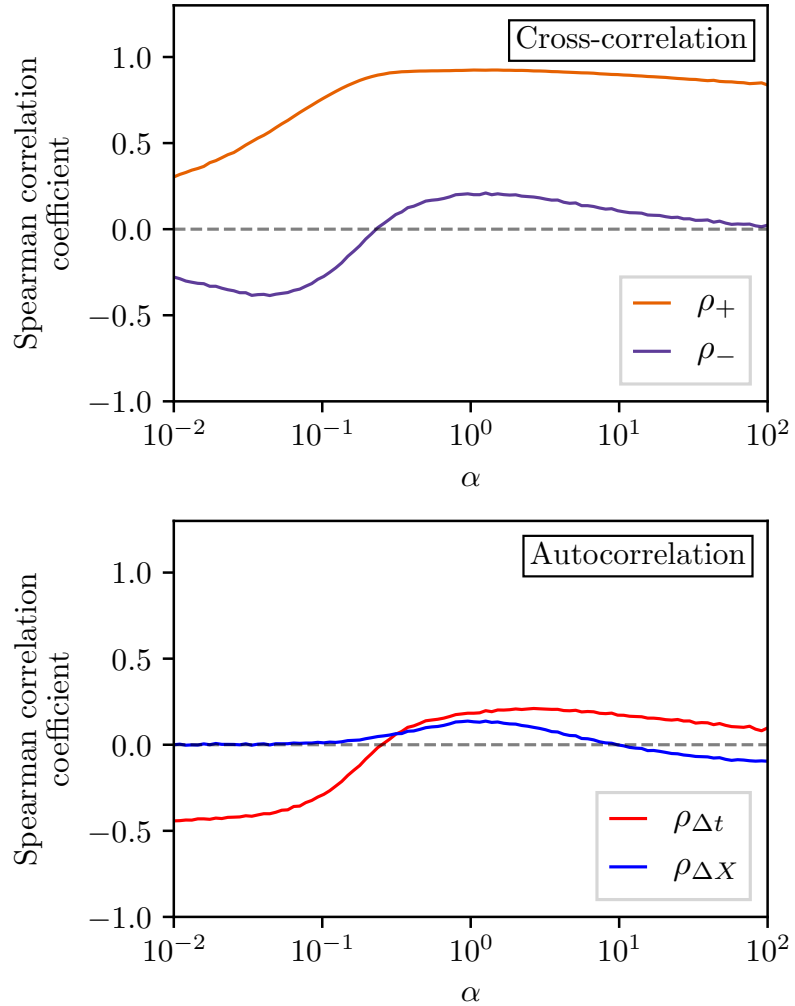


Figure 4.8: Top panel: Forward cross-correlation,  $\rho_+$ , and backward cross-correlation,  $\rho_-$ , as a function of  $\alpha$  (orange and purple curves respectively). Bottom panel: Auto-correlation between waiting times,  $\rho_{\Delta t}$ , and sizes,  $\rho_{\Delta X}$ , as a function of  $\alpha$  (red and blue curves respectively). Parameters:  $N = 10^5$  glitches generated at 100 logarithmically spaced values of  $\alpha$ ,  $X_{\text{th},\max} = 0.95$ ,  $K = X_{\text{th},\max}$ .

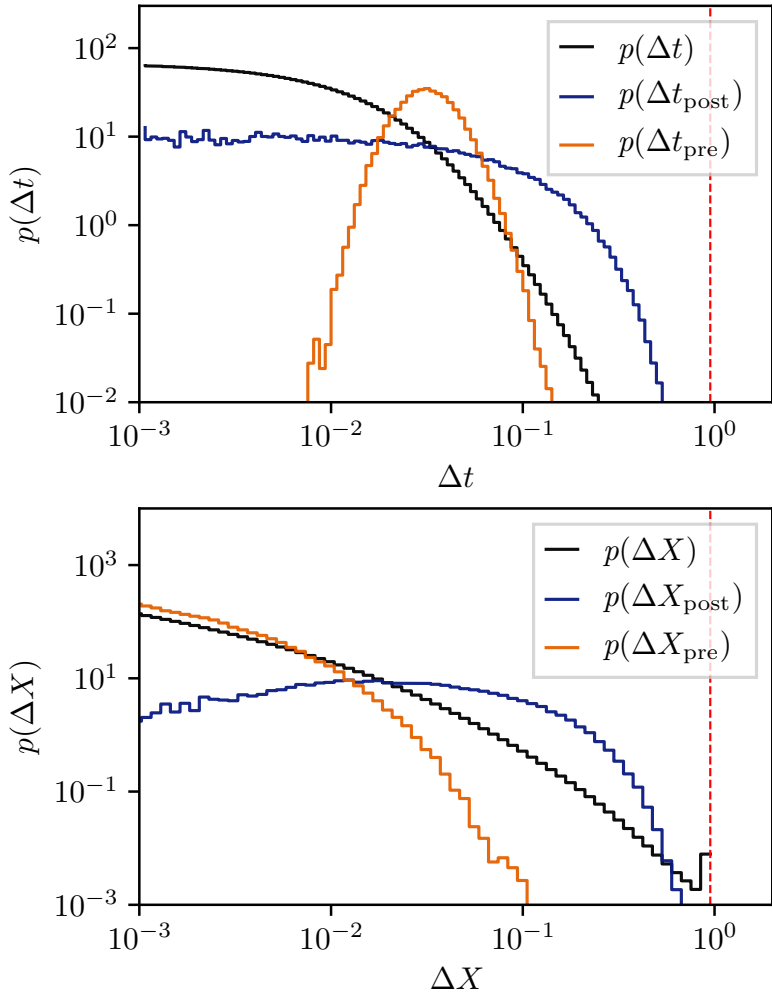


Figure 4.9: Top panel: PDFs of all waiting times,  $\Delta t$ , waiting times just prior to a system-resetting glitch,  $\Delta t_{\text{pre}}$ , and waiting times just after a system-resetting glitch,  $\Delta t_{\text{post}}$ . Bottom panel: Corresponding PDFs for sizes. Parameters:  $\alpha = 10$ ,  $N = 10^8$  total glitches,  $\sim 10^5$  of which reset the system completely,  $X_{\text{th},\text{max}} = 0.95$ ,  $K = X_{\text{th},\text{max}}$ .

due to the assumption that each pinning site experiences the same spatially-averaged stress. Aftershocks are not discussed in the context of the SDP or BSA meta-models, as large events in those meta-models do not correspond to a rearrangement of occupied pinning sites. A large event does not impact the next waiting time or size, beyond reducing the stress in the system.

We investigate whether the above naive expectation holds for the endogenous- $\eta$  meta-model by calculating the conditional waiting time and size PDFs for glitches immediately following a glitch that completely resets the system,  $p(\Delta t_{\text{post}})$  and  $p(\Delta X_{\text{post}})$  respectively. Figure 4.9 shows these PDFs, and the waiting time and size PDFs of events just prior to a glitch that completely resets the system,  $p(\Delta t_{\text{pre}})$  and  $p(\Delta X_{\text{pre}})$  respectively. There is an excess of longer waiting times in  $p(\Delta t_{\text{post}})$  compared to  $p(\Delta t)$ , as the system takes some time to build up stress before another glitch is likely, after such a system-resetting glitch. There is a corresponding excess of larger sizes in  $p(\Delta X_{\text{post}})$  compared to  $p(\Delta X)$ . The precursor waiting times,  $\Delta t_{\text{pre}}$ , are distributed as a log-normal distribution, with  $\langle \Delta t_{\text{pre}} \rangle > \langle \Delta t \rangle$ . There are relatively few small  $\Delta t_{\text{pre}}$  events, because the system-resetting condition  $\Delta X \geq X_{\text{th},\max}$  occurs only if enough stress accumulates before the glitch. There are few large glitches in  $p(\Delta X_{\text{pre}})$  compared to  $p(\Delta X)$ , as large glitches place the system in a configuration which is unlikely to fully reset at the next glitch, as  $X$  is low.

The behavior of aftershocks and precursors in Figure 4.9 is replicated qualitatively for other values of  $\alpha \neq 10$  and  $X_{\text{th},\max} \neq 0.95$ . That is, there is always an excess of longer waiting times, and larger glitches, following a system-resetting glitch, while the precursor waiting times are longer than average. For  $\alpha \lesssim 0.2$  these features in the PDFs are less prominent, as the system resets after almost every event.

## 4.6. ASTRONOMICAL OBSERVATIONS

How do the long-term statistical predictions in Section 4.5 compare to what we currently see in glitching pulsars? This question has been answered previously in the context of the SDP [1, 15, 351], and BSA [2] meta-models. For the five pulsars with the most recorded glitches, there are regimes of parameter space in the SDP meta-model which adequately explain observations. For example, PSR J0537–6910 is consistent with the SDP meta-model if  $\alpha \lesssim 0.1$  [1]. However this is not the case for the BSA meta-model, for which two pulsars, namely PSR J0534+2200 and PSR J1341–6220, are consistent with the meta-model only if there exists an undetected population of frequent small glitches.

The endogenous- $\eta$  meta-model presented here is falsifiable using the same approach: the meta-model must predict simultaneously, with one set of input parameters, the long-term  $p(\Delta t)$ ,  $p(\Delta X)$ , cross-correlations, and autocorrelations, otherwise it is rejected. In principle we have one additional potential observable in this meta-model, the aftershocks and precursors discussed in Section 4.5.3. However, due to the small number of glitches recorded in individual pulsars ( $N < 50$ ), it is not yet clear whether we have witnessed any large, system-resetting glitches in astronomical data, and so we cannot compare to the aftershock or precursor predictions of Section 4.5.3.

Current observations of glitch waiting time and size distributions [18, 19] do not show clear signs of a sharp cut-off at the upper end, as the meta-model predicts in Figure 4.7 for  $\alpha \lesssim 5$ . For  $\alpha \gtrsim 5$ , where the distributions are steeper, the sharp cut-off may have

escaped detection until now due to the paucity of recorded glitches. Even so, if most glitching pulsars fall in the  $\alpha \gtrsim 5$  regime we should expect to see significant forward cross-correlations,  $\rho_+ \gtrsim 0.8$ , in more pulsars, as seen in Figure 4.8. Yet only two pulsars, PSR J0537–6910 and PSR J1341–6220 have  $\rho_+$  significantly different from zero, at 95% confidence. Neither of these objects favor a power-law glitch size distribution, as the model predicts for  $\alpha \gtrsim 5$ . We therefore conclude provisionally that the endogenous- $\eta$  meta-model is incompatible with existing pulsar observations, although more data are needed to be confident of course. This is an important result, because the endogenous- $\eta$  meta-model codifies the traditional, popular understanding in the literature regarding how vortex pinning and unpinning occurs stochastically, as explained in Sections 4.2–4.4.

Model parameters such as  $\alpha$ , the dimensionless control parameter that determines the speed at which stress accumulates, and  $K$ , the coupling constant between changes in stress and the observable change in frequency, may be partially informed by independent (i.e. non-glitch) observations of pulsars. As discussed in Section 3 of Melatos et al. [351], and Section 5 of Carlin and Melatos [2], we have

$$\alpha \approx \frac{X_c}{\langle \Delta t \rangle \dot{\nu}}, \quad (4.14)$$

up to a factor of order unity, where  $\langle \Delta t \rangle$  is the mean waiting time between glitches, and  $\dot{\nu}$  is the long-term spin-down rate of the pulsar, after correcting for glitches and timing noise. The critical stress at which a glitch becomes certain,  $X_c$ , depends on the equation of state and is unknown in general [162, 164]. Nevertheless, the denominator in Equation (4.14) varies between pulsars by many orders of magnitude; see Table 2 of Melatos et al. [351], for example. The coupling constant  $K$  has even more uncertainties surrounding it, as described in Section 4.3.3. If a linear coupling between the crust and the stress is assumed at a glitch, we recover Equation (4.5), however non-linear couplings are also plausible, and may easily change the dependence of  $K$  on observables [194, 381, 400]. A preliminary exploration of how  $K$  impacts the endogenous- $\eta$  meta-model is presented in Appendix 4.A1.

Direct comparisons of the meta-model predictions to long-term statistics derived from glitch catalogues are predicated on the assumption that all glitches are detected, i.e. that the datasets are complete. Espinoza et al. [98] and Espinoza et al. [99] claimed that this assumption is true for PSR J0534+2200 and PSR0835–4510 respectively. Monte Carlo injection studies have been published which seek to quantify completeness, but they are hampered by human intervention in traditional glitch finding algorithms [134, 135]. Autonomous glitch finding algorithms, such as those based on hidden Markov models [62] and nested sampling [77, 95, 97], will probe this question quantitatively for more pulsars, especially as more pulsars are regularly timed.

## 4.7. CONCLUSION

The long-term predictions from meta-models of stress-relax processes are avenues to falsify otherwise plausible microphysical mechanisms that the meta-model encompasses. The SDP meta-model [16] encompasses mechanisms wherein glitches are triggered probabilistically, and are more likely to occur when the system-wide stress is higher. The

falsifiable predictions such as size and waiting-time cross-correlations [351], and auto-correlations [1], depend on the functional form of the conditional avalanche size PDF,  $\eta[\Delta X^{(n)}|X(t_n)]$  [15]. Previously, this PDF was fixed exogenously to be a power law [16, 351, 370], motivated by Gross-Pitaevskii simulations of vortex avalanches [173], and the sizes of stress-release avalanches in other self-organized critical systems [195]. However, when  $\eta[\Delta X^{(n)}|X(t_n^-)]$  is a power law, the SDP meta-model does not explain the quasiperiodic waiting times and unimodal size PDF seen in some pulsars [18]. This is ameliorated by adjusting “by hand”  $\eta[\Delta X^{(n)}|X(t_n^-)]$  to a unimodal distribution, whereupon the SDP meta-model remains consistent with the data [15].

In this paper, we generalize the SDP meta-model so that  $\eta[\Delta X^{(n)}|X(t_n^-)]$  is generated endogenously via the coherent stress mechanism [193, 204]. The coherent stress mechanism encapsulates the traditional understanding of how superfluid vortex pinning and unpinning proceeds stochastically in a neutron star. The memory of previous glitches is imprinted on the PDF of occupied pinning sites,  $g(X_{\text{th}}, t)$ , which we emphasize does not equal the distribution of available sites  $\phi(X_{\text{th}})$  in general. Vortices pinned at sites with thresholds below the stress at a glitch unpin when a glitch is triggered, repinning at sites with thresholds above the stress after the glitch. The size of the glitch is proportional to the fraction of vortices unpinned in this manner.

The endogenous- $\eta$  meta-model produces a broad phenomenology of observable waiting time and size PDFs, conditional on the choice of control parameters. In all circumstance, though, it produces high forward cross-correlations between glitch sizes and subsequent waiting times ( $\rho_+ \gtrsim 0.8$ ), which are largely absent from observational data. It also predicts that either i) the system stagnates, for  $X_{\text{th}, \max} \geq X_c$ , or ii) there is an excess of the largest waiting times and sizes, corresponding to events which completely reset the system by unpinning all vortices. Associated with these system-resetting events are aftershocks, which are larger and occur later than an average glitch, and precursors, which are smaller than an average glitch. There is no evidence for such large, system-resetting events in the size or waiting time PDFs of any glitching pulsar. We therefore conclude provisionally that the endogenous- $\eta$  version of the SDP meta-model is falsified by existing data, although more data are needed to be sure.

The provisional falsification of the endogenous- $\eta$  version of the SDP meta-model is important. The coherent stress process is not just any process; it embodies the traditional understanding of how vortex pinning and unpinning works throughout the literature [150]. Moreover it is intriguing that the version of the SDP meta-model in which  $\eta[\Delta X^{(n)}|X(t_n^-)]$  is specified exogenously is not falsified by existing pulsar data. What are we to make of this situation? Is it a hint that some microphysics other than superfluid vortex avalanches is at work? Is the success (at escaping falsification) of the SDP meta-model with exogenous  $\eta[\Delta X^{(n)}|X(t_n^-)]$  thanks simply to the flexibility it affords, when choosing  $\eta[\Delta X^{(n)}|X(t_n^-)]$  selectively to suit every individual pulsar? It is too early to say. The endogenous- $\eta$  meta-model is still an idealized, phenomenological representation of what happens inside a pulsar during a superfluid vortex avalanche. For example, recent  $N$ -body point-vortex simulations of collective, glitch-like vortex motion indicates that the stress is spatially correlated [137]. Spatial correlations are notoriously hard to treat theoretically, but it is known that they can alter the observable statistics of a far-from-equilibrium system comprehensively, e.g. in self-organized critical systems [195, 380]. Larger and more complete glitch catalogs generated by the latest generation of glitch

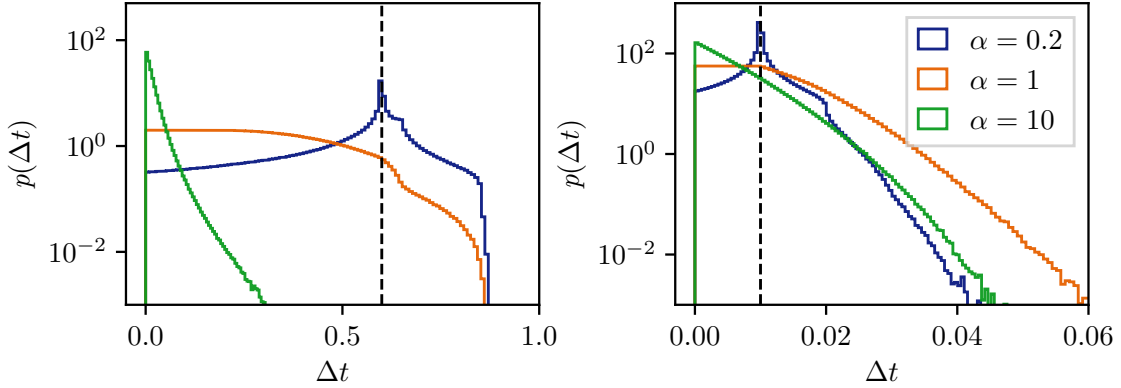


Figure 4.10: Waiting time PDFs for  $K = 0.6$  (left panel) and  $K = 0.01$  (right panel). Parameters:  $N = 10^7$  simulated glitches for each value of  $\alpha$ , with  $X_{\text{th},\text{max}} = 0.95$ . The black dashed vertical line indicates  $\Delta t = K$  in each panel.

monitoring campaigns at radio wavelengths are likely to play a central role in resolving some of the physical puzzles above [97, 406].

## ACKNOWLEDGEMENTS

Parts of this research are supported by the Australian Research Council (ARC) Centre of Excellence for Gravitational Wave Discovery (OzGrav) (project number CE170100004) and ARC Discovery Project DP170103625. JBC is supported by an Australian Postgraduate Award.

### 4.A1. NON-MAXIMAL STRESS-CRUST COUPLING

The coupling factor  $K$  defined in equation (4.3) and appearing in equations (4.4) and (4.5) relates changes in the stress variable  $X$  to the angular velocity  $2\pi\nu$  of the crust. The long-term observables in Section 4 are predicted assuming  $K$  takes its maximum value,  $X_{\text{th},\text{max}}$ . Somewhat counter-intuitively, the long-term statistics do change — modestly, but meaningfully — when non-maximal coupling is considered.

One always has  $K \leq X_{\text{th},\text{max}}$  to ensure  $X(t) \geq 0$ . In Section 4.3.3, we specialize to  $K = X_{\text{th},\text{max}}$  for the sake of definiteness. In this appendix we briefly check the case  $K < X_{\text{th},\text{max}}$ . Figure 4.10 shows the PDF of waiting times,  $p(\Delta t)$ , for two representative values of  $K < X_{\text{th},\text{max}} = 0.95$ . For  $K = 0.6$ ,  $p(\Delta t)$  looks broadly similar to the top panel of Figure 4.7 ( $K = X_{\text{th},\text{max}}$ ), except for  $\alpha = 0.2$ , which no longer has a peak at  $\Delta t = 1$ . Long waiting times are suppressed as  $K$  sets the maximum event size in equation (4.4). Smaller  $K$  increases the minimum stress in the system, as less stress is released at the largest glitches (i.e. when  $F = 1$ ). For  $K = 0.01$  and  $\alpha \gtrsim 1$ ,  $p(\Delta t)$  is exponentially distributed. For  $\alpha \lesssim 1$ ,  $p(\Delta t)$  is peaked around  $\Delta t = K$ , but has an exponential tail. The size PDFs,  $p(\Delta X)$ , are broadly the same shape as in the bottom panel of Figure 4.7 ( $K = X_{\text{th},\text{max}}$ ), but for  $K < X_{\text{th},\text{max}}$  and  $\alpha \lesssim 1$  they are more strongly peaked around  $\Delta X = K$ , and for  $\alpha \gtrsim 1$  they are power-law distributed over many decades, with a small peak at  $\Delta X = K$ .

In summary, if  $K < X_{\text{th}, \max}$ , in the high- $\alpha$  regime  $p(\Delta t)$  is exponentially distributed and  $p(\Delta X)$  is power-law distributed, while in the low- $\alpha$  regime  $p(\Delta t)$  is unimodal around a peak at  $\Delta t = K$  and  $p(\Delta X)$  is sharply peaked at  $\Delta X = K$ .

The behavior of the cross-correlations and autocorrelations as a function of  $\alpha$  does not change for  $K < X_{\text{th}, \max}$  compared to  $K = X_{\text{th}, \max}$ , beyond shifting the features seen in Figure 4.8 to the right, e.g. for  $K = 0.1$  the peak in  $\rho_+$  occurs at  $\alpha \approx 10$  instead of  $\alpha \approx 0.5$ . Reducing  $K$  has a similar impact as reducing  $X_{\text{th}, \max}$  on the fraction of events that completely reset the system, as shown in Figure 4.6. At a fixed  $\alpha$ , reducing  $K$  reduces the amount of stress released. Hence we reach  $X \geq X_{\text{th}, \max}$  more often by the time the next glitch is triggered.

#### 4.A2. ENSEMBLE-AVERAGED STRESS THRESHOLD DISTRIBUTION AT OCCUPIED PINNING SITES

The PDF  $g(X_{\text{th}}, t)$  is a stochastically fluctuating function, dependent on the random sequence of waiting times drawn up to time  $t$ , as described in Section 4.3.4. A stationary analogue,  $g_s(X_{\text{th}})$ , would allow for a priori prediction of long-term statistics that do not depend on the exact time-ordered nature of events, such as  $p(\Delta t)$  and  $p(\Delta X)$  [193, 204].

Following the notation in Daly and Porporato [207] and Fulgenzi et al. [16],  $p(\Delta t)$  and  $p(\Delta X)$  are related to the PDFs  $p_e(Y)dY$  and  $p_s(X)dX$ , the probabilities that the stress is in  $(Y, Y + dY)$  just before a glitch and in  $(X, X + dX)$  just after a glitch respectively. With these definitions we obtain

$$p(\Delta t) = \int_0^{1-\Delta t} dY p_s(Y) \lambda(Y + \Delta t) \exp[-\Lambda(Y + \Delta t) \Lambda(Y)], \quad (4.15)$$

and

$$p(\Delta X) = \int_{\Delta X}^1 dY p_e(Y) \eta(\Delta X | Y), \quad (4.16)$$

with  $\Lambda(x) = \int_0^x dx' \lambda(x')$ , and  $\Delta X = Y - X$ . In the endogenous- $\eta$  meta-model  $\eta(\Delta X | Y)$ , is a deterministic function of the occupied pinning site PDF,  $g(X_{\text{th}})$ , as discussed in Section 4.3.3. The relationship becomes probabilistic again, as in the SDP meta-model, if we consider the statistically stationary PDF,  $g_s(X_{\text{th}}) = \langle g(X_{\text{th}}, t) \rangle$ , where the brackets indicate an ensemble average. The PDF  $g_s(X_{\text{th}})$  is related to  $\eta(\Delta X | Y)$  via

$$\eta(\Delta X | Y) = K \int_0^{p_e(Y)} dX_{\text{th}} g_s(X_{\text{th}}). \quad (4.17)$$

Solving equations (4.15)–(4.17) analytically for  $g_s(X_{\text{th}})$  is outside the scope of this paper. Instead, we show an estimate of  $g_s(X_{\text{th}})$  at three values of  $\alpha$  in Figure 4.11, calculated by running the automaton outlined in Section 4.4.2 and sampling  $g(X_{\text{th}}, t)$  after every glitch. As expected,  $g_s(X_{\text{th}})$  is a strictly increasing function of  $X_{\text{th}}$ , i.e. sites with a higher threshold are occupied more often than those with a lower threshold. For  $\alpha \lesssim 1$ ,  $g_s(X_{\text{th}})$  is well approximated by a power law with upper and lower cut-offs, i.e.  $g_s(X_{\text{th}}) \propto X_{\text{th}}^\gamma H(X_{\text{th}})H(X_{\text{th}, \max} - X_{\text{th}})$ , with  $0 < \gamma \lesssim 3$ , and  $\gamma$  growing with  $\alpha$ .

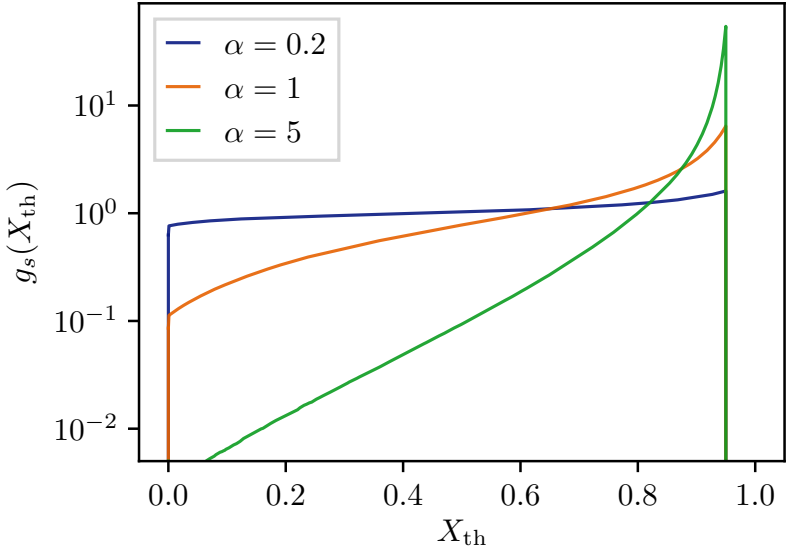


Figure 4.11: Ensemble averaged PDF of occupied pinning sites  $g_s(X_{\text{th}}) = \langle g(X_{\text{th}}, t) \rangle$  calculated empirically for three values of  $\alpha$ . Parameters:  $10^7$  samples of  $g(X_{\text{th}})$  for each value of  $\alpha$ ,  $X_{\text{th}, \max} = 0.95$ , with  $K = X_{\text{th}, \max}$ .

#### 4.A3. RELATION TO POINT PROCESSES AND TIME SERIES MODELING

The endogenous- $\eta$  meta-model in this paper and its exogenous- $\eta$  alternatives, such as the SDP [16] and BSA [2] meta-models, are examples of stochastic time series with jumps. We observe the jumps as a point process. In this appendix, we situate the endogenous- $\eta$  meta-model within canonical classification schemes for such processes. The classification schemes are not unique.

The SDP meta-model is an example of a doubly stochastic, marked point process [16, 407, 408]. It is a one-dimensional point process because it is a sequence of instantaneous events ordered in time. Marked refers to additional information (i.e. the event size) that is associated with the epoch of each event. It is doubly stochastic as both the event sizes and the waiting times between events are random processes. The endogenous- $\eta$  meta-model is not doubly stochastic, as the event sizes are deterministic, after the waiting time is chosen (given a certain history of past avalanches), as described in Section 4.3. For both the SDP and endogenous- $\eta$  meta-models, the state of the system jumps discontinuously at each event making them examples of a jump process. The SDP meta-model is Markovian, the current state only depends on the immediately previous state. However the endogenous- $\eta$  meta-model is not, as the threshold distribution of occupied pinning sites contains a long-lasting memory of states before the one immediately previous.

The analysis of point processes from a statistical perspective is often presented alongside time series modeling [409, 410]. Autoregressive models, such as the autoregressive integrated moving average (ARIMA) model, can be used to model a wide variety of astronomical time series data [411]. Adopting the formalism of autoregressive models unlocks a large, well-tested literature for common tasks such as maximum likelihood parameter estimation, model comparison, and model validation [410]. Recent advances

in filters for hidden semi-Markov models are another intriguing avenue, as these models are explicitly designed to track a process that jumps between states at irregularly spaced intervals [412].

In this paper and others investigating glitch meta-models, we elect not to analyze the problem in terms of autoregressive models for three reasons. i) Glitch sample sizes are small ( $N \lesssim 50$ ), so there is no practical imperative to exploit the computational efficiency offered by autoregressive models. ii) We are motivated by the astrophysical goal of exploring the long-term statistical behavior of an automaton which formalizes directly the popular intuitive picture of glitches as a stick-slip, stress-relax phenomenon. It is possible in principle to formulate the stress-relax dynamics less directly in the language of an autoregressive model, and we leave that for future work. iii) Some work has been done on parameter estimation by Markov chain Monte Carlo methods for the SDP meta-model [370]. Extending this work to other meta-models or larger data sets may benefit from the computational efficiency of autoregressive modeling, but is outside the scope of this work.

# CHAPTER 5

---

## A statistical search for a uniform trigger threshold in solar flares from individual active regions

---

This chapter is a reproduction of [4]

*J. B. Carlin, A. Melatos, and M. S. Wheatland*

The Astrophysical Journal, 948, 2 (2023)

reformatted with the following changes only:

- The erratum published as *J. B. Carlin, A. Melatos, and M. S. Wheatland*, The Astrophysical Journal, 953, 1 (2023) [5] is incorporated into the text, correcting the errors in the original published paper.
- Footnote 3 in Section 5.5.1 is included in response to a suggestion of the thesis examiner.
- The text is styled to match the rest of this thesis.
- Where necessary, bibliographic records are updated.

### 5.1. ABSTRACT

Solar flares result from the sudden release of energy deposited by sub-photospheric motions into the magnetic field of the corona. The deposited energy accumulates secularly between events. One may interpret the observed event statistics as resulting from a state-dependent Poisson process, in which the instantaneous flare rate is a function of the stress in the system, and a flare becomes certain as the stress approaches a threshold set by the micro-physics of the flare trigger. If the system is driven fast, and if the threshold is static and uniform globally, a cross-correlation is predicted between the size of a flare and the forward waiting time to the next flare. This cross-correlation is broadly absent from the *Geostationary Operational Environmental Satellite* (GOES) soft X-ray flare database. One also predicts higher cross-correlations in active regions where the shapes of the waiting time and size distributions match. Again there is no evidence for such an association in the GOES data. The data imply at least one of the following: i) the threshold at which a flare is triggered varies in time; ii) the rate at which energy is driven into active regions varies in time; iii) historical flare catalogs are incomplete;

or iv) the description of solar flares as resulting from a build-up and release of energy, once a threshold is reached, is incomplete.

## 5.2. INTRODUCTION

Broad consensus exists that the micro-physical process triggering individual solar flares is magnetic reconnection in the corona. A reconnection event becomes more likely to occur the more magnetic energy accumulates in the time between flares [209, 413]. This phenomenological class of stress–relax model was popularized by Rosner and Vaiana [221], and expounded by Wheatland and Glukhov [222], Wheatland [223, 224], Kanazir and Wheatland [225], and Hudson [226], among others. A complementary phenomenological description is the avalanche or self-organized criticality model [227, 228, 414], inspired by the canonical sandpiles of Bak et al. [197, 198]. These two classes of model are broadly compatible, but make different predictions about some long-term statistical observables [202, 223, 229, 415–417].

Upon aggregating historical datasets, the probability density function (PDF) of the energy released in solar flares is found to be a power law or log-normal over multiple decades [221, 227, 418]. The PDF of time intervals between successive flares in the same active region, henceforth termed waiting times, is less clear-cut. Wheatland [419] found evidence that the power-law-like shape of the tail of the waiting time PDF found by Boffetta et al. [415] is explained by a sum of exponentials, with individual rates themselves drawn from an exponential PDF. This interpretation is further developed by Aschwanden et al. [420]. Flaring rates that vary in time are also noted by Lepreti et al. [421] and Gorobets and Messerotti [422]. Cross-correlations between the size of a flare and the subsequent (preceding) waiting time, henceforth termed forward (backward) cross-correlations, are a key differentiator between the stress–relax and avalanche descriptions – the latter predicts no size–waiting-time cross-correlations [195]. Forward and backward correlations are broadly absent from solar flares datasets [223, 423–426], with the exception of strong forward cross-correlations found in two active regions [226].

Rotational glitches in rotation-powered pulsars [30, 150] are an astrophysical phenomenon analogous to solar flares, in the limited sense that they are consistent with a stress–relax process even though they do not involve magnetic reconnection as far as is currently known [380]. While the exact process that triggers a glitch is unknown, most models are encompassed by the fundamental idea that “stress” (possibly differential rotation or elastic deformation) builds up secularly between glitches and is released sporadically and partially at a glitch. The instantaneous glitch rate is assumed to grow with the stress in the system. This idea is formalized phenomenologically in the state-dependent Poisson (SDP) process popularized by Fulgenzi et al. [16]. Precise, falsifiable predictions about size and waiting time PDFs, auto-, and cross-correlations, as well as comparisons to current datasets, show the power and flexibility of the SDP model in the neutron star context [1, 15, 351, 370]. The same falsifiable predictions also deliver new physical insights when applied to solar flare data, as we show in this paper.

Our goal in this paper is to search the *Geostationary Operational Environmental Satellite* (GOES) soft X-ray flare database for signatures of a threshold-driven stress–relax process. We do this by de-aggregating the data from different active regions and studying summary statistics of flare waiting times and sizes. In Section 5.3 we outline the SDP

framework and how it maps to solar flares. In Section 5.4 we explore various regimes of the SDP process. We also specify precise, falsifiable tests for the question of whether solar flares are triggered once the energy reaches a static threshold, if it obeys a stress-relax process. The *GOES* soft X-ray dataset to which we apply these tests is described in Section 5.5. In Section 5.6 we look for associations between matching waiting time and size PDFs and high size-waiting-time cross-correlations, as predicted for the SDP process. We conclude with a discussion of the microphysical implications of the data analysis in Section 5.7.

### 5.3. STATE-DEPENDENT POISSON PROCESS

#### 5.3.1. *Equation of motion*

The SDP process is a doubly stochastic renewal process which models the “stress” in the system as a function of time,  $X(t)$ , as

$$X(t) = X(0) + t - \sum_{i=0}^{N(t)} \Delta X_i, \quad (5.1)$$

where  $X$  and  $t$  are expressed respectively in dimensionless units of  $X_c$  (the critical stress in the system at which a stress-release event becomes certain) and  $\tau$  (the time taken for the system to accumulate the critical stress  $X_c$ , in the absence of any stress-release events). We attach a physical interpretation to  $X(t)$ , in the solar flare context, in Section 5.3.3 and Appendix 5.A1. The amount of stress released at the  $i$ -th event,  $\Delta X_i$ , is a random variable, drawn from a user-specified PDF,  $\eta[\Delta X_i | X(t_i^-)]$ , where  $X(t_i^-)$  is the stress in the system immediately prior to the  $i$ -th event. In the standard configuration,  $\eta[\Delta X_i | X(t_i^-)]$  is fixed as a power law, but other options exist [3, 15]. Making  $\eta$  conditional on  $X(t_i^-)$  is necessary in order to ensure that the stress remains positive-definite and is plausible physically. The second random variable in Equation (5.1) is  $N(t)$ , a stochastic function which counts the number of events up to time  $t$ . It is determined iteratively via the waiting time between each event.

We assume the instantaneous event rate is a monotonically increasing function of the stress in the system, viz.

$$\lambda[X(t)] = \frac{\alpha}{1 - X(t)}, \quad (5.2)$$

where  $\alpha = \lambda_0 \tau$  is a dimensionless control parameter and  $\lambda_0 = \lambda(X = 1/2)/2$  is a reference rate. The long-term statistical output of the SDP process does not depend strongly on the functional form of  $\lambda[X(t)]$ , so long as it diverges in the limit  $X \rightarrow 1$  as in Equation (5.2) [15, 16]. Equation (5.2) implies that the probability of an event occurring approaches one as the stress approaches the critical stress. As the stress increases deterministically between events, the PDF of waiting times  $\Delta t$  following the  $i$ -th event is that of a variable-rate Poisson process [16, 235],

$$p[\Delta t | X(t_i^+)] = \lambda[X(t_i^+) + \Delta t] \exp\left\{-\int_{t_i^+}^{t_i^+ + \Delta t} dt' \lambda[X(t')]\right\}, \quad (5.3)$$

where  $X(t_i^+)$  is the stress immediately following the event at time  $t_i$ .

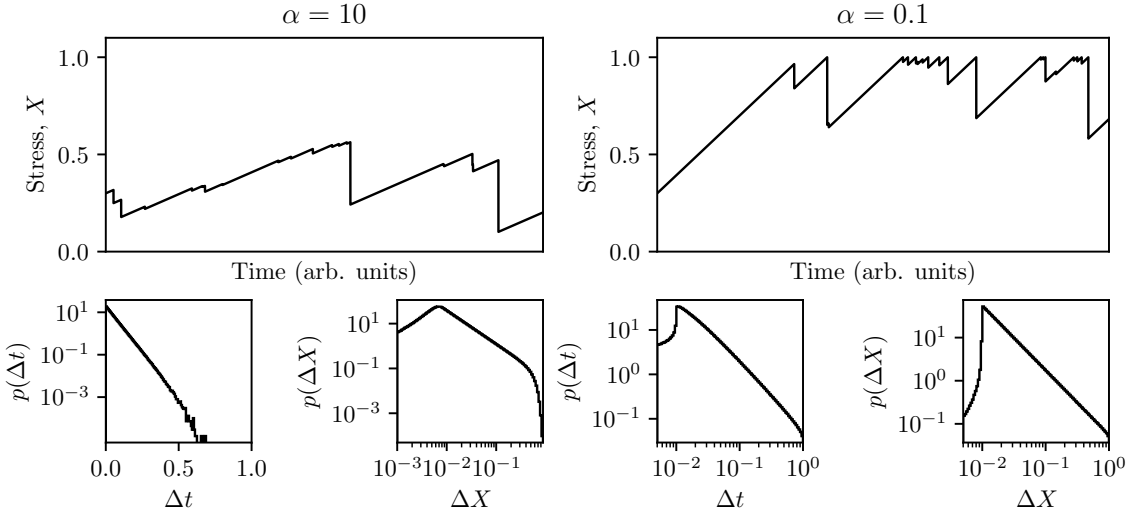


Figure 5.1: Top panels: qualitative behavior of the evolution of the stress,  $X(t)$ , in the SDP process in the two main regimes, slowly driven (left panel,  $\alpha = 10$ ), and rapidly driven (right panel,  $\alpha = 0.1$ ). Bottom panels: predicted waiting time and size PDFs  $p(\Delta t)$  and  $p(\Delta X)$  respectively in the above regimes. For all panels we fix  $\eta[\Delta X_i | X(t_i^-)] \propto (\Delta X_i)^{-3/2} H[\Delta X_i - 10^{-2} X(t_i^-)]$ , where the Heaviside function  $H(...)$  enforces a minimum stress-release size of 1% of the stress in the system, ensuring integrability. The histograms in the bottom panels each include  $N = 10^7$  events.

### 5.3.2. Monte Carlo automaton

Analytically solving the coupled equations (5.1)–(5.3) to calculate the PDFs of event waiting times or sizes is usually not feasible, except for particular choices of  $\eta[\Delta X_i | X(t_i^-)]$ ; see section 6 of Fulgenzi et al. [16] for an example. Instead, it is simple to run the following automaton to generate numerical solutions:

- i) Pick  $\Delta t$  from Equation (5.3), given the current stress  $X$ .
- ii) Update the stress to  $X + \Delta t$  to account for the deterministic evolution.
- iii) Pick  $\Delta X$  from  $\eta[\Delta X | X + \Delta t]$ , and subtract it from the stress.
- iv) Repeat from step 1.

Given  $\alpha$  and  $\eta[\Delta X_i | X(t_i^-)]$  the automaton generates a time-ordered sequence of waiting times and sizes. From the sequence we can calculate the long-term PDFs for waiting times and sizes [15, 16], as well as the cross-correlation [15, 351], autocorrelations [1], and other observables.

### 5.3.3. Mapping to solar flares

We identify the stress that accumulates between flares and relaxes at a flare with the spatially-averaged magnetic energy density in a given active region. One could equally choose a different physical quantity, such as the magnetic shear, depending on the particular microphysics of the flare trigger. We assume that active regions have independent

stress reservoirs, i.e. the coronal magnetic fields of different active regions do not interact strongly, and all flares from the same active region extract energy from one reservoir. An idealized toy model relating the foregoing definition of stress to magnetic energy input from the photosphere is outlined in Appendix 5.A1, as a simplified but concrete illustration of the physical picture under consideration.

Two major simplifying assumptions are that the rate at which energy is fed into the reservoir,  $\tau^{-1}$ , is constant in time, and so is the critical, spatially-averaged magnetic energy density,  $X_c$ , for a given active region. These assumptions are motivated in Appendix 5.A1, but a key goal of the paper is to test their veracity. We also assume that flares reduce  $X(t)$  instantaneously. This assumption is defensible, as the typical time between flares (typically hours) is much larger than the typical duration of flaring events (typically minutes) [208]. In what follows, we do not prescribe a particular functional form for  $\eta[\Delta X_i | X(t_i^-)]$ , to keep the SDP process as flexible as possible.

The SDP process generates sequences of dimensionless waiting times  $\{\Delta t_i^{\text{SDP}}\}$  and sizes  $\{\Delta X_i^{\text{SDP}}\}$ . It is natural to ask how they correspond to directly observable sequences of waiting times  $\{\Delta t_i^{\text{obs}}\}$  and sizes  $\{\Delta s_i\}$ . The waiting times satisfy

$$\Delta t_i^{\text{obs}} = \Delta t_i^{\text{SDP}} \tau, \quad (5.4)$$

where  $\tau$  is unknown a priori but can be estimated as discussed in Appendix 5.A2. The sizes are related in a more complicated way, because some energy is released through channels other than the soft X-ray flux. We make the simplifying assumption that the peak soft X-ray flux multiplied by the duration of the flare (henceforth  $\Delta s_i$  for the  $i$ -th flare in a given active region) is proportional to the stress released from the reservoir. This implies

$$\Delta s_i \propto \Delta X_i^{\text{SDP}} X_c. \quad (5.5)$$

The unknown constant of proportionality in Equation (5.5) hampers direct parameter estimation of  $X_c$  from an observed size PDF.

Full parameter estimation for the SDP process given a set of observed waiting times and sizes is discussed in Melatos and Drummond [370]. It lies outside the scope of this paper. For completeness, in Appendix 5.A2 we also describe an alternative parameter estimation procedure using a hierarchical Bayesian scheme. The advantage of the hierarchical scheme is that it clarifies, as a matter of principle, the information content and flow in the estimation problem, i.e. the parameter combinations that can be estimated uniquely, and the data components that inform each parameter estimate. The disadvantage is that it can be implemented in practice only if  $\eta[\Delta X_i | X(t_i^-)]$  is drawn from a certain class of mathematical functions. The favored class produces waiting time and size PDFs which do not match solar flare observations (see Section 5.6), so the hierarchical scheme is not applied to real data in this paper. Nonetheless, it is included for the benefit of the reader, who may wish to develop it further for solar flare analysis in the future.

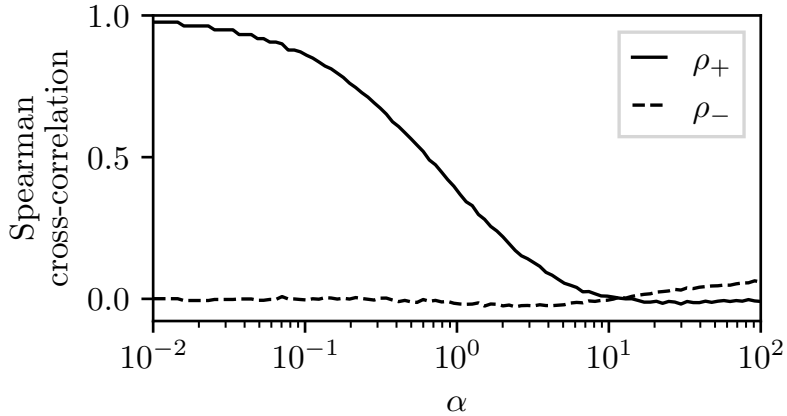


Figure 5.2: Forward,  $\rho_+$  (solid curve), and backward,  $\rho_-$  (dashed curve), cross-correlations between event sizes and waiting times for  $10^2$  values of  $10^{-2} \leq \alpha \leq 10^2$ , with  $N = 10^5$  events generated per value of  $\alpha$ . We fix  $\eta[\Delta X_i | X(t_i^-)]$  to the same functional form as in Figure 5.1. A version of this figure first appeared as figure 13 in Fulgenzi et al. [16].

## 5.4. OBSERVABLE SIGNATURES OF A RAPIDLY-DRIVEN PROCESS

Broadly speaking, an SDP process operates in one of two regimes: slowly-driven, with  $\alpha \gg 1$ , and rapidly-driven, with  $\alpha \ll 1$ . In this section we identify the key dynamics in both regimes, in Sections 5.4.1 and 5.4.2 respectively. We then infer, in Section 5.4.3, a set of observable signatures, which if absent rule out the operation of a rapidly-driven process of the form described in Section 5.4.2.

### 5.4.1. Slow driver

When the system is slowly driven, we have  $X(t) \ll 1$ , as events are usually triggered before the stress accumulates to near the threshold. When  $\eta[\Delta X_i | X(t_i^-)]$  is a power law, the predicted waiting time PDF  $p(\Delta t)$  is an exponential, and the predicted size PDF  $p(\Delta X)$  is a power law over multiple decades. We show the qualitative behavior of the stress in the slowly driven regime in the top-left panel of Figure 5.1, where for the sequence of 20 stress-release events shown we have  $0.1 < X(t) < 0.6$ . In the bottom-left panels of the same figure we show the predicted waiting time and size PDFs. The size PDF  $p(\Delta X)$  has a turn-over in logarithmic slope at  $\Delta X \approx 10^{-2}$  due to the particular choice of  $\eta[\Delta X_i | X(t_i^-)]$  (see caption for the functional form).

Depending on the choice of  $\eta[\Delta X_i | X(t_i^-)]$ , there may be detectable backward cross-correlations (i.e. a correlation between the size of an event and the waiting time since the preceding event). This is because the size of an event cannot exceed the amount of stress in the system, so longer periods of stress-accumulation allow for the possibility of larger events. This backward cross-correlation is especially pronounced with the choice  $\eta[\Delta X_i | X(t_i^-)] \propto \delta[\Delta X - X(t_i^-)]$ , where  $\delta(\dots)$  is the Dirac-delta function. This choice forces the stress reservoir to empty at each event, and collapses the SDP process to other stochastic processes in the literature, e.g. forest fire models [206]. In the solar

flare context, a backward cross-correlation is a long-standing prediction of the Rosner and Vaiana [221] stress build-up model; as well as the “reset” model of Hudson [226] and Hudson et al. [424]. If instead  $\eta[\Delta X_i | X(t_i^-)]$  prefers small stress-release events, e.g. if it is a power law [16], the backward cross-correlation is small.

#### 5.4.2. Fast driver

When the system is rapidly driven, we have  $X(t_i^-) \lesssim 1$ , i.e. the stress is driven close to the threshold before each event. As the dynamics of the system are strongly influenced by the presence of the threshold, we sometimes call this regime “threshold-driven”. A prediction of the SDP process in this regime is that the size and waiting time PDFs should “match”, i.e. they should be the same distribution, up to a linear scaling [16]. For example, if  $\eta[\Delta X_i | X(t_i^-)]$  is a power law, both the waiting time and size PDFs are power laws. We show this in the bottom-right panels of Figure 5.1. We also show the qualitative behavior of the stress versus time in this regime in the top-right panel of the same figure, where we see  $X(t) \rightarrow 1$  (i.e. unit critical stress) before every stress-release event.

A strong forward cross-correlation (i.e. a correlation between the size of an event and the waiting time to the next event) is observed in this regime. This is because a large stress-release event results in a longer delay before the system accumulates enough stress to approach the threshold. In the solar flare context, this cross-correlation is predicted by the “saturation” model of Hudson et al. [424] and Hudson [226]. The smooth transition between the fast-driven regime ( $\alpha \ll 1$ ), with high forward cross-correlations, and the slow-driven regime ( $\alpha \gg 1$ ), is shown in Figure 5.2.

#### 5.4.3. Heuristic test for a threshold-driven process

Ideally, we fit the parameters of the SDP process ( $\tau$ ,  $X_c$ ,  $\lambda_0$ , and  $\eta[\Delta X_i | X(t_i^-)]$ ) to a paired sequence of solar flare sizes and waiting times, and infer what regime applies. In practice, however, at least some of these parameters vary between active regions, which limits us to sequences of length  $N \lesssim 50$  (typical active regions have at most dozens of events; see Section 5.5), which are insufficient to infer four or more parameters. Instead, we combine the results in Sections 5.4.1 and 5.4.2 to deduce qualitative features, which must be present in multiple observables simultaneously (e.g. PDFs, cross-correlations), if the SDP process operates in a particular  $\alpha$  regime or indeed operates at all. Specifically, we summarize the behavior in Sections 5.4.1 and 5.4.2 into the following observationally testable prediction. If solar flares are well-modeled with a rapidly-driven process (e.g. the SDP process with  $\alpha \ll 1$ ), then we should see large forward cross-correlations, accompanied by waiting time and size PDFs with the same shape in individual active regions. This coincident signature should become more prominent as  $\alpha$  (or a proxy thereof) decreases. We quantify this prediction in Section 5.6.2.

With the test above we also ameliorate the impact of a potentially mis-specified model. Although it is agnostic about the microphysics, the SDP process is not the only possible prescription of stress accumulation and release. If some of the assumptions outlined in Section 5.3.3 do not hold, a different underlying model may underpin solar flares. For example, one may build a model in which stress accumulates according to a Brownian random walk with some underlying drift, until a threshold is breached, at

which point a stress-release event is triggered [2]. In the Brownian stress accumulation model,  $X(t)$  is always driven to the threshold before each event. If drift occurs faster than diffusion, we would predict the same coincident signature as for the SDP process: large forward cross-correlations are accompanied by matching waiting time and size PDFs.

## 5.5. GOES SOFT X-RAY OBSERVATIONS

The X-ray Sensor (XRS) on the *Geostationary Operational Environmental Satellites* (GOES) has continuously monitored the Sun in soft X-rays (0.5 to 8 Å) since 1975. In Section 5.5.1 we introduce the flare summary data analyzed in this paper. In Section 5.5.2 we remind the reader of the obscuration effect described in Wheatland [427], explain how it affects our analysis, and briefly touch on other biases the GOES flare detection algorithm may have on the completeness of the catalog as a whole. In Section 5.5.3 we analyze aggregated waiting time and size PDFs across all active regions.

### 5.5.1. Flare data

We use the publicly available flare summary data hosted by the National Geophysical Data Center (NGDC)<sup>1</sup> for flares before 2015 June 29, and by the Space Weather Prediction Center (SWPC)<sup>2</sup> for flares after 2015 June 28. We combine these two data sources into a homogeneous, cleaned database (henceforth “catalog”), with some anomalies corrected as described in Appendix 5.A3. These data are collated with the flare start epochs,  $t^s$ , peak epochs,  $t^p$ , and end epochs,  $t^e$ . The peak epoch is defined as the epoch which contains the highest peak flux, after the start epoch. The end epoch is defined as the epoch at which the flux returns to half of the difference between the peak flux and the background flux. The peak flux (irradiance) of each flare,  $f^p$ , is calculated with reference to the recorded flare class, in units of  $\text{W m}^{-2}$ . The longitude and latitude of the flare are also often available, if the flare is associated with an active region. For clarity, we henceforth denote as  $x_{i,k}$  an arbitrary measurement of the variable  $x$  in the  $i$ -th flare from the  $k$ -th active region.

We define the waiting time between two flare epochs as  $\Delta t_{i,k} = t_{i+1,k}^p - t_{i,k}^p$ . One could equally use the flare start or end epochs to define the waiting time. We use the flare peak epoch because it is less influenced by the background level, as discussed further in Section 5.5.2. We define the flare size as  $\Delta s_{i,k} = f_{i,k}^p (t_{i,k}^e - t_{i,k}^s)$ ; that is, we multiply the irradiance by the duration of the flare to obtain a flare size with dimensions of energy per unit area. The duration of an active region is  $\Delta T_k = t_{N_k,k}^e - t_{1,k}^s$ , where there are  $N_k$  flares in the region. The average flare rate in an active region is  $\lambda_k = N_k / \Delta T_k$ . The average  $\lambda_k$  systematically overestimates the true flare rate, as the duration  $\Delta T_k$  is between two flare epochs, both of which are counted in  $N_k$ <sup>3</sup>. An unbiased estimate would take  $\Delta T_k$  as the difference between the epochs when the active region appears and disappears,

---

<sup>1</sup><ftp://ftp.ngdc.noaa.gov/STP/space-weather/solar-data/solar-features/solar-flares/x-rays/GOES/xrs/>

<sup>2</sup><ftp://ftp.swpc.noaa.gov/pub/indices/events/>

<sup>3</sup>The true rate likely lies between  $N_k / \Delta T_k$  and  $(N_k + 1) / \Delta T_k$ . None of the analysis in this work depends on the accuracy of  $\lambda_k$ .

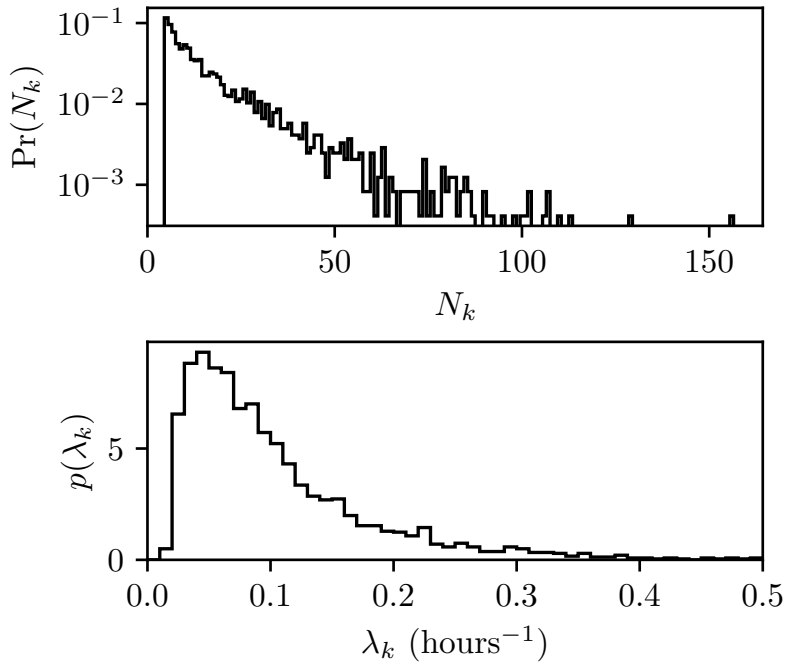


Figure 5.3: Top panel: Probability mass function of the number of flares per active region,  $N_k$ , for all active regions with  $N_k \geq 5$ . Regions with  $0 \leq N_k \leq 4$  are excluded, as the number of samples per region is too small for the statistical tests in this paper. Bottom panel: PDF of the flare rate,  $\lambda_k$ , for all active regions with  $N_k \geq 5$ , binned into 50 uniformly spaced bins between  $0 \text{ hours}^{-1}$  and  $0.5 \text{ hours}^{-1}$ .

but neither epoch is recorded in the GOES flare summary data<sup>4</sup>. A concern we touch on further in Section 5.5.3 is that  $\lambda_k = N_k/\Delta T_k$  assumes that the flare catalog is complete, i.e. all flares from a given region are detected and correctly attributed to that region.

As of 2022 September 1, there are 83283 flares in the catalog, 49328 of which are associated with an active region. There are 2429 active regions with  $N_k \geq 5$ , accounting for 42982 flares. The median number of flares in an active region (when considering only regions with  $N_k \geq 5$ ) is 12, but the average is 17.7, as the distribution is peaked at  $N_k = 5$  and monotonically decreases with  $N_k$ . We show the probability mass function of the number of flares in an active region,  $\Pr(N_k)$ , in the top panel of Figure 5.3 for regions with  $N_k \geq 5$ . The PDF of observed flare rates,  $p(\lambda_k)$ , across all active regions with  $N_k \geq 5$ , is displayed in the bottom panel of the same figure. The distribution of  $\lambda_k$  is well-described by a log-normal, with mean  $0.08 \text{ hours}^{-1}$ , and standard deviation  $0.7 \text{ hours}^{-1}$ . Henceforth, we typically only include regions with  $N_k \geq 5$  in our analysis unless stated otherwise, as many of the subsequent statistical tests, such as the cross-correlation(s), have low statistical power with smaller sample sizes.

### 5.5.2. Obscuration and flare size bias of subsequent flares after a large flare

As described in section 2.2 of Wheatland [427], the GOES flare detection algorithm involves a selection effect that obscures the detection of flares following a large flare, due to

---

<sup>4</sup>The epochs when the active region appears and disappears may be extracted from other records in some instances. Such an analysis lies outside the scope of this paper.

the enhanced background soft X-ray flux. To detect a flare, the flux must monotonically increase for four consecutive minutes, with the last value being 1.4 times the value from three minutes earlier. Hence, a flare must produce a 40% increase above the background flux. However, while flares typically rise rapidly to peak flux, the soft X-ray emission is observed to decay on a timescale of hours [209]. Thus, even large flares may be obscured by the enhanced background flux following, say, an X1 ( $f^P = 10^{-4} \text{ W m}^{-2}$ ) class flare.

The above detection algorithm introduces a secondary bias in the catalog. A flare, say with recorded peak flux  $f_i^P$ , that occurs during the decay of another flare, say with recorded peak flux  $f_{i-1}^P$ , has an enhanced peak flux compared to if the same flare occurs during a period of low background flux, viz.

$$f_i^P \approx f_{i,\text{true}}^P + f_{i-1}^P \exp\left(\frac{-\Delta t_{i-1}}{\tau}\right), \quad (5.6)$$

where  $\tau$  is the timescale on which the peak flux from the  $(i-1)$ -th flare decays, and  $f_{i,\text{true}}^P$  is the “true” peak flux of the  $i$ -th flare. A secondary effect is that the duration of the  $i$ -th flare will have a reduced duration due to the decaying contribution of the previous flare to the background flux. That is, during the  $i$ -th flare, the background flux decays by a factor of  $\exp[-(t_i^e - t_i^s)/\tau]$ , which reduces the time taken for the flux to decay back to half the difference between the peak and pre-flare fluxes. These two effects run counter to one another, as  $\Delta s_i$  is defined as the product of peak flux and duration. They are likely present in a small subset of the catalog, as only 1.2% of all flares from regions with  $N_k \geq 5$  have start times before the end time of the previous flare.

A comprehensive re-analysis of the soft X-ray flux time-series, with appropriate background subtraction, may reveal flares that were not detected with the original flare detection algorithm and correct the biases in flare size outlined above. Such a re-analysis lies outside the scope of this paper. Acknowledging that the GOES catalog is incomplete, we mitigate the impact on our analysis by creating a secondary masked catalog that only includes flares with  $\Delta s \geq 10^{-3} \text{ J m}^{-2}$  (i.e. class C1 multiplied by the median duration of  $10^3$  s, and higher), where we know the fraction of missed flares is smaller. This masked catalog is used in Sections 5.5.3 and 5.6.1 when we perform comparative studies and parametric fits for the waiting time and size PDFs.

### 5.5.3. Aggregate size and waiting time statistics

When we aggregate flare waiting times and sizes across all active regions with  $N_k \geq 5$ , we obtain the PDFs shown in the top and bottom panels of Figure 5.4 respectively. The data are shown as the black histograms. The grey region in the bottom panel shows the flare sizes that are not included in the masked catalog, as described in Section 5.5.2. The difference between the masked and full catalog is not visible in the top panel as the effect on  $p(\Delta t)$  is minimal.

Three empirical trial distributions with common analytic forms are overlaid on each PDF for the masked catalog. The overlaid distributions have parameters fixed to their maximum likelihood values, given the data. By eye, it is clear that the log-normal distribution best describes the aggregated waiting time PDF<sup>5</sup>,  $p(\Delta t)$ , while a power law dis-

---

<sup>5</sup>Waiting times that are best described with a log-normal are seen in many contexts. We provide a brief survey in Appendix 5.A4 for the interested reader.

tribution best describes the aggregated size PDF,  $p(\Delta s)$ . We formalize this comparison using the corrected Akaike Information Criterion (AICc) [144, 145]. The AICc calculates the model, among a set of possible models, which minimizes the information loss, while accounting for potential bias due to the number of model parameters and the sample size. When calculated for  $p(\Delta t)$ , the relative probability for a log-normal describing the data over an exponential or a power law is  $e^{3 \times 10^3}$  or  $e^{3 \times 10^4}$  respectively. When calculated for  $p(\Delta s)$ , the relative probability for a power law describing the data over an exponential or a log-normal is  $e^{3 \times 10^4}$  or  $e^{4 \times 10^3}$  respectively. If we instead only mask flares with peak flux less than  $10^{-6} \text{ W m}^{-2}$  (i.e. class C1), we find that a log-normal best describes the data. This preference is also noted in Verbeeck et al. [418]. It arises because of the small number of flares in this alternatively-masked catalog with  $10^{-4} < \Delta s / \text{J m}^{-2} \lesssim 10^{-3}$ . If we fit the full, unmasked catalog (i.e. include the flares shaded in grey in the bottom panel of Figure 5.4) we find that  $p(\Delta s)$  is again fitted best with a log-normal. We remind the reader that  $p(\Delta s)$  is an observed distribution; it is a function of both the underlying generative physics (i.e. how much energy is released in each flare) and the systematic observational biases (i.e. how many and what flares are detected or not). The masking described in Section 5.5.2 is a first pass at accounting for some of these biases.

If we assume that the same  $\alpha$  and  $\eta[\Delta X_i | X(t_i^-)]$  apply to all regions, Figure 5.4 is inconsistent with the SDP framework for any choice of  $\alpha$  and  $\eta[\Delta X_i | X(t_i^-)]$ . However, as we discuss in Section 5.3.3, there is good reason to believe that  $\alpha$  (and perhaps even  $\eta[\Delta X_i | X(t_i^-)]$ ) may vary region-to-region.

## 5.6. DISAGGREGATED DATA IN INDIVIDUAL ACTIVE REGIONS

The goal of this section is to search for signatures of a threshold-driven SDP process in individual active regions, rather than considering all flares in aggregate. In Section 5.6.1 we consider only waiting time and size PDFs, without regard to their potential cross-correlation. In Section 5.6.2 we calculate these cross-correlations, and in Section 5.6.3 we apply the test outlined in Section 5.4.3 by searching for an association between matching waiting time and size PDFs and the cross-correlation, in individual active regions. In Section 5.6.4 we perform a preliminary investigation of the longer-term memory in the system by calculating the autocorrelation between subsequent waiting times and subsequent sizes. The analysis in Section 5.6.1 involves parametric fitting of the size PDFs, so we use the masked catalog described in Section 5.5.2. However in Sections 5.6.2–5.6.4 we use the full, unmasked catalog, as the tests performed in these sections are non-parametric.

### 5.6.1. Waiting time and size PDFs versus flare rate

For regions with  $N_k \geq 5$  we disaggregate the data, and ask what PDF shape best characterizes each region's waiting time and size PDFs, rather than considering only the aggregated dataset as in Section 5.5.3. Using the AICc, we find that for waiting time PDFs, 63% of regions are fitted best with an exponential distribution, 20% with a log-normal, and the remainder with a power law. For size PDFs, 63% of regions are fitted best with a power law distribution, 24% with an exponential, and the remainder with a

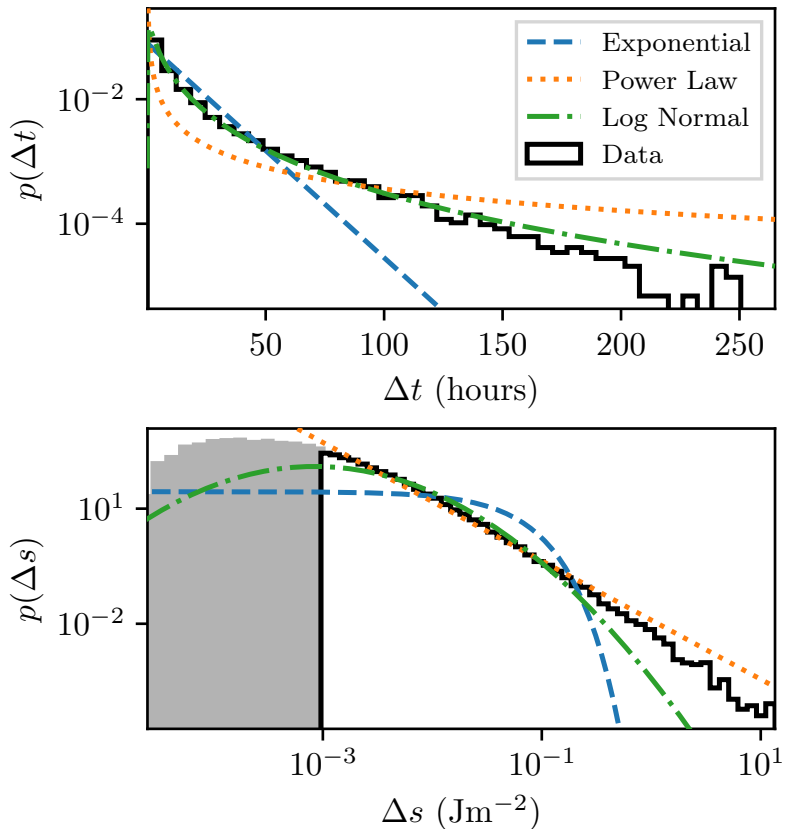


Figure 5.4: Top panel: PDF  $p(\Delta t)$  of waiting times (thick black stepped curve),  $\Delta t$ , aggregated over all active regions with  $N_k \geq 5$ , binned into 50 linearly spaced bins between the minimum and maximum  $\Delta t$  in the full, unmasked catalog. Overlaid are the best fit estimates of an exponential (blue dashed curve), power law (orange dotted curve), and log-normal (green dot-dashed curve) PDF. Bottom panel: As for top panel, but for sizes  $\Delta s$ , and the data is binned into 50 logarithmically spaced bins. The grey region in the bottom panel shows the difference between the size PDFs from the masked and full catalogs (see Section 5.5.2).

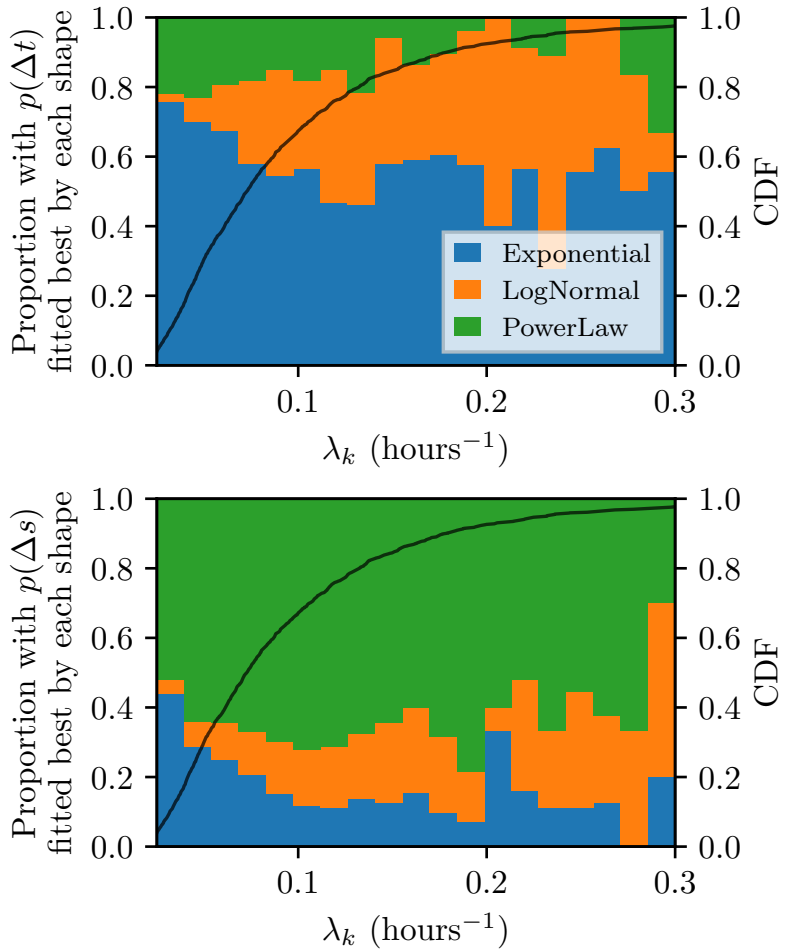


Figure 5.5: Top panel: Proportion of active regions with waiting time PDF fitted best by three possible shapes (a power law, an exponential, and a log-normal) as determined by the AICc, as a function of the region’s flare rate,  $\lambda_k$ . The CDF of  $\lambda_k$  is overlaid in black. Bottom panel: As in the top panel, but for size PDFs.

log-normal. These proportions are broadly consistent with previously published results, i.e. that while the aggregated  $p(\Delta t)$  is fitted best with a log-normal, individual regions are often fitted best with an exponential (with varying rates) [419]. Individual regions have  $p(\Delta s)$  that is usually fitted best with a power law, but can occasionally be better represented with log-normal or exponential distributions, especially in regions with lower  $N_k$ . As an example of the different shapes that distributions of waiting times and sizes can have in different regions, we display four arbitrary but representative per-active-region fits in Appendix 5.A5.

One may reasonably ask whether there are clear trends, or predictors, for the waiting time and size PDFs in any given region. An exhaustive search for predictors, e.g. with a multiple regression analysis, lies outside the scope of this paper, but one sensible first step is to see if the shape that fits best evolves with  $\lambda_k$ . This test is performed for the waiting time and size PDFs in the top and bottom panels of Figure 5.5 respectively. This figure is constructed by binning all active regions with  $N_k \geq 5$  into 20 uniformly spaced bins between  $\lambda_k = 0.025$  hours $^{-1}$  and  $\lambda_k = 0.3$  hours $^{-1}$ , then calculating which distri-

bution fits best the waiting times and sizes using the AICc. For the waiting time PDFs, the proportion of regions fitted best with a power law stays roughly constant as  $\lambda_k$  increases, at around 15%, while the proportion of regions fitted best with a log-normal grows with  $\lambda_k$ , at the expense of the exponential. For the size PDFs we see a similar trend, with the proportion of regions fitted best with a power law staying roughly constant as  $\lambda_k$  increases, this time at around 65%, while the proportion of regions fitted best with a log-normal grows with  $\lambda_k$ , at the expense of the exponential. In both panels we plot the cumulative distribution function (CDF) of  $\lambda_k$  to remind the reader that each  $\lambda_k$  bin does not contain the same number of regions; 90% of regions with  $N_k \geq 5$  have  $0.028 < \lambda_k / (1 \text{ hour}^{-1}) < 0.27$ .

Can the evolution of the proportion of each shape versus  $\lambda_k$  be explained with the SDP model? Under the assumption that  $\lambda_k$  is a tracer of the driving rate, i.e.,  $\lambda_k \propto \alpha + \alpha_0$  (assuming  $\tau$  does not vary region-to-region), we expect to see a greater proportion of exponentially distributed waiting times at high  $\lambda_k$  (high  $\alpha$ ). This is the regime in which the stress does not approach the threshold at  $X = X_c$  before each event, so waiting times are uncorrelated with sizes and are (broadly) Poissonian, i.e., the waiting times are exponentially distributed. Figure 5.5 shows the proportion of active regions with exponentially distributed waiting times slightly decreases with increasing  $\lambda_k$ , contrary to the SDP prediction.

The evolution versus  $\lambda_k$  in the bottom panel of Figure 5.5 is harder to explain with the SDP model, if each region has the same  $\eta[\Delta X_i | X(t_i^-)]$ . We expect  $p(\Delta s) \propto \eta$ , when  $\alpha$  is low, but we see multiple shapes represented at the lowest values of  $\lambda_k$ . This implies at least one of the following: i)  $\eta$  truly varies from one region to the next, which implies different stress-release mechanisms are at play in different regions; or ii)  $\lambda_k \lesssim 0.3 \text{ hr}^{-1}$  does not correspond to  $\alpha \ll 1$ , and hence  $p(\Delta s)$  need not have the same shape as  $\eta$ ; or iii) the small sample size of events in each region results in the AICc not favoring the “true” size distribution; or iv) the obscuration effects described in Section 5.5.2 is stronger with higher  $\lambda_k$ , due to the enhanced background flux in regions that have many flares in a short period of time. To test iii), we generate Figure 5.5 again for regions with  $N_k \geq 10$ , instead of  $N_k \geq 5$ . For both the waiting times and sizes, the proportion fitted best by an exponential drops by  $\sim 10\%$  in each  $\lambda_k$  bin, while the proportion fitted best by a log-normal increases. Qualitatively, however, the evolution with  $\lambda_k$  remains consistent with what is seen in Figure 5.5.

### 5.6.2. Size–waiting-time cross-correlations

The correlation between flare sizes and subsequent waiting times, i.e. the “forward” cross-correlation, is denoted as  $\rho_{+,k}$ , while the correlation between flare sizes and the preceding waiting times, i.e. the “backward” cross-correlation, is denoted as  $\rho_{-,k}$ . We calculate these correlations using the Spearman correlation coefficient [362].

The PDFs of forward and backward cross-correlations measured in all active regions with  $N_k \geq 5$  are displayed in the top panel of Figure 5.6. The PDFs are broad, mostly because the median  $N_k$  is 12 (i.e. small). However,  $p(\rho_{+,k})$  and  $p(\rho_{-,k})$  are different; the latter has a median of  $\rho_{-,k} = 0.0$ , while the former has a median of  $\rho_{+,k} = 0.08$ . A Kolmogorov-Smirnov (KS) two-sample test provides quantitative evidence of the difference, returning a  $p$ -value of  $10^{-14}$ .

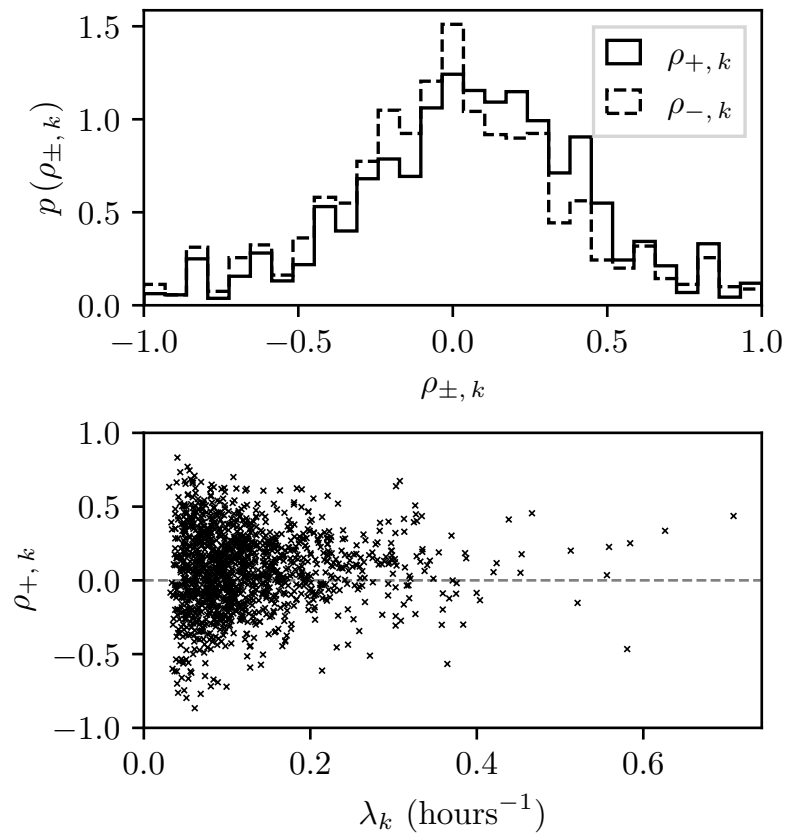


Figure 5.6: Top panel: PDF of forward cross-correlation,  $\rho_{+, k}$  (black stepped curve), and backward cross-correlation,  $\rho_{-, k}$  (black dashed curve), for all active regions with  $N_k \geq 5$ . Data binned into 30 uniformly spaced bins between  $\rho_{\pm, k} = -1$  and  $\rho_{\pm, k} = 1$ . Bottom panel: Scatter plot of the forward cross-correlation,  $\rho_{+, k}$ , and flare rate,  $\lambda_k$ , for all regions with  $N_k \geq 10$ . The dashed grey line corresponds to  $\rho_{+, k} = 0$ .

The SDP process predicts a high forward cross-correlation for  $\alpha \ll 1$ , as discussed in Section 5.4.2. The data do not show evidence in favor of such a correlation in the majority of active regions. In the bottom panel of Figure 5.6 we do not see a clear visual trend between  $\rho_{+,k}$  and  $\lambda_k$  (for regions with  $N_k \geq 10$ ), although a Spearman correlation test returns a small but non-zero correlation of  $5 \times 10^{-2}$  ( $p$ -value of 0.06). We remind the reader that both  $\rho_{+,k}$  and  $\lambda_k$  are empirical estimates for each active region, and the number of events per region is small. We do not plot uncertainties in the bottom panel of Figure 5.6, but they are typically large, of order the magnitude of the central estimate. These results imply that either i) all active regions have  $\alpha \gtrsim 1$ , where no forward cross-correlation is expected, i.e.  $\lambda_k \lesssim 0.3 \text{ hr}^{-1}$  does not correspond to the threshold-limited regime; or ii) some active regions have  $\alpha \ll 1$ , but either the trigger threshold or the driving rate is not constant with time, i.e. the random process triggering flares does not conform to the assumptions made in the SDP framework.

As described in Section 5.5.2 the *GOES* catalog is not complete, i.e. while a given active region is visible, not all flares that occur are recorded. Wheatland [223] noted that the obscuration in Section 5.5.2 creates an artificial forward cross-correlation, which explains why the median  $\rho_{+,k}$  is positive.

### 5.6.3. Matching the shapes of $p(\Delta t)$ and $p(\Delta s)$

Another way to probe these data is to ask whether regions with relatively high  $\rho_{+,k}$  exhibit “matching” functional forms for  $p(\Delta t)$  and  $p(\Delta s)$ , as the SDP model predicts for  $\alpha \lesssim 1$ . We quantify the degree to which the PDFs match via the  $p$ -value  $\mathcal{M}_k$  of the KS two-sample test applied to the sampled PDFs,  $\{\Delta t_{i,k}\}$  and  $\{\Delta s_{i,k}\}$ . To calibrate, we perform a Monte Carlo simulation using sequences of events drawn from the SDP model. For each value of  $\alpha$  we simulate  $10^5$  “regions”. For each region we generate  $M$  events, where  $M$  is a random number drawn from  $p(N_k)$ , restricted to values  $N_k \geq 10$ , as empirically measured for the *GOES* regions (the distribution for  $N_k \geq 5$  shown in Figure 5.3). From these  $M$  events we calculate summary statistics, e.g.  $\mathcal{M}$  and  $\rho_+$ . This results in  $10^5$  pairs of  $(\mathcal{M}, \rho_+)$ , from which we construct a two-dimensional kernel density estimate (KDE) [428]. The KDE estimates the true joint PDF  $p(\mathcal{M}, \rho_+)$ , and is qualitatively equivalent to a smoothed, two-dimensional histogram.

The result of this procedure for four values of  $\alpha$  is shown in the top panel of Figure 5.7a. For  $\alpha = 0.01$  (dark orange lines) the 10% and 50% credible interval contours are invisible in the top-right corner of the panel, as the vast majority of simulated regions have  $\rho_+ \approx 1$  and  $\mathcal{M} \approx 1$ . For  $\alpha = 0.1$  the KDE spreads out slightly, with the 50% credible interval reaching  $\rho_+ \approx 0.8$  and  $\mathcal{M} \approx 0.9$ . For  $\alpha = 1$ , the PDF shifts such that the 50% credible interval contour stretches from  $\mathcal{M} = 1$  to  $\mathcal{M} \approx 0.8$ , while we have  $0 \lesssim \rho_+ \lesssim 0.8$ . For  $\alpha = 10$  we find  $\rho_+$  centered around zero, while the 50% credible interval of  $\mathcal{M}$  extends to  $\mathcal{M} \approx 0.3$ . The bottom panel of Figure 5.7a repeats the exercise for the backward cross-correlation. It confirms that  $\rho_-$  and  $\mathcal{M}$  are uncorrelated, as predicted elsewhere [1, 15, 16]. Integrating over  $\rho_\pm$  the reader would find that the marginal distribution of  $\mathcal{M}$  is broad in both panels, for  $\alpha \gtrsim 1$ , as it is difficult to confidently reject the null hypothesis that two sets of samples are from the same distribution, when dealing with small sample sizes.

Monte Carlo calibration in hand, we present the equivalent data for all regions in

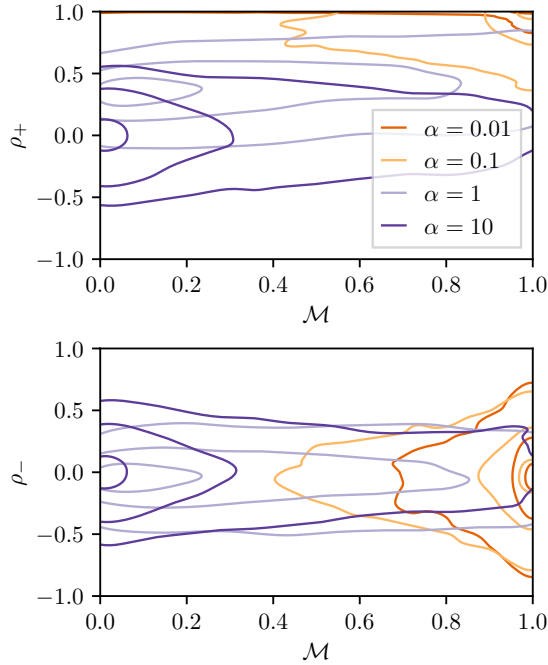


Figure 5.7a: Calibrating the cross-correlation test in Section 5.6.3: two-dimensional KDEs of the relationship between  $\rho_+$  and  $M$  (top panel), and  $\rho_-$  and  $M$  (bottom panel), for events simulated from the SDP model with four values of  $\alpha$  (see legend for color code). The text in Section 5.6.3 reports details about the Monte Carlo procedure. Contours correspond to the 10%, 50%, and 90% credible intervals.

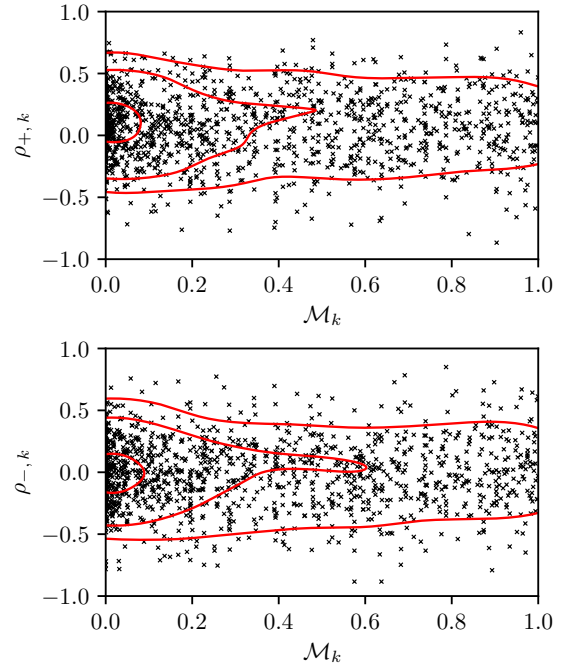


Figure 5.7b: As for Figure 5.7a but for GOES data with black crosses marking all regions in the full, unmasked GOES catalog with  $N_k \geq 10$ . Red contours correspond to the 10%, 50%, and 90% credible intervals inferred from the black crosses.

the GOES catalog with  $N_k \geq 10$  in Figure 5.7b. To compute  $\mathcal{M}_k$  for each region we first normalize both the waiting times and the sizes by their respective means for that region, before applying the KS two-sample test. In the top (bottom) panel we see no clear relationship between  $\rho_{+,k}$  ( $\rho_{-,k}$ ) and  $\mathcal{M}_k$ . Marginalizing over  $\mathcal{M}_k$  we recover the PDFs of  $\rho_{+,k}$  and  $\rho_{-,k}$ , shown in the top panel of Figure 5.6. If, for the sake of argument, we assume that all regions have the same value of  $\alpha$ , we can compare the KDEs in Figure 5.7b to those in Figure 5.7a. Under this assumption we are pushed into the regime  $1 \lesssim \alpha \lesssim 10$ , as the  $p(\rho_{+,k}, \mathcal{M}_k)$  KDE is slightly off-set from the horizontal axis (i.e. median  $\rho_{+,k} > 0$ ), but the 50% credible interval for  $\mathcal{M}_k$  only extends to  $\mathcal{M}_k \lesssim 0.6$ . Even if  $\alpha$  is not exactly the same in each region, we can interpret the above result as ruling out that a large proportion of regions have  $\alpha \lesssim 1$ , as if that were the case we would see higher values of  $\mathcal{M}_k$  associated with higher  $\rho_{+,k}$  more often than in Figure 5.7b.

#### 5.6.4. Autocorrelations and longer term memory

While there is a wealth of information available in flare waiting time and size PDFs, as in Section 5.6.1, and cross-correlations, as in Sections 5.6.2 and 5.6.3, one may also consider statistics that quantify the longer term memory of the stress in the system. For example, as in the context of neutron star glitches [1], studying the autocorrelation between consecutive waiting times,  $\rho_{\Delta t}$ , or between consecutive sizes,  $\rho_{\Delta s}$ , allows one to place constraints on applicable SDP model parameters. In the fast-driven regime,  $\alpha \ll 1$ , we predict  $\rho_{\Delta t} = 0$  and  $\rho_{\Delta s} = 0$ , as we have  $X(t) \rightarrow X_c$  before every stress-release event resulting in the system resetting at every event. If we have  $\eta[\Delta X_i | X(t_i^-)] \propto \delta[X(t_i^-)]$ , i.e. all stress in the system is released at each event, the same prediction of no autocorrelations holds — again the system is reset at every event. Observations of non-zero autocorrelations therefore rule out certain regimes in the SDP framework.

When we calculate  $\rho_{\Delta t,k}$  and  $\rho_{\Delta s,k}$  for all regions in the GOES catalog with  $N_k \geq 10$ , we find that the PDFs  $p(\rho_{\Delta t,k})$  and  $p(\rho_{\Delta s,k})$  are broad, akin to  $p(\rho_{+,k})$  shown in Figure 5.6. The medians are 0.11 and 0.10 respectively. This result is incongruent with the assumption  $\alpha \ll 1$  in all regions, as  $\alpha \ll 1$  implies both PDFs should have a median of zero. These results likely stem from the obscuration effects described in Section 5.5.2. One tentative physical interpretation of a positive  $\rho_{\Delta t}$  and  $\rho_{\Delta s}$  is via analogy to terrestrial earthquakes which exhibit aftershocks, i.e. large events are often followed by larger-than-average events, with smaller-than-average waiting times [353].

## 5.7. CONCLUSION

In this paper, we revisit the long-standing question of whether solar flares in different active regions are triggered by a stress–relax process with a trigger threshold which is constant in time. We do so by mapping the flaring process to a SDP process, which operates independently in each active region. The SDP framework has been applied in related contexts to forest fires [206] and solar flares [224], before being extended in the context of neutron star glitches [1, 15, 16, 351]. If one assumes a constant driving rate, and a constant “stress” threshold at which relaxation events are guaranteed to occur, the model makes precise, falsifiable predictions regarding the statistics of sequences of

waiting times and sizes, such as their PDFs, and cross-correlations. It is agnostic about the underlying microphysical mechanism.

Analyzing the historical *GOES* soft X-ray flare catalog, using data from 1975 until 2022, we systematically search all active regions for signatures that flares are consistent with the SDP model with  $\alpha \ll 1$  (rapidly driven). We find no evidence that this is the case. Specifically, when considering just the waiting time and size PDFs of each active region we find that either i) the conditional PDF of stress-release sizes,  $\eta[\Delta X_i | X(t_i^-)]$ , varies from one region to another, or ii) a flare rate of  $\lambda_k \lesssim 0.3 \text{ hr}^{-1}$  does not correspond to  $\alpha \ll 1$  (assuming that  $\lambda_k$  traces  $\alpha$ ). The analysis takes into account the selection effect that obscures the detection of flares following a large flare due to enhancement of the soft X-ray background.

On the other hand, if many active regions house a SDP process driven rapidly towards a static-in-time threshold before each event, i.e. have  $\alpha \ll 1$ , then those regions that have large cross-correlations between event sizes and subsequent waiting times should also have waiting time and size PDFs of the same shape. This prediction is not supported by the data, as proved clearly by Figure 5.7b. The match between  $p(\Delta t)$  and  $p(\Delta s)$ , quantified by  $\mathcal{M}_k$  (the  $p$ -value from a KS two-sample test) for the  $k$ -th active region, does not correlate with the forward cross-correlation,  $\rho_{+,k}$ . If we assume each region has the same  $\alpha$ , this test implies  $1 \lesssim \alpha \lesssim 10$ .

We emphasize that the prediction that  $\mathcal{M}_k$  should correlate with  $\rho_{+,k}$  for a process driven to a threshold does not rely on the specific details of the SDP framework, such as the relationship between flare rate and stress in Equation (5.2), nor the functional form of  $\eta[\Delta X_i | X(t_i^-)]$ . Any stochastic process that drives the stress towards a static threshold before each event would predict an equivalent observable, for example the Brownian stress-accumulation model [2].

There are many ways to interpret the results in Sections 5.5.3 and 5.6: i) solar flares may not be triggered by stress (e.g. magnetic energy density) breaching a threshold; a completely different process may trigger a flare. ii) The *GOES* flare catalog is incomplete; flares that occur in the aftermath of large flares are not recorded, creating an artificial cross-correlation. iii) The threshold at which a glitch is triggered and/or iv) the driving rate at which stress accumulates may vary with time; either of options iii) and iv) could wash out the observable signature. Untangling these explanations entails exploiting the entire wealth of data available in the flare catalog(s), rather than focussing on individual special flares or regions.

In closing, we touch on the following question: if option iii) above is true, is a threshold that varies with time compatible with any plausible microphysical flare triggers? The question falls outside the scope of this paper, which focuses on the microphysics-agnostic analysis in Sections 5.5 and 5.6, so we limit ourselves to the following brief remark. Magnetohydrodynamic instabilities relevant to solar flare activity are triggered above a threshold, which typically depends on the detailed geometry of a flaring magnetic loop, not just its bulk properties (e.g. magnetic energy density). The geometry of a flaring loop does vary with time in general. For example, the ideal kink instability occurs, when the total twist  $\Phi = lB_\phi(r)/[rB_z(r)]$  satisfies  $\Phi > \Phi_{\text{cr}}(a) \sim 10$ , where  $l$  and  $r$  are the length and minor radius of the current-carrying loop,  $B_\phi(r)$  and  $B_z(r)$  are the toroidal and axial magnetic field components, and  $a$  is the loop aspect ratio [429]. As sub-photospheric turbulence perturbs randomly the footpoints of a magnetic flux

tube, the variables  $a$  and hence  $\Phi_{\text{cr}}(a)$  fluctuate stochastically. Quantifying the amplitude (drift and diffusion) of the fluctuations is a task for detailed magnetohydrodynamic simulations and lies well outside the scope of this paper, but it is conceivable that the amplitude is sufficiently large to render option iii) above viable.

## ACKNOWLEDGEMENTS

We acknowledge helpful discussions with Kai Yang in the early stages of this paper. JBC, AM, and MSW are supported by the Australian Research Council (ARC) Centre of Excellence for Gravitational Wave Discovery (OzGrav) (project number CE170100004) and ARC Discovery Project DP220102201. JBC is supported by an Australian Postgraduate Award.

*Software:* Numpy [430], Scipy [431], Matplotlib [432], and Stan [433] through the cmdstanpy interface.

### 5.A1. MAGNETIC ENERGY DENSITY AS A STRESS VARIABLE IN AN ACTIVE REGION

The SDP framework described in Sections 5.3 and 5.4 is agnostic about the microphysics of solar flares, beyond the general assumption that the flaring rate increases with the stress in the system and diverges at a stress threshold. In this appendix, we sketch briefly one possible mapping between the SDP model and a specific microphysical flare model, in which the stress variable is the spatially-averaged magnetic energy density in an active region. We emphasize that the model is phenomenological and highly idealized. We do not favor it over the many alternatives; it is merely one possible illustration of how such a mapping may work, as a guide to the interested reader.

Let  $X(t)$  correspond to the spatially-averaged magnetic energy density in an active region. The spatial average is taken in order to package the stress into a single variable, noting that the magnetic energy density is nonuniform in reality. Let the active region have characteristic linear dimension  $L$ . Let  $S$  be the magnetohydrodynamic Poynting flux through the photosphere. We assume that the Poynting flux deposits magnetic energy into the active region without losses and at a constant rate, so that one has  $X(t) = X(t_i^+) + St/L$  between flares ( $t_i^+ \leq t \leq t_{i+1}^-$ ). Recent vector magnetogram measurements allow direct observation of the Poynting flux, and the magnetic energy density of an active region, which are at odds with our assumption that  $S$  is steady in time [434–437]. Putting aside the latter consideration for the moment, we can write the control parameter  $\alpha$  as

$$\alpha = \frac{\lambda_0 X_{\text{cr}} L}{S}, \quad (5.7)$$

where  $X_{\text{cr}}$  is the magnetic energy density threshold for a magnetohydrodynamic instability, for example, and  $\lambda_0$  is the instability's trigger reference rate.

Several plausible magnetohydrodynamic instabilities have been suggested as solar flare triggers in the literature [438]. Some of them do not involve a magnetic energy density threshold at all. For example, the kink instability discussed at the end of Section 5.7 is triggered when the field-line twist  $\Phi$  exceeds a threshold  $\Phi_{\text{cr}}(a)$ , whose value

depends on the aspect ratio  $a$  of the flaring loop [429]. However, instabilities triggered by a magnetic energy density threshold do exist. One example is plasmoid-induced magnetic reconnection via tearing modes in a fractal current sheet [439], whose threshold depends on fractional powers of the Alfvén speed (or equivalently the Lundquist number) and hence on the magnetic energy density; see Ji and Daughton [438] or section 5 in Shibata and Tanuma [439] for example. In the latter reference, the threshold condition also depends on the aspect ratio  $a$  (width divided by length) of the current sheet, which can vary with time, as a flaring loop responds to sub-photospheric turbulence.

What are the time-scales on which  $S$  and  $X_c$  vary? In the SDP picture, both variables are steady, but the *GOES* analysis in Section 5.6 implies that one or both may vary in reality (although other scenarios are possible too, as discussed in Section 5.7). As far as  $S$  is concerned, one expects to find statistical fluctuations on the eddy turnover time-scale of sub-photospheric turbulence and flux emergence,  $\tau_{\text{flux}}$ , as observed with vector magnetograms and Doppler measurements [434]. Magnetohydrodynamic simulations and G-band radiative signatures suggest  $\tau_{\text{flux}} \sim$  minutes for magnetic features associated with solar granulation, with peak-to-peak fluctuation amplitude  $\lesssim 30\%$  [440–442]. As far as  $X_c$  is concerned, in the plasmoid-induced reconnection picture as one illustrative example, the magnetic energy density threshold for a Sweet-Parker current sheet to undergo secondary tearing depends not only on the magnetic diffusivity, which fluctuates on the same time-scale as the local temperature, but also on  $a$  and  $L$ , which fluctuate on the turnover time-scale  $\tau_{\text{flux}}$ , e.g. equation (15) in [439]. Flare waiting times are typically comparable to or longer than  $\tau_{\text{flux}}$ , so it is conceivable that the constant- $X_c$  approximation in the SDP theory does not apply to every active region.

We emphasize again that the mapping in this appendix is idealized and illustrative. None of the statistical analysis in Sections 5.5.3 and 5.6 is predicated on the microphysics in this appendix.

## 5.A2. HIERARCHICAL BAYESIAN FRAMEWORK

This appendix lays out a complementary approach to the heuristic tests with which we analyze individual active regions in Section 5.6. We first write down the likelihood for a set of observed waiting times and sizes in an individual region, given a set of model parameters, in Appendix 5.A2.1. We introduce the hierarchical Bayesian framework which combines inference in different regions to estimate population-level parameters, in Appendix 5.A2.2. In Appendix 5.A2.3 we test the efficacy of this approach with synthetic data, and explain why it is not appropriate in this paper to apply this framework to the real *GOES* catalog despite its efficacy. Finally, in Appendix 5.A2.4 we propose an alternative approach using only the average waiting time in each region, as a motivation for future studies. The recipes in this appendix are included for completeness and as a starting point for readers, who wish to develop hierarchical methods of solar flare analysis further.

### 5.A2.1. Likelihood and Bayes' theorem

Solving Equations (5.1)–(5.3) for the long-term observable PDFs,  $p(\Delta t)$  and  $p(\Delta X)$ , is intractable analytically for most choices of  $\eta[\Delta X_i | X(t_i^-)]$ . However, for the special case

$$\eta[\Delta X_i | X(t_i^-)] \propto [X(t_i^-) - \Delta X_i]^\delta, \quad (5.8)$$

we obtain the analytic result

$$p(z) = (\alpha + \delta + 1)(1 - z)^{\alpha + \delta}, \quad (5.9)$$

where the variable  $z$  is either  $\Delta t$  or  $\Delta X$ , i.e. the waiting time and size PDFs are identical [16]. In Equation (5.8) we have  $\delta > 0$  and the constant of proportionality is set by the condition that  $\eta$  must integrate to unity between  $\Delta X_i = 0$  and  $\Delta X_i = X(t_i^-)$ ; see section 6 and appendix D of Fulgenzi et al. [16] for a full derivation. Equation (5.8) is a monotonically decreasing function of  $\Delta X_i$ , i.e. small stress-release events are preferred over large events. Its specific functional form is reasonable but arbitrary; it is not inferred from solar flare data. We adopt it here as a pedagogical device to illustrate the advantages and disadvantages of a hierarchical Bayesian approach to analyzing flare data.

When we restore the dimensions to Equation (5.9), and consider the set of observations in the  $k$ -th active region,  $D_k = \{\Delta t_{i,k}, \Delta s_{i,k}\}$ , with  $1 \leq i \leq N_k$ , we can write the likelihood

$$\mathcal{L}(D_k | \boldsymbol{\theta}_k) = \prod_{i=1}^{N_k-1} p(\Delta t_{i,k} | \boldsymbol{\theta}_k) \prod_{i=1}^{N_k} p(\Delta s_{i,k} | \boldsymbol{\theta}_k) \quad (5.10)$$

$$= \tau_k^{1-N_k} \xi_k^{-N_k} (\beta_k + 1)^{2N_k-1} \prod_{i=1}^{N_k-1} \left(1 - \frac{\Delta t_{i,k}}{\tau_k}\right)^{\beta_k} \prod_{i=1}^{N_k} \left(1 - \frac{\Delta s_{i,k}}{\xi_k}\right)^{\beta_k} \quad (5.11)$$

where  $\xi_k$  is the constant of proportionality in Equation (5.5) which translates the drop in magnetic energy density  $\Delta X$  to the observed flare size,  $\Delta s$ , and one has  $\beta_k = \lambda_{0,k} \tau_k + \delta_k$ . While there are  $N_k$  flare sizes in the region, there are only  $N_k - 1$  waiting times. The three model parameters  $\boldsymbol{\theta}_k = \{\tau_k, \xi_k, \beta_k\}$  are assumed constant in time for the lifetime of the active region. Bayes' theorem calculates the posterior probability distribution (henceforth “posterior”),  $p(\boldsymbol{\theta}_k | D_k)$ , i.e. the probability density of parameter vector  $\boldsymbol{\theta}_k$  given the data  $D_k$ , using the prior probability distribution (henceforth “prior”),  $\pi(\boldsymbol{\theta}_k)$ , viz.

$$p(\boldsymbol{\theta}_k | D_k) \propto \mathcal{L}(D_k | \boldsymbol{\theta}_k) \pi(\boldsymbol{\theta}_k). \quad (5.12)$$

The normalizing constant of proportionality is often called the evidence and, while essential for model comparison, is not relevant for the parameter estimation exercise below [146].

### 5.A2.2. Population-level parameter estimation

Suppose, for the sake of illustration, that  $X_c$ ,  $\lambda_0$ , and every component of  $\boldsymbol{\theta}_k$  are approximately the same in all active regions. In the language of hierarchical Bayesian inference, this corresponds to assuming that the value of  $\boldsymbol{\theta}_k$  for each region is a random

number drawn from a population-level distribution known as a “hyper-prior”, with narrow extent. For concreteness, we assume the hyper-prior for each model parameter is a Gaussian with mean and standard deviation  $\mu_a$  and  $\sigma_a$  respectively, with  $a \in \{\tau, \xi, \beta\}$ . While  $\beta_k$  does depend on  $\tau_k$ , the inference remains accurate so long as the covariance between  $\tau_k$ ,  $\lambda_{0,k}$ , and  $\delta_k$  is minimal. The marginal posterior distribution for the parameters describing the hyper-priors is calculated as

$$p(\boldsymbol{\Lambda} | \mathcal{D}) \propto \pi(\boldsymbol{\Lambda}) \prod_k^M \int d\boldsymbol{\theta}_k \mathcal{L}(D_k | \boldsymbol{\theta}_k) \pi(\boldsymbol{\theta}_k | \boldsymbol{\Lambda}), \quad (5.13)$$

with  $\boldsymbol{\Lambda} = \{\mu_a, \sigma_a\}$ . In Equation (5.13),  $\pi(\boldsymbol{\Lambda})$  is the prior on  $\boldsymbol{\Lambda}$ , and  $\mathcal{D} = \{D_1, \dots, D_k, \dots, D_M\}$  is the set of all data,  $D_k$ , from  $M$  different active regions.

In practice, we can use a Monte Carlo sampler to estimate Equation (5.13), and thus infer the posterior predictive distributions,  $p(\boldsymbol{\theta})$ , where we drop the subscript  $k$  to signify that these distributions bring together information from all active regions to inform the inference. We opt to sample using a Hamiltonian Monte Carlo No U-Turn Sampler [443], as implemented in the Stan programming language [433].

### 5.A2.3. Validation with synthetic data

To estimate the efficacy of the scheme in Appendix 5.A2.2 to infer population-level parameters, we first apply it to a set of synthetic data generated directly from the model. That is, we generate  $M = 50$  fake “active regions”, each with  $N_k = 100$  events, with flare sizes and waiting times generated from the SDP framework with  $\eta[\Delta X_i | X(t_i^-)]$  as in Equation (5.8). In what follows we use the compact notation  $x \sim \mathcal{N}(\mu, \sigma)$  to denote that the random variable  $x$  is drawn from a Gaussian distribution with mean  $\mu$  and standard deviation  $\sigma$ . To generate the data for each region we select a value  $\tau_k \sim \mathcal{N}(\mu_\tau = 3 \text{ day}, \sigma_\tau = 0.5 \text{ day})$ , a value  $\xi_k \sim \mathcal{N}(\mu_\xi = 2 \text{ arb. units}, \sigma_\xi = 0.3 \text{ arb. units})$ , and a value  $\beta_k \sim \mathcal{N}(\mu_\beta = 5, \sigma_\beta = 0.3)$ . Each Gaussian is truncated such that all variates are positive.

After running the sampler with the synthetic data we perform a posterior predictive check, i.e. compare the samples from our posterior distributions  $p(\tau)$ ,  $p(\xi)$ , and  $p(\beta)$  with the injected distributions and the priors on the hyper-parameters. We show the results in Figure 5.8. We see that the posterior samples (blue) appropriately overlap with the injected ground truth (red) for  $\tau$ ,  $\xi$ , and  $\beta$ .

Despite the encouraging results in Figure 5.8, we do not apply this hierarchical Bayesian scheme to the GOES catalog in this paper. This is because in most regions neither the waiting time nor the size PDFs follow the functional form in Equation (5.9). When we include Equation (5.9) in the set of options available for the AICc to select between, as in Section 5.6.1, fewer than 0.1% of active regions are fitted best with Equation (5.9). Therefore Equation (5.11) is not an appropriate likelihood for the data. Other choices of the jump distribution in Equation (5.8) may alleviate this problem but they lie outside the scope of this paper.

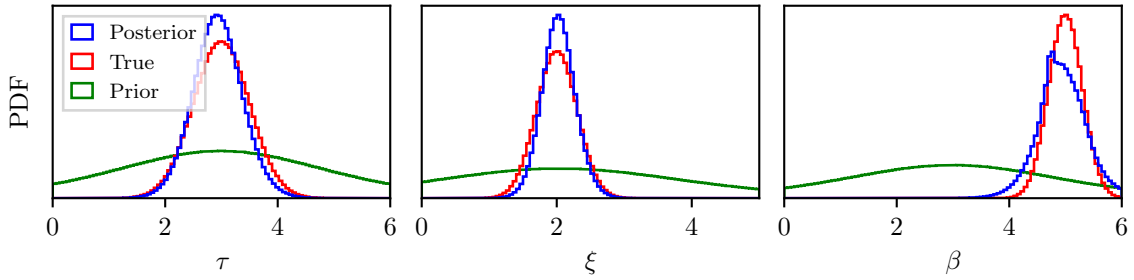


Figure 5.8: Posterior predictive check demonstrating the recovery of injected population-level parameters. The weakly informative priors set on the hyper-parameters  $\tau$ ,  $\xi$ , and  $\beta$  are shown in green, histograms of samples from the injected population parameters are shown in red, while histograms of samples from the posterior distributions are shown in blue. See text in Appendix 5.A2.3 for details on the procedure.

#### 5.A2.4. Likelihood based on the average waiting time

An alternative approach is to build the likelihood out of a summary statistic, such as the average waiting time in a given region,  $\langle \Delta t \rangle_k$ , rather than each observed waiting time and/or size. In the SDP framework, we find [11, 16]

$$\langle \Delta t \rangle^{\text{SDP}} = \frac{1}{\alpha + \alpha_0}, \quad (5.14)$$

where  $\alpha_0 \sim 1$  is a dimensionless constant, whose exact value depends on the particular form of  $\eta[\Delta X_i | X(t_i^-)]$ . Restoring the dimensions to Equation (5.14) we can write the likelihood as

$$\mathcal{L}(\langle \Delta t \rangle_k | \boldsymbol{\theta}_k) = \frac{1}{\sqrt{2\pi}\sigma_k} \exp\left[ \frac{-\left(\langle \Delta t \rangle_k - \frac{\tau_k}{\lambda_{0,k}\tau_k + \alpha_{0,k}}\right)^2}{2\sigma_k^2} \right], \quad (5.15)$$

with  $\boldsymbol{\theta}_k = \{\tau_k, \lambda_{0,k}, \alpha_{0,k}, \sigma_k\}$ , where we assume the residual of  $\langle \Delta t \rangle_k$  with the model subtracted is normally distributed, with zero mean and standard deviation  $\sigma_k$ . With the likelihood in Equation (5.15) one could perform population-level parameter estimation, as described in Section 5.A2.2. We leave this, and an exploration of how  $\boldsymbol{\theta}_k$  depends on parameters intrinsic to each active region, to future work.

### 5.A3. CLEANING GOES FLARE SUMMARY DATA

The SWPC and NGDC File Transfer Protocol servers that host the *GOES* flare summary data, as well as other data portals such as the Heliophysics Event Knowledgebase<sup>6</sup>, contain numerous typographical anomalies found when collating the data into a homogeneous catalog. These anomalies are found in the recorded active region number by checking whether one has  $\Delta t_{i,k} < 14$  days for  $1 \leq i \leq N_k - 1$  for each active region. The limit of 14 days applies because active regions are typically only visible for two weeks

---

<sup>6</sup> Accessible through [http://hec.helio-vo.eu/hec/hec\\_gui.php](http://hec.helio-vo.eu/hec/hec_gui.php).

due to the rotation period of the Sun. The one exception in the *GOES* flare summary data is a set of eight flares that occurred on 2002 November 2, and were assigned to active region number 10198. Two weeks later, the active region appeared on the eastern limb of the Sun, and 33 additional flares were assigned to active region number 10198, from 2002 November 17 until 2002 November 28. We opt not to consider the former eight flares as part of active region number 10198, and we do not include them in the catalog.

The anomalies, and hand-corrected values, are tabulated in Table 5.1. The corrected values are determined manually by referring to the context of surrounding flares in the database. For example, the flare starting at 1981 July 18 11:46 is recorded with active region number 3121. Yet the other 11 flares associated with the latter region occurred between 1981 May 24 and 1981 June 1, while active region number 3221 has 32 flares recorded between 1981 July 17 and 1981 July 29, indicating that the anomalous flare should be associated with the latter active region. The latitude of the anomalous flare is also within  $\pm 5^\circ$  of other flares from active region number 3221, while flares in active region number 3121 are  $\gtrsim 10^\circ$  higher in latitude.

#### 5.A4. LOG-NORMAL WAITING TIME DISTRIBUTIONS

A sequence of instantaneous events ordered in time is known as a point process. If the instantaneous event rate does not change with time, and if the process is memoryless, it is called a Poisson point process, and exhibits exponentially distributed waiting times [409]. If the instantaneous rate does change with time it is a non-homogeneous Poisson process, which can exhibit waiting times that are distributed as a log-normal for certain rate functions [375, 444]. The SDP is one example of a non-homogeneous Poisson process that can generate waiting times distributed as a log-normal, for certain choices of  $\eta[\Delta X_i | X(t_i^-)]$  and  $\alpha$ . One can alternatively generate log-normally distributed values via a multiplicative process, e.g. an organism that grows in proportion to its current size multiplied by a random variable generates (at least approximately) log-normally distributed sizes, due to the Central Limit Theorem [445].

Log-normal waiting time distributions are observed in many other contexts besides solar flares, including but not limited to gamma-ray bursts [446], X-ray bursts [447–449], fast radio bursts [450], network traffic [451, 452], mining equipment failure [453], earthquake aftershocks [454], and test response times [455].

#### 5.A5. EXAMPLE FITS FOR INDIVIDUAL ACTIVE REGIONS

The reader may be curious to examine some examples of the variety of distributions fitted to individual active regions. To this end, in Figure 5.9 we show the complementary cumulative distribution function (CCDF) for the flare waiting times and sizes from four arbitrary but representative active regions with  $N_k \geq 20$ . We display the distributions as CCDFs instead of PDFs to avoid binning the data. The black stepped curves indicate the empirical CCDF constructed from the *GOES* catalog, while the colored curves are the various fits to the data, with parameters fixed to their maximum likelihood values. The distribution with bold type-face in the legend is the shape that best fits the data according to the AICc.

Table 5.1: Anomalous active region numbers found in the GOES flare summary data by checking whether one has  $\Delta t_{i,k} < 14$  days for  $1 \leq i \leq N_k - 1$  for each active region. Corrected values are determined manually, by considering the context of what active regions are present at the time of the anomalous flare at a similar latitude. Corrected values of “—” indicate that we cannot identify a reasonable active region to associate with the anomalous flare.

Flare start time	Anomalous active region number	Corrected active region number
1978-05-30 06:19	1000	1134
1981-07-18 11:46	3121	3221
1981-08-22 06:58	366	3266
1983-03-01 18:24	2102	4102
1983-03-01 18:54	2102	4102
1983-07-04 06:09	4135	4235
1983-07-29 03:53	4236	4263
1993-09-27 01:35	7500	7590
2000-11-09 21:13	9125	—
2002-06-14 20:18	1	10001
2003-07-31 07:59	422	10422
2003-12-21 04:10	10000	—
2011-12-22 13:04	11281	11381
2017-07-11 01:09	12655	12665
2017-07-16 10:25	12655	12665
2021-05-10 23:46	12282	12822
2021-09-01 03:03	12680	12860
2021-09-01 04:27	12680	12860
2021-11-06 22:01	12984	12894
2021-12-18 11:17	12807	12907
2021-12-18 17:27	12807	12907

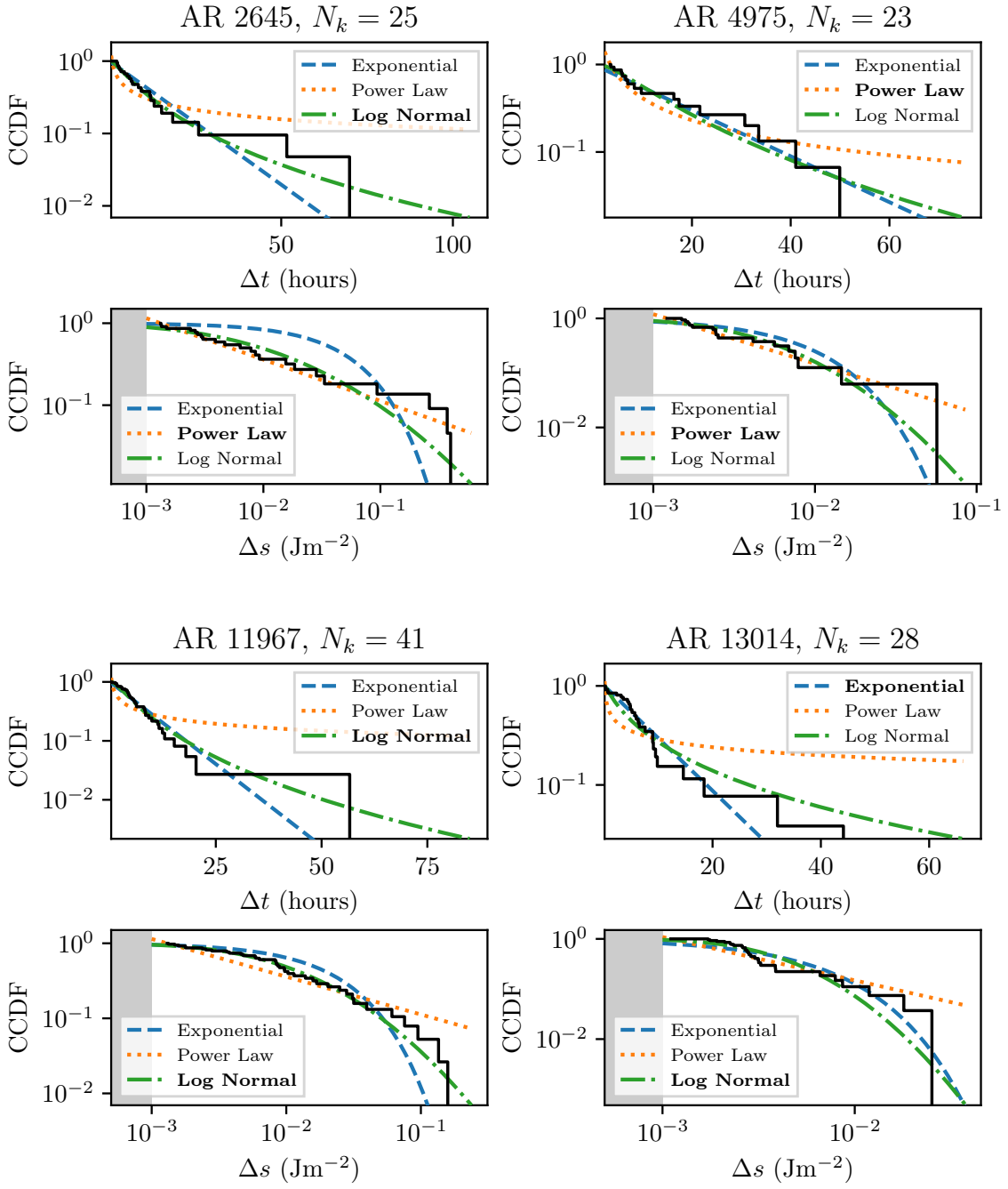


Figure 5.9: Complementary cumulative distribution functions (CCDFs) for four arbitrary but representative active regions with  $N_k \geq 20$ . The distribution that best describes the data in each panel (black stepped curve), according to the AICc, is in bold type-face in the legend for each panel. The grey regions in the bottom panels indicate  $\Delta s \leq 10^{-3} \text{ Jm}^{-2}$ , i.e. where the masking described in Section 5.5.2 is applied.

# CHAPTER 6

---

## Search for continuous gravitational waves from 20 accreting millisecond x-ray pulsars in O3 LIGO data

---

This chapter is a reproduction of [6]

*R. Abbott et al. (LIGO Scientific Collaboration, Virgo Collaboration, and KAGRA Collaboration),  
Physical Review D, 105, 2, 022002 (2022)*

reformatted with the following changes only:

- Footnote 2 in Section 6.3.2 is amended in response to a suggestion of the thesis examiner.
- The text is styled to match the rest of this thesis.
- To fit page constraints, the caption for Table 6.4 is placed on the page previous to the table.
- Where necessary, bibliographic records are updated.

### 6.1. ABSTRACT

Results are presented of searches for continuous gravitational waves from 20 accreting millisecond X-ray pulsars with accurately measured spin frequencies and orbital parameters, using data from the third observing run of the Advanced LIGO and Advanced Virgo detectors. The search algorithm uses a hidden Markov model, where the transition probabilities allow the frequency to wander according to an unbiased random walk, while the  $\mathcal{J}$ -statistic maximum-likelihood matched filter tracks the binary orbital phase. Three narrow sub-bands are searched for each target, centered on harmonics of the measured spin frequency. The search yields 16 candidates, consistent with a false alarm probability of 30% per sub-band and target searched. These candidates, along with one candidate from an additional target-of-opportunity search done for SAX J1808.4–3658, which was in outburst during one month of the observing run, cannot be confidently associated with a known noise source. Additional follow-up does not provide convincing evidence that any are a true astrophysical signal. When all candidates are assumed non-astrophysical, upper limits are set on the maximum wave strain detectable at 95%

confidence,  $h_0^{95\%}$ . The strictest constraint is  $h_0^{95\%} = 4.7 \times 10^{-26}$  from IGR J17062–6143. Constraints on the detectable wave strain from each target lead to constraints on neutron star ellipticity and  $r$ -mode amplitude, the strictest of which are  $\epsilon^{95\%} = 3.1 \times 10^{-7}$  and  $\alpha^{95\%} = 1.8 \times 10^{-5}$  respectively. This analysis is the most comprehensive and sensitive search of continuous gravitational waves from accreting millisecond X-ray pulsars to date.

## 6.2. INTRODUCTION

Second generation, ground-based gravitational wave detectors, specifically the Advanced Laser Interferometer Gravitational wave Observatory (Advanced LIGO) [456] and Advanced Virgo [457], have detected more than 50 compact binary coalescence events in recent years [458–460]. Continuous gravitational waves from rapidly-rotating neutron stars are also potential sources, e.g. a non-axisymmetry due to mountains on the surface, or stellar oscillation modes in the interior [461–463]. There are no reported detections of continuous gravitational waves to date, despite a number of searches in Advanced LIGO and Advanced Virgo data [9, 291, 305, 311–314, 333, 464–477].

Low-mass X-ray binaries (LMXBs) are a high-priority target for continuous gravitational wave searches. LMXBs are composed of a compact object, such as a neutron star<sup>1</sup>, which accretes matter from a stellar-mass ( $\lesssim 1M_\odot$ ) companion [324]. The accretion exerts a torque that may spin up the compact object. Electromagnetic (EM) observations show that even the pulsar with the highest known frequency, PSR J1748–2446ad at 716 Hz [320], rotates well below the centrifugal break-up frequency, estimated at  $\sim 1400$  Hz [323]. Gravitational wave emission may provide the balancing torque in binary systems such as these, stopping the neutron star from spinning up to the break-up frequency [87, 343]. If so, there should thus be a correlation between accretion rate (which is inferred via X-ray flux) and the strength of the continuous gravitational wave emission [87, 268, 331, 343]. The LMXB Scorpius X-1 is the brightest extra-Solar X-ray source in the sky, making it a prime target for searches for continuous gravitational waves [293, 314, 332, 333].

Some LMXBs have EM observations of pulsations during “outburst” events lasting days to months, which allow for measurement of their rotational frequency,  $f_\star$ , to an accuracy of  $\sim 10^{-8}$  Hz, and measurement of their binary ephemerides [44, 324]. LMXBs that are observed to go into outburst and have measurable pulsations with millisecond periods are sometimes called accreting millisecond X-ray pulsars (AMXPs). If the rotational frequency is known, computationally cheap narrowband searches are possible. Six AMXPs were previously searched for continuous gravitational waves, one in Science Run 6 (S6) using the TwoSpect algorithm [302, 303], and five in Observing Run 2 (O2) using the same Hidden Markov Model (HMM) algorithm we use in this work [8, 9]. No significant candidates were found in either search. Searches for continuous gravitational waves from LMXBs are difficult as the rotation frequency may wander stochastically on timescales of  $\lesssim 1$  yr [89], limiting the duration of coherent integration. A HMM tracks a wandering signal, and is the search algorithm we use here, following Suvorova et al. [7,

---

<sup>1</sup>LMXBs in which the compact object is a stellar-mass black hole are not expected to function as continuous gravitational wave sources and are not discussed in this paper.

[8](#), Middleton et al. [\[9\]](#), and LVC et al. [\[314\]](#).

Advanced LIGO and Advanced Virgo began the third Observing Run (O3) on April 1 2019, 15:00 UTC. There was a month-long commissioning break between October 1 2019, 15:00 UTC, and November 1 2019, 15:00 UTC, after which observations resumed until March 27, 2020, 17:00 UTC. This month-long break divides O3 into two segments: O3a and O3b. In this work we search the full O3 data set for continuous gravitational wave signals from AMXPs with known rotational frequencies. The search is a more sensitive version of an analogous search in O2 data [\[9\]](#), with an expanded target list. We briefly review the algorithm and O2 search in Sec. 6.3. In Secs. 6.4 and 6.5 we describe the targets and the parameter space respectively. We discuss the data used in Sec. 6.6. In Sec. 6.7 we describe the vetoes applied to discriminate between terrestrial and astrophysical candidates. In Sec. 6.8 we present the results of the search. In Sec. 6.9 we describe an additional target-of-opportunity search performed for one of the targets that was in outburst during O3a. We provide upper limits for the detectable wave-strain, and astrophysical implications thereof, in Sec. 6.10. We conclude in Sec. 6.11.

### 6.3. SEARCH ALGORITHM

The search in this paper follows the same prescription as the O2 searches for Scorpius X-1 [\[314\]](#) and LMXBs with known rotational frequency [\[9\]](#). It is composed of two parts: a HMM which uses the Viterbi algorithm to efficiently track the most likely spin history, and the  $\mathcal{J}$ -statistic, which calculates the likelihood a gravitational wave is present given the detector data, and the orbital parameters of both the Earth and the LMXB. The HMM formalism is identical to that used in Suvorova et al. [\[7, 8\]](#), Middleton et al. [\[9\]](#), and LVC et al. [\[293, 314\]](#), and the  $\mathcal{J}$ -statistic was first introduced in Suvorova et al. [\[8\]](#). Below, we provide a brief review of both the HMM and the  $\mathcal{J}$ -statistic.

#### 6.3.1. HMM

In a Markov process, the probability of finding the system in the current state depends only on the previous state. In a hidden Markov process the states are not directly observable and must be inferred from noisy data. In this paper, the hidden state of interest is the gravitational wave frequency  $f(t)$ . Although the rotation frequency  $f_\star(t)$  of every target in this search is measured accurately from EM pulsations, we allow  $f(t) \neq f_\star(t)$  in general for three reasons: i) different emission mechanisms emit at different multiples of  $f_\star$  [\[278\]](#); ii) a small, fluctuating drift may arise between  $f(t)$  and  $f_\star(t)$ , if the star's core (where the gravitational-wave-emitting mass or current quadrupole may reside) decouples partially from the crust (to which EM pulsations are locked) [\[7, 478\]](#); and, iii) the rotational frequency of the crust may also drift stochastically due to a fluctuating accretion torque [\[89, 324\]](#). The gravitational-wave frequency is therefore hidden even though the EM measurement of  $f_\star$  helps restrict the searched frequency space, as described in Sec. 6.5.

Following the notation of Middleton et al. [\[9\]](#) and LVC et al. [\[314\]](#) we label the hidden state variable as  $q(t)$ . In our model, it transitions between a discrete set of allowed values  $\{q_1, \dots, q_{N_Q}\}$  at discrete times  $\{t_0, \dots, t_{N_T}\}$ . The probability of the state transitioning from  $q_i$  at time  $t_n$  to  $q_j$  at time  $t_{n+1}$  is determined by the transition matrix  $A_{q_j q_i}$ . In this search,

as in previous searches of LMXBs [9, 293, 314], the transition matrix is

$$A_{q_j q_i} = \frac{1}{3} (\delta_{q_j q_{i+1}} + \delta_{q_j q_i} + \delta_{q_j q_{i-1}}), \quad (6.1)$$

where  $\delta_{ij}$  is the Kronecker delta. Eq. (6.1) corresponds to allowing  $f(t)$  to move 0, or  $\pm 1$  frequency bins, with equal probability, at each discrete transition. It implicitly defines the signal model for  $f(t)$  to be a piece-wise constant function, with jumps in frequency allowed at the discrete times  $\{t_0, \dots, t_{N_T}\}$ . This is a well-tested approximation for an unbiased random walk [7, 8].

The total duration of the search is  $T_{\text{obs}}$ , which we split into  $N_T$  coherent equal chunks of length  $T_{\text{drift}}$ , where  $N_T = \lfloor T_{\text{obs}}/T_{\text{drift}} \rfloor$ , and  $\lfloor \dots \rfloor$  indicates rounding down to the nearest integer. We justify our choice of  $T_{\text{drift}}$  in Sec. 6.5. In essence, it needs to be short enough to ensure that  $f_\star(t)$  does not wander by more than one frequency bin during each time segment, but ideally no shorter in order to maximize the signal-to-noise ratio in each segment. For each time segment the likelihood that the observation  $o_j$  is related to the hidden state  $q_i$  is given by the emission matrix  $L_{o_j q_i}$ . We calculate  $L_{o_j q_i}$  from the data via a frequency domain estimator, e.g. the  $\mathcal{J}$ -statistic, as discussed in Sec. 6.3.2.

The probability that the hidden path is  $Q = \{q(t_0), \dots, q(t_{N_T})\}$  given a set of observations  $O = \{o(t_0), \dots, o(t_{N_T})\}$  is

$$\begin{aligned} P(Q|O) &= \Pi_{q(t_0)} A_{q(t_1)q(t_0)} L_{o(t_1)q(t_1)} \dots \\ &\quad \times A_{q(t_{N_T})q(t_{N_T-1})} L_{o(t_{N_T})q(t_{N_T})}, \end{aligned} \quad (6.2)$$

where  $\Pi_{q(t_0)}$  is the prior probability of starting in the state  $q(t_0)$ , and is taken to be uniform within a certain range guided by EM measurements of  $f_\star$ . The Viterbi algorithm is a computationally efficient way to find the path  $Q^*$  that maximizes Eq. (6.2) [308].

The detection statistic we use in this work is  $\mathcal{L} = \ln P(Q^*|O)$ , i.e. the log-likelihood of the most likely path given the data. The search outputs one  $P(Q^*|O)$  value per frequency bin, corresponding to the optimal path  $Q^*$  terminating in that frequency bin.

### 6.3.2. $\mathcal{J}$ -statistic

Any long-lived gravitational wave signal from an LMXB observed by the detectors is Doppler modulated by the orbital motion of the detectors around the Solar System barycenter, and by the orbital motion of the compact object in its binary. The  $\mathcal{F}$ -statistic is a frequency domain estimator originally designed for isolated neutron stars, and accounts for the Earth's annual orbital motion (as well as the amplitude modulation caused by the Earth's diurnal rotation) [262]. Algorithms that implement the  $\mathcal{F}$ -statistic, such as `lalapps_ComputeFstatistic_v2` [282], have subsequently added functionality to account for modulation of the signal due to binary motion.

The  $\mathcal{J}$ -statistic accounts for the binary modulation via a Jacobi-Anger expansion of the orbit [8]. It ingests  $\mathcal{F}$ -statistic “atoms” as calculated for an isolated source as an input, assumes the binary is in a circular orbit<sup>2</sup>, and requires three binary orbital parameters:

---

<sup>2</sup>This assumption is justified as none of the targets described in Sec. 6.4 have measured eccentricity greater than zero. That is, for the analyses which fit eccentricity, it is found to be consistent with zero (at 95% confidence) [44, 324].

the period  $P$ , the projected semi-major axis  $a_0$ , and the time of passage of the ascending node  $T_{\text{asc}}$ . We use the  $\mathcal{J}$ -statistic as the frequency domain estimator  $L_{o_i q_i}$  in this paper, as in Middleton et al. [9] and LVC et al. [314]. The  $\mathcal{J}$ -statistic is a computationally efficient algorithm, as it re-uses  $\mathcal{F}$ -statistic atoms when searching over a template bank of binary orbital parameters.

## 6.4. TARGETS

The AMXPs chosen as targets for this search, along with their positions, orbital elements, and pulsation frequencies are listed in Table 6.1. These 20 targets constitute all known AMXPs with observed coherent pulsations and precisely measured orbital elements as of April 2021<sup>3</sup>. For details on the relevant EM observations, principally in the X-ray band, see Di Salvo and Sanna [44], Patruno and Watts [324], Marino et al. [335], and Watts et al. [348].

Most AMXPs are transient, with “active” (outburst) and “quiescent” phases. Pulsations, and therefore  $f_\star$ , are only observed during the active phase. Active phases are typically associated with accretion onto the neutron star, however accretion can also happen during quiescence [481]. The frequency derivatives,  $\dot{f}_\star$ , in the active phase and in the quiescent phase are set by the accretion torque and magnetic dipole braking respectively [45, 481]. The value of  $\dot{f}_\star$  has implications for the continuous gravitational wave signal strength (see Sec. 6.10.3), as well as the choice of  $T_{\text{drift}}$  (see Sec. 6.5.1).

One target, SAX J1808.4–3658, went into outburst during O3a [482–484]. It may be the case that continuous gravitational waves are only emitted when an AMXP is in outburst [342]. If so, we increase our signal-to-noise ratio by searching only data from the times that it was in outburst, compared to searching the entirety of O3 data. To investigate this possibility, we perform in Sec. 6.9 an additional target-of-opportunity search for continuous gravitational waves from SAX J1808.4–3658 while it is in outburst.

---

<sup>3</sup>We do not include the AMXP Aquila X-1 [479, 480] in our target list as there is a large uncertainty on all three binary orbital elements, compared to the other 20 AMXPs. One would need to search  $> 10^{10}$  binary orbital templates, an order of magnitude more than the rest of the targets combined. The number of binary orbital templates is calculated as a function of the uncertainty in orbital elements in Sec. 6.5.2.

Table 6.1: Target list: position (RA and Dec), orbital period ( $P$ ), projected semi-major axis in light-seconds ( $a_0$ ), time of passage through the ascending node as measured near the time of the most recent outburst ( $T_{\text{asc}}$ ), the time of passage through the ascending node as propagated to the start of O3 ( $T_{\text{asc}, \text{O3}}$ ), as described in Sec. 6.5.2, and frequency of observed pulsations ( $f_\star$ ). Numbers in parentheses indicate reported  $1\sigma$  errors (68% confidence level), unless otherwise noted. All objects have positional uncertainty  $\leq 1$ s in RA and  $\leq 0.5''$  in Dec.

Target	RA	Dec	P/s	$a_0/\text{lt-s}$	$T_{\text{asc}}/\text{GPS time}$	$T_{\text{asc}, \text{O3}}/\text{GPS time}$	$f_\star/\text{Hz}$	Refs.
IGR J00291+5934	00h29m03.05s	+59°34'18.93''	8844.07673(9)	0.064993(2)	1122149932.93(5)	1238157687(1)	598.89213099(6)	[322, 485]
MAXI J0911–655	09h12m02.46s	-64°52'06.37''	2659.93312(47)	0.017595(9)	1145507148.0(9)	1238165918(16)	339.9750123(3)	[486, 487]
XTE J0929–314	09h29m20.19s	-31°23'03.2''	2614.746(3)	0.006290(9)	705152406.1(9)	1238165763(612)	185.105254297(9)	[488, 489]
IGR J16597–3704	16h59m32.902s	-37°07'14.3''	2758.2(3)	0.00480(3)	1193053416(9)	1238163777(4907)	105.1758271(3)	[490, 491]
IGR J17062–6143	17h06m16.29s	-61°42'40.6''	2278.21124(2)	0.003963(6)	1239389342(4)	1238165942(4)	163.656110049(9)	[492]
IGR J17379–3747	17h37m58.836s	-37°46'18.35''	6765.8388(17)	0.076979(14)	1206573046.6(3)	1238162748(8)	468.083266605(7)	[493, 494]
SAX J1748.9–2021	17h48m52.161s	-20°21'32.406''	31555.300(3)	0.38757(2)	1109500772.5(8)	1238151731(12)	442.3610957(2)	[44, 495]
NGC 6440 X–2	17h48m52.76s	-20°21'24.0''	3457.8929(7)	0.00614(1)	956797704(2)	1238166449(57)	205.89221(2)	[496, 497]
IGR J17494–3030	17h49m23.62s	-30°29'58.999''	4496.67(3)	0.015186(12)	1287797911(1)	1238163668(331)	376.05017022(4)	[498]
Swift J1749.4–2807	17h49m31.728s	-28°08'05.064''	31740.8417(27)	1.899568(11)	1298634645.85(12)	1238136602(5)	517.92001385(6)	[499–501]
IGR J17498–2921	17h49m56.02s	-29°19'20.7''	13835.619(1) <sup>a</sup>	0.365165(5) <sup>a</sup>	997147537.43(7) <sup>a</sup>	1238164020(6)	400.99018734(9) <sup>a</sup>	[502, 503]
IGR J17511–3057	17h51m08.66s	-30°57'41.0''	12487.5121(4)	0.2751952(18)	936924316.03(3)	1238160570(10)	244.83395145(9)	[504, 505]
XTE J1751–305	17h51m13.49s	-30°37'23.4''	2545.3414(38) <sup>b</sup>	0.010125(5) <sup>b</sup>	701914663.57(3) <sup>b</sup>	1238164644(487)	435.31799357(3) <sup>b</sup>	[506, 507]
Swift J1756.9–2508	17h56m57.43s	-25°06'27.4''	3282.40(4)	0.00596(2)	1207196675(9)	1238166119(378)	182.06580377(11)	[508]
IGR J17591–2342	17h59m02.86s	-23°43'08.3''	31684.7503(5)	1.227714(4)	1218341207.72(8)	1238144176.7(3)	527.425700578(9)	[509, 510]
XTE J1807–294	18h06m59.8s	-29°24'30''	2404.4163(3)	0.004830(3)	732384720.7(3)	1238165711(63)	190.62350702(4)	[511, 512]
SAX J1808.4–3658	18h08m27.647s	-36°58'43.90''	7249.155(3)	0.062809(7)	1250296258.5(2)	1238161173(5)	400.97521037(1)	[483]
XTE J1814–338	18h13m39.02s	-33°46'22.3''	15388.7229(2) <sup>b</sup>	0.390633(9) <sup>b</sup>	739049147.41(8) <sup>b</sup>	1238151597(4)	314.35610879(1) <sup>b</sup>	[513, 514]
IGR J18245–2452	18h24m32.51s	-24°52'07.9''	39692.812(7)	0.76591(1)	1049865088.37(9)	1238128096(33)	254.3330310(1)	[515, 516]
HETE J1900.1–2455	19h00m08.65s	-24°55'13.7''	4995.2630(5)	0.01844(2)	803963262.3(8)	1238161513(43)	377.296171971(5)	[517–519]

<sup>a</sup>  $3\sigma$  error<sup>b</sup> 90% confidence level

## 6.5. SEARCH PARAMETERS

The  $\mathcal{J}$ -statistic matched filter requires specification of the source sky position [right ascension (RA) and declination (Dec)], the orbital period  $P$ , the projected semi-major axis  $a_0$ , and the orbital phase  $\phi_a$  at the start of the search. The orbital phase can be equivalently specified via a time of passage through the ascending node,  $T_{\text{asc}}$ . EM observations constrain all of these parameters, as well as the spin frequency  $f_\star$ . These measurements, along with their associated uncertainties, are listed in Table 6.1.

There are several mechanisms that could lead to continuous gravitational wave emission from an AMXP, in its active or quiescent phase. “Mountains” on the neutron star surface, be they magnetically or elastically supported, emit at  $2f_\star$  and potentially  $f_\star$  [276]. The dominant continuous gravitational wave emission from  $r$ -mode oscillations (Rossby waves excited by radiation-reaction instabilities) is predicted to be at  $\sim 4f_\star/3$  [263, 264, 266, 520]. Thus, we search frequency sub-bands centered on  $\{1, 4/3, 2\} f_\star$  for each target. As in Middleton et al. [9] and LVC et al. [314] we choose a sub-band width of  $\sim 0.61 \text{ Hz}^4$ .

Recent work indicates that the continuous gravitational wave signal from  $r$ -modes could emit at a frequency far from  $4f_\star/3$  due to equation-of-state-dependent relativistic corrections, and so comprehensive searches for  $r$ -modes may need to cover hundreds of Hz for the targets listed in Table 6.1 [271, 272]. The exact range of frequencies to search is a non-linear function of  $f_\star$ , and does not necessarily include  $4f_\star/3$  (see equation (17) of Caride et al. [272]). However, these estimates are still uncertain. We deliberately search  $\sim 0.61 \text{ Hz}$  sub-bands centered on  $4f_\star/3$ , as an exhaustive broadband search lies outside the scope of this paper, which aims to conduct fast, narrowband searches at astrophysically motivated harmonics of  $f_\star$  while accommodating frequency wandering within those sub-bands, a challenge in its own right.

### 6.5.1. Coherence time and frequency binning

Another key parameter for the search algorithm described in Sec. 6.3 is the coherence time  $T_{\text{drift}}$ . As in Middleton et al. [9] and LVC et al. [314] we fix  $T_{\text{drift}} = 10 \text{ d}$  for each target<sup>5</sup>. This choice of  $T_{\text{drift}}$  is guided by observations of Scorpius X-1 [89]. Quantitative studies of how X-ray flux variability in AMXPs impacts searches for continuous gravitational waves are absent from the literature. The choice to use  $T_{\text{drift}} = 10 \text{ d}$  balances the increased sensitivity achieved via longer coherence times with the knowledge that the gravitational wave frequency may wander stochastically, e.g. due to fluctuations in the mass accretion rate. The particular value  $T_{\text{drift}} = 10 \text{ d}$  has been adopted in all previous Viterbi LMXB searches [9, 293, 314] and is justified approximately with reference to a simple random-walk interpretation of fluctuations in the X-ray flux of Scorpius X-1 [89, 284, 522], but other values are reasonable too.

---

<sup>4</sup>Other narrowband searches, such as LVC et al. [465, 521], search sub-bands whose width,  $\sim 10^{-3} f$ , scales with frequency. We note that  $0.61 \text{ Hz}$  is comparable to  $10^{-3} f$  for the harmonics of  $f_\star$  that we search in this paper, but is  $2^{20} \Delta f$ , where  $\Delta f$  is the frequency bin size defined in Sec. 6.5.1. Having the number of frequency bins in the sub-band equal a power of two speeds up the Fourier transform [314].

<sup>5</sup>We consider additional  $T_{\text{drift}}$  durations for the target-of-opportunity search for continuous gravitational waves from SAX J1808.4–3658 during its O3a outburst in Sec. 6.9.

We remind the reader that the choice of  $T_{\text{drift}}$  implicitly fixes the proposed signal model as one in which the frequency may wander step-wise zero, plus or minus one frequency bin every  $T_{\text{drift}} = 10$  d. The size of the frequency bins,  $\Delta f$ , is fixed by the resolution implied by the coherence time, i.e.  $\Delta f = 1/(2 T_{\text{drift}}) = 5.787037 \times 10^{-7}$  Hz, for  $T_{\text{drift}} = 10$  d. As  $\Delta f$  depends on  $T_{\text{drift}}$ , changing the coherence time explicitly changes the signal model, e.g. if  $T_{\text{drift}}$  is halved and  $T_{\text{obs}}$  is kept constant, then both  $N_T$  and  $\Delta f$  double; thus the signal can move up to a factor of four more in frequency in the same  $T_{\text{obs}}$ . The connection between the coherence time and signal model features in all semi-coherent search methods. However, for a HMM-based search such as this, the choice of coherence time is not limited by computational cost, as it is in all-sky searches or searches based on the  $\mathcal{F}$ -statistic [470, 523].

This analysis does not search over any frequency derivatives. The maximum absolute frequency derivative,  $|\dot{f}_{\max}|$ , that does not change the frequency more than one frequency bin over the course of one coherent chunk is

$$|\dot{f}_{\max}| = \frac{\Delta f}{T_{\text{drift}}} \approx 6.7 \times 10^{-13} \text{ Hz s}^{-1}. \quad (6.3)$$

When measured, the long-term secular frequency derivative is well below this value for all of our targets, see Sec. 6.10.3 for details.

### 6.5.2. Number of orbital templates

The orbital elements are known to high precision, with the uncertainty in  $P$  satisfying  $\sigma_P \lesssim 10^{-3}$  s, the uncertainty in  $a_0$  satisfying  $\sigma_{a_0} \lesssim 10^{-4}$  light-seconds (lt-s), and the uncertainty in  $T_{\text{asc}}$  satisfying  $\sigma_{T_{\text{asc}}} \lesssim 1$  s. However,  $T_{\text{asc}}$  is measured relative to the target's most recent outburst, which is often years before the start of O3 ( $T_{\text{O3,start}} = 1238166483$  GPS time). We need to propagate it forward in time. This propagation compounds the uncertainty in  $T_{\text{asc}}$ , viz. [9, 314, 332]

$$\sigma_{T_{\text{asc,O3}}} = [\sigma_{T_{\text{asc}}}^2 + (N_{\text{orb}} \sigma_P)^2]^{1/2}, \quad (6.4)$$

where  $N_{\text{orb}}$  is the number of orbits between the observed  $T_{\text{asc}}$  and  $T_{\text{asc,O3}}$ . Henceforth  $T_{\text{asc}}$  and  $\sigma_{T_{\text{asc}}}$  symbolize their values when propagated to  $T_{\text{O3,start}}$ .

To conduct the search over the orbital elements for each target and sub-band we construct a rectangular grid in the parameter space defined by  $(P \pm 3\sigma_P, a_0 \pm 3\sigma_{a_0}, T_{\text{asc}} \pm 3\sigma_{T_{\text{asc}}})$ . For three targets, XTE J0929–314, IGR J16597–3704, and IGR J17494–3030, the range  $(T_{\text{asc}} \pm P/2)$  is smaller than  $(T_{\text{asc}} \pm 3\sigma_{T_{\text{asc}}})$  and we use the former. We assume that  $P$  and  $a_0$  remain within the same bin for the entire search. While some targets have a non-zero measurement of  $\dot{P} T_{\text{obs}}$  ( $\dot{a}_0 T_{\text{obs}}$ ), in all cases it is much smaller than the template spacing in  $P$  ( $a_0$ ) [322, 339, 492].

It is unlikely that the true source parameters lie exactly on a grid point in the parameter space. Thus the grid is spaced such that the maximum mismatch,  $\mu_{\max}$ , is never more than an acceptable level. The mismatch is defined as the fractional loss in signal-to-noise ratio between the search executed at the true parameters and at the nearest grid point [88]. We calculate the number of grid points required for  $P$ ,  $a_0$  and  $T_{\text{asc}}$  using Eq. (71) of

Leaci and Prix [88], i.e.

$$N_P = \pi^2 \sqrt{6} \mu_{\max}^{-1/2} f a_0 \frac{\gamma T_{\text{drift}}}{P^2} \sigma_P, \quad (6.5)$$

$$N_{a_0} = 3\pi \sqrt{2} \mu_{\max}^{-1/2} f \sigma_{a_0}, \quad (6.6)$$

$$N_{T_{\text{asc}}} = 6\pi^2 \sqrt{2} \mu_{\max}^{-1/2} f a_0 \frac{1}{P} \sigma_{T_{\text{asc}}}, \quad (6.7)$$

where  $\gamma$  is a refinement factor defined in general in Eq. (67) of Leaci and Prix [88]. In the case of O3, the semi-coherent segments are contiguous so we have  $\gamma = N_T = 36$ . We fix  $\mu_{\max} = 0.1$ . A set of software injections into O3 data verifies that a template grid constructed with  $\mu_{\max} = 0.1$  results in a maximum fractional loss in signal-to-noise ratio of 10%. We make the conservative choice of rounding  $N_P$ ,  $N_{a_0}$ , and  $N_{T_{\text{asc}}}$  up to the nearest integer, after setting  $f$  to the highest frequency in each 0.61 Hz sub-band. As in Middleton et al. [9] we find  $N_{a_0} = 1$  for each target and sub-band, and so hold  $a_0$  constant at its central value while searching over  $P$  and  $T_{\text{asc}}$ . Table 6.2 shows  $N_P$ ,  $N_{T_{\text{asc}}}$ , and  $N_{\text{tot}} = N_P N_{T_{\text{asc}}}$  for each target and sub-band. When Eq. (6.5) or (6.7) predicts only two templates for a given sub-band we round up to three, ensuring that the central value of  $P$  or  $T_{\text{asc}}$  from EM observations is included in the template bank. Note that the EM observations are sufficiently precise that  $< 5 \times 10^4$  templates are required across all targets and sub-bands. This is in contrast to the O2 search for continuous gravitational waves from Scorpius X-1, for which  $\sim 10^9$  templates were needed, mainly due to the large uncertainty in  $a_0$ , and the unknown rotation frequency [314].

Table 6.2: Starting frequencies,  $f_s$ , for each  $\sim 0.61$  Hz-wide sub-band, number of templates needed to cover the  $P$  and  $T_{\text{asc}}$  domains in that sub-band,  $N_P$  and  $N_{T_{\text{asc}}}$  respectively, and the total number of templates for each sub-band,  $N_{\text{tot}} = N_P N_{T_{\text{asc}}}$ . The projected semi-major axis  $a_0$  is known precisely enough that we have  $N_{a_0} = 1$  for each sub-band.

Target	$f_s$ (Hz)	$N_P$	$N_{T_{\text{asc}}}$	$N_{\text{tot}}$	Target	$f_s$ (Hz)	$N_P$	$N_{T_{\text{asc}}}$	$N_{\text{tot}}$
IGR J00291+5934	598.6	1	3	3	IGR J17498–2921	400.7	1	17	17
	798.5	1	3	3		534.7	1	22	22
	1197.8	1	3	3		802.0	3	33	99
MAXI J0911–655	339.7	1	10	10	IGR J17511–3057	244.5	1	14	14
	453.3	3	14	42		326.4	1	19	19
	679.9	3	20	60		489.7	1	28	28
XTE J0929–314	184.8	3	52	156	XTE J1751–305	435.0	4	195	780
	246.8	3	69	207		580.4	5	260	1300
	370.2	3	104	312		870.6	8	390	3120
IGR J16597–3704	104.9	49	23	1127	Swift J1756.9–2508	181.8	10	34	340
	140.2	65	31	2015		242.8	13	45	585
	210.4	97	46	4462		364.1	20	67	1340
IGR J17062–6143	163.4	1	1	1	IGR J17591–2342	527.1	1	3	3
	218.2	1	1	1		703.2	3	3	9
	327.3	1	1	1		1054.9	3	4	12
IGR J17379–3747	467.8	4	12	48	XTE J1807–294	190.3	1	7	7
	624.1	5	15	75		254.2	1	9	9
	936.2	7	23	161		381.2	1	13	13
SAX J1748.9–2021	442.1	3	18	54	SAX J1808.4–3658	400.7	4	5	20
	589.8	3	24	72		534.6	5	7	35
	884.7	3	36	108		802.0	7	10	70
NGC 6440 X–2	205.6	1	6	6	XTE J1814–338	314.1	1	9	9
	274.5	1	8	8		419.1	1	12	12
	411.8	1	12	12		628.7	1	17	17
IGR J17494–3030	375.7	21	112	2352	IGR J18245–2452	254.0	3	44	132
	501.4	27	150	4050		339.1	3	58	174
	752.1	41	224	9184		508.7	5	87	435
Swift J1749.4–2807	517.6	7	43	301	HETE J1900.1–2455	377.0	1	17	17
	690.6	9	57	513		503.1	1	22	22
	1035.8	13	85	1105		754.6	1	33	33

### 6.5.3. Thresholds

The output of the search algorithm outlined in Sec. 6.3 is a  $\mathcal{L}$  value corresponding to the most likely path through each sub-band for each orbital template  $(P, a_0, T_{\text{asc}})$ . We flag a template for further follow-up if  $\mathcal{L}$  exceeds a threshold,  $\mathcal{L}_{\text{th}}$ , given an acceptable probability of false alarm. To determine  $\mathcal{L}_{\text{th}}$  we need to know how often pure noise yields  $\mathcal{L} > \mathcal{L}_{\text{th}}$ . The distribution of  $\mathcal{L}$  in noise-only data is unknown analytically, but depends on  $P$ ,  $a_0$ , and the frequency, so Monte-Carlo simulations are used to determine  $\mathcal{L}_{\text{th}}$  in each sub-band for each target.

We estimate the distribution of  $\mathcal{L}$  in noise via two methods: i) using realizations of synthetic Gaussian noise generated using the `lalapps_Makefakedata_v5` program in the LIGO Scientific Collaboration Algorithm Library (LALSuite) [282], and ii) searching O3 data in off-target locations to simulate different realizations of true detector noise. As in Middleton et al. [9] and LVC et al. [314] we generate realizations for each target and sub-band, and apply the search algorithm described in Sec. 6.3 to each realization to recover samples from the noise-only distribution of  $\mathcal{L}$ . Details on how we use these samples to find  $\mathcal{L}_{\text{th}}$  for each sub-band are given in Appendix 6.A1. Unless otherwise noted,  $\mathcal{L}_{\text{th}}$  refers to the lower of the two thresholds derived from the methods listed above to minimize false dismissals.

To define  $\mathcal{L}_{\text{th}}$  we must also account for a “trials factor” due to the number of templates searched in each sub-band. We assume that in noise-only data the spacing between templates is sufficiently large such that each template returns a statistically independent  $\mathcal{L}$ . We can therefore relate the false alarm probability for a search of a sub-band with  $N_{\text{tot}}$  templates,  $\alpha_{N_{\text{tot}}}$ , to the probability of a false alarm for a single template,  $\alpha$ , viz.

$$\alpha_{N_{\text{tot}}} = 1 - (1 - \alpha)^{N_{\text{tot}}}. \quad (6.8)$$

Previous comparable searches have set  $\alpha_{N_{\text{tot}}}$  between 0.01 and 0.3 [9, 293, 314, 332]. In this search, we fix  $\alpha_{N_{\text{tot}}} = 0.3$ , i.e. set the acceptable probability of false alarm at 30% per sub-band. As we search a total of  $20 \times 3 = 60$  sub-bands, we expect  $\sim 18$  candidates above  $\mathcal{L}_{\text{th}}$  due to noise alone (i.e. false alarms), a reasonable number on which to perform more exhaustive follow-up. Looking ahead to the results in Sec. 6.8 we recover 4611 candidates above  $\mathcal{L}_{\text{th}}$ . While this number is much higher than the  $\sim 18$  false alarms expected, almost all of these candidates are non-Gaussian noise artifacts in one (or both) of the detectors. All but 16 of the 4611 candidates are eliminated by the vetoes outlined in Sec. 6.7. We reiterate that  $\mathcal{L}_{\text{th}}$  in each sub-band is the lower of the two thresholds described in Appendix 6.A1, lowering conservatively the probability of false dismissal.

### 6.5.4. Computing resources

A mix of central processing unit (CPU) and graphical processing unit (GPU) resources are used. The GPU implementation of the  $\mathcal{J}$ -statistic is identical to that used in Middleton et al. [9] and LVC et al. [314]. The entire search across all targets and sub-bands takes  $\sim 30$  CPU-hours and  $\sim 40$  GPU-hours when using compute nodes equipped with Xeon Gold 6140 CPUs and NVIDIA P100 12GB PCIe GPUs. Producing  $\mathcal{L}_{\text{th}}$  for each sub-band, as described in Sec. 6.5.3, takes an additional  $\sim 5 \times 10^2$  CPU-hours and  $\sim 4 \times 10^3$  GPU-hours to perform the search on different noise realizations. The additional follow-up in Appendix 6.A2.1 requires an additional  $\sim 10^3$  CPU-hours and  $\sim 10^2$  GPU-hours.

## 6.6. O3 DATA

We use the full dataset from O3, spanning from April 1, 2019, 15:00 UTC to March 27, 2020, 17:00 UTC, from the LIGO Livingston and Hanford observatories. We do not use any data from the Virgo interferometer in this analysis, due to its lower sensitivity compared to the two LIGO observatories in the frequency sub-bands over which we search [524]. The data products ingested by the search algorithm described in Sec. 6.3 are short Fourier transforms (SFTs) lasting 1800 s. Times when the detectors were offline, poorly calibrated, or were impacted by egregious noise, are excluded from analysis by using “Category 1” vetoes as defined in section 5.2 of Davis et al. [524]. The SFTs are generated from the “C01 calibrated self-gated” dataset, which is the calibrated strain data with loud transient glitches removed [525]. Transient glitches otherwise impact the noise floor, as described in section 6.1 of Davis et al. [524]. The median systematic error of the strain magnitude across O3 is < 2% [526, 527].

The coherence time  $T_{\text{drift}} = 10$  d splits the data into  $N_T = 36$  segments. However, due to the month-long commissioning break between O3a and O3b there are two segments without any SFTs. These two segments, starting at October 8, 2019, 15:00 UTC and October 15, 2019, 15:00 UTC, are replaced with a uniform log-likelihood for all frequency bins, which allows the HMM to effectively skip over them while still allowing spin wandering. When generating synthetic data in Secs. 6.5.3 and 6.10 the same two data segments are also replaced with uniform log-likelihoods to emulate the real search.

## 6.7. VETOES

When a candidate is returned with  $\mathcal{L} > \mathcal{L}_{\text{th}}$  we must decide whether there are reasonable grounds to veto the candidate as non-astrophysical. We use three of the vetoes from Middleton et al. [9]: the known line veto, detailed in Sec. 6.7.1, the single interferometer veto, detailed in Sec. 6.7.2, and the off-target veto, detailed in Sec. 6.7.3. The false dismissal rate of these vetoes is less than 5% (see detailed safety investigations in section IVB of Ref. [293] and section IVB of LVC et al. [314]).

### 6.7.1. Known line veto

As part of the detector characterization process many harmonic features are identified as instrumental “known lines” [524, 528]. However, the exact source of these harmonic features is sometimes unidentified, and their impact cannot always be mitigated through isolating hardware components or post-processing the data [524, 528]. We use the vetted known lines list in Goetz et al. [529].

Any candidate close to a known line at frequency  $f_{\text{line}}$  is vetoed. Precisely, if for any time  $0 \leq t \leq T_{\text{obs}}$  the candidate’s frequency path  $f(t)$  satisfies

$$|f(t) - f_{\text{line}}| < 2\pi a_0 f_{\text{line}}/P, \quad (6.9)$$

then the candidate is vetoed<sup>6</sup>.

---

<sup>6</sup>One might consider an additional Doppler broadening factor of  $2\pi a_{\oplus}/1$  yr, where  $a_{\oplus}$  is the mean Earth-Sun distance, as stationary lines in the detector frame get Doppler shifted when transforming the

### 6.7.2. Single interferometer veto

An instrumental artifact is unlikely to be coincident in both detectors, so the candidate's  $\mathcal{L}$  should be dominated by only one of the detectors if the signal is non-astrophysical. On the other hand, an astrophysical signal may need data from both detectors to be detected, or if it is particularly strong may be seen in both detectors individually.

We label the original log-likelihood as  $\mathcal{L}_{\cup}$ , and we also calculate the two single interferometer log-likelihoods  $\mathcal{L}_a$  and  $\mathcal{L}_b$  (where the higher  $\mathcal{L}$  is labeled with  $b$  for definiteness). There are four possible outcomes for this veto:

- i) If the  $\mathcal{L}$  value in one detector is sub-threshold, while the other is above the two-detector  $\mathcal{L}$  value, i.e. one has  $\mathcal{L}_a < \mathcal{L}_{\text{th}}$  and  $\mathcal{L}_b > \mathcal{L}_{\cup}$  and  $f_b(t)$ , the frequency path associated with  $\mathcal{L}_b$ , is close to the frequency path of the candidate when using data from both detectors,  $f_{\cup}(t)$ , i.e.

$$|f_{\cup}(t) - f_b(t)| < 2\pi a_0 f_{\cup}/P, \quad (6.10)$$

then the candidate is likely to be a noise artifact in detector  $b$ , and is vetoed.

- ii) If one has  $\mathcal{L}_a < \mathcal{L}_{\text{th}}$  and  $\mathcal{L}_b > \mathcal{L}_{\cup}$ , but Eq. (6.10) does not hold then the candidate signal cannot be vetoed, as the single-interferometer searches did not find the same candidate. This could indicate that the candidate is a weak astrophysical signal that needs data from both detectors to be detectable.
- iii) If one has  $\mathcal{L}_a > \mathcal{L}_{\text{th}}$  and  $\mathcal{L}_b > \mathcal{L}_{\text{th}}$ , the candidate could represent a strong astrophysical signal that is visible in data from both detectors independently, or it could represent a common noise source. Candidates in this category cannot be vetoed.
- iv) If one has  $\mathcal{L}_a < \mathcal{L}_{\text{th}}$  and  $\mathcal{L}_b < \mathcal{L}_{\cup}$ , data from both detectors is needed for the candidate to be above threshold, possibly indicating a weak astrophysical signal. Candidates in this category cannot be vetoed.

### 6.7.3. Off-target veto

The third veto we apply to a candidate is to search an off-target sky position with the same orbital template. If the off-target search returns  $\mathcal{L} > \mathcal{L}_{\text{th}}$  then the candidate is likely instrumental rather than astrophysical. For this veto, off-target corresponds to shifting the target sky position +40 m in RA and +10° in Dec.

## 6.8. O3 SEARCH RESULTS

The results of the search of all 20 targets are summarized in Fig. 6.1, with  $\alpha_{N_{\text{tot}}} = 0.3$ , i.e. a nominal probability of false alarm per sub-band of 30%. Each symbol indicates, for all templates with  $\mathcal{L} > \mathcal{L}_{\text{th}}$ , the terminating frequency bin and  $p_{\text{noise}}$ , the probability that

---

data to the frame of reference of the source. We opt not to apply this factor for simplicity in this search, as the exact pattern of Doppler modulation depends strongly on the sky location of the target. Looking ahead to the results in Sec. 6.8, we note that none of the 16 surviving candidates is within  $2\pi f a_{\oplus}/1 \text{ yr}$  of any known line.

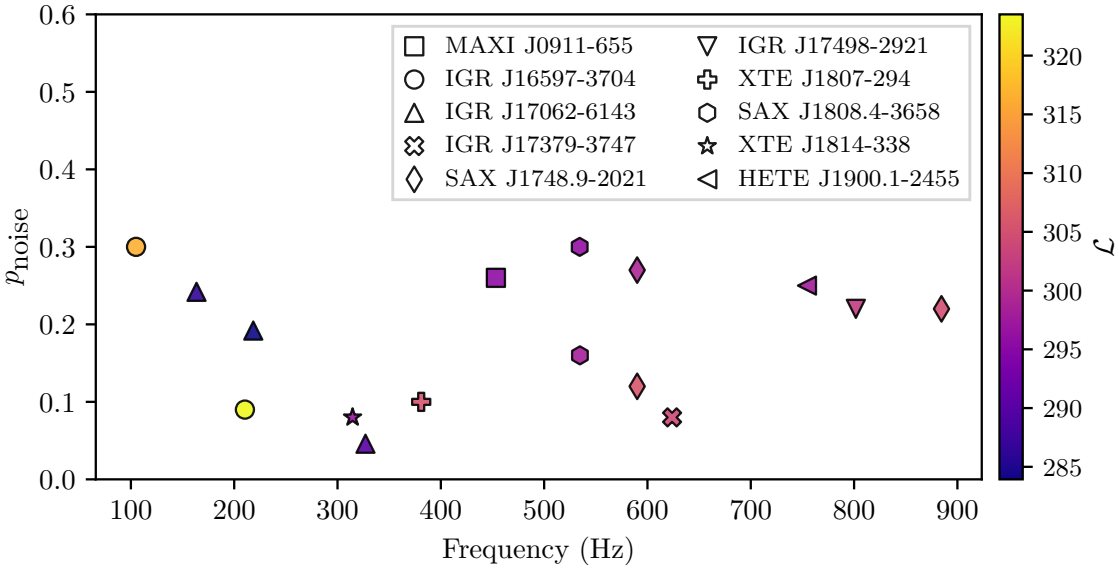


Figure 6.1: Summary of search results across all targets and sub-bands with  $\mathcal{L} > \mathcal{L}_{\text{th}}$ . The different symbols correspond to candidates from different targets. The ordinate shows  $p_{\text{noise}}$  for each candidate, the probability that a search of that candidate’s sub-band in pure noise would return at least one candidate at least as loud as the one seen. The color of each candidate indicates  $\mathcal{L}$  (see color bar at right). Candidates that are eliminated by the vetoes outlined in Sec. 6.7 are not shown for clarity. Details on the search results are in Sec. 6.8 and Appendix 6.A2.

a search of that candidate’s sub-band in pure noise would return at least one candidate at least as loud as the one seen. Equation (6.21) in Appendix 6.A1.5 defines  $p_{\text{noise}}$  explicitly. Each candidate is colored according to  $\mathcal{L}$ . We note that high  $\mathcal{L}$  does not always correspond to low  $p_{\text{noise}}$  due to the differing “trials factors” in each sub-band, as accounted for when calculating  $\mathcal{L}_{\text{th}}$  via Eq. (6.8). A low value of  $p_{\text{noise}}$  corresponds to a higher probability that the candidate is a true astrophysical signal. Targets not listed in the legend return zero candidates above threshold. We do not display in Fig. 6.1 candidates that are eliminated by any of the vetoes described in Sec. 6.7 for clarity.

In total, across all targets and sub-bands, there are 4611 candidates with  $\mathcal{L} > \mathcal{L}_{\text{th}}$ , before the vetoes are applied. All but 100 are eliminated by veto A (known line veto). A further 84 candidates are eliminated by veto B (single interferometer veto). None of the remaining candidates are eliminated by veto C (off-target veto), leaving 16 candidates passing all of the vetoes outlined in Sec. 6.7. None of the surviving candidates from the O3 search coincide in their orbital template and terminating frequency bin with the seven above- or sub-threshold candidates from the O2 search (c.f. Table VI of Middleton et al. [9]). If we set  $\alpha_{N_{\text{tot}}} = 0.01$ , i.e. set the probability of false alarm per sub-band to 1%, the search does not return any candidates with  $\mathcal{L} > \mathcal{L}_{\text{th}}$  for any target or sub-band, after vetoes are applied.

In Secs. 6.8.1–6.8.20 we summarize the search results for each of the 20 targets. To guide the reader, and not clutter the main body of the paper, the full search results for one target, IGR J18245–2452, are shown in Fig. 6.2, while the full search results for the other 19 targets are shown in Figs. 6.4a–6.4s in Appendix 6.A2. The orbital template,

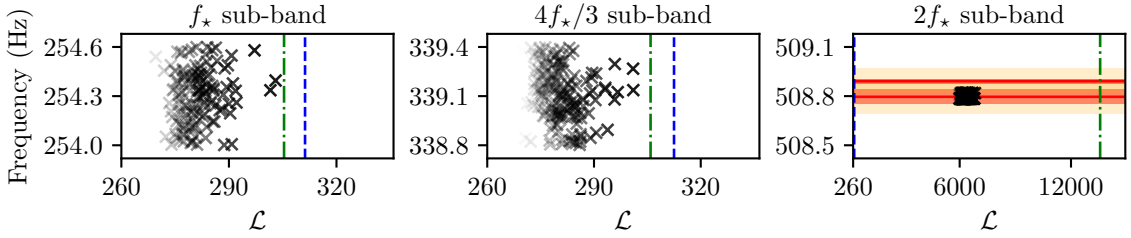


Figure 6.2: Search results for IGR J18245–2452. Black crosses indicate the terminating frequency and  $\mathcal{L}$  for the most likely path through the sub-band for each binary template. The vertical blue dashed (green dot-dashed) lines correspond to the threshold set via Gaussian (off-target) noise realizations,  $\mathcal{L}_{\text{th},G}$  ( $\mathcal{L}_{\text{th},\text{OT}}$ ), in each sub-band. Solid red lines in the right panel indicate the peak frequency of known instrumental lines in the Hanford detector; the orange band indicates the width of the line in the detector frame and the yellow band indicates the increased effective width due to Doppler broadening, as described in Sec. 6.7.1. Multiple overlapping orange bands creates the red bands. The sub-band around 508.8 Hz is especially noisy due to test mass suspension violin mode resonances [524]. The transparency of crosses in sub-bands with many templates, is adjusted relative to the maximum  $\mathcal{L}$  in that sub-band for clarity.

terminating frequency bin,  $\mathcal{L}$ , and  $p_{\text{noise}}$  for all 16 candidates with  $\mathcal{L} > \mathcal{L}_{\text{th}}$  are collated in Table 6.6 in Appendix 6.A2. We present further follow-up of the 16 candidates in Appendix 6.A2.1. We find no convincing evidence that any are a true astrophysical signal.

### 6.8.1. *IGR J18245–2452*

The search results for IGR J18245–2452 are presented in Fig. 6.2. Each marker in Fig. 6.2 shows the terminating frequency and associated  $\mathcal{L}$  of the most likely path through the sub-band for a given template, i.e. choice of  $P$  and  $T_{\text{asc}}$ . The vertical blue dashed (green dot-dashed) lines correspond to the threshold set via Gaussian (off-target) noise realizations,  $\mathcal{L}_{\text{th},G}$  ( $\mathcal{L}_{\text{th},\text{OT}}$ ), in each sub-band, with  $\alpha_{N_{\text{tot}}} = 0.3$ . See Appendix 6.A1 for details on how we set thresholds in each sub-band. The horizontal red lines indicate known instrumental lines in the detector with bandwidth indicated by the shading. There are zero above-threshold candidates in the  $f_*$  and  $4f_*/3$  sub-bands. There are 435 above-threshold candidates in the  $2f_*$  sub-band, which are all coincident with known noise lines in both the Livingston and Hanford detectors, and are therefore eliminated by veto A. The sub-band around 508 Hz is especially noisy due to violin mode resonances [524].

### 6.8.2. *IGR J00291+5934*

The search results for IGR J00291+5934 are shown in Fig. 6.4a, which is laid out identically to Fig. 6.2. There are zero above-threshold candidates in the  $4f_*/3$  and  $2f_*$  sub-bands. There are three above-threshold candidates in the  $f_*$  sub-band, however all three of these candidates are coincident with known noise lines in the Hanford detector, and are therefore eliminated with veto A.

### 6.8.3. *MAXI J0911–655*

The search results for MAXI J0911–655 are shown in Fig. 6.4b, which is laid out identically to Fig. 6.2. There are zero above-threshold candidates in the  $f_\star$  and  $2f_\star$  sub-bands. There is one above-threshold candidate in the  $4f_\star/3$  sub-band which survives all of the vetoes and has  $p_{\text{noise}} = 0.26$ . Additional follow-up, presented in Appendix 6.A2.1, does not provide any evidence that this candidate is a true astrophysical signal.

### 6.8.4. *XTE J0929–314*

The search results for XTE J0929–314 are shown in Fig. 6.4c, which is laid out identically to Fig. 6.2. There are zero above-threshold candidates across all three sub-bands.

### 6.8.5. *IGR J16597–3704*

The search results for IGR J16597–3704 are shown in Fig. 6.4d, which is laid out identically to Fig. 6.2. Each sub-band for this target is contaminated with known noise lines. There are 84 above-threshold candidates in the  $4f_\star/3$  sub-band, however they are all eliminated by veto B. One above-threshold candidate is returned in each of the  $f_\star$  and  $2f_\star$  sub-bands. Both of these candidates survive all of the vetoes, and have  $p_{\text{noise}} = 0.30$  and  $p_{\text{noise}} = 0.09$  respectively. Further follow-up, including the frequency path and cumulative log-likelihood for the latter candidate, is presented in Appendix 6.A2.1. This follow-up does not provide any evidence that either candidate is a true astrophysical signal.

### 6.8.6. *IGR J17062–6143*

The search results for IGR J17062–6143 are shown in Fig. 6.4e, which is laid out identically to Fig. 6.2. Given the long-term timing presented in Bult et al. [492] there is only one template needed in each of the three sub-bands for this target. The template returns  $\mathcal{L} > \mathcal{L}_{\text{th}}$  in all three of the  $f_\star$ ,  $4f_\star/3$ , and  $2f_\star$  sub-bands. All of these candidates survive all of the vetoes, and have  $p_{\text{noise}} = 0.24$ ,  $p_{\text{noise}} = 0.19$ , and  $p_{\text{noise}} = 0.05$  respectively. Further follow-up, including the frequency path and cumulative log-likelihood for the candidate with  $p_{\text{noise}} = 0.05$ , is presented in Appendix 6.A2.1. This follow-up does not provide any evidence that any of the three candidates are a true astrophysical signal.

### 6.8.7. *IGR J17379–3747*

The search results for IGR J17379–3747 are shown in Fig. 6.4f, which is laid out identically to Fig. 6.2. There are zero above-threshold candidates in the  $f_\star$  and  $2f_\star$  sub-bands. There is one above-threshold candidate in the  $4f_\star/3$  sub-band which survives all of the vetoes and has  $p_{\text{noise}} = 0.08$ . Further follow-up, including the frequency path and cumulative log-likelihood, for this candidate is presented in Appendix 6.A2.1. This follow-up does not provide any evidence that the candidate is a true astrophysical signal.

### 6.8.8. *SAX J1748.9–2021*

The search results for SAX J1748.9–2021 are shown in Fig. 6.4g, which is laid out identically to Fig. 6.2. There are zero above-threshold candidates in the  $f_\star$  sub-band. There are two above-threshold candidates in the  $4f_\star/3$  sub-band which survive all of the vetoes and have  $p_{\text{noise}} = 0.12$  and  $p_{\text{noise}} = 0.27$ . There is one above-threshold candidate in the  $2f_\star$  sub-band which survives all of the vetoes and has  $p_{\text{noise}} = 0.22$ . Additional follow-up, presented in Appendix 6.A2.1, does not provide any evidence that any of the three candidates are a true astrophysical signal.

### 6.8.9. *NGC 6440 X–2*

The search results for NGC 6440 X–2 are shown in Fig. 6.4h, which is laid out identically to Fig. 6.2. There are zero above-threshold candidates across all three sub-bands.

### 6.8.10. *IGR J17494–3030*

The search results for IGR J17494–3030 are shown in Fig. 6.4i, which is laid out identically to Fig. 6.2. There are zero above-threshold candidates in the  $f_\star$  and  $2f_\star$  sub-bands. All 4050 candidates in the  $4f_\star/3$  sub-band are above threshold, however all of them are coincident with a known noise line in the Hanford detector, and are therefore eliminated with veto A. The sub-band around 501.7 Hz is especially noisy due to violin mode resonances [524].

### 6.8.11. *Swift J1749.4–2807*

The search results for Swift J1749.4–2807 are shown in Fig. 6.4j, which is laid out identically to Fig. 6.2. There are zero above-threshold candidates in the  $f_\star$  and  $4f_\star/3$  sub-bands. There is one above threshold candidate in the  $2f_\star$  sub-band. However it is coincident with a known noise line in the Hanford detector, and is therefore eliminated by veto A.

### 6.8.12. *IGR J17498–2921*

The search results for IGR J17498–2921 are shown in Fig. 6.4k, which is laid out identically to Fig. 6.2. There are zero above-threshold candidates in the  $f_\star$ , and  $4f_\star/3$  sub-bands. There is one above-threshold candidate in the  $2f_\star$  sub-band which survives all of the vetoes and has  $p_{\text{noise}} = 0.22$ . Additional follow-up, presented in Appendix 6.A2.1, does not provide any evidence that this candidate is a true astrophysical signal.

### 6.8.13. *IGR J17511–3057*

The search results for IGR J17511–3057 are shown in Fig. 6.4l, which is laid out identically to Fig. 6.2. There are zero above-threshold candidates across all three sub-bands.

#### 6.8.14. *XTE J1751–305*

The search results for XTE J1751–305 are shown in Fig. 6.4m, which is laid out identically to Fig. 6.2. There are zero above-threshold candidates across all three sub-bands.

#### 6.8.15. *Swift J1756.9–2508*

The search results for Swift J1756.9–2508 are shown in Fig. 6.4n, which is laid out identically to Fig. 6.2. There are zero above-threshold candidates across all three sub-bands.

#### 6.8.16. *IGR J17591–2342*

The search results for IGR J17591–2342 are shown in Fig. 6.4o, which is laid out identically to Fig. 6.2. There are zero above-threshold candidates across all three sub-bands.

#### 6.8.17. *XTE J1807–294*

The search results for XTE J1807–294 are shown in Fig. 6.4p, which is laid out identically to Fig. 6.2. There are zero above-threshold candidates in the  $f_\star$  and  $4f_\star/3$  sub-bands. There is one above-threshold candidate in the  $2f_\star$  sub-band which survives all of the vetoes and has  $p_{\text{noise}} = 0.10$ . Further follow-up, including the frequency path and cumulative log-likelihood, for this candidate is presented in Appendix 6.A2.1. This follow-up does not provide any evidence that the candidate is a true astrophysical signal.

#### 6.8.18. *SAX J1808.4–3658*

The search results for SAX J1808.4–3658 are shown in Fig. 6.4q, which is laid out identically to Fig. 6.2. There are zero above-threshold candidates in the  $f_\star$  and  $2f_\star$  sub-bands. There are two above-threshold candidates in the  $4f_\star/3$  sub-band which survive all of the vetoes and have  $p_{\text{noise}} = 0.16$  and  $p_{\text{noise}} = 0.30$ . Additional follow-up, presented in Appendix 6.A2.1, does not provide any evidence that either candidate is a true astrophysical signal.

SAX J1808.4–3658 was observed in outburst in August 2019, during O3a [483, 484]. This allows us to perform an additional target-of-opportunity search during only its active phase. If the target only emits continuous gravitational waves during outburst, searching a shorter duration of data increases the probability of detection by increasing the signal-to-noise ratio. The details and results of this target-of-opportunity search are in Sec. 6.9. In summary, after searching with three separate coherence times of  $T_{\text{drift}} = 1 \text{ d}$ ,  $T_{\text{drift}} = 8 \text{ d}$ , and  $T_{\text{drift}} = 24 \text{ d}$ , only one candidate is above threshold and survives all of the vetoes. The candidate is found using  $T_{\text{drift}} = 24 \text{ d}$  in the  $f_\star$  sub-band, and has  $p_{\text{noise}} = 0.02$ . Additional follow-up does not reveal any informative features that would distinguish between an astrophysical signal and noise. It does not coincide with either of the two candidates in the  $4f_\star/3$  sub-band found in the semi-coherent search using the full O3 data set.

### 6.8.19. *XTE J1814–338*

The search results for XTE J1814–338 are shown in Fig. 6.4r, which is laid out identically to Fig. 6.2. There are zero above-threshold candidates in the  $4f_\star/3$  and  $2f_\star$  sub-bands. There is one above-threshold candidate in the  $f_\star$  sub-band which survives all of the vetoes and has  $p_{\text{noise}} = 0.08$ . Further follow-up, including the frequency path and cumulative log-likelihood, for this candidate is presented in Appendix 6.A2.1. This follow-up does not provide any evidence that the candidate is a true astrophysical signal.

### 6.8.20. *HETE J1900.1–2455*

The search results for HETE J1900.1–2455 are shown in Fig. 6.4s, which is laid out identically to Fig. 6.2. There are zero above-threshold candidates in the  $f_\star$  sub-band. All 22 templates in the  $4f_\star/3$  sub-band return candidates above  $\mathcal{L}_{\text{th}}$ , however these candidates are all coincident with known noise lines in the Hanford detector, and are summarily eliminated with veto A. The sub-band around 503 Hz is especially noisy due to violin mode resonances [524]. There is one above-threshold candidate in the  $2f_\star$  sub-band which survives all of the vetoes and has  $p_{\text{noise}} = 0.25$ . Additional follow-up, presented in Appendix 6.A2.1, does not provide any evidence that this candidate is a true astrophysical signal.

## 6.9. TARGET-OF-OPPORTUNITY SEARCH: SAX J1808.4–3658 IN OUTBURST

On August 7 2019 SAX J1808.4–3658 went into outburst [482]. The Neutron star Interior Composition Explorer (NICER) team undertook a high-cadence monitoring campaign, and performed a timing analysis of the pulsations [483]. The outburst lasted for roughly 24 days, with enhanced X-ray flux observed between August 7 2019 and August 31 2019 (see Fig. 1 of Bult et al. [483]). We note that the *Swift* X-ray Telescope observed increased X-ray activity from August 6 2019, and observations in the optical  $i'$ -band with the Las Cumbres Observatory network detected an increased flux from July 25 2019 [484].

Outburst events are attributed to in-falling plasma that is channeled by the magnetosphere onto a localized region on the neutron star surface, creating a hot spot that rotates with the star [530]. As the observed X-ray flux is assumed to be linearly proportional to the mass accretion rate, an outburst could result in a larger mountain on the neutron star surface (or excite  $r$ -modes in the interior), compared to when the AMXP is in quiescence [342, 349].

If continuous gravitational waves are only emitted from SAX J1808.4–3658 when it is in outburst, searching all of the O3 data decreases the signal-to-noise ratio, as compared to only searching data from the outburst. To protect against this possibility, we do an additional search for continuous gravitational waves from SAX J1808.4–3658 using data from both LIGO observatories between 1249171218 GPS time (August 7 2019) and 1251244818 GPS time (August 31 2019), rather than data from the entirety of O3, as in Sec. 6.8.18.

### 6.9.1. Search parameters

The search algorithm is laid out in Sec. 6.3. We run the search using three different coherence times, setting  $T_{\text{drift}} = 1 \text{ d}$ ,  $T_{\text{drift}} = 8 \text{ d}$ , and  $T_{\text{drift}} = 24 \text{ d}$ . We search three sub-bands centered on  $\{1, 4/3, 2\}f_\star$ , for each  $T_{\text{drift}}$ . The width of the sub-band depends on  $T_{\text{drift}}$ . It is  $\sim 0.76 \text{ Hz}$  for the searches with  $T_{\text{drift}} = 1 \text{ d}$  and  $8 \text{ d}$ , and is  $\sim 1.01 \text{ Hz}$  for the search with  $T_{\text{drift}} = 24 \text{ d}$ . Given the precise timing achieved during the outburst in 2019 [483], and the shorter search duration, only one  $\{P, T_{\text{asc}}, a_0\}$  template is required for each sub-band, according to Eqs. (6.5)–(6.7). Due to the different values of  $T_{\text{drift}}$ , shorter total duration, and different number of templates, we re-calculate  $\mathcal{L}_{\text{th}}$  for each sub-band and value of  $T_{\text{drift}}$ , using the procedure outlined in Sec. 6.5.3 and Appendix 6.A1. As in the full O3 search, we set the probability of false alarm in each sub-band at  $\alpha_{N_{\text{tot}}} = 0.3$ . For all candidates that have  $\mathcal{L} > \mathcal{L}_{\text{th}}$  we apply the three vetoes described in 6.7.

### 6.9.2. Search results

For  $T_{\text{drift}} = 1 \text{ d}$ , the search in the  $f_\star$  sub-band returns one candidate above  $\mathcal{L}_{\text{th}}$ . The candidate survives both veto A (known line) and veto B (single interferometer), but fails veto C (off-target). The searches in the  $4/3f_\star$  and  $2f_\star$  sub-bands do not return any candidates above  $\mathcal{L}_{\text{th}}$ .

For  $T_{\text{drift}} = 8 \text{ d}$ , there are no candidates above  $\mathcal{L}_{\text{th}}$  in any of the three sub-bands.

For  $T_{\text{drift}} = 24 \text{ d}$ , the searches in the  $4f_\star/3$  and  $2f_\star$  sub-bands do not return any candidates above  $\mathcal{L}_{\text{th}}$ . The search in the  $f_\star$  sub-band does return one candidate above  $\mathcal{L}_{\text{th}}$ . This candidate survives all of the vetoes outlined in Sec. 6.7. We remind the reader that with  $\alpha_{N_{\text{tot}}} = 0.3$  and nine sub-bands searched (three for each of the three choices of  $T_{\text{drift}}$ ), we should expect  $\sim 3$  candidates above threshold purely due to noise. The probability that we would see a value of  $\mathcal{L}$  at least this large if this sub-band is pure noise,  $p_{\text{noise}}$ , is 0.02. The template and frequency of the candidate are not coincident with any candidate from the full O3 search (see Table 6.6) or the sub-threshold candidate found in the search of this sub-band in O2 data [9]. By setting  $T_{\text{drift}} = T_{\text{obs}} = 24 \text{ d}$  we perform a fully coherent search across this time period, with a frequency bin size of  $\Delta f = 2.4 \times 10^{-7} \text{ Hz}$ . We describe in Appendix 6.A3 further follow-up of this candidate. In summary, we find no significant evidence that it is an astrophysical signal rather than a noise fluctuation.

## 6.10. FREQUENTIST UPPER LIMITS

If we assume that the remaining candidates reported in Sec. 6.8 and Appendix 6.A2 are false alarms, we can place an upper limit on the wave strain that is detectable at a confidence level of 95%,  $h_0^{95\%}$ , in a sub-band. The value of  $h_0^{95\%}$  is a function of our algorithm, the detector configuration during O3, and our assumptions about the signal model. We describe the method used to estimate  $h_0^{95\%}$  in Sec. 6.10.1, present the upper limits in each sub-band in Sec. 6.10.2, and compare the results to indirect methods that calculate the expected strain in the  $2f_\star$  sub-band in Sec. 6.10.3. The astrophysical implications are discussed in Sec. 6.10.4.

### 6.10.1. Upper limit procedure in a sub-band

We set empirical frequentist upper limits in each sub-band using a sequence of injections into O3 SFTs. For each sub-band we inject  $N_{\text{trials}} = 100$  simulated binary signals at 12–15 fixed values of  $h_0$  using `1a1apps_Makefakedata_v5` [282]. For each of the  $N_{\text{trials}}$  injections at a fixed  $h_0$  we select a constant injection frequency,  $f_{\text{inj}}$ , uniformly from the sub-band. While the injected signal has zero spin-wandering, we still use  $T_{\text{drift}} = 10$  d in the search algorithm outlined in Sec. 6.3 to mimic the real search. The injected period,  $P_{\text{inj}}$ , and time of ascension,  $T_{\text{asc,inj}}$  are chosen uniformly from the ranges  $[P - 3\sigma_P, P + 3\sigma_P]$  and  $[T_{\text{asc}} - 3\sigma_{T_{\text{asc}}}, T_{\text{asc}} + 3\sigma_{T_{\text{asc}}}]$  respectively. We keep  $a_0$  fixed at the precisely known value for each target. The polarization,  $\psi$ , is chosen uniformly from the range  $[0, 2\pi]$ . The cosine of the projected inclination angle of the neutron star spin axis with our line of sight,  $\cos \iota$ , is chosen uniformly from the range  $[-1, 1]$ <sup>7</sup>. We then search for the injected signal with the template in this sub-band’s template grid that is nearest to  $\{P_{\text{inj}}, T_{\text{asc,inj}}\}$ . We re-calculate  $\mathcal{L}_{\text{th}}$  such that the probability of false alarm in each sub-band is  $\alpha_{N_{\text{tot}}} = 0.01$ . This allows us to set conservative upper limits, even in sub-bands where we have marginal candidates above a threshold corresponding to a probability of false alarm of 30% per sub-band. By recording the fraction of injected signals we recover at each  $h_0$  with  $\mathcal{L} > \mathcal{L}_{\text{th}}$  we estimate the efficiency,  $\varepsilon$ , as a function of  $h_0$ . We then perform a logistic regression [146] to obtain a sigmoid fit to  $\varepsilon(h_0)$ , and solve

$$\varepsilon(h_0^{95\%}) = 0.95 , \quad (6.11)$$

to find an estimate of  $h_0^{95\%}$  in the given sub-band.

One might reasonably ask, how precise is this estimate of  $h_0^{95\%}$ ? The main factors impacting the precision are: i) the precision of the most likely parameters of the sigmoid, as estimated via logistic regression, when solving Eq. (6.11) for  $h_0^{95\%}$ , given the  $N_{\text{trials}}$  injections done at 12–15 values of  $h_0$ ; and ii) the assumption that the strain data (and hence the SFTs) are perfectly calibrated. We investigate the impact of (i) by drawing alternative sigmoid fits of  $\varepsilon(h_0)$  using the covariance matrix of the parameters returned by the logistic regression. We find that inverting these alternative fits through Eq. (6.11) results in a value of  $h_0^{95\%}$  that varies by less than 5% from the value calculated via the most likely parameters (at the 95% confidence level). The impact of (ii) is trickier to quantify. As described in Sun et al. [526, 527] the median systematic error in the magnitude of the strain is less than 2% in the 20–2000 Hz frequency band across O3a. The statistical uncertainty around the measurement of calibration bias means that in the worst case the true magnitude of the calibration bias may be as large as 7%. However, the calibration bias at a given frequency is not correlated between the detectors (see Figures 16 and 17 in Sun et al. [526]), and so the impact on a continuous gravitational wave search that combines data from both detectors is likely to be less than 7%.

In light of the above considerations we quote  $h_0^{95\%}$  to a precision of two significant figures, but we emphasize that estimating  $h_0^{95\%}$  involves many (potentially compounding) uncertainties. Subsequent conclusions about the physical system that are drawn from estimates of  $h_0^{95\%}$  cannot be more precise than the estimate of  $h_0^{95\%}$  itself.

---

<sup>7</sup>While the inclination angle of the binary with respect to our line of sight is restricted via EM observations for some of our targets, we opt to marginalize over  $\cos \iota$  as the neutron star spin axis may not necessarily align with the orbital axis of the binary. It is possible to scale our results via equation (19) of Messenger et al. [522], if one wishes to fix  $\cos \iota$ .

Table 6.3: Upper limits on the detectable gravitational wave strain at a 95% confidence level,  $h_0^{95\%}$ , in each of the sub-bands for each target. See Sec. 6.10.1 for details on how they are estimated, and the precision to which they are known. Upper limits are not estimated in sub-bands marked with a “–” as these sub-bands are highly contaminated with known noise lines.

Target	$f_\star$	$h_0^{95\%}$ in each sub-band ( $\times 10^{-26}$ )		
		$4f_\star/3$	$2f_\star$	
IGR J00291+5934	–	7.6	11	
MAXI J0911–655	7.7	6.4	7.3	
XTE J0929–314	5.1	5.3	6.4	
IGR J16597–3704	7.5	–	5.6	
IGR J17062–6143	8.1	4.7	4.7	
IGR J17379–3747	8.5	7.4	10	
SAX J1748.9–2021	9.2	7.7	10	
NGC 6440 X–2	6.2	7.2	5.8	
IGR J17494–3030	8.3	–	9.0	
Swift J1749.4–2807	11	17	24	
IGR J17498–2921	7.0	6.6	8.4	
IGR J17511–3057	7.5	5.5	6.6	
XTE J1751–305	10	8.3	9.7	
Swift J1756.9–2508	8.1	8.8	6.3	
IGR J17591–2342	9.5	11	14	
XTE J1807–294	6.1	5.0	5.6	
SAX J1808.4–3658	6.4	6.9	8.8	
XTE J1814–338	9.4	6.0	6.9	
IGR J18245–2452	9.0	6.3	–	
HETE J1900.1–2455	5.6	–	8.4	

### 6.10.2. Upper limits

The estimates of  $h_0^{95\%}$  for each target and sub-band are listed in Table 6.3. Dashes correspond to sub-bands that are highly contaminated with noise lines, which preclude the procedure described in Sec. 6.10.1, as one always finds  $\mathcal{L} > \mathcal{L}_{\text{th}}$ , regardless of  $h_0$ . The most sensitive sub-bands are for IGR J17062–6143 with  $h_0^{95\%} = 4.7 \times 10^{-26}$  in both the  $4f_\star/3$  and  $2f_\star$  sub-bands (centered around 218.2 Hz and 327.6 Hz respectively). These sub-bands lie in the most sensitive band of the detector, and the binary elements are known to high precision [492], so only one template is needed in each sub-band, corresponding to a relatively lower  $\mathcal{L}_{\text{th}}$  at fixed probability of false alarm.

No estimates of  $h_0^{95\%}$  were established in Middleton et al. [9] for the five targets therein. The search of XTE J1751–305 in S6 data estimated  $h_0^{95\%} \approx 3.3 \times 10^{-24}$ ,  $4.7 \times 10^{-24}$ , and  $7.8 \times 10^{-24}$  in three sub-bands corresponding to  $f_\star$ , an  $r$ -mode frequency, and  $2f_\star$  respectively [303]. Our estimates of  $h_0^{95\%}$  for XTE J1751–305 improve these results by two orders of magnitude, because the detector is more sensitive, and  $T_{\text{drift}}$  is longer.

### 6.10.3. Comparison to expected strain from AMXPs

It is valuable to consider how strong the signal from our targets could be, given EM observations. If we assume that all rotational energy losses, as observed in the frequency derivative  $\dot{f}_\star$ , are converted into gravitational radiation, the indirect spin-down limit on the maximum strain,  $h_{0,\text{sd}}$ , is [278]

$$h_{0,\text{sd}} = 4.0 \times 10^{-28} \left( \frac{8 \text{ kpc}}{D} \right) \times \left( \frac{600 \text{ Hz}}{f_{\text{GW}}} \right)^{1/2} \left( \frac{-\dot{f}_{\text{GW}}}{10^{-14} \text{ Hz s}^{-1}} \right)^{1/2}, \quad (6.12)$$

where  $D$  is the distance to the target,  $f_{\text{GW}}$  is the gravitational wave frequency, and  $\dot{f}_{\text{GW}}$  is its derivative. In Eq. (6.12) we assume  $I_{zz}/I_0 \approx 1$ , i.e. the  $zz$  component of the moment-of-inertia tensor ( $I_{zz}$ ) is very close to the moment-of-inertia of an undeformed star ( $I_0$ ). We assume  $f_{\text{GW}} \approx 2\dot{f}_\star$  when computing Eq. (6.12) for each of our targets. We list the best estimates for the distance to each target in the second column of Table 6.4. These estimates are typically poorly known, especially if there is no known counterpart observed in wavelengths other than X-ray for the target. We use the central estimate of the distance in Eq. (6.12).

For AMXPs,  $\dot{f}_\star$  is estimated by constructing a phase-connected timing solution when the target is in outburst, but estimates for  $\dot{f}_\star$  in quiescence are also possible for targets that have gone into outburst multiple times. The  $\dot{f}_\star$  observed during outburst can be either positive (corresponding to spin-up) or negative (corresponding to spin-down), while in quiescence  $\dot{f}_\star$  is typically (but not always) negative [45, 481]. The third column of Table 6.4 records  $\dot{f}_\star$  for each of our targets. When  $\dot{f}_\star$  has been measured in multiple outburst events, only the  $\dot{f}_\star$  from the most recent outburst is listed. For  $\dot{f}_\star < 0$  we assume  $\dot{f}_{\text{GW}} \approx 2\dot{f}_\star$  in Eq. (6.12). For targets with  $\dot{f}_\star < 0$  (in either quiescent or active phases) we find  $10^{-28} \lesssim h_{0,\text{sd}} \lesssim 10^{-27}$  (fourth column of Table 6.4), an order of magnitude lower than the estimated value of  $h_0^{95\%}$ .

As argued in Middleton et al. [9], for  $\dot{f}_\star > 0$  the torque due to gravitational radiation reaction may be masked by the accretion torque, allowing larger values of  $\dot{f}_{\text{GW}}$ , as long as one has  $\dot{f}_\star = \dot{f}_{\text{acc}} + \dot{f}_{\text{GW}}$ , where  $\dot{f}_{\text{acc}}$  is the spin-up rate due to accretion. A reasonable choice, without excessive fine-tuning, is to set  $\dot{f}_{\text{GW}} \approx -\dot{f}_\star$ , for an order-of-magnitude estimate in Eq. (6.12), i.e. assuming  $|\dot{f}_{\text{acc}}| \approx 2|\dot{f}_{\text{GW}}|$ . The resultant values for  $h_{0,\text{sd}}$  for targets with  $\dot{f}_\star > 0$  are all well below the estimates of  $h_0^{95\%}$  set in Sec. 6.10.2, and fall in the range  $10^{-28} \lesssim h_{0,\text{sd}} \lesssim 10^{-27}$ .

Another avenue through which EM observations can constrain  $h_0$  is by assuming that the X-ray flux is proportional to the mass accretion rate, and that the torque due to accretion balances the gravitational radiation reaction. The torque-balance limit is [278, 333]

$$h_{0,\text{torque}} = 5 \times 10^{-27} \left( \frac{600 \text{ Hz}}{f_{\text{GW}}} \right)^{1/2} \times \left( \frac{F_X}{10^{-8} \text{ erg s}^{-1} \text{ cm}^{-2}} \right)^{1/2}, \quad (6.13)$$

where  $F_X$  is the observed bolometric X-ray flux. Eq. (6.13) has a few hidden assumptions, namely: i) that the mass of the neutron star is  $1.4M_\odot$ , ii) that all of the accretion luminosity is radiated as an X-ray flux, and iii) that the accretion torque is applied at the radius of the neutron star, which is set to 10 km. The exact dependence of the torque-balance limit on these assumptions is discussed in Zhang et al. [333]. We take  $f_{\text{GW}} \approx 2f_\star$  for each of our targets, as for Eq. (6.12). We take  $F_X = F_{X,\text{max}}$ , the maximum recorded X-ray flux from each target when it was in outburst (fifth column of Table 6.4), providing an upper limit on  $h_{0,\text{torque}}$  (sixth column of Table 6.4). We find  $5 \times 10^{-28} \lesssim h_{0,\text{torque}} \lesssim 1 \times 10^{-27}$  across all targets.

*Full caption for Table 6.4:* Maximum expected strain from each target, as inferred from EM observations. The second column contains the best estimate for the distance to the target. Targets with “-” listed as the frequency derivative (third column),  $\dot{f}_\star$ , do not have a measured value during outburst, and also do not have a long-term (quiescent)  $\dot{f}_\star$  measured either. The labels (A) and (Q) indicate that  $\dot{f}_\star$  is measured in outburst and quiescence respectively. The scaling equations used to estimate the maximum spin-down strain (fourth column),  $h_{0,\text{sd}}$ , and the maximum strain assuming torque-balance (sixth column),  $h_{0,\text{torque}}$ , are Eqs. (6.12) and (6.13) respectively. The  $h_{0,\text{sd}}$  value is calculated using the central distance and  $\dot{f}_\star$  estimates. The  $h_{0,\text{torque}}$  value is calculated using the maximum bolometric X-ray flux measured during outburst (fifth column),  $F_{X,\text{max}}$ , which is typically measured to a precision of  $\sim 10\%$ . The X-ray flux of each target in quiescence is not shown, as it is only measured for half of the targets, and is usually  $\sim 1 - 2$  orders of magnitude lower than  $F_{X,\text{max}}$ . The seventh column contains  $h_0^{95\%}$  in the  $2f_\star$  sub-band (fourth column of Table 6.3) to facilitate comparisons between  $h_0^{95\%}$  and  $h_{0,\text{torque}}$  or  $h_{0,\text{sd}}$ .

Table 6.4: Full caption on previous page.

Target	Distance (kpc)	$\dot{f}_\star$ (Hz s $^{-1}$ )	$h_{0,\text{sd}}$ ( $\times 10^{-26}$ )	$F_{X,\text{max}}$ ( $\times 10^{-8}$ erg s $^{-1}$ cm $^{-2}$ )	$h_{0,\text{torque}}$ ( $\times 10^{-26}$ )	$h_0^{95\%}$ ( $\times 10^{-26}$ )	Refs.
IGR J00291+5934	4.2(5)	$-4.0(1.4) \times 10^{-15}$ (Q)	0.05	0.35	0.2	11	[337, 348, 531, 532]
MAXI J0911–655	9.45(15)	-	-	0.047	0.1	7.3	[196, 486, 487]
XTE J0929–314	7.4 <sup>a</sup>	$-9.2(4) \times 10^{-14}$ (A)	0.2	0.1	0.2	6.4	[348, 488, 533]
IGR J16597–3704	9.1 <sup>b</sup>	-	-	0.065	0.2	5.6	[491]
IGR J17062–6143	7.3(5)	$+3.77(9) \times 10^{-15}$ (A)	0.04 <sup>c</sup>	0.006	0.05	4.7	[492, 534]
IGR J17379–3747	8 <sup>d</sup>	$-1.2(1.9) \times 10^{-14}$ (A)	0.05	0.04	0.08	10	[493, 494, 535, 536]
SAX J1748.9–2021	8.5 <sup>b</sup>	-	-	0.077	0.1	10	[348, 495, 537, 538]
NGC 6440 X–2	8.5 <sup>b</sup>	-	-	0.02	0.09	5.8	[497, 537]
IGR J17494–3030	8 <sup>d</sup>	$-2.1(7) \times 10^{-14}$ (Q)	0.07	0.0143	0.05	9.0	[498]
Swift J1749.4–2807	6.7(1.3)	-	-	0.0352	0.07	24	[500, 501, 539]
IGR J17498–2921	7.6(1.1)	$-6.3(1.9) \times 10^{-14}$ <sup>e</sup> (A)	0.1	0.2	0.2	8.4	[502, 503, 540]
IGR J17511–3057	3.6(5)	$+4.8(1.4) \times 10^{-14}$ (A)	0.2 <sup>c</sup>	0.2	0.2	6.6	[505]
XTE J1751–305	6.7 <sup>f</sup>	$-5.5(1.2) \times 10^{-15}$ (Q)	0.04	0.29	0.2	9.7	[338, 348, 507]
		$+3.7(1.0) \times 10^{-13}$ (A)	0.2 <sup>c</sup>				
Swift J1756.9–2508	8 <sup>d</sup>	$-4.8(6) \times 10^{-16}$ (Q)	0.02	0.288	0.3	6.3	[348, 508]
		$-4.3(2.1) \times 10^{-11}$ <sup>e</sup> (A)	5				
IGR J17591–2342	7.6(7)	$-7.1(4) \times 10^{-14}$ (A)	0.1	0.0535	0.09	14	[510, 541, 542]
XTE J1807–294	8 <sup>d</sup>	$+2.7(1.0) \times 10^{-14}$ (A)	0.08 <sup>c</sup>	0.2	0.3	8.8	[348, 512, 543]
SAX J1808.4–3658	3.3 <sup>+0.3</sup> <sub>−0.2</sub>	$-1.01(7) \times 10^{-15}$ (Q)	0.04	0.103	0.1	5.6	[348, 483, 544, 545]
		$-3.02(13) \times 10^{-13}$ (A)	0.7				
XTE J1814–338	10.25(1)	$-6.7(7) \times 10^{-14}$ (A)	0.1	0.069	0.1	6.9	[348, 514, 546]
IGR J18245–2452	5.5 <sup>b</sup>	-	-	0.0466	0.1	-	[49, 516, 537]
HETE J1900.1–2455	4.5(2)	$+4.2(1) \times 10^{-13}$ (A)	0.4 <sup>c</sup>	0.09	0.1	8.4	[348, 519, 547, 548]

<sup>a</sup>Estimate assumes conservative mass transfer during accretion. An alternative estimate gives less than 4 kpc [533]. <sup>b</sup>Uncertainty not quoted as target located in a globular cluster. <sup>c</sup>Assumes  $\dot{f}_{\text{GW}} \approx -\dot{f}_\star$ , see text for details. <sup>d</sup>Unknown, but as the target is in the direction of the galactic centre a fiducial value of 8 kpc is assumed in the literature. <sup>e</sup>Estimate of  $\dot{f}_\star$  consistent with zero at a  $3\sigma$  level. <sup>f</sup>Lower limit.

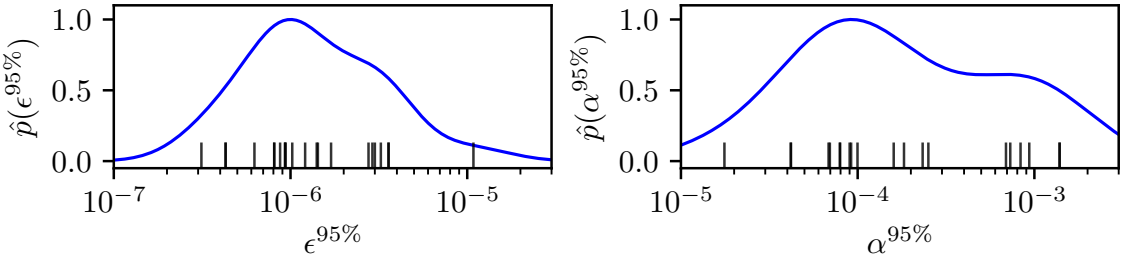


Figure 6.3: Kernel density estimate of the PDF of the constraints on ellipticity  $\epsilon^{95\%}$  (left panel) and dimensionless  $r$ -mode amplitude  $\alpha^{95\%}$  (right panel) via Eqs. (6.14) and (6.15) respectively. Both PDFs are normalized to a height of one. The black dashes in both panels correspond to the individual estimates of  $\epsilon^{95\%}$  or  $\alpha^{95\%}$  from each target.

#### 6.10.4. Astrophysical implications

The estimates of  $h_0^{95\%}$  given in Sec. 6.10.2 can be converted into constraints on the physical parameters that govern the mechanism putatively generating continuous gravitational waves in each sub-band.

In the  $2f_\star$  sub-band the simplest emission mechanism is that of a perpendicular biaxial rotator (using the language from Sun et al. [309]), for which we calculate the upper limit of the ellipticity of the neutron star as [262]

$$\epsilon^{95\%} = 2.1 \times 10^{-6} \left( \frac{h_0^{95\%}}{10^{-25}} \right) \left( \frac{D}{8 \text{ kpc}} \right) \left( \frac{600 \text{ Hz}}{f_{\text{GW}}} \right)^2, \quad (6.14)$$

assuming  $I_{zz} = 10^{38} \text{ kg m}^2$ . Using the central estimate for  $D$  (second column of Table 6.4), we find the strictest constraint, from all of our targets,  $\epsilon^{95\%} = 3.1 \times 10^{-7}$  for IGR J00291+5934. A kernel density estimate of the probability density function (PDF) of the constraints  $\epsilon^{95\%}$ ,  $\hat{p}(\epsilon^{95\%})$ , for all our targets, is shown in the left panel of Fig. 6.3. It is peaked around  $\epsilon^{95\%} \sim 10^{-6}$ .

In the  $4f_\star/3$  sub-band the emission mechanism is via  $r$ -modes, the strength of which is parametrized as [273]

$$\alpha^{95\%} = 1.0 \times 10^{-4} \left( \frac{h_0^{95\%}}{10^{-25}} \right) \left( \frac{D}{8 \text{ kpc}} \right) \left( \frac{600 \text{ Hz}}{f_{\text{GW}}} \right)^3. \quad (6.15)$$

Eq. (6.15) assumes  $f_{\text{GW}} \approx 4f_\star/3$ , which may not be true, as discussed in Sec. 6.5 [271, 272]. The strictest constraint, from all of our targets, is  $\alpha^{95\%} = 1.8 \times 10^{-5}$ , again for IGR J00291+5934. A kernel density estimate of the PDF of the constraints  $\alpha^{95\%}$ ,  $\hat{p}(\alpha^{95\%})$ , for all our targets, is shown in the right panel of Fig. 6.3. It is peaked around  $\alpha^{95\%} \sim 10^{-4}$ .

The kernel density estimates of the PDFs  $\hat{p}(\epsilon^{95\%})$  and  $\hat{p}(\alpha^{95\%})$  in Fig. 6.3 are not constraints on  $\epsilon$  and  $\alpha$  respectively, nor are they expressing the uncertainty in each individual estimate of  $\epsilon^{95\%}$  or  $\alpha^{95\%}$  (which are dominated by the uncertainty in  $h_0^{95\%}$ , and the distance, see column two of Table 6.4). They are instead presented to indicate where the constraints on  $\epsilon^{95\%}$  and  $\alpha^{95\%}$  lie, given the strain upper limits calculated for the targets in this search. That is, they are estimates of the true probability distribution of the constraints one would obtain for  $\epsilon$  and  $\alpha$ , given a large population of AMXPs

(assuming the targets studied here are representative of this larger population). The kernel density estimates are calculated by summing Gaussian kernels centered on each data point, with bandwidth chosen to minimize the asymptotic mean integrated square error [428].

The physical mechanism for emission in the  $f_\star$  sub-band is less well-defined. A biaxial non-perpendicular rotator emits gravitational radiation at both  $f_\star$  and  $2f_\star$  [262, 276, 549]. The emission at  $f_\star$  dominates the  $2f_\star$  emission for both  $\theta \lesssim 20^\circ$  and  $|\cos i| \lesssim 0.8$ , where  $\theta$  is the wobble angle (see figure 5 of Sun et al. [309] for details). The value of  $\theta$  is low for certain models involving pinned superfluid interiors [276, 277]. Other possibilities exist, including a triaxial rotator [256, 260, 550]. We recommend future searches to also consider searching the  $f_\star$  sub-band, due to the wealth of information that a continuous gravitational wave detection at this frequency would provide regarding neutron star structure.

## 6.11. CONCLUSIONS

We present the results of a search for continuous gravitational waves from 20 accreting low-mass X-ray binaries in the Advanced LIGO O3 dataset. Five of these targets were searched before in O2 [9], and one was searched in S6 [303]. The search pipeline we use allows for spin-wandering and tracks the orbital phase of the binary via a hidden Markov model and the  $\mathcal{J}$ -statistic respectively. The targets have well-constrained rotational frequencies,  $f_\star$ , and orbital elements from electromagnetic observations of outburst events, restricting the parameter space. For each target we search three  $\sim 0.61$  Hz-wide sub-bands centered on  $\{1, 4/3, 2\}f_\star$ . We also perform a target-of-opportunity search for emission from SAX J1808.4–3658, which went into outburst during O3a.

We find no candidates that survive our veto procedure and are above a threshold corresponding to a 1% false alarm probability per sub-band. We find 16 candidates that survive our astrophysical vetoes when we set the threshold to 30% false alarm probability per sub-band. As we search a total of 60 sub-bands, this number of surviving candidates is consistent with the expected number of false alarms. These candidates are systematically investigated with further follow-up. In all cases, the follow-up does not provide convincing evidence that any are real astrophysical signals. However, they could not be convincingly ruled out, which is not surprising given their borderline significance. We record the orbital template and frequencies recovered for these candidates, and recommend that they are followed up in future gravitational wave data sets, and with different pipelines.

The target-of-opportunity search returns one candidate above threshold that survives our veto procedure. Additional, detailed follow-up of this candidate does not produce convincing evidence that it is a true astrophysical signal rather than a noise fluctuation.

Assuming all of the candidates are not astrophysical, we set upper limits on the strain at 95% confidence in each sub-band. Using these estimates, the strictest constraint on neutron star ellipticity is  $\epsilon^{95\%} = 3.1 \times 10^{-7}$ . The strictest constraint we place on the  $r$ -mode amplitude is  $\alpha^{95\%} = 1.8 \times 10^{-5}$ . Both of these constraints come from IGR J00291+5934.

## ACKNOWLEDGMENTS

This material is based upon work supported by NSF's LIGO Laboratory which is a major facility fully funded by the National Science Foundation. The authors also gratefully acknowledge the support of the Science and Technology Facilities Council (STFC) of the United Kingdom, the Max-Planck-Society (MPS), and the State of Niedersachsen/Germany for support of the construction of Advanced LIGO and construction and operation of the GEO600 detector. Additional support for Advanced LIGO was provided by the Australian Research Council. The authors gratefully acknowledge the Italian Istituto Nazionale di Fisica Nucleare (INFN), the French Centre National de la Recherche Scientifique (CNRS) and the Netherlands Organization for Scientific Research, for the construction and operation of the Virgo detector and the creation and support of the EGO consortium. The authors also gratefully acknowledge research support from these agencies as well as by the Council of Scientific and Industrial Research of India, the Department of Science and Technology, India, the Science & Engineering Research Board (SERB), India, the Ministry of Human Resource Development, India, the Spanish Agencia Estatal de Investigación, the Vicepresidència i Conselleria d'Innovació, Recerca i Turisme and the Conselleria d'Educació i Universitat del Govern de les Illes Balears, the Conselleria d'Innovació, Universitats, Ciència i Societat Digital de la Generalitat Valenciana and the CERCA Programme Generalitat de Catalunya, Spain, the National Science Centre of Poland and the Foundation for Polish Science (FNP), the Swiss National Science Foundation (SNSF), the Russian Foundation for Basic Research, the Russian Science Foundation, the European Commission, the European Regional Development Funds (ERDF), the Royal Society, the Scottish Funding Council, the Scottish Universities Physics Alliance, the Hungarian Scientific Research Fund (OTKA), the French Lyon Institute of Origins (LIO), the Belgian Fonds de la Recherche Scientifique (FRS-FNRS), Actions de Recherche Concertées (ARC) and Fonds Wetenschappelijk Onderzoek – Vlaanderen (FWO), Belgium, the Paris Île-de-France Region, the National Research, Development and Innovation Office Hungary (NKFIH), the National Research Foundation of Korea, the Natural Science and Engineering Research Council Canada, Canadian Foundation for Innovation (CFI), the Brazilian Ministry of Science, Technology, and Innovations, the International Center for Theoretical Physics South American Institute for Fundamental Research (ICTP-SAIFR), the Research Grants Council of Hong Kong, the National Natural Science Foundation of China (NSFC), the Leverhulme Trust, the Research Corporation, the Ministry of Science and Technology (MOST), Taiwan, the United States Department of Energy, and the Kavli Foundation. The authors gratefully acknowledge the support of the NSF, STFC, INFN and CNRS for provision of computational resources. This work was supported by MEXT, JSPS Leading-edge Research Infrastructure Program, JSPS Grant-in-Aid for Specially Promoted Research 26000005, JSPS Grant-in-Aid for Scientific Research on Innovative Areas 2905: JP17H06358, JP17H06361 and JP17H06364, JSPS Core-to-Core Program A. Advanced Research Networks, JSPS Grant-in-Aid for Scientific Research (S) 17H06133, the joint research program of the Institute for Cosmic Ray Research, University of Tokyo, National Research Foundation (NRF) and Computing Infrastructure Project of KISTI-GSDC in Korea, Academia Sinica (AS), AS Grid Center (ASGC) and the Ministry of Science and Technology (MoST) in Taiwan under grants including AS-CDA-105-M06, Advanced Technology Center (ATC) of NAOJ, and Mechanical Engineering

Center of KEK.

This work is supported by NASA through the NICER mission and the Astrophysics Explorers Program and uses data and software provided by the High Energy Astrophysics Science Archive Research Center (HEASARC), which is a service of the Astrophysics Science Division at NASA/GSFC and High Energy Astrophysics Division of the Smithsonian Astrophysical Observatory.

## 6.A1. THRESHOLD SETTING

In this Appendix we outline two alternative methods to set thresholds for the search. In Appendix 6.A1.1 we detail the method in LVC et al. [314] to set thresholds by modeling the tail of the log-likelihood distribution in noise as an exponential. In Appendix 6.A1.2 we review the non-parametric method in Middleton et al. [9], LVC et al. [293], Millhouse et al. [310], Beniwal et al. [311], and Jones and Sun [312], which takes a certain percentile detection statistic from noise-only realizations as the threshold. We compare the methods in Appendix 6.A1.3. In Appendix 6.A1.4 we discuss generating noise realizations using off-target searches, and justify the approach taken in this paper. In Appendix 6.A1.5 we specify how to calculate  $p_{\text{noise}}$ , the probability that we see a value of  $\mathcal{L}$  at least as high as a certain candidate in a given sub-band.

Whatever the method, the threshold depends on both the target's projected semi-major axis,  $a_0$ , and the sub-band frequency,  $f$ , as log-likelihoods depend non-linearly on  $a_0 f$  as an increased number orbital sidebands are included in the  $\mathcal{J}$ -statistic at higher  $a_0 f$  [see equation (6) in LVC et al. [314] and Suvorova et al. [8] for details]. For this reason we set thresholds independently for each target and sub-band.

### 6.A1.1. Exponential tail method

The PDF of the log-likelihood,  $p(\mathcal{L})$ , for the most likely path for a given template is observed to have an exponentially distributed tail in noise,

$$p(\mathcal{L}) = A \lambda \exp[-\lambda(\mathcal{L} - \mathcal{L}_{\text{tail}})] \quad \text{for } \mathcal{L} > \mathcal{L}_{\text{tail}}, \quad (6.16)$$

where  $A$  is a normalization constant,  $\lambda$  is a parameter to be found empirically, and  $\mathcal{L}_{\text{tail}}$  is a cut-off that must also be determined empirically.

For each target and sub-band we estimate  $\lambda$  and  $\mathcal{L}_{\text{tail}}$  using a set of  $M$  sample log-likelihoods, a subset of which have  $\mathcal{L} > \mathcal{L}_{\text{tail}}$ . This subset is denoted  $S_{N_{\text{tail}}} \equiv \{\mathcal{L}_i\}$ ,  $i \in \{1, \dots, N_{\text{tail}}\}$ . The entire set of  $M$  samples is generated by running the search on  $N_G = 100$  realizations of Gaussian noise. To keep  $N_G$  small enough to be computationally feasible we include log-likelihoods from all possible Viterbi paths through the sub-band for each template, instead of just the log-likelihood from the most likely path. Thus, we have  $M = N_G N_f N_B$ , where  $N_f = 2^{20}$  is the number of frequency bins in each sub-band, and  $N_B$  is the number of binary orbital templates needed for each individual sub-band, as listed in Table 6.2. Separate tests, not shown here, indicate that including the log-likelihoods from non-maximal paths does not change the shape of  $p(\mathcal{L})$ , and therefore does not change the thresholds  $\mathcal{L}_{\text{th}}$ , if the appropriate trials factor is taken into account.

Assuming each  $\mathcal{L}_i$  is independent, the maximum likelihood estimator,  $\hat{\lambda}$ , for  $\lambda$  is

$$\hat{\lambda} = \frac{N_{\text{tail}}}{\sum_{i=1}^{N_{\text{tail}}} (\mathcal{L}_i - \mathcal{L}_{\text{tail}})} . \quad (6.17)$$

The normalization  $A = N_{\text{tail}}/M$  is fixed via the fraction of total samples used to construct  $p(\mathcal{L})$ . The cut-off  $\mathcal{L}_{\text{tail}}$  is estimated in each sub-band as the smallest value  $\mathcal{L}^*$  where a histogram of the samples  $\mathcal{L}_i > \mathcal{L}^*$  has approximately constant slope when viewed on log-linear axes. Each  $\mathcal{L}_i$  is independent for the long coherence times ( $T_{\text{drift}} = 10$  d) used in this search, as  $N_T \ll N_f$  implies most optimal paths through the sub-band are not correlated.

The probability,  $\alpha$ , that  $\mathcal{L}$  is above some threshold  $\mathcal{L}_{\text{th}} > \mathcal{L}_{\text{tail}}$  if no signal is present (i.e. in pure noise) is

$$\int_{\mathcal{L}_{\text{th}}}^{\infty} d\mathcal{L} p(\mathcal{L}) = \alpha . \quad (6.18)$$

Combining Eqs. (6.8), (6.16), and (6.18) we solve for  $\mathcal{L}_{\text{th}}$  in a given sub-band, viz.

$$\mathcal{L}_{\text{th}} = -\frac{1}{\hat{\lambda}} \log \left( \frac{N_G \alpha_{N_{\text{tot}}}}{N_{\text{tail}}} \right) + \mathcal{L}_{\text{tail}} , \quad (6.19)$$

where Eq. (6.8) is simplified via the binomial approximation ( $N_{\text{tot}} = N_f N_B \gg 1$ ), and  $\alpha_{N_{\text{tot}}}$  is the desired false alarm probability for the search over the sub-band. Note Eq. (6.19) depends implicitly on the sub-band frequency and  $N_B$ , through  $\hat{\lambda}$  and  $N_{\text{tail}}$ .

Across all targets and sub-bands we find  $0.195 < \hat{\lambda} < 0.248$ , with larger values corresponding to higher frequency sub-bands, and those with larger  $N_B$ . A simple rule-of-thumb is that, for a median value of  $\hat{\lambda} = 0.218$ , an increment of  $\approx 3$  in  $\mathcal{L}$  is  $\approx 50\%$  less likely to occur in pure noise.

### 6.A1.2. Percentile method

Given a sorted set of most likely log-likelihoods  $\{\mathcal{L}_i\}$ ,  $i \in \{1, \dots, M\}$  with  $M = N_G N_B$ , generated via running the search algorithm over  $N_G$  realizations of noise for a single target and sub-band, one can pick as the threshold the  $\mathcal{L}_i$  corresponding to the percentile equal to the desired false alarm probability, i.e.

$$\mathcal{L}_{\text{th}} = \mathcal{L}_j , \quad (6.20)$$

with  $j = \lfloor \alpha_{N_{\text{tot}}} M \rfloor$ . As with the method described in Appendix 6.A1.1 we may opt to use the log-likelihoods from all possible Viterbi paths through the sub-band for a given orbital template, to reduce the number of realizations of noise we need to generate. With this set of log-likelihoods, we have  $M = N_G N_f N_B$ .

### 6.A1.3. Comparison of methods

The two methods described in Appendices 6.A1.1 and 6.A1.2 give broadly similar results for  $\mathcal{L}_{\text{th}}$  for a given probability of false alarm. LVC et al. [314] opts for the method in Appendix 6.A1.1. When Viterbi scores are used as the detection statistic, as in LVC et al.

[314], the PDF of the score in noise does not vary with frequency, and thus the thresholds in each sub-band can be extrapolated from a small set of Gaussian noise realizations. If the PDF of the detection statistic varies with target search parameters, then the method in Appendix 6.A1.2 is used, as in Middleton et al. [9], Millhouse et al. [310], Beniwal et al. [311], and Jones and Sun [312]. The percentile method has inherently fewer assumptions, as it does not fit a parametric model to  $p(\mathcal{L})$ . However it is not possible to extrapolate thresholds calculated in one sub-band to other sub-bands.

For our targets and sub-bands, we find  $\mathcal{L}_{\text{th}}^e - \mathcal{L}_{\text{th}}^p \approx 2$ , where the superscripts  $e$  and  $p$  correspond to the exponential tail and percentile methods respectively. However the exact difference depends on the realizations of Gaussian noise; Monte Carlo simulations indicate that with  $N_G = 100$  the calculated threshold is usually within 2% of the true value, so thresholds should only be considered precise to 2%.

#### 6.A1.4. Off-target thresholds

Both methods derive  $\mathcal{L}_{\text{th}}$  based on realizations of Gaussian noise. However, the noise in real detector data is non-Gaussian in general [524]. To account for this we search O3 data at  $N_{\text{OT}}$  randomly chosen, but well-separated, off-target positions, to generate  $N_{\text{OT}}$  realizations of real detector noise, as originally done in Middleton et al. [9]. We set  $N_{\text{OT}}$  such that  $N_B N_{\text{OT}} > 500$ , with a minimum value of  $N_{\text{OT}} = 100$ , to ensure enough samples are generated.

If there are no known noise lines in the sub-band, we find  $4 < \mathcal{L}_{\text{th},G}^e - \mathcal{L}_{\text{th},\text{OT}}^p < 12$ , where the subscripts G and OT correspond to thresholds calculated using Gaussian and off-target noise realizations respectively. That is, the thresholds calculated from Gaussian noise, using the exponential tail method are considerably more conservative than those calculated from off-target noise and the percentile method. If there are loud noise lines in the sub-band,  $\mathcal{L}_{\text{th},\text{OT}}$  is often much higher, as these lines appear in the off-target noise realizations. Because off-target noise realizations are impacted by noise lines,  $p(\mathcal{L})$  is not necessarily exponential in its tail. We thus opt to use the percentile method when calculating thresholds with off-target noise realizations. Table 6.5 contains the calculated  $\mathcal{L}_{\text{th},G}^e$  and  $\mathcal{L}_{\text{th},\text{OT}}^p$  for each target and sub-band.

As in Middleton et al. [9] we consider  $\mathcal{L}_{\text{th}}$  for each sub-band to be the minimum of  $\mathcal{L}_{\text{th},G}^e$  and  $\mathcal{L}_{\text{th},\text{OT}}^p$ , with  $\alpha_{N_{\text{tot}}} = 0.3$ . This choice minimizes the probability that we will miss a potential candidate due to inadvertently setting our threshold too high.

#### 6.A1.5. Probability that a candidate arises due to noise

As discussed in Sec. 6.5.3, when we set  $\alpha_{N_{\text{tot}}} = 0.3$  we expect  $\sim 18$  candidates above  $\mathcal{L}_{\text{th}}$ , across all targets and sub-bands. Let us quantify empirically the probability,  $p_{\text{noise}}$ , that, if the data in a given sub-band are pure noise, we see at least one template with log-likelihood higher than that of the candidate,  $\mathcal{L}_{\text{cand}}$ . We have

$$p_{\text{noise}} = \frac{\sum_{i=1}^M \mathbb{1}(\mathcal{L}_i > \mathcal{L}_{\text{cand}})}{M}, \quad (6.21)$$

where  $\mathbb{1}(\dots)$  is the indicator function which returns 1 when the argument is true, otherwise 0. In this paper we calculate Eq. (6.21) for each candidate with  $\mathcal{L} > \mathcal{L}_{\text{th}}$  using the

Table 6.5: Target, starting frequency,  $f_s$ , for each  $\sim 0.61$  Hz-wide sub-band, threshold calculated using Gaussian noise realizations and the exponential tail method,  $\mathcal{L}_{\text{th},G}^e$ , and threshold calculated using off-target noise realizations and the percentile method,  $\mathcal{L}_{\text{th},\text{OT}}^p$ . All thresholds are calculated with  $\alpha_{N_{\text{tot}}} = 0.3$ .

Target	$f_s$ (Hz)	$\mathcal{L}_{\text{th},G}^e$	$\mathcal{L}_{\text{th},\text{OT}}^p$	Target	$f_s$ (Hz)	$\mathcal{L}_{\text{th},G}^e$	$\mathcal{L}_{\text{th},\text{OT}}^p$
IGR J00291+5934	598.6	291.9	1136.7	IGR J17498–2921	400.7	304.6	298.4
	798.2	294.9	288.4		534.4	304.7	297.9
	1197.5	295.2	287.6		801.7	311.2	304.5
MAXI J0911–655	339.7	297.0	290.0	IGR J17511–3057	244.5	302.0	293.7
	453.0	305.4	298.2		326.1	303.4	295.8
	679.6	305.5	300.4		489.4	305.1	297.9
XTE J0929–314	184.8	311.9	304.9	XTE J1751–305	435.0	312.8	316.0
	246.5	307.4	301.2		580.1	312.9	306.6
	369.9	310.4	304.5		870.3	319.9	315.7
IGR J16597–3704	104.9	321.6	316.4	Swift J1756.9–2508	181.8	308.7	302.8
	139.9	322.9	625.5		242.5	317.4	312.8
	210.0	323.7	318.5		363.8	315.3	309.0
IGR J17062–6143	163.4	292.1	285.1	IGR J17591–2342	527.1	299.3	289.4
	217.9	289.1	281.8		702.9	302.0	295.7
	327.0	293.3	283.3		1054.5	304.7	298.2
IGR J17379–3747	467.8	307.4	298.9	SAX J1808.4–3658	400.7	303.8	294.8
	623.8	307.4	299.9		534.3	305.0	296.1
	935.9	311.1	305.7		801.6	309.3	301.4
SAX J1748.9–2021	442.1	308.2	300.3	XTE J1807–294	190.3	295.5	287.0
	589.5	310.1	301.6		253.9	296.8	289.0
	884.4	311.5	304.9		380.9	299.7	292.0
NGC 6440 X–2	205.6	292.8	281.3	XTE J1814–338	314.1	301.8	293.3
	274.2	298.3	288.6		418.8	302.3	294.3
	411.5	295.9	287.2		628.4	305.8	298.4
IGR J17494–3030	375.7	315.3	309.3	IGR J18245–2452	254.0	311.2	305.4
	501.1	317.5	13763.8		338.8	312.5	305.9
	751.8	322.2	316.5		508.4	317.3	13569.7
Swift J1749.4–2807	517.6	316.4	308.8	HETE J1900.1–2455	377.0	299.6	288.1
	690.3	318.4	311.9		502.8	303.1	8459.4
	1035.5	321.0	316.3		754.3	303.8	294.7

set of log-likelihoods,  $\{\mathcal{L}_i\}$ , generated via off-target realizations as discussed in Appendix 6.A1.4. As in Appendix 6.A1.2, we set  $M = N_G N_B$  to account for the extra “trials factor” needed for sub-bands with multiple templates.

## 6.A2. FULL SEARCH RESULTS AND SURVIVOR FOLLOW-UP

This Appendix collates the full search results for reference and reproducibility for all targets in Figs. 6.4a–6.4s (except for IGR J18245–2452 which is shown in Fig. 6.2). Each of Figs. 6.4a–6.4s is laid out identically to Fig. 6.2.

The orbital parameters ( $P$ ,  $a_0$ , and  $T_{\text{asc}}$ ), terminating frequency bin [ $f(N_T)$ ], log-likelihood ( $\mathcal{L}$ ), and  $p_{\text{noise}}$ , the probability that a search of that candidate’s sub-band in pure noise would return at least one candidate at least as loud as the one seen are shown in Table 6.6, for each of the candidates that survive all vetoes and have  $\mathcal{L} > \mathcal{L}_{\text{th}}$ .

Table 6.6: Orbital template,  $(P, a_0, T_{\text{asc}})$ , terminating frequency bin,  $f(N_T)$ , log-likelihood,  $\mathcal{L}$ , and the probability that a search of the candidate’s sub-band in pure noise would return a candidate just as loud,  $p_{\text{noise}}$ , for the 16 candidates with  $\mathcal{L} > \mathcal{L}_{\text{th}}$  that cannot be eliminated by any of the vetoes detailed in Sec. 6.7.

Target	Candidate	$P$ (s)	$a_0$ (lt-s)	$T_{\text{asc}}$ (GPS time)	$f(N_T)$ (Hz)	$\mathcal{L}$	$p_{\text{noise}}$
MAXI J0911–655	1	2659.933	0.0176	1238165869.0437	453.309532	299.2	0.26
IGR J16597–3704	1	2758.61	0.0048	1238163275.6122	105.002195	316.5	0.30
	2	2757.90	0.0048	1238163010.7583	210.359055	323.5	0.09
IGR J17062–6143	1	2278.2112	0.0040	1238165942.2745	163.531805	286.4	0.24
	2	2278.2112	0.0040	1238165942.2745	218.452091	283.9	0.19
	3	2278.2112	0.0040	1238165942.2745	327.058287	290.0	0.05
IGR J17379–3747	1	6765.84	0.0770	1238162768.3832	623.819568	303.9	0.08
SAX J1748.9–2021	1	31555.29	0.3876	1238151700.2214	590.048237	304.9	0.12
	2	31555.30	0.3876	1238151760.9764	590.040010	302.3	0.27
	3	31555.31	0.3876	1238151710.6406	884.592276	305.6	0.22
IGR J17498–2921	1	13835.619	0.36517	1238164013.8774	801.703605	305.8	0.22
XTE J1807–294	1	2404.416	0.00483	1238165585.2721	381.000852	296.7	0.10
SAX J1808.4–3658	1	7249.15	0.0628	1238161168.0040	534.633578	298.2	0.16
	2	7249.16	0.0628	1238161183.0831	534.407934	296.2	0.30
XTE J1814–338	1	15388.723	0.3906	1238151585.3941	314.564137	297.7	0.08
HETE J1900.1–2455	1	4995.26	0.0184	1238161529.0866	754.378543	295.8	0.25

### 6.A2.1. Additional follow-up for survivors

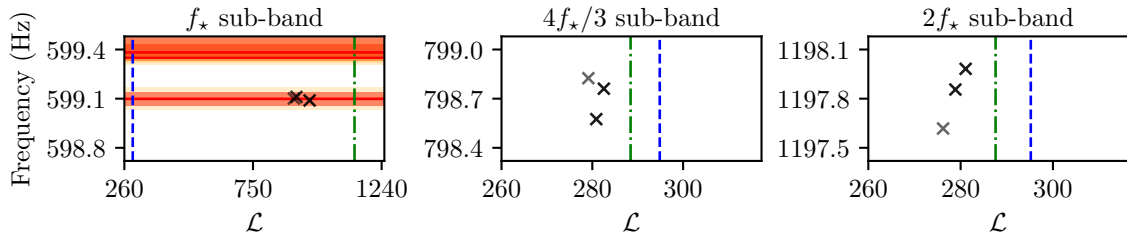
The full frequency paths,  $f(t) - f(N_T)$ , for all candidates with  $p_{\text{noise}} \leq 0.1$  are shown in the top panels of Figs. 6.5a–6.5e. The bottom panels of Figs. 6.5a–6.5e display the cumulative log-likelihood along the frequency path relative to the average sum log-likelihood needed to reach  $\mathcal{L}_{\text{th}}$ , namely  $C\mathcal{L} \equiv \sum_{i=0}^{t=t} [\mathcal{L}(i) - \mathcal{L}_{\text{th}}/N_T]$ , where  $\sum_{i=0}^{t=t} \mathcal{L}(i)$  is  $\ln P(Q^*|O)$  from Eq. (6.2) truncated after the  $t$ -th segment. Over-plotted (blue dashed line) is the average cumulative log-likelihood needed at each data segment in order to reach  $\mathcal{L}_{\text{th}}$ . This diagnostic indicates whether a handful of segments dominate in making the candidate’s frequency path the optimal one for that template. If the candidate is a true signal, we would expect the signal strength to be approximately constant, and thus the cumulative log-likelihood should grow linearly as more data are considered. However, Monte Carlo tests with injections show that the cumulative log-likelihood only becomes linear for  $\mathcal{L} \gtrsim \mathcal{L}_{\text{th}} + 200$ . This is not the case for any of the 16 survivor candidates, and thus their cumulative log-likelihood cannot help us distinguish whether they are truly astrophysical signals.

The sky resolution of the algorithm described in Sec. 6.3 is roughly 2 arcmin in RA and Dec., for an injection with  $\mathcal{L}_{\text{th}} \lesssim \mathcal{L} \lesssim \mathcal{L}_{\text{th}} + 50$ . The point-spread-function of an injection is an ellipse, which has a varying orientation and eccentricity dependent on the sky position. For each of our candidates we calculate  $\mathcal{L}$  at 440 regularly spaced sky positions in a  $100 \text{ arcmin}^2$  grid around the target’s true location, using the template recovered from the search and listed in Table 6.6. For almost all survivor candidates, the distribution of  $\mathcal{L}$  values in the patch of sky around the candidate does not match the elliptical point-spread-function we see in injections for their respective sky locations.

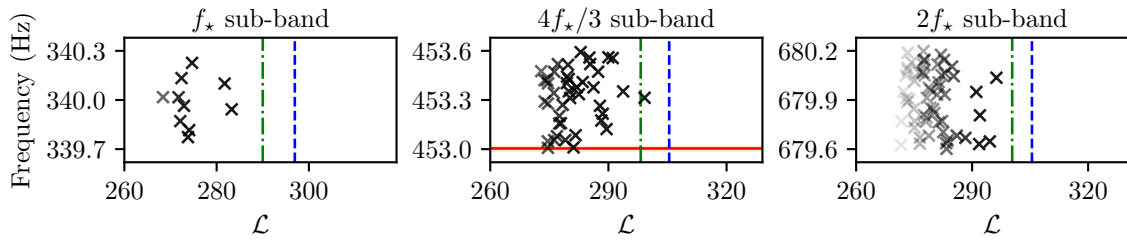
The sole exception is Candidate 2 from IGR J16597–3704. Figure 6.6 shows  $\mathcal{L}$  at 3721 regularly spaced sky positions in a  $100 \text{ arcmin}^2$  grid around the target’s true location, again using the template as listed in Table 6.6. The roughly elliptical shape is consistent with the point-spread-function of injections at this sky location. However, the region of sky with  $\mathcal{L} \gtrsim \mathcal{L}_{\text{th}}$  is centered  $\sim 1 \text{ arcmin}$  lower in Dec. than the true declination of the source, which is known to a precision of 0.01 arcmin [490].

One final follow-up we perform for these candidates is to calculate  $\mathcal{L}$  in a small, densely sampled patch of the  $\{P, T_{\text{asc}}\}$  parameter space around each candidate’s template. Moderately loud injections ( $\mathcal{L} \gtrsim \mathcal{L}_{\text{th}} + 100$ ) are seen to “spread out” in the  $\{P, T_{\text{asc}}\}$  plane, and are detectable with  $\mathcal{L} > \mathcal{L}_{\text{th}}$  even when searching a template that has a slightly incorrect value of  $P$  and  $T_{\text{asc}}$ . However, none of our candidates are this loud, so this diagnostic does not help us distinguish whether they are truly astrophysical signals or merely noise fluctuations.

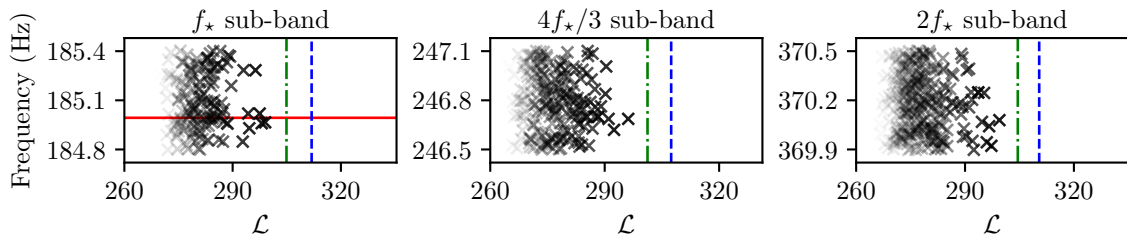
We do not use any data from LIGO’s Observing Runs 1 or 2 (O1 and O2 respectively) to aid in following up these candidates, as the detector is considerably more sensitive in O3. The duration of O3 was also longer than the durations of O1 and O2. If a candidate is only marginally above threshold in O3 data, it may be hidden in the noise in O1 and O2 data, so including data from those observing runs is not likely to increase the candidate’s signal-to-noise ratio.



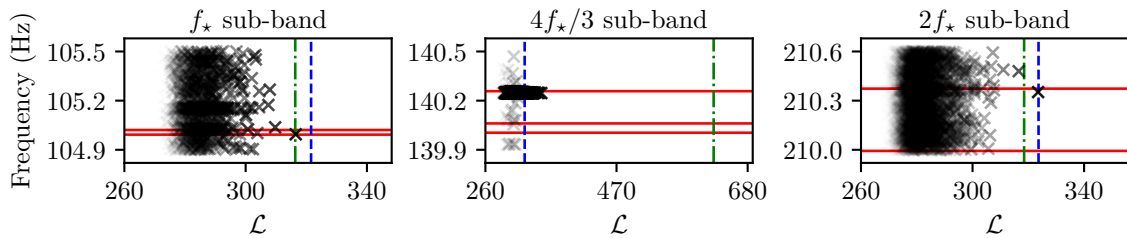
(a) Search results for IGR J00291+5934.



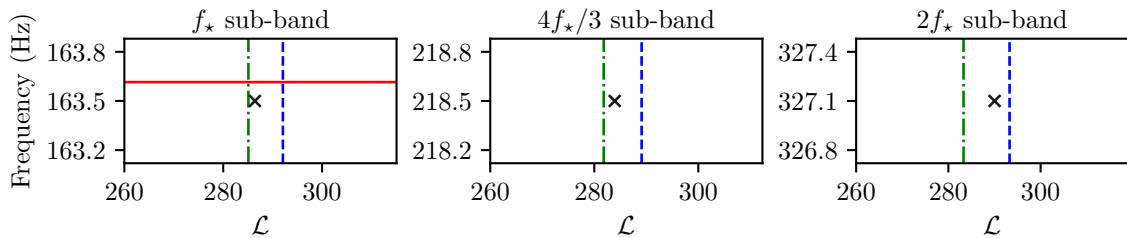
(b) Search results for MAXI J0911-655.



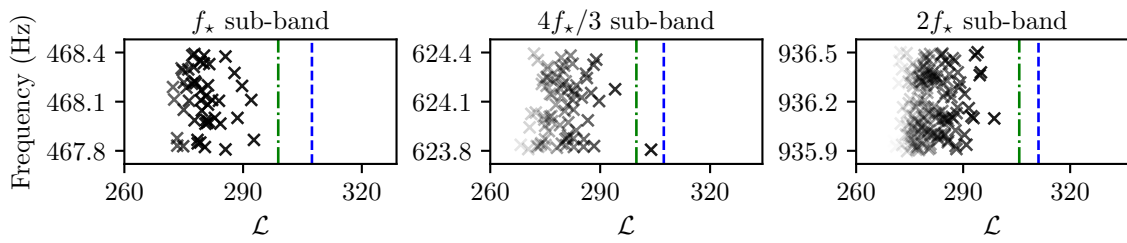
(c) Search results for XTE J0929-314.



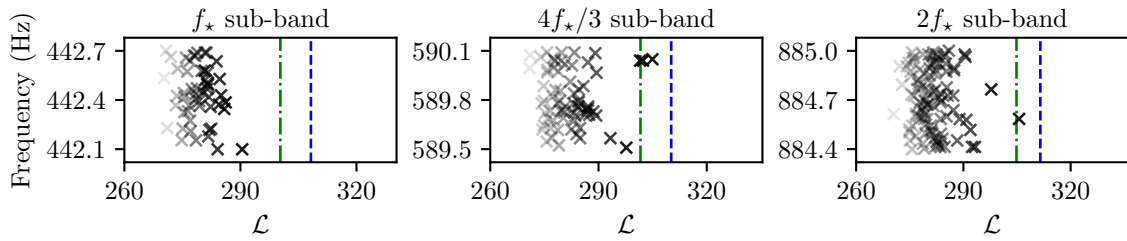
(d) Search results for IGR J16597-3704.



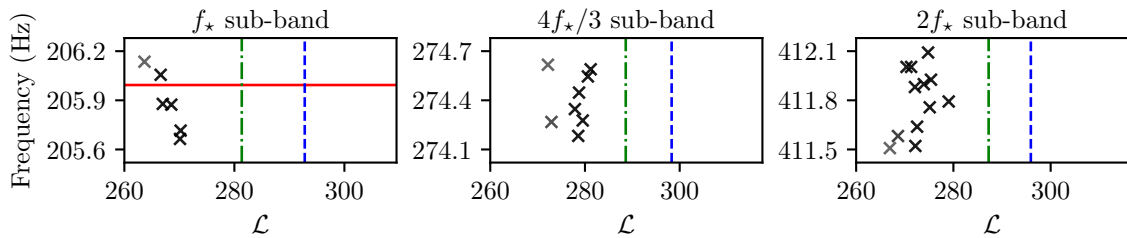
(e) Search results for IGR J17062-6143.



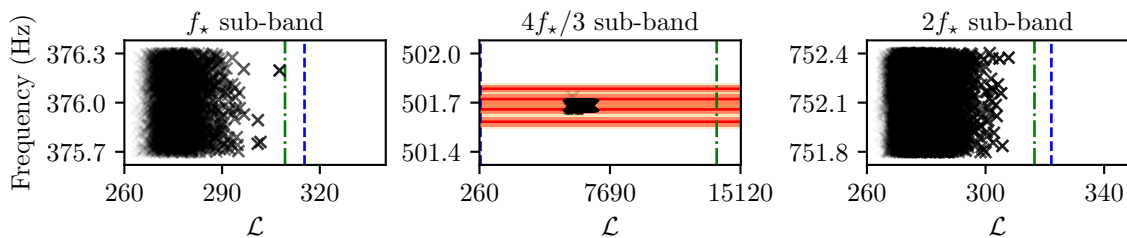
(f) Search results for IGR J17379–3747.



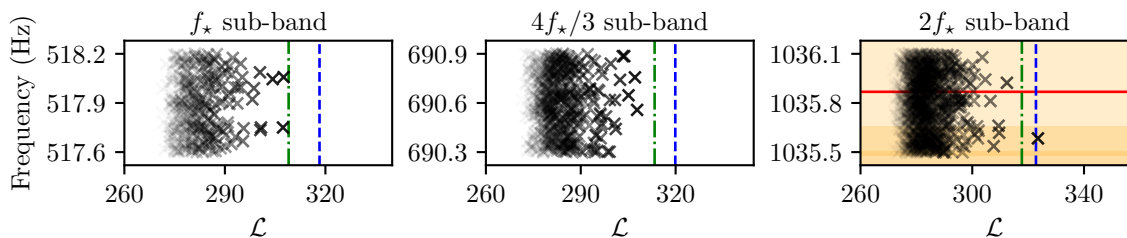
(g) Search results for SAX J1748.9–2021.



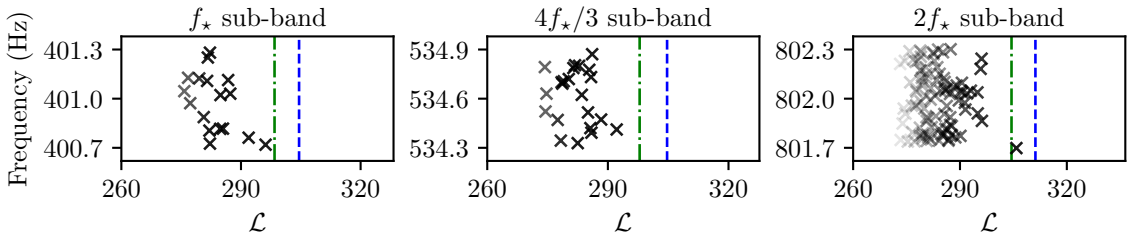
(h) Search results for NGC 6440 X–2.



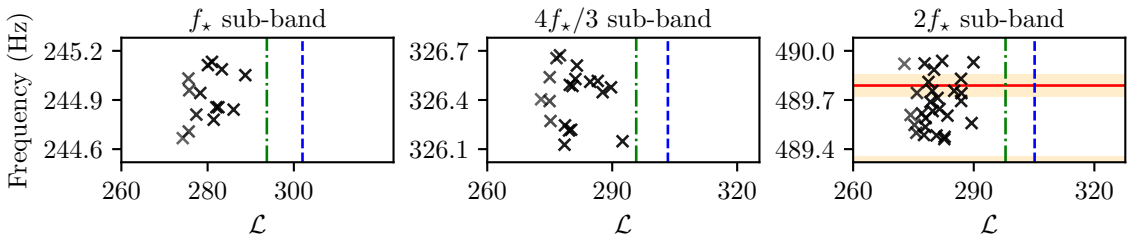
(i) Search results for IGR J17494–3030.



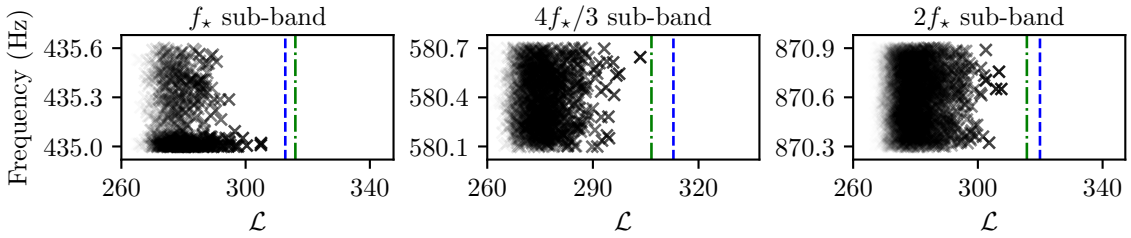
(j) Search results for Swift J1749.4–2807.



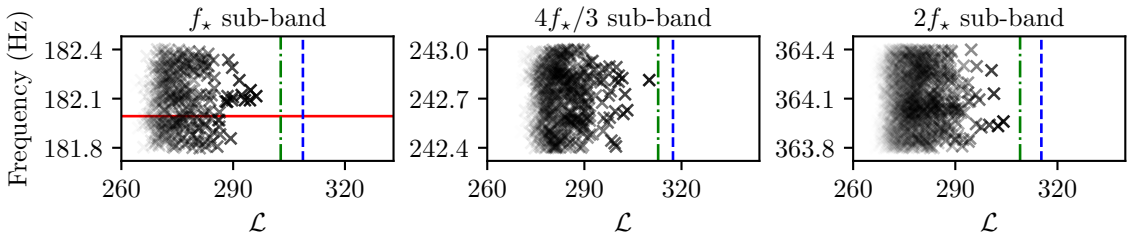
(k) Search results for IGR J17498–2921.



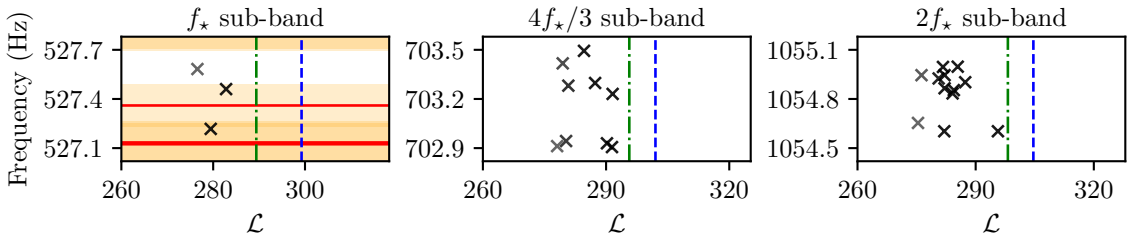
(l) Search results for IGR J17511–3057.



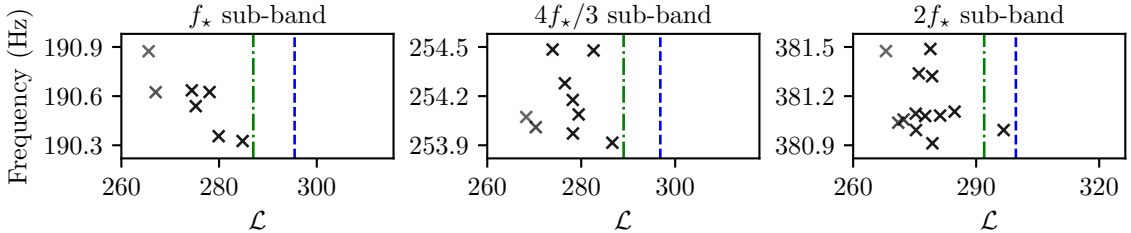
(m) Search results for XTE J1751–305.



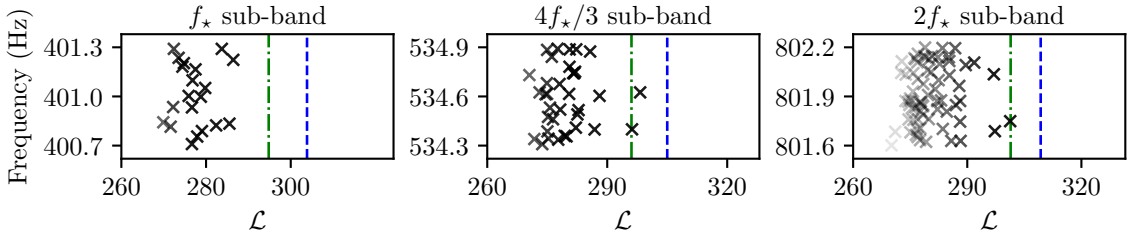
(n) Search results for Swift J1756.9–2508.



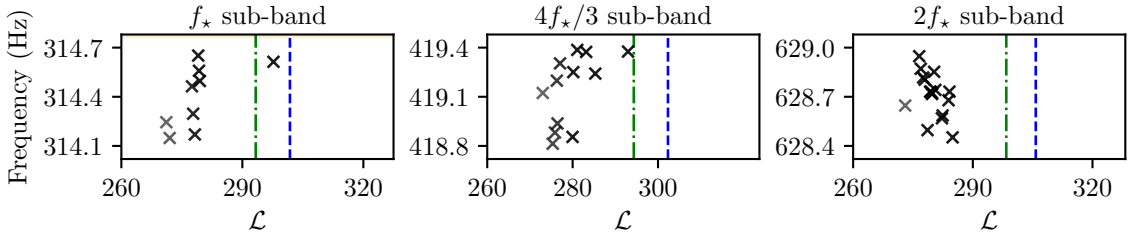
(o) Search results for IGR J17591–2342.



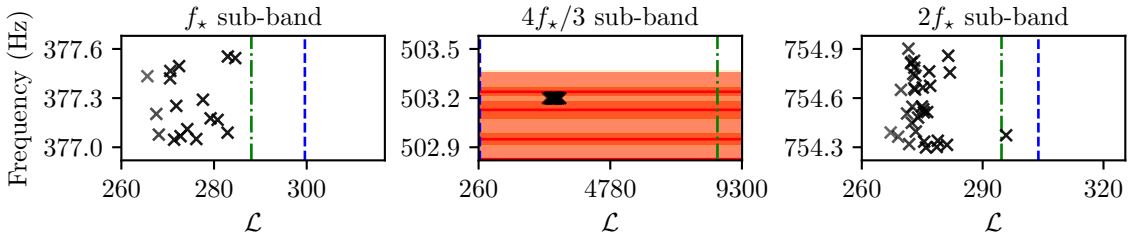
(p) Search results for XTE J1807–294.



(q) Search results for SAX J1808.4–3658.



(r) Search results for XTE J1814–338.



(s) Search results for HETE J1900.1–2455.

Figure 6.4: Search results for each target and sub-band, laid out as in Fig 6.2. Black crosses indicate the frequency and  $\mathcal{L}$  for the most likely path through the sub-band for each binary template. The vertical blue dashed (green dot-dashed) lines correspond to the threshold set via Gaussian (off-target) noise realizations,  $\mathcal{L}_{\text{th},G}$  ( $\mathcal{L}_{\text{th},\text{OT}}$ ), in each sub-band. Solid red lines indicate the peak frequency of known instrumental lines in the detectors; the red band indicates the width of the line and the yellow band indicates the increased effective width due to Doppler broadening, as described in Sec. 6.7.1. The transparency of crosses in sub-bands with many templates, e.g. the sub-bands of IGR J16597–3704, is adjusted relative to the maximum  $\mathcal{L}$  in that sub-band for clarity.

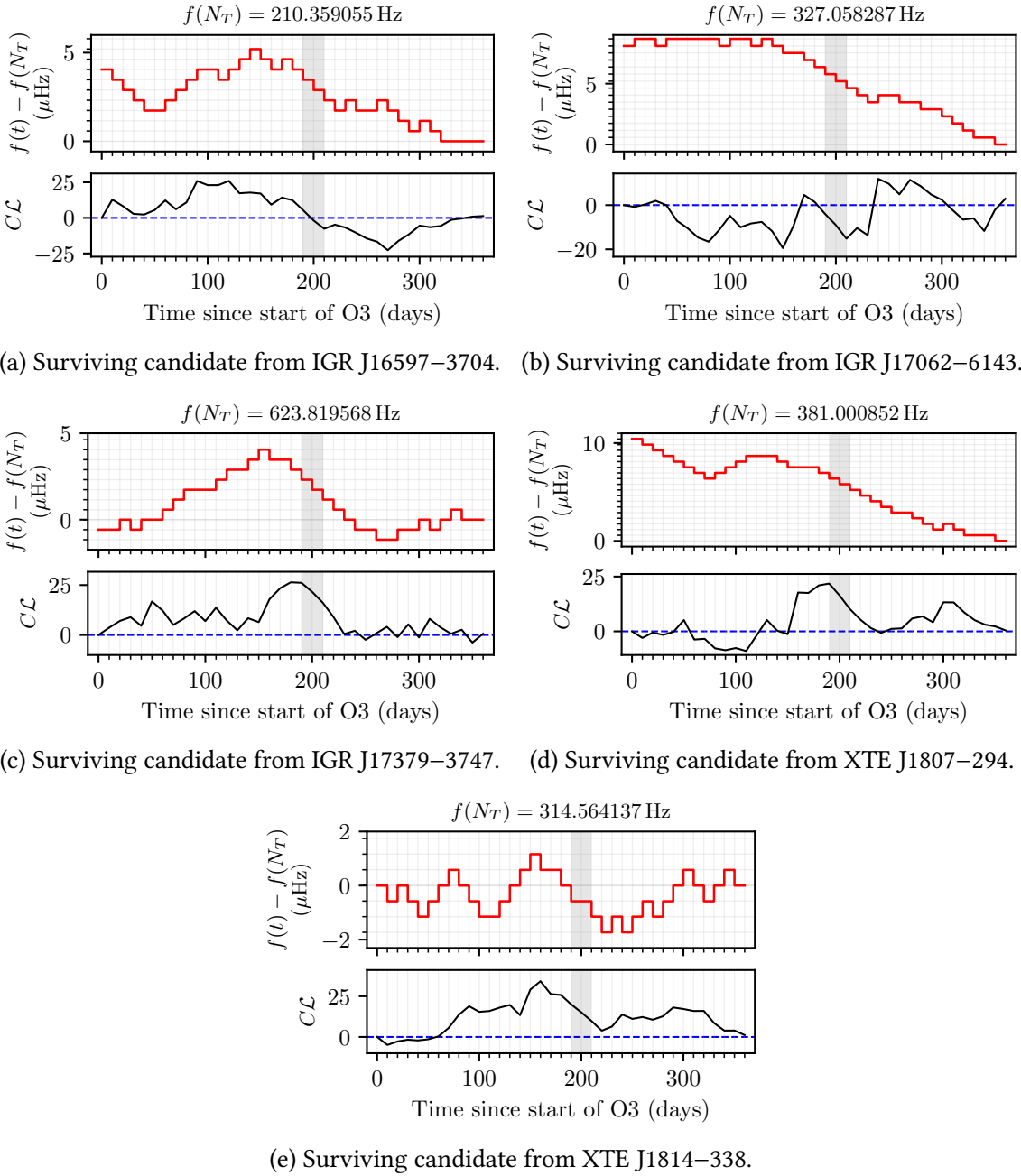


Figure 6.5: Top panels: frequency paths,  $f(t)$ , for candidates with  $p_{\text{noise}} \leq 0.1$ . The terminating frequency bin,  $f(N_T)$ , is subtracted and displayed in the title of each figure for clarity. Faint horizontal grey lines demarcate frequency bins of size  $\Delta f = 5.787037 \times 10^{-7}$  Hz, while faint vertical grey lines demarcate chunks of length  $T_{\text{drift}} = 10$  d. Bottom panels: the cumulative log-likelihood along the frequency path relative to the average sum log-likelihood needed to reach  $\mathcal{L}_{\text{th}}$ ,  $C\mathcal{L} \equiv \sum_{i=0}^{t-1} [\mathcal{L}(i) - \mathcal{L}_{\text{th}}/N_T]$ , where  $\sum_{i=0}^{t-1} \mathcal{L}(i)$  is  $\ln P(Q^*|O)$  from Eq. (6.2) truncated after the  $t$ -th segment. The horizontal blue dashed line corresponds to  $\sum_{i=0}^{t-1} \mathcal{L}(i) = t\mathcal{L}_{\text{th}}/N_T$ . The grey shaded regions in both top and bottom panels correspond to the segments which have no SFTs and are therefore filled with a uniform log-likelihood, as described in Sec. 6.6.

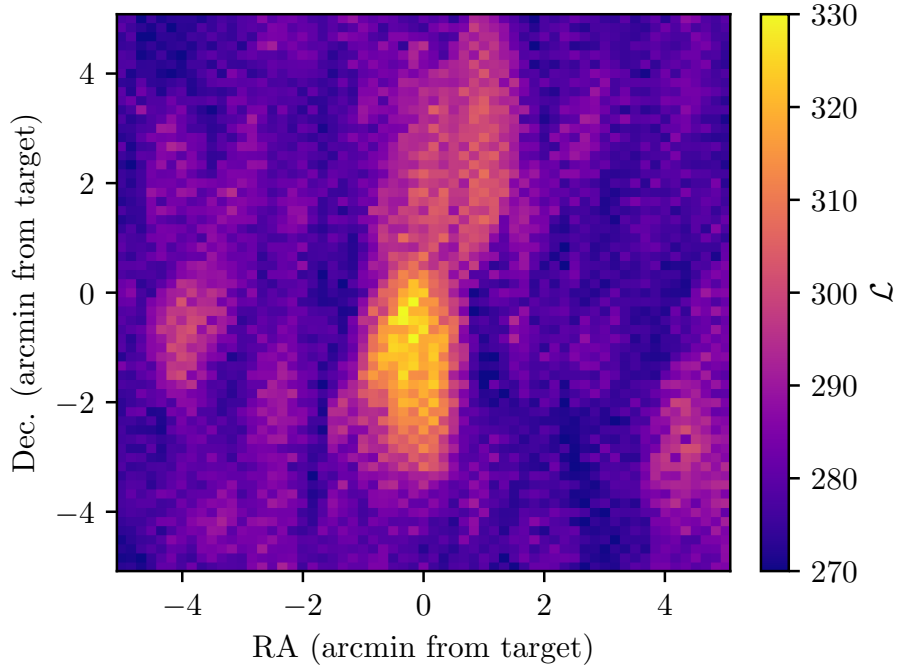


Figure 6.6:  $\mathcal{L}$ , as represented by the color of each pixel, calculated at 3721 regularly spaced sky locations in a  $100 \text{ arcmin}^2$  patch of sky, centered on IGR J16597–3704. See text in Appendix 6.A2.1 for details.

### 6.A3. SURVIVOR FOLLOW-UP FOR TARGET-OF-OPPORTUNITY SEARCH CANDIDATE

For posterity, and to aid future follow-up with different pipelines, we record in Table 6.7 the template, the frequency  $f$ , the log-likelihood  $\mathcal{L}$ , and  $p_{\text{noise}}$ , of the candidate from the target-of-opportunity search in Sec. 6.9 that survives all vetoes.

As in Appendix 6.A2.1, we perform additional follow-up for this remaining candidate. With  $T_{\text{obs}} = 24 \text{ d}$  the point-spread-function of a moderately loud injection ( $\mathcal{L} \gtrsim \mathcal{L}_{\text{th}} + 20$ ), at the sky location of the target, is a narrow ellipse  $\sim 2 \text{ arcmin}$  wide in RA, but over  $\sim 30 \text{ arcmin}$  tall in Dec. When we search a  $100 \text{ arcmin}^2$  patch of sky around the location of SAX J1808.4–3658 we do not see any evidence of this point-spread-function at the source location. There is an ellipse with  $\mathcal{L} > \mathcal{L}_{\text{th}}$  roughly  $-2 \text{ arcmin}$  away in RA from SAX J1808.4–3658, but as the location of the target is known to sub-arcsec precision [483], this ellipse is likely a noise fluctuation, rather than an astrophysical signal.

We also calculate  $\mathcal{L}$  in a small, densely sampled patch of the  $\{P, T_{\text{asc}}\}$  parameter space around the candidate’s template. As discussed in Appendix 6.A2.1, moderately loud injections ( $\mathcal{L} \gtrsim \mathcal{L}_{\text{th}} + 20$ ) “spread out” in the  $\{P, T_{\text{asc}}\}$  plane. However, the candidate is not loud enough for this diagnostic to provide evidence for or against the hypothesis that the candidate is a noise fluctuation.

If we assume that the remaining candidate is a false alarm, we calculate  $h_0^{95\%}$  for the  $24 \text{ d}$  coherent search, using the procedure outlined in Sec. 6.10.1. We find  $h_0^{95\%} = 1.3 \times 10^{-25}$  for the sub-bands centered on  $f_\star$  and  $4f_\star/3$ , and  $h_0^{95\%} = 1.7 \times 10^{-25}$  for the sub-band centered on  $2f_\star$ . These upper limits are higher than the ones listed in

Table 6.7: Orbital template,  $(P, a_0, T_{\text{asc}})$ , frequency,  $f$ , log-likelihood,  $\mathcal{L}$ , and the probability of seeing a candidate at least this loud in pure noise,  $p_{\text{noise}}$ , for the remaining candidate from the target-of-opportunity, 24 d coherent search when SAX J1808.4–3658 was in outburst. The candidate cannot be eliminated by any of the vetoes detailed in Sec. 6.7.

$P$ (s)	$a_0$ (lt-s)	$T_{\text{asc}}$ (GPS time)	$f$ (Hz)	$\mathcal{L}$	$p_{\text{noise}}$
7249.155	0.062809	1249163578.03125	400.59656098	42.5	0.02

Sec. 6.10.2 because the longer coherence time does not completely compensate for the shorter observation time.

Finally, we perform a complementary follow-up search using a deterministic signal template on the candidate of interest using PyFstat [10, 551]. The use of the PyFstat algorithm as a follow-up technique was applied to the last surviving outlier of LVK et al. [476] and previously in LVC et al. [291] and Covas and Sintes [552]. The follow-up procedure, thoroughly described in Tenorio et al. [553], uses a Markov chain Monte Carlo (MCMC) sampler [554, 555] to explore a parameter-space region using the  $\mathcal{F}$ -statistic as log-likelihood [262]. Two coherence times are used here, namely  $T_{\text{coh}} = 12$  d and  $T_{\text{coh}} = 24$  d. Prior distributions are Gaussian distributions centered at the outlier parameters (Table 6.7) using a standard deviation of one parameter-space bin with maximum mismatch  $\mu_{\text{max}} = 1$  [88]. The results of the follow-up are evaluated using a Bayes factor,  $\mathcal{B}_{\text{S/N}}$ , that compares the evidence for a model that the data contain a coherent signal to the evidence for a model that the data contain only noise. The value of  $\mathcal{B}_{\text{S/N}}$  is computed by comparing the change in the  $\mathcal{F}$ -statistic of the loudest candidate between the two follow-up stages with different coherence times: if a signal is present in the data, the  $\mathcal{F}$ -statistic should provide a consistent estimate of the signal-to-noise ratio; otherwise, the loudest candidate is a result of noise, the distribution of which follows a Gumbel distribution. This noise distribution is estimated using a similar method to the one described in Appendix 6.A1.4, with 600 off-source calculations performed.

The loudest candidate of the follow-up returns a log-Bayes factor of  $\log_{10} \mathcal{B}_{\text{S/N}} = 1.45$ . We characterize the  $\log_{10} \mathcal{B}_{\text{S/N}}$  distribution using 400 isotropically distributed sources injected into the real data with an amplitude of  $h_0^{95\%}$ . We obtain a 1% false dismissal threshold of 8.75, which is significantly larger than the candidate’s log-Bayes factor of 1.45. That is, if this were a true signal, with  $h_0 = h_0^{95\%}$ , we would expect the log-Bayes factor to be higher than what we see in the real data by about 7. We conclude that there is no significant evidence of continuous gravitational wave emission from this target.

---

## Conclusions and future directions

---

In this chapter we summarize the main results of the thesis. Section 7.1 reviews the work presented in Chapters 2–4, in which we attempt to falsify various underlying mechanisms which may cause pulsar glitches, by understanding the long-term statistical predictions of phenomenological stress-accumulation and relaxation meta-models, and comparing to observations. In Section 7.2 we review the application of one such meta-model to solar flares, as discussed in Chapter 5. Section 7.3 reviews the search for continuous gravitational waves from AMXPs in O3 LIGO data, as presented in Chapter 6. We sketch various avenues for future work throughout.

### 7.1. UNDERSTANDING PULSAR GLITCHES THROUGH THE LENS OF STRESS-ACCUMULATION AND RELAXATION META-MODELS

What causes pulsar glitches is unknown. There are numerous physical mechanisms popular in the literature (see Haskell and Melatos [150], Antonopoulou et al. [151], Antonelli et al. [152], and Zhou et al. [153] for modern reviews). Almost all of these mechanisms are, at an abstract level, stress-accumulation and relaxation processes. That is, while the glitch trigger mechanism varies, there is broad agreement that stress accumulates in the pulsar between glitches, and some of this stress is released at each glitch.

The state-dependent Poisson (SDP) process is a doubly-stochastic system, wherein a globally-averaged stress  $X$  is tracked as a function of time. The waiting times  $\Delta t$  between stress-release events are random, but events become more likely as  $X$  approaches the critical stress  $X_c$ , at which point a stress-release event becomes certain. The speed at which the system is driven towards  $X_c$  is determined by the control parameter  $\alpha$ . The amount of stress released at each event is another random variable, and is governed by the conditional jump-size distribution  $\eta[\Delta X_i | X(t_i^-)]$ . This distribution is determined by fiat, and can be treated as a free parameter in the meta-model, or it can encode one’s belief regarding the underlying physical mechanism. For example, if  $\eta$  is a power law, the amount of stress released at each event is scale-free, which is a hallmark of an avalanche-type process. While keeping  $\eta$  as a free parameter, the SDP framework can successfully and self-consistently generate sequences of glitch waiting times, sizes, and cross-correlations thereof which match those from the most-glitching pulsars [15, 16, 351]. The SDP process is a broad framework, that encompasses many, but not all, microphysical trigger mechanisms. To test, and potentially falsify, specific mechanisms

we adapt and probe the SDP framework in different ways in this thesis.

In Chapter 2 we investigate the autocorrelation between subsequent waiting times  $\rho_{\Delta t}$ , or subsequent sizes  $\rho_{\Delta X}$ . These are long-term statistical quantities easily calculable in the SDP framework, and measurable from glitch observations. We find that most configurations of the SDP process, i.e. combinations  $\eta$  and  $\alpha$ , result in autocorrelations that are consistent with zero. However, there are certain regimes that are ruled out. For example, if  $\eta$  is a Gaussian, we always have  $\rho_{\Delta t} \leq 0$ . The waiting times, sizes and cross-correlations of the quasiperiodic glitching pulsar PSR J0537–6910 are only consistent with the SDP process if we have  $\eta$  unimodal and  $\alpha \lesssim 10^{-2}$ . Thus, if we detected  $\rho_{\Delta t} > 0$  in this pulsar, we would falsify the SDP process. We find  $\rho_{\Delta t} \lesssim 0$ . We also find configurations of  $\eta$  and  $\alpha$  that can simultaneously explain the observed waiting time and size PDFs [15], cross-correlations [351], and autocorrelations [1] in all other glitching pulsars that have enough recorded glitches to make such measurements. That is, we cannot currently falsify the SDP process in any glitching pulsar. However, this may change as more glitches are discovered, both in historic datasets [138, 556, 557], and through continued monitoring of known pulsars [97, 558–560].

In Chapter 3 we explore the impact that a stochastic stress driver has on long-term statistical predictions. A stochastic driver may be connected to timing noise (see Section 1.3.1) or superfluid turbulence [83, 368, 373]. By replacing the secular intra-glitch evolution of the stress with a stochastic process, we in turn require that the stress reach a threshold before each event is triggered. The waiting times between events depend on how much stress was released at the previous event, and the balance between drift and diffusion in the Brownian walk of the stress. As for the SDP framework, we make precise, falsifiable predictions regarding what combinations of long-term statistical observables are possible to generate within the Brownian stress accumulation meta-model. When we compare these predictions to pulsar data, we find the meta-model is falsified in at least some pulsars. For example PSR J0534+2200 has a very low forward cross-correlation, which can only be generated from the meta-model if diffusion dominates over drift in the Brownian random walk. In this regime, we should see an excess of events with very small waiting times, however there is no evidence of such in the data. Therefore, unless we are missing many glitches with  $\Delta t \lesssim 0.25\langle\Delta t\rangle$ , this meta-model cannot explain all glitches from all pulsars.

The final glitch meta-model we investigate in this thesis returns to the SDP framework, but prescribes the size of stress-release events endogenously. In Chapter 4 we assume pulsar glitches are caused by superfluid vortex avalanches, triggered via a coherent stress mechanism. Under this assumption, we codify the current understanding of the microphysical rules regarding how vortices pin and unpin, to phenomenologically track the pinning strength of pinning sites that are occupied, as a function of time. Doing so allows us to know what fraction of vortices unpin once a stress-release event is triggered, i.e. the size of stress-release events is no longer a random variable, but is instead determined by the history of past avalanches in the system. This meta-model again makes precise, falsifiable predictions regarding combinations of long-term statistical observables. We find these predictions broadly inconsistent with observational data from most glitching pulsars, provisionally falsifying the meta-model. This does not imply that glitches must be caused by a mechanism other than superfluid vortex avalanches. The meta-model idealizes much of the detailed microphysics. Simulations suggest that

spatial correlations play a key role in vortex motion [137], while the coherent stress mechanism addressed here assumes one, globally-averaged stress is felt at all pinning sites.

One limiting factor in drawing concrete conclusions from glitch meta-models is the paucity of data. As seen in Table 1.1, only six pulsars have more than 15 recorded glitches. Millhouse et al. [11] and Melatos and Millhouse [561] use even the non-detection of glitches to estimate glitch rates across the population of pulsars, and by implementing a hierarchical Bayesian scheme, estimate various SDP parameters. However, the analysis in the aforementioned papers does not incorporate glitch sizes, or long-term observables such as cross- or autocorrelations. Incorporating this additional information is not trivial, as it would result in fitting a complicated, non-convex likelihood to the data [370]. A reformulation of stress-relax meta-models into the mathematical language of jump-diffusion processes might unlock optimal filtration techniques (e.g. the Kushner and Zakai equations [562, 563]), allowing us to optimally estimate parameters of the process given noisy, sparse measurements [564].

Detecting more glitches is possible via a combination of: i) observing known glitching pulsars with a higher cadence; ii) observing known glitching pulsars with a longer dwell time, or higher sensitivity; iii) applying and developing more sensitive glitch detection algorithms; and/or iv) finding more pulsars which glitch. Point (i) will allow for earlier detection of glitches, and the detection of smaller glitches with fast recoveries (i.e. glitches that with a longer cadence may not have a noticeable impact on the timing solution). Relatedly, a higher cadence will also allow for easier discrimination between timing noise and small glitches [62, 556], something that point (ii) will also assist with. Point (iii) is an ongoing area of research [61, 62, 96]. Sensitive future facilities, such as the Square Kilometer Array, will allow for the discovery and continuous monitoring of many more glitching pulsars than are currently known [565, 566]. That is, they will assist points (ii) and (iv). However, unless the proposed fortnightly cadence of observations is reduced, these future facilities will not help us accurately determine the low end of the glitch size or waiting time distribution, which is crucial for distinguishing between the meta-models discussed in Chapters 2–4.

A natural question remains: how many glitches will we need to detect before we can confidently discriminate between different meta-models? This is non-trivial to answer quantitatively. Appendix B of Melatos and Drummond [370] approaches this question in terms of how many glitches are needed before the SDP meta-model can more accurately predict future glitch epochs, compared to a simple Poisson process, assuming glitches truly arise from the SDP process. They find that at least 50, and up to hundreds of glitches are necessary. However, if certain pulsars are found to have, for example, a waiting time or size autocorrelation statistically different from zero, certain meta-models (such as the one discussed in Chapter 3) are immediately disfavored. This could occur with as few as  $\sim 30$  glitches, dependent on the true underlying autocorrelation (c.f. Equation (2.6)).

## 7.2. ARE SOLAR FLARES THE RESULT OF STRESS APPROACHING A THRESHOLD BEFORE EACH EVENT?

In Chapter 5 we turn our attention to solar flares. The typical explanation for flares is that subphotospheric, convective motion transports energy into the magnetic field of the corona. This energy accumulates over time, and releases suddenly when the footpoints of coronal loops or arcades shift, triggering a reconnection event [209, 413]. Accordingly, there is a long history of building phenomenological stress-relax models that track this energy and predict statistical signatures [221–224, 226]. One such signature is a cross-correlation,  $\rho_+$ , between size of a flare and the subsequent waiting time. We should see a large  $\rho_+$ , if the stress threshold does not vary from flare to flare, and the stress reaches this threshold before every flare. Searches for statistical signatures of these models in data has a similarly long history [226, 232, 423–426]. However, barring a few exceptions [226, 567], the vast majority of these studies do not find any evidence of a large  $\rho_+$ , nor evidence of a static-in-time threshold. For example, in summarizing the Flare Build-Up Study, Gaizauskas and Svestka [232] state that there is “no consistent relationship [...] between the repetition rate of homologous flares and their X-ray [...] brightness” (verbatim quote).

An alternative set of phenomenological models in the literature posits solar flares as analogous to systems in a state of self-organized criticality, such as sandpiles or avalanches, in which case there should exist no cross-correlations between sizes and waiting times, and one should see a power law size PDF [227, 230, 414, 568]. The SDP framework broadly encompasses both sets of phenomenological models. If we have  $\alpha \ll 1$  the process is threshold-driven, i.e. approaches a static-in-time threshold before each event. On the other hand, for  $\alpha \gg 1$ , there is little long-term memory in the system, and the dynamics are largely determined by the choice of  $\eta$ , which can be fixed as a power law, producing a power law size PDF.

We analyze the GOES soft X-ray flare dataset, which contains over  $8 \times 10^5$  events. We look for statistical signatures of a SDP process in sequences of flare sizes and waiting times in individual active regions. For example, we investigate whether the flare rate  $\lambda_k$  (a potential proxy for  $\alpha$ ) is associated with larger  $\rho_+$ , and find a small but non-zero Spearman correlation of  $5 \times 10^{-2}$  (p-value of 0.06), see Figure 5.6. Another test is to see whether the regions which have similar waiting time and size PDFs also have large  $\rho_+$ , another key prediction of the SDP framework if we have  $\alpha \ll 1$ . We see no evidence for this association in the GOES data, see Figure 5.7b. These results are predicated on the completeness of the flare catalog, which is not guaranteed, as discussed in detail in Section 5.5.2. We find no strong evidence that flares are the result of a SDP process in the  $\alpha \ll 1$  regime, where stress approaches a static-in-time threshold before every flare. However, the SDP process assumes that stress is driven into the system at a constant rate, and that the threshold does not vary from flare to flare. Alternative meta-models may soften these assumptions in the future.

There are many open questions regarding the physics behind solar flares that can be guided by the SDP framework. For example, one may look for a correlation between statistical measurements that are directly linked to SDP predictions or input parameters, such as  $\rho_+$  or  $\lambda_k$  respectively, with other observables for a given active region. This regression should at minimum include the phase of the solar cycle, as a proxy for the Sun’s

large-scale magnetic field strength [569], the morphology of the active region [570], and vector magnetogram estimates of both the perpendicular and line-of-sight magnetic field strength in the active region [217, 571]. Such an exercise could help untangle the potential causal links between the physical properties of the active region, and the SDP parameters that govern the statistical behavior of flare occurrence. Estimating SDP parameters in individual regions may also lead to an improvement in our ability to predict flares, although this will likely only be possible in regions that already have many flares observed, see Appendix B of Melatos and Drummond [370] for an exploration of this possibility in the context of pulsar glitch epoch prediction. Flare prediction using purely data-driven algorithms is difficult [218, 572, 573], but astrophysically motivated models can help in some circumstances [220].

### 7.3. SEARCHING FOR CONTINUOUS GRAVITATIONAL WAVES FROM ACCRETING MILLISECOND X-RAY PULSARS

Despite much effort, continuous gravitational waves are yet to be detected. Detecting a small signal in noise requires an accurate signal model. Continuous gravitational wave searches for neutron stars in binary systems, such as AMXPs, require us to model not just the deterministic evolution of the gravitational wave frequency, but also allow for some degree of stochastic variation due to spin-wandering. In Chapter 6, we use the  $\mathcal{J}$ -statistic [8] as a matched filter for the signal over coherent chunks of  $T_{\text{drift}} = 10\text{ d}$ . That is, we assume that the gravitational wave frequency stays within one frequency bin over the 10 d chunk, after accounting for the Doppler modulations due to Earth’s motion around the solar system barycentre, as well as the target’s motion in its binary. The slow stochastic variation over time is accounted for with a hidden Markov model [7]. That is, between chunks we allow the (Doppler corrected) gravitational wave frequency to vary by up to one bin. We reconstruct the most likely path through the time–frequency trellis using the Viterbi algorithm [308].

AMXPs pulsate in X-rays while they are in outburst, a period of increased X-ray flux due to an increase in mass accretion rate [44]. These pulsations allow for phase-coherent timing of the rotation of the neutron star, giving precise estimates for the rotation frequency and binary orbital elements. We use these precise estimates to guide our continuous gravitational wave search for 20 AMXPs. We search for gravitational waves at three  $\sim 0.61\text{ Hz}$  subbands, centered at once, twice, and  $\sim 4/3$  the spin frequency  $f_\star$  of the neutron star. These harmonics are the most likely frequencies for gravitational wave emission, as discussed in Section 1.7.3. The narrow sub-bands allow for a slight mismatch of rotation frequency between the mass quadrupole or current quadrupole that emits the gravitational waves, and the rotation frequency of the surface of the neutron star.

We find no strong evidence in LIGO O3 data for continuous gravitational waves in any subband from any of the targets. When we set a permissive false alarm probability of 30% per subband, we find 16 candidates that survive a series of astrophysical vetoes, and we recommend that these candidates are followed up in searches using future, more sensitive datasets. We also performed an additional, target-of-opportunity search for gravitational waves from SAX J1808.4–3657. This target went into outburst for one month during the first half of O3, and so we search data from only that month, under

the speculative hypothesis that it is only emitting gravitational waves for a short time after the outburst begins. We again find no strong evidence of a signal. Assuming all of our candidates are false alarms, we compute frequentist upper limits on the detectable strain at 95% confidence via sequences of software injections. The lowest constraint is in the  $2f_\star$  subband of IGR J17062–6143, where we find  $h_0^{95\%} = 4.7 \times 10^{-26}$ . Constraints on  $h_0^{95\%}$  are converted to astrophysical constraints on the ellipticity  $\epsilon$  and  $r$ -mode amplitude  $\alpha$  for all targets, using Equations (6.14) and (6.15) respectively. The most constraining AMXP for these quantities is IGR J00291+5934, where we find  $\epsilon^{95\%} = 3.1 \times 10^{-7}$  and  $\alpha^{95\%} = 1.8 \times 10^{-5}$ .

Theoretical estimates for the expected ellipticity in accreting systems vary, but current estimates for magnetically or elastically supported mountains propose  $\epsilon \sim 10^{-10} - 10^{-6}$ , dependent on modelling details such as the equation of state [184, 330, 574, 575]. Our upper limits on ellipticity therefore already provide constraints on which of these theoretical models may apply in AMXPs. Theoretical estimates for the expected  $r$ -mode amplitude in accreting systems propose  $\alpha \sim 10^{-3} - 10^{-4}$  [344, 576], but are of course conditional on many unknown neutron star parameters. Again, our upper limits from AMXPs place constraints on these models.

The upper limit we place on detectable strain depends on many factors. It is a function of the noise floor of the detector, the total observing time, choices in the signal model, and the size of the searched parameter space. The first two aspects will improve in the next observing run of the LVK, Observing Run 4 (O4). Current, publicly available information indicates that O4 will begin at the end of May 2023, and include at least 18 months of data collection, at an increased sensitivity compared to O3<sup>1</sup>. The improvement in sensitivity is hard to quantitatively assess while commissioning is ongoing, but a first-order estimate is possible by comparing the quoted binary neutron star (BNS) inspiral range, the distance to which a canonical binary neutron star merger is detectable with a signal-to-noise ratio of eight in a single detector. For O3, this distance was around 120 Mpc, while in O4 it is estimated to be at least 160 Mpc [577]. This “range” incorporates sensitivity improvements across a broad frequency band. The exact improvement for a continuous gravitational wave search will depend on the subband. The detectable strain scales inversely with the distance to the source, i.e. an increase in the inspiral range corresponds to lower detectable strains, c.f. Equation (1.11). That is, if the BNS range increases by a factor of  $160 \text{ Mpc}/120 \text{ Mpc} = 4/3$ , we are sensitive to  $3/4$  smaller strains from a source at a fixed distance. For a semi-coherent search, we have

$$h_0^{95\%} \propto (T_{\text{obs}} T_{\text{drift}})^{-1/4}, \quad (7.1)$$

where  $T_{\text{obs}}$  is the total observing time [578]. The proportionality constant in Equation (7.1) is set by the noise floor of the detectors, and the search pipeline. Detailed, individual analysis of X-ray flux variability in AMXPs may allow us to increase  $T_{\text{drift}}$  to (say)  $T_{\text{drift}} = 20 \text{ d}$ , if the stochastic variations in spin frequency are low enough [92].

We can further improve the detectable strain by modifying the search space. As discussed in Section 6.5.2, while the orbital elements  $P$ ,  $T_{\text{asc}}$ , and  $a_0$  are precisely known from X-ray pulsation timing, we must still search over a set of templates to ensure the mismatch between the true signal parameters and those used in the search does not

---

<sup>1</sup><https://observing.docs.ligo.org/plan/>

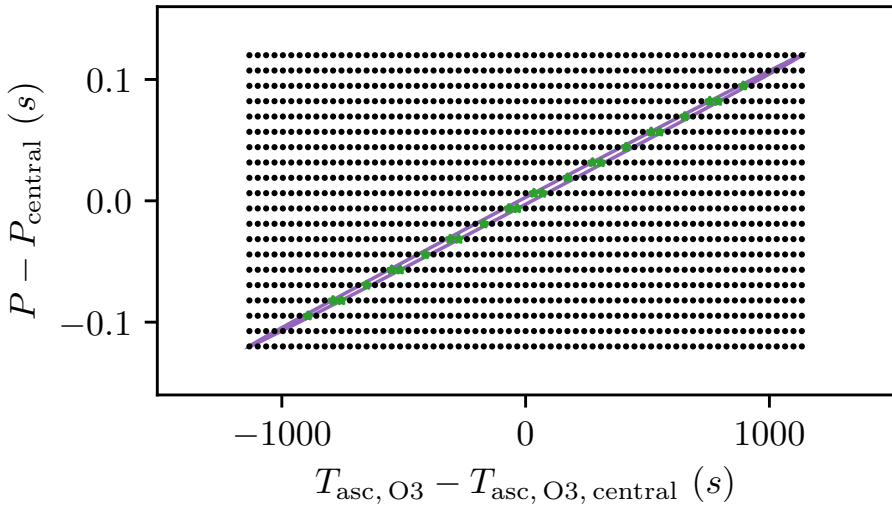


Figure 7.1: Template placement in the  $P - P_{\text{central}}$  space for the  $2f_\star$  subband of Swift J1756.9–2508. Black dots correspond to the templates in the O3 search present in Chapter 6. The purple ellipse is the true  $3\sigma$  joint prior on these parameters, and the green crosses indicate which templates lie within this prior.  $P_{\text{central}}$  and  $T_{\text{asc}, \text{central}}$  refer to the central  $P$  and propagated  $T_{\text{asc}}$  values for this target, as recorded in Table 6.1.

result in an unacceptable loss in signal-to-noise ratio. The size of the template bank feeds into the calculation for the threshold  $\mathcal{L}_{\text{th}}$  for a given subband, as it changes the necessary trials factor to keep the total false alarm rate at a fixed value, see Section 6.5.3 and Appendix 6.A1. The  $P - T_{\text{asc}}$  search space we use in Chapter 6 conservatively covers a rectangular grid. However, the joint prior on  $P$  and  $T_{\text{asc}}$  measured electromagnetically is a multivariate Gaussian. This Gaussian has a non-diagonal covariance matrix once  $T_{\text{asc}}$  is propagated to the start of O3. By searching a rectangular grid in  $P$  and the propagated  $T_{\text{asc}}$  we are ignoring this covariance, and search the marginal joint priors in the two parameters independently. For concreteness, we calculate this effect for the  $2f_\star$  subband of Swift J175.96–2508. The true  $3\sigma$  joint prior is shown as the purple ellipse in Figure 7.1, while the black dots mark the templates used in the O3 search. The green stars mark the O3 search templates that lie within the true joint prior. There are 24 templates within the joint prior compared to the 1340 templates we searched in O3. This indicates that we can reduce our search space by 98.2% for this subband without any loss in probability of detection. Initial investigations indicate that comparable reductions in search space are possible in most of the other subbands.

One may use the optimal template placement described in Wagner et al. [579] to further reduce the total number of templates, but this effect is minor compared to searching only the templates enclosed in the true joint prior. Another potential reduction in total templates needed is to under-sample regions of the  $P - T_{\text{asc}}$  space depending on the prior probability. That is, currently we search uniformly between the  $3\sigma$  bounds of the prior, however as the prior is a multivariate Gaussian, the true parameters are less likely to lie on the outskirts of the prior, compared to the center. Thus, we can potentially reduce our search space by another order of magnitude.

How much does reducing the number of templates, and thus  $\mathcal{L}_{\text{th}}$ , affect the detectable wave strain? If we calculate  $\mathcal{L}_{\text{th}}$  using an exponential fit of the tail of the distribution of

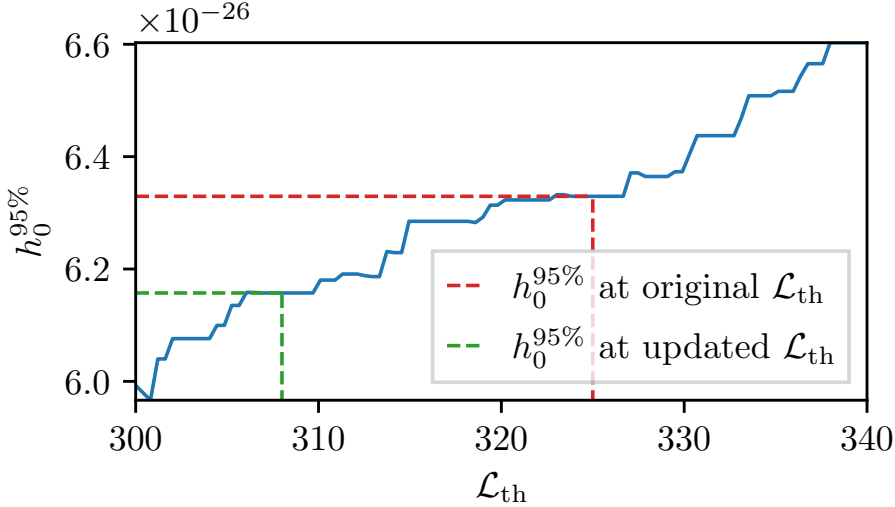


Figure 7.2: Detectable strain  $h_0^{95\%}$  as a function of the threshold  $\mathcal{L}_{\text{th}}$  for the  $2f_\star$  subband of Swift J1756.9–2508. The original  $\mathcal{L}_{\text{th}}$  used in the O3 search, and corresponding  $h_0^{95\%}$ , is marked with a red dashed line. The updated  $\mathcal{L}_{\text{th}}$  obtained by restricting the search space in  $P-T_{\text{asc}}$  to only the templates contained within the true joint prior, as shown in Figure 7.1, results in an updated  $h_0^{95\%}$ , and is marked with a green dashed line.

$\mathcal{L}$  in noise, as discussed in Appendix 6.A1.1, we see via Equation (6.19) that the threshold will vary as

$$\mathcal{L}_{\text{th}}^{\text{new}} = \mathcal{L}_{\text{th}}^{\text{orig}} - \frac{1}{\hat{\lambda}} \log \left( \frac{N_{\text{tot}}^{\text{orig}}}{N_{\text{tot}}^{\text{new}}} \right) \quad (7.2)$$

where  $N_{\text{tot}}$  is the total number of templates, and “orig” and “new” superscripts denote the original and updated parameters respectively. For the illustrative  $2f_\star$  subband of Swift J1756.9–2508, a reduction of the number of templates searched by 98.2% (c.f. Figure 7.1) results in  $\mathcal{L}^{\text{new}} \approx \mathcal{L}^{\text{old}} - 16.7$ . The connection between  $\mathcal{L}_{\text{th}}$  and  $h_0^{95\%}$  is hard to assess analytically, but it is easy to calculate empirically. We show in Figure 7.2 that grows  $h_0^{95\%}$  approximately linearly with  $\mathcal{L}_{\text{th}}$ , and a difference of 16.7 in  $\mathcal{L}_{\text{th}}$  corresponds to a difference of  $1.7 \times 10^{-27}$  in  $h_0^{95\%}$ , i.e. we are able to detect signals that are  $\sim 3\%$  weaker. The additional template-placement considerations discussed above conceivably result in an additional improvement, up to perhaps 5% in  $h_0^{95\%}$ . Updating the HMM tracking scheme to include the gravitational wave phase allows one to detect  $\sim 10\%$  smaller strains, at an increased computational cost [316].

Combining the five improvements described above allows us to estimate the improvement in sensitivity that we may achieve for a search for continuous gravitational waves from AMXPs using O4 data. Substituting fiducial values we find

$$h_0^{95\%, \text{O4}} \approx 0.48 h_0^{95\%, \text{O3}} \left( \frac{1.33}{\text{BNS}_{\text{range}}^{\text{O4}} / \text{BNS}_{\text{range}}^{\text{O3}}} \right) \left( \frac{1.64}{T_{\text{obs}}^{\text{O4}} / T_{\text{obs}}^{\text{O3}}} \right)^{1/4} \left( \frac{2}{T_{\text{drift}}^{\text{O4}} / T_{\text{drift}}^{\text{O3}}} \right)^{1/4} \times \left( \frac{95\%}{\text{Search space reduction}} \right)^{-1} \left( \frac{90\%}{\text{Phase tracking HMM}} \right)^{-1}, \quad (7.3)$$

where superscripts of O3 and O4 refer to parameter values in those respective observing runs. The first two terms in parentheses correspond to the improvement in detector sensitivity and the increase in observation duration respectively. The third term corresponds to increasing  $T_{\text{drift}}$  from 10 to 20 d. The fourth term arises due to reducing the number of templates, and the effect this has on  $\mathcal{L}_{\text{th}}$ , i.e. by reducing the trials factor. The fifth term is a rough estimate of the potential benefit from using the HMM scheme described by Melatos et al. [316]. We find that the fiducial upper limits we set in O4 should improve on the upper limits set in O3 by over a factor of two, increasing our probability of detection.

If a factor of two is insufficient in producing a detection, we can look to future, even more sensitive detectors such as the Einstein Telescope [580] and Cosmic Explorer [581]. These proposed detectors will reduce the single-sided noise power spectral density compared to current LIGO detectors by over an order of magnitude [580, 581], thus improving our sensitivity by a factor of  $\sim$ five. However, these detectors are not yet built or fully funded, and are unlikely to come online before the 2040s. Our best prospects for detecting continuous gravitational waves in the medium-term therefore lie in the factors discussed in Equation (7.3): i) improving the sensitivity of current-generation detectors; ii) ingesting longer spans of data, with longer coherence lengths (if the physics allows); and iii) optimizing search algorithms.

---

## References

---

- <sup>1</sup>J. B. Carlin and A. Melatos, *Monthly Notices of the Royal Astronomical Society* **488**, 4890–4896 (2019).
- <sup>2</sup>J. B. Carlin and A. Melatos, *Monthly Notices of the Royal Astronomical Society* **494**, 3383–3391 (2020).
- <sup>3</sup>J. B. Carlin and A. Melatos, *The Astrophysical Journal* **917**, 1 (2021).
- <sup>4</sup>J. B. Carlin, A. Melatos, and M. S. Wheatland, *The Astrophysical Journal* **948**, 76 (2023).
- <sup>5</sup>J. B. Carlin, A. Melatos, and M. S. Wheatland, *The Astrophysical Journal* **953**, 120 (2023).
- <sup>6</sup>LIGO Scientific Collaboration et al., *Physical Review D* **105**, 022002 (2022).
- <sup>7</sup>S. Suvorova, L. Sun, A. Melatos, W. Moran, and R. J. Evans, *Physical Review D* **93**, 123009 (2016).
- <sup>8</sup>S. Suvorova, P. Clearwater, A. Melatos, L. Sun, W. Moran, and R. J. Evans, *Physical Review D* **96**, 102006 (2017).
- <sup>9</sup>H. Middleton, P. Clearwater, A. Melatos, and L. Dunn, *Physical Review D* **102**, 023006 (2020).
- <sup>10</sup>D. Keitel, R. Tenorio, G. Ashton, and R. Prix, *Journal of Open Source Software* **6**, 3000 (2021).
- <sup>11</sup>M. Millhouse, A. Melatos, G. Howitt, J. B. Carlin, L. Dunn, and G. Ashton, *Monthly Notices of the Royal Astronomical Society* **511**, 3304–3319 (2022).
- <sup>12</sup>D. Jones et al., *Physical Review D* **106**, 123011 (2022).
- <sup>13</sup>A. Weinstein and S. Privitera, *Sensitivity to Gravitational Waves from Compact Binary Coalescences Achieved during LIGO’s Fifth and Virgo’s First Science Run*, tech. rep. T0900499 (May 2010).
- <sup>14</sup>E. Goetz, *L1 Calibrated Sensitivity Spectra Jan 04 2020 (Representative best of O3b – C01\_CLEAN\_SUB60HZ)*, tech. rep. G2100675 (Mar. 2021).
- <sup>15</sup>J. B. Carlin and A. Melatos, *Monthly Notices of the Royal Astronomical Society* **483**, 4742–4750 (2019).
- <sup>16</sup>W. Fulgenzi, A. Melatos, and B. D. Hughes, *Monthly Notices of the Royal Astronomical Society* **470**, 4307–4329 (2017).
- <sup>17</sup>A. Melatos, C. Peralta, and J. S. B. Wyithe, *The Astrophysical Journal* **672**, 1103–1118 (2008).
- <sup>18</sup>G. Howitt, A. Melatos, and A. Delaigle, *The Astrophysical Journal* **867**, 60 (2018).

- <sup>19</sup>J. R. Fuentes, C. M. Espinoza, and A. Reisenegger, *Astronomy and Astrophysics* **630**, A115 (2019).
- <sup>20</sup>S. Shapiro and S. Teukolsky, *Black holes, white dwarfs, and neutron stars: The physics of compact objects* (Wiley-Interscience, New York, 1983).
- <sup>21</sup>W. Baade and F. Zwicky, *Proceedings of the National Academy of Science* **20**, 254–259 (1934).
- <sup>22</sup>A. Hewish, S. J. Bell, J. D. H. Pilkington, P. F. Scott, and R. A. Collins, *Nature* **217**, 709–713 (1968).
- <sup>23</sup>T. Gold, *Nature* **218**, 731–732 (1968).
- <sup>24</sup>F. Pacini, *Nature* **219**, 145–146 (1968).
- <sup>25</sup>J. D. H. Pilkington, A. Hewish, S. J. Bell, and T. W. Cole, *Nature* **218**, 126–129 (1968).
- <sup>26</sup>M. I. Large, A. E. Vaughan, and B. Y. Mills, *Nature* **220**, 340–341 (1968).
- <sup>27</sup>A. J. Turtle and A. E. Vaughan, *Nature* **219**, 845–846 (1968).
- <sup>28</sup>A. J. Turtle and A. E. Vaughan, *Nature* **219**, 689–690 (1968).
- <sup>29</sup>J. M. Comella, H. D. Craft, R. V. E. Lovelace, J. M. Sutton, and G. L. Tyler, *Nature* **221**, 453–454 (1969).
- <sup>30</sup>A. Lyne and F. Graham-Smith, *Pulsar Astronomy*, 4th ed., Cambridge Astrophysics (Cambridge University Press, Cambridge, 2012).
- <sup>31</sup>E. F. Keane, M. Kramer, A. G. Lyne, B. W. Stappers, and M. A. McLaughlin, *Monthly Notices of the Royal Astronomical Society* **415**, 3065–3080 (2011).
- <sup>32</sup>G. G. Pavlov, D. Sanwal, and M. A. Teter, *Nature* **218**, 239 (2004).
- <sup>33</sup>R. A. Chevalier, *The Astrophysical Journal* **619**, 839 (2005).
- <sup>34</sup>B. Cerutti and A. M. Beloborodov, *Space Science Reviews* **207**, 111–136 (2017).
- <sup>35</sup>A. K. Harding, *Proceedings of the International Astronomical Union* **13**, 52–57 (2017).
- <sup>36</sup>D. B. Melrose, M. Z. Rafat, and A. Mastrano, *Monthly Notices of the Royal Astronomical Society* **500**, 4530–4548 (2021).
- <sup>37</sup>D. B. Melrose, M. Z. Rafat, and A. Mastrano, *Monthly Notices of the Royal Astronomical Society* **500**, 4549–4559 (2021).
- <sup>38</sup>A. Philippov, A. Timokhin, and A. Spitkovsky, *Physical Review Letters* **124**, 245101 (2020).
- <sup>39</sup>V. E. Zavlin, “Theory of Radiative Transfer in Neutron Star Atmospheres and Its Applications”, in *Neutron Stars and Pulsars*, edited by W. Becker, Astrophysics and Space Science Library (Springer, Berlin, Heidelberg, 2009), pp. 181–211.
- <sup>40</sup>D. Psaltis, “Accreting neutron stars and black holes: a decade of discoveries”, in *Compact Stellar X-ray Sources*, edited by M. van der Klis and W. Lewin, Cambridge Astrophysics (Cambridge University Press, Cambridge, 2006), pp. 1–38.
- <sup>41</sup>H. Bondi and F. Hoyle, *Monthly Notices of the Royal Astronomical Society* **104**, 273–282 (1944).

- <sup>42</sup>S. Karino, K. Nakamura, and A. Taani, *Publications of the Astronomical Society of Japan* **71**, 58 (2019).
- <sup>43</sup>S. Galaudage, K. Wette, D. K. Galloway, and C. Messenger, *Monthly Notices of the Royal Astronomical Society* **509**, 1745–1754 (2022).
- <sup>44</sup>T. Di Salvo and A. Sanna, “Accretion Powered X-ray Millisecond Pulsars”, in *Millisecond Pulsars*, edited by S. Bhattacharyya, A. Papitto, and D. Bhattacharya, Astrophysics and Space Science Library (Springer International Publishing, Cham, 2022), pp. 87–124.
- <sup>45</sup>P. Ghosh, F. K. Lamb, and C. J. Pethick, *The Astrophysical Journal* **217**, 578–596 (1977).
- <sup>46</sup>P. Ghosh and F. K. Lamb, *The Astrophysical Journal* **234**, 296–316 (1979).
- <sup>47</sup>T. M. Tauris, N. Langer, and M. Kramer, *Monthly Notices of the Royal Astronomical Society* **425**, 1601–1627 (2012).
- <sup>48</sup>V. M. Kaspi, *Proceedings of the National Academy of Sciences* **107**, 7147–7152 (2010).
- <sup>49</sup>S. Campana and T. Di Salvo, “Accreting Pulsars: Mixing-up Accretion Phases in Transitional Systems”, in *The Physics and Astrophysics of Neutron Stars*, edited by L. Rezzolla, P. Pizzochero, D. I. Jones, N. Rea, and I. Vidaña, Astrophysics and Space Science Library (Springer International Publishing, Cham, 2018), pp. 149–184.
- <sup>50</sup>P. M. Woods and C. Thompson, “Soft gamma repeaters and anomalous X-ray pulsars: magnetar candidates”, in *Compact Stellar X-ray Sources*, edited by M. van der Klis and W. Lewin, Cambridge Astrophysics (Cambridge University Press, Cambridge, 2006), pp. 547–586.
- <sup>51</sup>R. N. Manchester, G. B. Hobbs, A. Teoh, and M. Hobbs, *The Astronomical Journal* **129**, 1993–2006 (2005).
- <sup>52</sup>F. Pacini, *Nature* **216**, 567–568 (1967).
- <sup>53</sup>J. E. Gunn and J. P. Ostriker, *Nature* **221**, 454–456 (1969).
- <sup>54</sup>N. U. Mayall, *Leaflet of the Astronomical Society of the Pacific* **3**, 145 (1939).
- <sup>55</sup>A. G. Lyne, C. A. Jordan, F. Graham-Smith, C. M. Espinoza, B. W. Stappers, and P. Weltevrede, *Monthly Notices of the Royal Astronomical Society* **446**, 857–864 (2015).
- <sup>56</sup>J. J. Hester, *Annual Review of Astronomy and Astrophysics* **46**, 127–155 (2008).
- <sup>57</sup>D. R. Lorimer and M. Kramer, *Handbook of Pulsar Astronomy*, Vol. 4, Cambridge observing handbooks for research astronomers (Cambridge University Press, Cambridge, Dec. 2004).
- <sup>58</sup>G. B. Hobbs, R. T. Edwards, and R. N. Manchester, *Monthly Notices of the Royal Astronomical Society* **369**, 655–672 (2006).
- <sup>59</sup>R. T. Edwards, G. B. Hobbs, and R. N. Manchester, *Monthly Notices of the Royal Astronomical Society* **372**, 1549–1574 (2006).
- <sup>60</sup>W. H. Press, S. A. Teukolsky, W. T. Vetterling, and B. P. Flannery, *Numerical Recipes 3rd Edition: The Art of Scientific Computing* (Cambridge University Press, Sept. 2007).
- <sup>61</sup>L. Lentati, P. Alexander, M. P. Hobson, F. Feroz, R. van Haasteren, K. J. Lee, and R. M. Shannon, *Monthly Notices of the Royal Astronomical Society* **437**, 3004–3023 (2014).

- <sup>62</sup>A. Melatos, L. M. Dunn, S. Suvorova, W. Moran, and R. J. Evans, *The Astrophysical Journal* **896**, 78 (2020).
- <sup>63</sup>J. M. Cordes and D. J. Helfand, *The Astrophysical Journal* **239**, 640–650 (1980).
- <sup>64</sup>R. M. Shannon and J. M. Cordes, *The Astrophysical Journal* **725**, 1607–1619 (2010).
- <sup>65</sup>J. M. Cordes and G. S. Downs, *The Astrophysical Journal Supplement Series* **59**, 343–382 (1985).
- <sup>66</sup>F. D'Alessandro, P. M. McCulloch, P. A. Hamilton, and A. A. Deshpande, *Monthly Notices of the Royal Astronomical Society* **277**, 1033–1046 (1995).
- <sup>67</sup>B. B. Perera et al., *Monthly Notices of the Royal Astronomical Society* **490**, 4666–4687 (2019).
- <sup>68</sup>Z. Arzoumanian et al., *The Astrophysical Journal Letters* **905**, L34 (2020).
- <sup>69</sup>S. Chen et al., *Monthly Notices of the Royal Astronomical Society* **508**, 4970–4993 (2021).
- <sup>70</sup>B. Goncharov et al., *Monthly Notices of the Royal Astronomical Society* **502**, 478–493 (2021).
- <sup>71</sup>I. H. Stairs, A. G. Lyne, and S. L. Shemar, *Nature* **406**, 484–486 (2000).
- <sup>72</sup>P. R. Brook, A. Karastergiou, S. Buchner, S. J. Roberts, M. J. Keith, S. Johnston, and R. M. Shannon, *The Astrophysical Journal Letters* **780**, L31 (2013).
- <sup>73</sup>M. Kerr, G. Hobbs, S. Johnston, and R. M. Shannon, *Monthly Notices of the Royal Astronomical Society* **455**, 1845–1854 (2016).
- <sup>74</sup>J. M. Cordes and R. M. Shannon, *The Astrophysical Journal* **682**, 1152 (2008).
- <sup>75</sup>M. Kerr, S. Johnston, G. Hobbs, and R. M. Shannon, *The Astrophysical Journal Letters* **809**, L11 (2015).
- <sup>76</sup>P. R. Brook, A. Karastergiou, S. Johnston, M. Kerr, R. M. Shannon, and S. J. Roberts, *Monthly Notices of the Royal Astronomical Society* **456**, 1374–1393 (2016).
- <sup>77</sup>R. M. Shannon, L. T. Lentati, M. Kerr, S. Johnston, G. Hobbs, and R. N. Manchester, *Monthly Notices of the Royal Astronomical Society* **459**, 3104–3111 (2016).
- <sup>78</sup>M. Kramer, A. G. Lyne, J. T. O'Brien, C. A. Jordan, and D. R. Lorimer, *Science* **312**, 549–551 (2006).
- <sup>79</sup>A. Lyne, G. Hobbs, M. Kramer, I. Stairs, and B. Stappers, *Science* **329**, 408–412 (2010).
- <sup>80</sup>K. S. Cheng, *The Astrophysical Journal* **321**, 805 (1987).
- <sup>81</sup>G. Greenstein, *Nature* **227**, 791–794 (1970).
- <sup>82</sup>B. Link, *Monthly Notices of the Royal Astronomical Society* **422**, 1640–1647 (2012).
- <sup>83</sup>A. Melatos and B. Link, *Monthly Notices of the Royal Astronomical Society* **437**, 21–31 (2014).
- <sup>84</sup>J. M. Cordes and G. Greenstein, *The Astrophysical Journal* **245**, 1060–1079 (1981).
- <sup>85</sup>K. S. Cheng, *The Astrophysical Journal* **321**, 799 (1987).
- <sup>86</sup>P. B. Jones, *Monthly Notices of the Royal Astronomical Society* **246**, 364 (1990).

- <sup>87</sup>L. Bildsten, *The Astrophysical Journal Letters* **501**, L89 (1998).
- <sup>88</sup>P. Leaci and R. Prix, *Physical Review D* **91**, 102003 (2015).
- <sup>89</sup>A. Mukherjee, C. Messenger, and K. Riles, *Physical Review D* **97**, 043016 (2018).
- <sup>90</sup>P. M. Meyers, A. Melatos, and N. J. O'Neill, *Monthly Notices of the Royal Astronomical Society* **502**, 3113–3127 (2021).
- <sup>91</sup>P. M. Meyers, N. J. O'Neill, A. Melatos, and R. J. Evans, *Monthly Notices of the Royal Astronomical Society* **506**, 3349–3363 (2021).
- <sup>92</sup>A. Melatos, N. J. O'Neill, P. M. Meyers, and J. O'Leary, *The Astrophysical Journal* **944**, 64 (2023).
- <sup>93</sup>A. G. Lyne, R. S. Pritchard, F. Graham-Smith, and F. Camilo, *Nature* **381**, 497–498 (1996).
- <sup>94</sup>L. Dunn, M. E. Lower, and A. Melatos, *Monthly Notices of the Royal Astronomical Society* **504**, 3399–3411 (2021).
- <sup>95</sup>M. E. Lower et al., *Monthly Notices of the Royal Astronomical Society* **494**, 228–245 (2020).
- <sup>96</sup>J. Singha, A. Basu, M. A. Krishnakumar, B. C. Joshi, and P. Arumugam, *Monthly Notices of the Royal Astronomical Society* **505**, 5488–5496 (2021).
- <sup>97</sup>F. Jankowski et al., *Monthly Notices of the Royal Astronomical Society* **484**, 3691–3712 (2019).
- <sup>98</sup>C. M. Espinoza, D. Antonopoulou, B. W. Stappers, A. Watts, and A. G. Lyne, *Monthly Notices of the Royal Astronomical Society* **440**, 2755–2762 (2014).
- <sup>99</sup>C. M. Espinoza, D. Antonopoulou, R. Dodson, M. Stepanova, and A. Scherer, *Astronomy and Astrophysics* **647**, A25 (2021).
- <sup>100</sup>C. Ishizuka, T. Suda, H. Suzuki, A. Ohnishi, K. Sumiyoshi, and H. Toki, *Publications of the Astronomical Society of Japan* **67**, 13 (2015).
- <sup>101</sup>S. Typel, M. Oertel, and T. Klähn, *Physics of Particles and Nuclei* **46**, 633–664 (2015).
- <sup>102</sup>T. E. Riley et al., *The Astrophysical Journal Letters* **887**, L21 (2019).
- <sup>103</sup>M. C. Miller et al., *The Astrophysical Journal Letters* **887**, L24 (2019).
- <sup>104</sup>T. E. Riley et al., *The Astrophysical Journal Letters* **918**, L27 (2021).
- <sup>105</sup>M. C. Miller et al., *The Astrophysical Journal Letters* **918**, L28 (2021).
- <sup>106</sup>The LIGO Scientific Collaboration and the Virgo Collaboration et al., *Physical Review Letters* **121**, 161101 (2018).
- <sup>107</sup>G. Raaijmakers, *The Astrophysical Journal Letters*, 13 (2019).
- <sup>108</sup>G. Raaijmakers, S. K. Greif, K. Hebeler, T. Hinderer, S. Nissanke, A. Schwenk, T. E. Riley, A. L. Watts, J. M. Lattimer, and W. C. G. Ho, *The Astrophysical Journal Letters* **918**, L29 (2021).
- <sup>109</sup>P. T. H. Pang, I. Tews, M. W. Coughlin, M. Bulla, C. V. D. Broeck, and T. Dietrich, *The Astrophysical Journal* **922**, 14 (2021).
- <sup>110</sup>N. Chamel and P. Haensel, *Living Reviews in Relativity* **11**, 10 (2008).

- <sup>111</sup>D. G. Ravenhall, C. J. Pethick, and J. R. Wilson, *Physical Review Letters* **50**, 2066–2069 (1983).
- <sup>112</sup>G. Watanabe, K. Iida, and K. Sato, *Nuclear Physics A* **676**, 455–473 (2000).
- <sup>113</sup>C. J. Horowitz, D. K. Berry, C. M. Briggs, M. E. Caplan, A. Cumming, and A. S. Schneider, *Physical Review Letters* **114**, 031102 (2015).
- <sup>114</sup>M. Alford and S. Reddy, *Physical Review D* **67**, 074024 (2003).
- <sup>115</sup>C. O. Heinke and W. C. G. Ho, *Astrophysical Journal Letters* **719**, 167–171 (2010).
- <sup>116</sup>P. S. Shternin, D. G. Yakovlev, C. O. Heinke, W. C. Ho, and D. J. Patnaude, *Monthly Notices of the Royal Astronomical Society: Letters* **412**, 108–112 (2011).
- <sup>117</sup>D. Page, M. Prakash, J. M. Lattimer, and A. W. Steiner, *Physical Review Letters* **106**, 8–11 (2011).
- <sup>118</sup>M. J. P. Wijngaarden, W. C. G. Ho, P. Chang, C. O. Heinke, D. Page, M. Beznogov, and D. J. Patnaude, *Monthly Notices of the Royal Astronomical Society* **484**, 974–988 (2019).
- <sup>119</sup>B. Posselt, G. G. Pavlov, V. Suleimanov, and O. Kargaltsev, *The Astrophysical Journal* **779**, 186 (2013).
- <sup>120</sup>B. Posselt and G. G. Pavlov, *The Astrophysical Journal* **864**, 135 (2018).
- <sup>121</sup>P. S. Ray et al., *The Astrophysical Journal* **879**, 130 (2019).
- <sup>122</sup>G. Younes, P. S. Ray, M. G. Baring, C. Kouveliotou, C. Fletcher, Z. Wadiasingh, A. K. Harding, and A. Goldstein, *The Astrophysical Journal Letters* **896**, L42 (2020).
- <sup>123</sup>G. Howitt and A. Melatos, *Monthly Notices of the Royal Astronomical Society* **514**, 863–874 (2022).
- <sup>124</sup>R. Dib, V. M. Kaspi, and F. P. Gavriil, *The Astrophysical Journal* **673**, 1044 (2008).
- <sup>125</sup>R. Dib and V. M. Kaspi, *The Astrophysical Journal* **784**, 37 (2014).
- <sup>126</sup>F. García and I. F. Ranea-Sandoval, *Monthly Notices of the Royal Astronomical Society: Letters* **449**, L73–L76 (2015).
- <sup>127</sup>A. Mastrano, A. G. Suvorov, and A. Melatos, *Monthly Notices of the Royal Astronomical Society* **453**, 522–530 (2015).
- <sup>128</sup>C. M. Espinoza, A. G. Lyne, B. W. Stappers, and M. Kramer, *Monthly Notices of the Royal Astronomical Society* **414**, 1679–1704 (2011).
- <sup>129</sup>J. Palfreyman, J. M. Dickey, A. Hotan, S. Ellingsen, and W. van Straten, *Nature* **556**, 219–222 (2018).
- <sup>130</sup>G. Ashton, P. D. Lasky, V. Gruber, and J. Palfreyman, *Nature Astronomy* **3**, 1143–1148 (2019).
- <sup>131</sup>M. Yu et al., *Monthly Notices of the Royal Astronomical Society* **429**, 688–724 (2013).
- <sup>132</sup>G. Hobbs, A. G. Lyne, and M. Kramer, *Monthly Notices of the Royal Astronomical Society* **402**, 1027–1048 (2010).
- <sup>133</sup>S. J. Dang, J. P. Yuan, R. N. Manchester, L. Li, N. Wang, J. B. Wang, G. Hobbs, Z. Y. Liu, and F. F. Kou, *The Astrophysical Journal* **896**, 140 (2020).

- <sup>134</sup>G. H. Janssen and B. W. Stappers, *Astronomy and Astrophysics* **457**, 611–618 (2006).
- <sup>135</sup>M. Yu and Q.-J. Liu, *Monthly Notices of the Royal Astronomical Society* **468**, 3031–3041 (2017).
- <sup>136</sup>A. E. Chukwude and J. O. Urama, *Monthly Notices of the Royal Astronomical Society* **406**, 1907–1917 (2010).
- <sup>137</sup>G. Howitt, A. Melatos, and B. Haskell, *Monthly Notices of the Royal Astronomical Society* **498**, 320–331 (2020).
- <sup>138</sup>A. Basu, B. Shaw, D. Antonopoulou, M. J. Keith, A. G. Lyne, M. B. Mickaliger, B. W. Stappers, P. Weltevrede, and C. A. Jordan, *Monthly Notices of the Royal Astronomical Society* **510**, 4049–4062 (2022).
- <sup>139</sup>A. G. Lyne, S. L. Shemar, and F. G. Smith, *Monthly Notices of the Royal Astronomical Society* **315**, 534–542 (2000).
- <sup>140</sup>J. R. Fuentes, C. M. Espinoza, A. Reisenegger, B. Shaw, B. W. Stappers, and A. G. Lyne, *Astronomy and Astrophysics* **131**, 1–9 (2017).
- <sup>141</sup>G. Ashton, R. Prix, and D. I. Jones, *Physical Review D* **96**, 063004 (2017).
- <sup>142</sup>I. O. Eya, J. O. Urama, and A. E. Chukwude, *Research in Astronomy and Astrophysics* **19**, 089 (2019).
- <sup>143</sup>W. C. G. Ho, C. M. Espinoza, Z. Arzoumanian, T. Enoto, T. Tamba, D. Antonopoulou, M. Bejger, S. Guillot, B. Haskell, and P. S. Ray, *Monthly Notices of the Royal Astronomical Society* **498**, 4605–4614 (2020).
- <sup>144</sup>H. Akaike, *IEEE Transactions on Automatic Control* **19**, 716 (1974).
- <sup>145</sup>C. M. Hurvich and C.-L. Tsai, *Biometrika* **76**, 297–307 (1989).
- <sup>146</sup>A. Gelman, J. B. Carlin, H. S. Stern, D. Dunson, A. Vehtari, and D. B. Rubin, *Bayesian data analysis*, 3rd Editio (Chapman and Hall/CRC, New York, 2013).
- <sup>147</sup>J. Middleditch, F. E. Marshall, Q. D. Wang, E. V. Gotthelf, and W. Zhang, *The Astrophysical Journal* **652**, 1531–1546 (2006).
- <sup>148</sup>R. D. Ferdman, R. F. Archibald, K. N. Gourgouliatos, and V. M. Kaspi, *The Astrophysical Journal* **852**, 123 (2018).
- <sup>149</sup>D. Antonopoulou, C. M. Espinoza, L. Kuiper, and N. Andersson, *Monthly Notices of the Royal Astronomical Society* **473**, 1644–1655 (2018).
- <sup>150</sup>B. Haskell and A. Melatos, *International Journal of Modern Physics D* **24**, 1530008 (2015).
- <sup>151</sup>D. Antonopoulou, B. Haskell, and C. M. Espinoza, *Reports on Progress in Physics* **85**, 126901 (2022).
- <sup>152</sup>M. Antonelli, A. Montoli, and P. M. Pizzochero, “Insights Into the Physics of Neutron Star Interiors from Pulsar Glitches”, in *Astrophysics in the XXI Century with Compact Stars* (WORLD SCIENTIFIC, 2022), pp. 219–281.
- <sup>153</sup>S. Zhou, E. Gügercinoğlu, J. Yuan, M. Ge, and C. Yu, *Universe* **8**, 641 (2022).
- <sup>154</sup>L. Onsager, *Il Nuovo Cimento* **6**, 279–287 (1949).

- <sup>155</sup>A. B. Migdal, Nuclear Physics **13**, 655–674 (1959).
- <sup>156</sup>H. E. Hall and W. F. Vinen, Proceedings of the Royal Society of London, A **238**, 215–234 (1956).
- <sup>157</sup>G. Mendell, The Astrophysical Journal **380**, 515 (1991).
- <sup>158</sup>K. Glampedakis, N. Andersson, and L. Samuelsson, Monthly Notices of the Royal Astronomical Society **410**, 805–829 (2011).
- <sup>159</sup>P. W. Anderson and N. Itoh, Nature **256**, 25–27 (1975).
- <sup>160</sup>M. A. Alpar, The Astrophysical Journal **213**, 527–530 (1977).
- <sup>161</sup>R. I. Epstein and G. Baym, The Astrophysical Journal **328**, 680 (1988).
- <sup>162</sup>B. K. Link and R. I. Epstein, The Astrophysical Journal **373**, 592–603 (1991).
- <sup>163</sup>P. M. Pizzochero, L. Viverit, and R. A. Broglia, Physical Review Letters **79**, 3347–3350 (1997).
- <sup>164</sup>P. Donati and P. M. Pizzochero, Physics Letters B **640**, 74–81 (2006).
- <sup>165</sup>P. Avogadro, F. Barranco, R. A. Broglia, and E. Vigezzi, Physical Review C **75**, 012805 (2007).
- <sup>166</sup>B. Link, Physical Review Letters **102**, 131101 (2009).
- <sup>167</sup>S. Seveso, P. M. Pizzochero, F. Grill, and B. Haskell, Monthly Notices of the Royal Astronomical Society **455**, 3952–3967 (2016).
- <sup>168</sup>B. Link and Y. Levin, The Astrophysical Journal **941**, 148 (2022).
- <sup>169</sup>M. Ruderman, T. Zhu, and K. Chen, The Astrophysical Journal **492**, 267–280 (1998).
- <sup>170</sup>E. Gügercinoğlu and M. A. Alpar, The Astrophysical Journal Letters **788**, L11 (2014).
- <sup>171</sup>G. Baym, C. Pethick, and D. Pines, Nature **224**, 673–674 (1969).
- <sup>172</sup>M. A. Alpar, S. A. Langer, and J. A. Sauls, The Astrophysical Journal **282**, 533 (1984).
- <sup>173</sup>L. Warszawski and A. Melatos, Monthly Notices of the Royal Astronomical Society **415**, 1611–1630 (2011).
- <sup>174</sup>L. Warszawski and A. Melatos, Monthly Notices of the Royal Astronomical Society **428**, 1911–1926 (2013).
- <sup>175</sup>J. R. Lönnborn, A. Melatos, and B. Haskell, Monthly Notices of the Royal Astronomical Society **487**, 702–710 (2019).
- <sup>176</sup>D. Pines and J. Shaham, Nature Physical Science **235**, 43–49 (1972).
- <sup>177</sup>M. Ruderman, Nature **223**, 597–598 (1969).
- <sup>178</sup>G. Baym and D. Pines, Annals of Physics **66**, 816–835 (1971).
- <sup>179</sup>M. Ruderman, The Astrophysical Journal **203**, 213–222 (1976).
- <sup>180</sup>N. Chamel and B. Carter, Monthly Notices of the Royal Astronomical Society **368**, 796–808 (2006).
- <sup>181</sup>C. J. Horowitz and K. Kadau, Physical Review Letters **102**, 101103/PhysRevLett. 102, 191102 (2009).

- <sup>182</sup>J. A. Rencoret, C. Aguilera-Gómez, and A. Reisenegger, *Astronomy & Astrophysics* **654**, A47 (2021).
- <sup>183</sup>G. Ushomirsky, C. Cutler, and L. Bildsten, *Monthly Notices of the Royal Astronomical Society* **319**, 902–932 (2000).
- <sup>184</sup>F. Gittins, N. Andersson, and D. I. Jones, *Monthly Notices of the Royal Astronomical Society* **500**, 5570–5582 (2021).
- <sup>185</sup>A. D. Kerin and A. Melatos, *Monthly Notices of the Royal Astronomical Society* **514**, 1628–1644 (2022).
- <sup>186</sup>A. Mastrano and A. Melatos, *Monthly Notices of the Royal Astronomical Society* **361**, 927–941 (2005).
- <sup>187</sup>N. Andersson, G. L. Comer, and R. Prix, *Physical Review Letters* **90**, 091101 (2003).
- <sup>188</sup>N. Andersson, G. L. Comer, and R. Prix, *Monthly Notices of the Royal Astronomical Society* **354**, 101–110 (2004).
- <sup>189</sup>C. Peralta, A. Melatos, M. Giacobello, and A. Ooi, *The Astrophysical Journal* **651**, 1079–1091 (2006).
- <sup>190</sup>N. Andersson, T. Sidery, and G. L. Comer, *Monthly Notices of the Royal Astronomical Society* **381**, 747–756 (2007).
- <sup>191</sup>M. S. Mongiovì, F. G. Russo, and M. Sciacca, *Monthly Notices of the Royal Astronomical Society* **469**, 2141–2150 (2017).
- <sup>192</sup>B. Haskell, D. Antonopoulou, and C. Barenghi, *Monthly Notices of the Royal Astronomical Society* **499**, 161–170 (2020).
- <sup>193</sup>A. Melatos and L. Warszawski, *The Astrophysical Journal* **700**, 1524 (2009).
- <sup>194</sup>E. Gürgencinoğlu and M. A. Alpar, *Monthly Notices of the Royal Astronomical Society* **488**, 2275–2282 (2019).
- <sup>195</sup>H. J. Jensen, *Self-Organized Criticality. Emergent Complex Behavior in Physical and Biological Systems*, Cambridge Lecture Notes in Physics (Cambridge University Press, Cambridge, 1998).
- <sup>196</sup>L. L. Watkins, R. P. van der Marel, A. Bellini, and J. Anderson, *The Astrophysical Journal* **812**, 149 (2015).
- <sup>197</sup>P. Bak, C. Tang, and K. Wiesenfeld, *Physical Review Letters* **59**, 381–384 (1987).
- <sup>198</sup>P. Bak, C. Tang, and K. Wiesenfeld, *Physical Review A* **38**, 364–374 (1988).
- <sup>199</sup>T. Hwa and M. Kardar, *Physical Review A* **45**, 7002–7023 (1992).
- <sup>200</sup>J. Rosendahl, M. Vekić, and J. Kelley, *Physical Review E* **47**, 1401–1404 (1993).
- <sup>201</sup>M. De Menech and A. L. Stella, *Physical Review E* **62**, R4528–R4531 (2000).
- <sup>202</sup>E. Lippiello, L. de Arcangelis, and C. Godano, *Astronomy and Astrophysics* **511**, L2 (2010).
- <sup>203</sup>M. E. J. Newman and K. Sneppen, *Physical Review E* **54**, 6226–6231 (1996).
- <sup>204</sup>K. Sneppen and M. Newman, *Physica D: Nonlinear Phenomena* **110**, 209–222 (1997).
- <sup>205</sup>N. V. Sarlis and S.-R. G. Christopoulos, *Physical Review E* **85**, 051136 (2012).

- <sup>206</sup>E. Daly and A. Porporato, *Physical Review E* **74**, 1–9 (2006).
- <sup>207</sup>E. Daly and A. Porporato, *Physical Review E* **75**, 11119 (2007).
- <sup>208</sup>L. Fletcher et al., *Space Science Reviews* **159**, 19 (2011).
- <sup>209</sup>A. O. Benz, *Living Reviews in Solar Physics* **14**, 2 (2016).
- <sup>210</sup>S. K. Solanki, *The Astronomy and Astrophysics Review* **11**, 153–286 (2003).
- <sup>211</sup>G. E. Hale, *The Astrophysical Journal* **28**, 315 (1908).
- <sup>212</sup>L. M. Green, T. Török, B. Vršnak, W. Manchester, and A. Veronig, *Space Science Reviews* **214**, 46 (2018).
- <sup>213</sup>U. Anzer and G. W. Pneuman, *Solar Physics* **79**, 129–147 (1982).
- <sup>214</sup>M. S. Wheatland, *The Astrophysical Journal* **609**, 1134 (2004).
- <sup>215</sup>R. Qahwaji and T. Colak, *Solar Physics* **241**, 195–211 (2007).
- <sup>216</sup>J. P. Mason and J. T. Hoeksema, *The Astrophysical Journal* **723**, 634 (2010).
- <sup>217</sup>M. G. Bobra and S. Couvidat, *The Astrophysical Journal* **798**, 135 (2015).
- <sup>218</sup>G. Barnes et al., *The Astrophysical Journal* **829**, 89 (2016).
- <sup>219</sup>E. Camporeale, *Space Weather* **17**, 1166–1207 (2019).
- <sup>220</sup>C. Thibeault, A. Strugarek, P. Charbonneau, and B. Tremblay, *Solar Physics* **297**, 125 (2022).
- <sup>221</sup>R. Rosner and G. S. Vaiana, *The Astrophysical Journal* **222**, 1104 (1978).
- <sup>222</sup>M. S. Wheatland and S. Glukhov, *The Astrophysical Journal* **494**, 858–863 (1998).
- <sup>223</sup>M. S. Wheatland, *Solar Physics* **191**, 381–389 (2000).
- <sup>224</sup>M. S. Wheatland, *The Astrophysical Journal* **679**, 1621–1628 (2008).
- <sup>225</sup>M. Kanazir and M. S. Wheatland, *Solar Physics* **266**, 301–321 (2010).
- <sup>226</sup>H. S. Hudson, *Monthly Notices of the Royal Astronomical Society*, stz3121 (2019).
- <sup>227</sup>E. T. Lu and R. J. Hamilton, *The Astrophysical Journal Letters* **380**, L89 (1991).
- <sup>228</sup>E. T. Lu, R. J. Hamilton, J. M. McTiernan, and K. R. Bromund, *The Astrophysical Journal* **412**, 841 (1993).
- <sup>229</sup>E. T. Lu, *The Astrophysical Journal* **447**, 416 (1995).
- <sup>230</sup>P. Charbonneau, S. W. McIntosh, H.-L. Liu, and T. J. Bogdan, *Solar Physics* **203**, 321–353 (2001).
- <sup>231</sup>L. Warszawski and A. Melatos, *Monthly Notices of the Royal Astronomical Society* **390**, 175–191 (2008).
- <sup>232</sup>V. Gaizauskas and Z. Svestka, *Solar Physics* **114**, 389–398 (1987).
- <sup>233</sup>W. H. G. Lewin et al., *The Astrophysical Journal* **207**, L95–L99 (1976).
- <sup>234</sup>M. S. Wheatland, *Solar Physics* **255**, 211–227 (2009).
- <sup>235</sup>D. R. Cox, *Journal of the Royal Statistical Society, B* **17**, 129–164 (1955).
- <sup>236</sup>B. Schutz, *A First Course in General Relativity*, 3rd ed. (Cambridge University Press, Cambridge, June 2022).

- <sup>237</sup>K. S. Thorne, *Reviews of Modern Physics* **52**, 299–339 (1980).
- <sup>238</sup>J. Mathews, *Journal of the Society for Industrial and Applied Mathematics* **10**, 768–780 (1962).
- <sup>239</sup>A. I. Renzini, B. Goncharov, A. C. Jenkins, and P. M. Meyers, *Galaxies* **10**, 34 (2022).
- <sup>240</sup>LIGO Scientific Collaboration and Virgo Collaboration et al., *Physical Review Letters* **116**, 061102 (2016).
- <sup>241</sup>The LIGO Scientific Collaboration et al., *GWTC-3: Compact Binary Coalescences Observed by LIGO and Virgo During the Second Part of the Third Observing Run*, Nov. 2021.
- <sup>242</sup>J. M. Weisberg and J. H. Taylor, *General Relativity and Gravitation* **13**, 1–6 (1981).
- <sup>243</sup>J. Powell and B. Müller, *Monthly Notices of the Royal Astronomical Society* **487**, 1178–1190 (2019).
- <sup>244</sup>D. Radice, V. Morozova, A. Burrows, D. Vartanyan, and H. Nagakura, *The Astrophysical Journal Letters* **876**, L9 (2019).
- <sup>245</sup>T. Vachaspati and A. Vilenkin, *Physical Review D* **31**, 3052–3058 (1985).
- <sup>246</sup>M. Sakellariadou, *Physical Review D* **42**, 354–360 (1990).
- <sup>247</sup>L. Warszawski and A. Melatos, *Monthly Notices of the Royal Astronomical Society* **423**, 2058–2074 (2012).
- <sup>248</sup>G. Yim and D. I. Jones, *Monthly Notices of the Royal Astronomical Society* **498**, 3138–3152 (2020).
- <sup>249</sup>W. C. G. Ho, D. I. Jones, N. Andersson, and C. M. Espinoza, *Physical Review D* **101**, 103009 (2020).
- <sup>250</sup>t. V. C. The LIGO Scientific Collaboration and the KAGRA Collaboration et al., *Physical Review D* **104**, 122004 (2021).
- <sup>251</sup>V. C. LIGO Scientific Collaboration and KAGRA Collaboration et al., *Physical Review Letters* **126**, 241102 (2021).
- <sup>252</sup>R. Weiss, *Quarterly Progress Report, MIT Research Lab of Electronics* **105** (1972).
- <sup>253</sup>N. K. Johnson-McDaniel and B. J. Owen, *Physical Review D* **88**, 044004 (2013).
- <sup>254</sup>C. Cutler, *Physical Review D* **66**, 084025 (2002).
- <sup>255</sup>A. Mastrano, A. Melatos, A. Reisenegger, and T. Akgün, *Monthly Notices of the Royal Astronomical Society* **417**, 2288–2299 (2011).
- <sup>256</sup>P. D. Lasky and A. Melatos, *Physical Review D* **88**, 103005 (2013).
- <sup>257</sup>A. I. Chugunov and C. J. Horowitz, *Monthly Notices of the Royal Astronomical Society: Letters* **407**, 54–58 (2010).
- <sup>258</sup>E. Giliberti and G. Cambiotti, *Monthly Notices of the Royal Astronomical Society* **511**, 3365–3376 (2022).
- <sup>259</sup>M. Zimmermann and E. Szedenits, *Physical Review D* **20**, 351–355 (1979).
- <sup>260</sup>M. Zimmermann, *Physical Review D* **21**, 891–898 (1980).

- <sup>261</sup>D. I. Jones and N. Andersson, *Monthly Notices of the Royal Astronomical Society* **331**, 203–220 (2002).
- <sup>262</sup>P. Jaranowski, A. Królak, and B. F. Schutz, *Physical Review D* **58**, 063001 (1998).
- <sup>263</sup>N. Andersson, *The Astrophysical Journal* **502**, 708 (1998).
- <sup>264</sup>J. L. Friedman and S. M. Morsink, *The Astrophysical Journal* **502**, 714 (1998).
- <sup>265</sup>B. J. Owen, L. Lindblom, C. Cutler, B. F. Schutz, A. Vecchio, and N. Andersson, *Physical Review D* **58**, 084020 (1998).
- <sup>266</sup>M. G. Alford, S. Mahmoodifar, and K. Schwenzer, *Physical Review D* **85**, 024007 (2012).
- <sup>267</sup>P. Arras, E. E. Flanagan, S. M. Morsink, A. K. Schenk, S. A. Teukolsky, and I. Wasserman, *The Astrophysical Journal* **591**, 1129 (2003).
- <sup>268</sup>J. Papaloizou and J. E. Pringle, *Monthly Notices of the Royal Astronomical Society* **184**, 501–508 (1978).
- <sup>269</sup>L. Lindblom, B. J. Owen, and S. M. Morsink, *Physical Review Letters* **80**, 4843–4846 (1998).
- <sup>270</sup>N. Andersson, K. Kokkotas, and B. F. Schutz, *The Astrophysical Journal* **510**, 846 (1999).
- <sup>271</sup>A. Idrisy, B. J. Owen, and D. I. Jones, *Physical Review D* **91**, 024001 (2015).
- <sup>272</sup>S. Caride, R. Inta, B. J. Owen, and B. Rajbhandari, *Physical Review D* **100**, 064013 (2019).
- <sup>273</sup>B. J. Owen, *Physical Review D* **82**, 104002 (2010).
- <sup>274</sup>C. A. van Eysden and A. Melatos, *Classical and Quantum Gravity* **25**, 225020 (2008).
- <sup>275</sup>M. F. Bennett, C. A. van Eysden, and A. Melatos, *Monthly Notices of the Royal Astronomical Society* **409**, 1705–1718 (2010).
- <sup>276</sup>D. I. Jones, *Monthly Notices of the Royal Astronomical Society* **402**, 2503–2519 (2010).
- <sup>277</sup>A. Melatos, J. A. Douglass, and T. P. Simula, *The Astrophysical Journal* **807**, 132 (2015).
- <sup>278</sup>K. Riles, *Progress in Particle and Nuclear Physics* **68**, 1–54 (2013).
- <sup>279</sup>K. Wette, *Astroparticle Physics* **153**, 102880 (2023).
- <sup>280</sup>S. Bhattacharyya, A. Papitto, and D. Bhattacharya, eds., *Millisecond Pulsars*, Vol. 465, Astrophysics and Space Science Library (Springer International Publishing, Cham, 2022).
- <sup>281</sup>R. Prix and K. Wette, *The F-statistic and its implementation in ComputeFstatistic\_v2*, tech. rep. T0900149 (Apr. 2009).
- <sup>282</sup>LIGO Scientific Collaboration, *LIGO Algorithm Library - LALSuite*, free software (GPL), 2018.
- <sup>283</sup>C. Messenger and G. Woan, *Classical and Quantum Gravity* **24**, S469–S480 (2007).
- <sup>284</sup>L. Sammut, C. Messenger, A. Melatos, and B. J. Owen, *Physical Review D* **89**, 043001 (2014).
- <sup>285</sup>O. J. Piccinni, *Galaxies* **10**, 72 (2022).

- <sup>286</sup>K. Riles, *Living Reviews in Relativity* **26**, 3 (2023).
- <sup>287</sup>P. Astone, A. Colla, S. D’Antonio, S. Frasca, and C. Palomba, *Journal of Physics: Conference Series* **363**, 012038 (2012).
- <sup>288</sup>A. Singhal et al., *Classical and Quantum Gravity* **36**, 205015 (2019).
- <sup>289</sup>R. Abbott et al., *The Astrophysical Journal* **935**, 1 (2022).
- <sup>290</sup>P. B. Covas and A. M. Sintes, *Physical Review D* **99**, 124019 (2019).
- <sup>291</sup>The LIGO Scientific Collaboration and the Virgo Collaboration et al., *Physical Review D* **103**, 064017 (2021).
- <sup>292</sup>P. B. Covas, M. A. Papa, R. Prix, and B. J. Owen, *The Astrophysical Journal Letters* **929**, L19 (2022).
- <sup>293</sup>B. P. Abbott et al., *Physical Review D* **95**, 122003 (2017).
- <sup>294</sup>S. Dhurandhar, B. Krishnan, H. Mukhopadhyay, and J. T. Whelan, *Physical Review D* **77**, 082001 (2008).
- <sup>295</sup>J. T. Whelan, S. Sundaresan, Y. Zhang, and P. Peiris, *Physical Review D* **91**, 102005 (2015).
- <sup>296</sup>R. Abbott et al., *The Astrophysical Journal Letters* **941**, L30 (2022).
- <sup>297</sup>J. T. Whelan et al., *The Astrophysical Journal* **949**, 117 (2023).
- <sup>298</sup>V. C. LIGO Scientific Collaboration and KAGRA Collaboration et al., *Physical Review D* **106**, 062002 (2022).
- <sup>299</sup>A. F. Vargas and A. Melatos, *Physical Review D* **107**, 064062 (2023).
- <sup>300</sup>P. Jaranowski and A. Królak, *Classical and Quantum Gravity* **27**, 194015 (2010).
- <sup>301</sup>M. Pitkin, M. Isi, J. Veitch, and G. Woan, *A nested sampling code for targeted searches for continuous gravitational waves from pulsars*, May 2017.
- <sup>302</sup>E. Goetz and K. Riles, *Classical and Quantum Gravity* **28**, 215006 (2011).
- <sup>303</sup>G. D. Meadors, E. Goetz, K. Riles, T. Creighton, and F. Robinet, *Physical Review D* **95**, 042005 (2017).
- <sup>304</sup>LIGO Scientific Collaboration and Virgo Collaboration et al., *Physical Review D* **90**, 062010 (2014).
- <sup>305</sup>R. Abbott et al., *The Astrophysical Journal Letters* **902**, L21 (2020).
- <sup>306</sup>R. Abbott et al., *The Astrophysical Journal* **932**, 133 (2022).
- <sup>307</sup>L. E. Baum and T. Petrie, *The Annals of Mathematical Statistics* **37**, 1554–1563 (1966).
- <sup>308</sup>A. Viterbi, *IEEE Transactions on Information Theory* **13**, 260–269 (1967).
- <sup>309</sup>L. Sun, A. Melatos, and P. D. Lasky, *Physical Review D* **99**, 123010 (2019).
- <sup>310</sup>M. Millhouse, L. Strang, and A. Melatos, *Physical Review D* **102**, 083025 (2020).
- <sup>311</sup>D. Beniwal, P. Clearwater, L. Dunn, A. Melatos, and D. Ottaway, *Physical Review D* **103**, 083009 (2021).
- <sup>312</sup>D. Jones and L. Sun, *Physical Review D* **103**, 023020 (2021).

- <sup>313</sup>R. Abbott et al., *The Astrophysical Journal* **921**, 80 (2021).
- <sup>314</sup>LIGO Scientific Collaboration and Virgo Collaboration et al., *Physical Review D* **100**, 122002 (2019).
- <sup>315</sup>J. Bayley, C. Messenger, and G. Woan, *Physical Review D* **100**, 023006 (2019).
- <sup>316</sup>A. Melatos, P. Clearwater, S. Suvorova, L. Sun, W. Moran, and R. J. Evans, *Physical Review D* **104**, 042003 (2021).
- <sup>317</sup>K. Chen and M. Ruderman, *The Astrophysical Journal* **402**, 264 (1993).
- <sup>318</sup>V. Radhakrishnan and G. Srinivasan, *Current Science* **51**, 1096–1099 (1982).
- <sup>319</sup>M. A. Alpar, A. F. Cheng, M. A. Ruderman, and J. Shaham, *Nature* **300**, 728–730 (1982).
- <sup>320</sup>J. W. T. Hessels, S. M. Ransom, I. H. Stairs, P. C. C. Freire, V. M. Kaspi, and F. Camilo, *Science* **311**, 1901–1904 (2006).
- <sup>321</sup>D. Chakrabarty, E. H. Morgan, M. P. Muno, D. K. Galloway, R. Wijnands, M. van der Klis, and C. B. Markwardt, *Nature* **424**, 42–44 (2003).
- <sup>322</sup>A. Patruno, *The Astrophysical Journal* **839**, 51 (2017).
- <sup>323</sup>G. B. Cook, S. L. Shapiro, and S. A. Teukolsky, *The Astrophysical Journal* **424**, 823–845 (1994).
- <sup>324</sup>A. Patruno and A. L. Watts, “Accreting Millisecond X-ray Pulsars”, in *Timing Neutron Stars: Pulsations, Oscillations and Explosions*, edited by T. M. Belloni, M. Méndez, and C. Zhang, Astrophysics and Space Science Library (Springer, Berlin, Heidelberg, 2021), pp. 143–208.
- <sup>325</sup>C. R. D’Angelo and H. C. Spruit, *Monthly Notices of the Royal Astronomical Society* **406**, 1208–1219 (2010).
- <sup>326</sup>N. E. White and W. Zhang, *The Astrophysical Journal* **490**, L87 (1997).
- <sup>327</sup>Y. .-. Wang, *Astronomy and Astrophysics* **183**, 257–264 (1987).
- <sup>328</sup>S. A. Rappaport, J. M. Fregeau, and H. Spruit, *The Astrophysical Journal* **606**, 436 (2004).
- <sup>329</sup>A. Melatos and D. J. B. Payne, *The Astrophysical Journal* **623**, 1044 (2005).
- <sup>330</sup>B. Haskell, D. I. Jones, and N. Andersson, *Monthly Notices of the Royal Astronomical Society* **373**, 1423–1439 (2006).
- <sup>331</sup>R. V. Wagoner, *The Astrophysical Journal* **278**, 345–348 (1984).
- <sup>332</sup>B. P. Abbott et al., *The Astrophysical Journal* **847**, 47 (2017).
- <sup>333</sup>Y. Zhang, M. A. Papa, B. Krishnan, and A. L. Watts, *The Astrophysical Journal* **906**, L14 (2021).
- <sup>334</sup>T. L. Killestein, M. Mould, D. Steeghs, J. Casares, D. K. Galloway, and J. T. Whelan, *Monthly Notices of the Royal Astronomical Society* **520**, 5317–5330 (2023).
- <sup>335</sup>A. Marino, T. Di Salvo, L. Burderi, A. Sanna, A. Riggio, A. Papitto, M. Del Santo, A. F. Gambino, R. Iaria, and S. M. Mazzola, *Astronomy and Astrophysics* **627**, 11 (2019).
- <sup>336</sup>A. Patruno, R. Wijnands, and M. van der Klis, *The Astrophysical Journal* **698**, L60 (2009).

- <sup>337</sup>A. Papitto, A. Riggio, L. Burderi, T. di Salvo, A. D’Áí, and R. Iaria, *Astronomy and Astrophysics* **528**, A55 (2011).
- <sup>338</sup>A. Riggio, L. Burderi, T. di Salvo, A. Papitto, A. D’Áí, R. Iaria, and M. T. Menna, *Astronomy and Astrophysics* **531**, A140 (2011).
- <sup>339</sup>A. Patruno, P. Bult, A. Gopakumar, J. M. Hartman, R. Wijnands, M. van der Klis, and D. Chakrabarty, *The Astrophysical Journal Letters* **746**, L27 (2012).
- <sup>340</sup>A. Patruno, B. Haskell, and C. D’Angelo, *The Astrophysical Journal* **746**, 9 (2012).
- <sup>341</sup>S. Bhattacharyya and D. Chakrabarty, *The Astrophysical Journal* **835**, 4 (2017).
- <sup>342</sup>B. Haskell and A. Patruno, *Physical Review Letters* **119**, 161103 (2017).
- <sup>343</sup>N. Andersson, K. D. Kokkotas, and N. Stergioulas, *The Astrophysical Journal* **516**, 307–314 (1999).
- <sup>344</sup>R. Bondarescu and I. Wasserman, *The Astrophysical Journal* **778**, 9 (2013).
- <sup>345</sup>M. G. Alford and K. Schwenzer, *Monthly Notices of the Royal Astronomical Society* **446**, 3631–3641 (2015).
- <sup>346</sup>S. Mahmoodifar and T. Strohmayer, *The Astrophysical Journal* **773**, 140 (2013).
- <sup>347</sup>T. Strohmayer and S. Mahmoodifar, *The Astrophysical Journal* **784**, 72 (2014).
- <sup>348</sup>A. L. Watts, B. Krishnan, L. Bildsten, and B. F. Schutz, *Monthly Notices of the Royal Astronomical Society* **389**, 839–868 (2008).
- <sup>349</sup>B. Haskell, M. Priymak, A. Patruno, M. Oppenoorth, A. Melatos, and P. D. Lasky, *Monthly Notices of the Royal Astronomical Society* **450**, 2393–2403 (2015).
- <sup>350</sup>S. L. Shemar and A. G. Lyne, *Monthly Notices of the Royal Astronomical Society* **282**, 677 (1996).
- <sup>351</sup>A. Melatos, G. Howitt, and W. Fulgenzi, *The Astrophysical Journal* **863**, 196 (2018).
- <sup>352</sup>J. B. Carlin, A. Melatos, and D. Vukcevic, *Monthly Notices of the Royal Astronomical Society* **482**, 3736–3743 (2019).
- <sup>353</sup>T. Utsu, Y. Ogata, R. S, and Matsu’ura, *Journal of Physics of the Earth* **43**, 1–33 (1995).
- <sup>354</sup>S. B. Santra, S. R. Chanu, and D. Deb, *Physical Review E* **75**, 041122 (2007).
- <sup>355</sup>M. Paczuski, S. Boettcher, and M. Baiesi, *Physical Review Letters* **95**, 181102 (2005).
- <sup>356</sup>F. Caruso, A. Pluchino, V. Latora, S. Vinciguerra, and A. Rapisarda, *Physical Review E* **75**, 055101 (2007).
- <sup>357</sup>C. Ng, *Proceedings of the International Astronomical Union* **13**, 179–182 (2018).
- <sup>358</sup>S. Buchner and C. Flanagan, *AIP Conference Proceedings* **983**, 145–147 (2008).
- <sup>359</sup>J. L. Palfreyman, J. M. Dickey, S. P. Ellingsen, I. R. Jones, and A. W. Hotan, *The Astrophysical Journal* **820**, 64 (2016).
- <sup>360</sup>Z. Arzoumanian et al., *The Astrophysical Journal Supplement Series* **235**, 37 (2018).
- <sup>361</sup>G. S. Downs, *The Astrophysical Journal* **249**, 687–697 (1981).
- <sup>362</sup>E. L. Lehmann and H. J. M. D’Abrera, *Nonparametrics: Statistical Methods Based on Ranks* (Springer-Verlag, New York, 2006).

- <sup>363</sup>P. Hall, *The Bootstrap and Edgeworth Expansion*, Springer Series in Statistics (Springer-Verlag, New York, 1992).
- <sup>364</sup>P. Good, *Permutation, Parametric and Bootstrap Tests of Hypotheses*, Springer Series in Statistics (Springer-Verlag, New York, 2005).
- <sup>365</sup>M. B. Larson and B. Link, *Monthly Notices of the Royal Astronomical Society* **333**, 613–622 (2002).
- <sup>366</sup>J. Grandell, *Doubly Stochastic Poisson Processes*, Lecture Notes in Mathematics (Springer-Verlag, Berlin Heidelberg, 1976).
- <sup>367</sup>D. G. Bonett and T. A. Wright, *Psychometrika* **65**, 23–28 (2000).
- <sup>368</sup>A. Melatos and C. Peralta, *The Astrophysical Journal* **662**, L99–L102 (2007).
- <sup>369</sup>K. Glampedakis and N. Andersson, *Physical Review Letters* **102**, 141101 (2009).
- <sup>370</sup>A. Melatos and L. V. Drummond, *The Astrophysical Journal* **885**, 37 (2019).
- <sup>371</sup>S. Price, B. Link, S. N. Shore, and D. J. Nice, *Monthly Notices of the Royal Astronomical Society* **426**, 2507–2521 (2012).
- <sup>372</sup>A. Parthasarathy et al., *Monthly Notices of the Royal Astronomical Society* **489**, 3810 (2019).
- <sup>373</sup>V. Khomenko, M. Antonelli, and B. Haskell, *Physical Review D* **100**, 123002 (2019).
- <sup>374</sup>D. R. Cox and H. D. Miller, *The Theory of Stochastic Processes*, 1st (Chapman and Hall, London, 1965).
- <sup>375</sup>C. Gardiner, *Stochastic Methods: A Handbook for the Natural and Social Sciences*, 4th ed. (Springer-Verlag, Berlin Heidelberg, 2009).
- <sup>376</sup>P. E. Kloeden and E. Platen, “Stochastic Differential Equations”, in *Numerical Solution of Stochastic Differential Equations*, edited by P. E. Kloeden and E. Platen, Applications of Mathematics (Springer, Berlin, Heidelberg, 1992), pp. 103–160.
- <sup>377</sup>A. L. Sweet and J. C. Hardin, *Journal of Applied Probability* **7**, 423–431 (1970).
- <sup>378</sup>M. A. Alpar and A. Baykal, *Monthly Notices of the Royal Astronomical Society* **372**, 489–496 (2006).
- <sup>379</sup>O. Akbal, M. A. Alpar, S. Buchner, and D. Pines, *Monthly Notices of the Royal Astronomical Society* **469**, 4183–4192 (2017).
- <sup>380</sup>M. J. Aschwanden et al., *Space Science Reviews* **214**, 55 (2018).
- <sup>381</sup>T. Celora, V. Khomenko, M. Antonelli, and B. Haskell, *Monthly Notices of the Royal Astronomical Society* **496**, 5564–5574 (2020).
- <sup>382</sup>C. A. van Eysden and A. Melatos, *Monthly Notices of the Royal Astronomical Society* **409**, 1253 (2010).
- <sup>383</sup>N. Andersson, K. Glampedakis, W. C. G. Ho, and C. M. Espinoza, *Physical Review Letters* **109**, 241103 (2012).
- <sup>384</sup>J. Hooker, W. G. Newton, and B.-A. Li, *Monthly Notices of the Royal Astronomical Society* **449**, 3559–3567 (2015).
- <sup>385</sup>B. Link, R. I. Epstein, and J. M. Lattimer, *Physical Review Letters* **83**, 3362–3365 (1999).

- <sup>386</sup>A. Melatos and C. Peralta, *The Astrophysical Journal* **709**, 77–87 (2010).
- <sup>387</sup>P. M. Morse and H. Feshbach, *Methods of Theoretical Physics* (McGraw-Hill, New York, 1953).
- <sup>388</sup>L. Warszawski, A. Melatos, and N. G. Berloff, *Physical Review B* **85**, 10 . 1103 / *PhysRevB*. 85 . 104503 (2012).
- <sup>389</sup>V. Khomenko and B. Haskell, *Publications of the Astronomical Society of Australia* **35**, e020 (2018).
- <sup>390</sup>S. Field, J. Witt, F. Nori, and X. Ling, *Physical Review Letters* **74**, 1206–1209 (1995).
- <sup>391</sup>M. E. J. Newman, *Proceedings of the Royal Society of London, B* **263**, 1605–1610 (1996).
- <sup>392</sup>B. Haskell, *Monthly Notices of the Royal Astronomical Society: Letters* **461**, L77–L81 (2016).
- <sup>393</sup>P. M. Pizzochero, *The Astrophysical Journal* **743**, L20 (2011).
- <sup>394</sup>B. Haskell and D. Antonopoulou, *Monthly Notices of the Royal Astronomical Society* **438**, L16–L20 (2014).
- <sup>395</sup>P. B. Jones, *Monthly Notices of the Royal Astronomical Society* **296**, 217–224 (1998).
- <sup>396</sup>M. A. Alpar, H. F. Chau, K. S. Cheng, and D. Pines, *The Astrophysical Journal* **459**, 706 (1996).
- <sup>397</sup>P. M. McCulloch, P. A. Hamilton, D. McConnell, and E. A. King, *Nature* **346**, 822 (1990).
- <sup>398</sup>R. G. Dodson, P. M. McCulloch, and D. R. Lewis, *The Astrophysical Journal Letters* **564**, L85–L88 (2002).
- <sup>399</sup>G. Srinivasan, D. Bhattacharya, A. G. Muslimov, and A. J. Tsygan, *Current Science* **59**, 31–38 (1990).
- <sup>400</sup>P. M. Pizzochero, A. Montoli, and M. Antonelli, *Astronomy and Astrophysics* **636**, A101 (2020).
- <sup>401</sup>B. Haskell and A. Melatos, *Monthly Notices of the Royal Astronomical Society* **461**, 2200–2211 (2016).
- <sup>402</sup>C. F. Barenghi, R. J. Donnelly, and W. F. Vinen, *Journal of Low Temperature Physics* **52**, 189–247 (1983).
- <sup>403</sup>N. Andersson, T. Sidery, and G. L. Comer, *Monthly Notices of the Royal Astronomical Society* **368**, 162–170 (2006).
- <sup>404</sup>V. Graber, A. Cumming, and N. Andersson, *The Astrophysical Journal* **865**, 23 (2018).
- <sup>405</sup>Y. Y. Kagan and D. D. Jackson, *Geophysical Journal International* **104**, 117–134 (1991).
- <sup>406</sup>B. W. Stappers et al., *Astronomy and Astrophysics* **530**, A80 (2011).
- <sup>407</sup>D. R. Cox and P. A. W. Lewis, *The Statistical Analysis of Series of Events* (Chapman and Hall, 1966).
- <sup>408</sup>E. Çinlar, *Introduction to stochastic processes* (Englewood Cliffs, N.J. : Prentice-Hall, 1975).
- <sup>409</sup>J. F. C. Kingman, *Poisson processes* (Oxford University Press, Oxford, 1993).

- <sup>410</sup>G. E. P. Box, G. M. Jenkins, G. C. Reinsel, and G. M. Ljung, *Time Series Analysis: Forecasting and Control* (John Wiley and Sons Inc., Hoboken, New Jersey, June 2015).
- <sup>411</sup>E. D. Feigelson, G. J. Babu, and G. A. Caceres, *Frontiers in Physics* **6**, 80 (2018).
- <sup>412</sup>J. van der Hoek and R. J. Elliott, *Introduction to Hidden Semi-Markov Models*, London Mathematical Society Lecture Note Series (Cambridge University Press, Cambridge, 2018).
- <sup>413</sup>E. Priest and T. Forbes, *The Astronomy and Astrophysics Review* **10**, 313–377 (2002).
- <sup>414</sup>E. T. Lu, *The Astrophysical Journal Letters* **446**, L109–L112 (1995).
- <sup>415</sup>G. Boffetta, V. Carbone, P. Giuliani, P. Veltri, and A. Vulpiani, *Physical Review Letters* **83**, 4662–4665 (1999).
- <sup>416</sup>N. Farhang, M. S. Wheatland, and H. Safari, *The Astrophysical Journal Letters* **883**, L20 (2019).
- <sup>417</sup>M. J. Aschwanden and J. R. Johnson, *The Astrophysical Journal* **921**, 82 (2021).
- <sup>418</sup>C. Verbeeck, E. Kraaijkamp, D. F. Ryan, and O. Podladchikova, *The Astrophysical Journal* **884**, 50 (2019).
- <sup>419</sup>M. S. Wheatland, *The Astrophysical Journal Letters* **536**, L109 (2000).
- <sup>420</sup>M. J. Aschwanden, J. R. Johnson, and Y. I. Nurhan, *The Astrophysical Journal* **921**, 166 (2021).
- <sup>421</sup>F. Lepreti, V. Carbone, and P. Veltri, *The Astrophysical Journal Letters* **555**, L133 (2001).
- <sup>422</sup>A. Gorobets and M. Messerotti, *Solar Physics* **281**, 651–667 (2012).
- <sup>423</sup>D. A. Biesecker, “On the Occurrence of Solar Flares Observed with the Burst and Transient Source Experiment”, PhD thesis (University of New Hampshire, Jan. 1994).
- <sup>424</sup>H. S. Hudson, B. J. Labonte, A. C. Sterling, and T. Watanabe, “NOAA 7978: The Last Best Old-Cycle Region?”, in *Observational Plasma Astrophysics: Five Years of Yohkoh and Beyond*, Vol. 229, Space Science Library (Springer Dordrecht, 1998), p. 237.
- <sup>425</sup>N. Crosby, N. Vilmer, N. Lund, and R. Sunyaev, *Astronomy and Astrophysics* **334**, 299–313 (1998).
- <sup>426</sup>H. S. Hudson, *Solar Physics* **295**, 132 (2020).
- <sup>427</sup>M. Wheatland, *Solar Physics* **203**, 87–106 (2001).
- <sup>428</sup>M. P. Wand and M. C. Jones, *Kernel Smoothing* (Chapman & Hall, London; New York, 1995).
- <sup>429</sup>T. Török, B. Kliem, and V. S. Titov, *Astronomy and Astrophysics* **413**, L27–L30 (2004).
- <sup>430</sup>C. R. Harris et al., *Nature* **585**, 357–362 (2020).
- <sup>431</sup>P. Virtanen et al., *Nature Methods* **17**, 261–272 (2020).
- <sup>432</sup>J. D. Hunter, *Computing in Science and Engineering* **9**, 90–95 (2007).
- <sup>433</sup>Stan Development Team, *Stan Modeling Language Users Guide and Reference Manual*, 2.30, 2022.

- <sup>434</sup>G. H. Fisher, B. T. Welsch, and W. P. Abbett, *Solar Physics* **277**, 153–163 (2012).
- <sup>435</sup>X. Sun, J. T. Hoeksema, Y. Liu, T. Wiegmann, K. Hayashi, Q. Chen, and J. Thalmann, *The Astrophysical Journal* **748**, 77 (2012).
- <sup>436</sup>X. Sun, J. T. Hoeksema, Y. Liu, M. Kazachenko, and R. Chen, *The Astrophysical Journal* **839**, 67 (2017).
- <sup>437</sup>S. Sahu, B. Joshi, A. Prasad, and K.-S. Cho, *Evolution of magnetic fields and energy release processes during homologous eruptive flares*, Dec. 2022.
- <sup>438</sup>H. Ji and W. Daughton, *Physics of Plasmas* **18**, 111207 (2011).
- <sup>439</sup>K. Shibata and S. Tanuma, *Earth, Planets and Space* **53**, 473–482 (2001).
- <sup>440</sup>P. H. Keys, M. Mathioudakis, D. B. Jess, S. Shelyag, P. J. Crockett, D. J. Christian, and F. P. Keenan, *The Astrophysical Journal Letters* **740**, L40 (2011).
- <sup>441</sup>S. Shelyag, P. Keys, M. Mathioudakis, and F. P. Keenan, *Astronomy and Astrophysics* **526**, A5 (2011).
- <sup>442</sup>S. Shelyag, V. Fedun, F. P. Keenan, R. Erdélyi, and M. Mathioudakis, *Annales Geophysicae* **29**, 883–887 (2011).
- <sup>443</sup>M. Betancourt, *arXiv e-prints* (2018).
- <sup>444</sup>G. Last and M. Penrose, *Lectures on the Poisson Process*, October (Cambridge University Press, 2017).
- <sup>445</sup>M. Mitzenmacher, *Internet Mathematics* **1**, 226–251 (2003).
- <sup>446</sup>H. Li and E. E. Fenimore, *The Astrophysical Journal* **469**, L115 (1996).
- <sup>447</sup>E. Göğüş, P. M. Woods, C. Kouveliotou, J. van Paradijs, M. S. Briggs, R. C. Duncan, and C. Thompson, *The Astrophysical Journal Letters* **526**, L93 (1999).
- <sup>448</sup>E. Göğüş, P. M. Woods, C. Kouveliotou, J. van Paradijs, M. S. Briggs, R. C. Duncan, and C. Thompson, *The Astrophysical Journal Letters* **532**, L121 (2000).
- <sup>449</sup>F. P. Gavriil, V. M. Kaspi, and P. M. Woods, *The Astrophysical Journal* **607**, 959 (2004).
- <sup>450</sup>K. Gourdji, D. Michilli, L. G. Spitler, J. W. T. Hessels, A. Seymour, J. M. Cordes, and S. Chatterjee, *The Astrophysical Journal Letters* **877**, L19 (2019).
- <sup>451</sup>V. Paxson and S. Floyd, *ACM SIGCOMM Computer Communication Review* **24**, 257–268 (1994).
- <sup>452</sup>R. Singhai, S. D. Joshi, and R. K. P. Bhatt, in *2007 15th International Conference on Software, Telecommunications and Computer Networks* (Sept. 2007), pp. 1–5.
- <sup>453</sup>N. La Roche-Carrier, G. Dituba Ngoma, Y. Kocaeli, and F. Erchiqui, *International Journal of Quality & Reliability Management* **37**, 223–242 (2019).
- <sup>454</sup>Z. Peng and P. Zhao, *Nature Geoscience* **2**, 877–881 (2009).
- <sup>455</sup>W. J. van der Linden, *Journal of Educational and Behavioral Statistics* **31**, 181–204 (2006).
- <sup>456</sup>J. Aasi et al., *Classical and Quantum Gravity* **32**, 074001 (2015).
- <sup>457</sup>F. Acernece et al., *Classical and Quantum Gravity* **32**, 024001 (2014).

- <sup>458</sup>LIGO Scientific Collaboration and Virgo Collaboration et al., *Physical Review X* **9**, 031040 (2019).
- <sup>459</sup>LIGO Scientific Collaboration and Virgo Collaboration et al., *Physical Review X* **11**, 021053 (2021).
- <sup>460</sup>The LIGO Scientific Collaboration et al., arXiv e-prints, arXiv:2108.01045 (2021).
- <sup>461</sup>K. Glampedakis and L. Gualtieri, “Gravitational Waves from Single Neutron Stars: An Advanced Detector Era Survey”, in *The Physics and Astrophysics of Neutron Stars*, edited by L. Rezzolla, P. Pizzochero, D. I. Jones, N. Rea, and I. Vidaña, Astrophysics and Space Science Library (Springer International Publishing, Cham, 2018), pp. 673–736.
- <sup>462</sup>M. Sieniawska and M. Bejger, *Universe* **5**, 217 (2019).
- <sup>463</sup>B. Haskell and K. Schwenzer, “Isolated Neutron Stars”, in *Handbook of Gravitational Wave Astronomy*, edited by C. Bambi, S. Katsanevas, and K. D. Kokkotas (Springer, Singapore, 2021), pp. 1–28.
- <sup>464</sup>B. P. Abbott et al., *The Astrophysical Journal* **875**, 160 (2019).
- <sup>465</sup>LIGO Scientific Collaboration and Virgo Collaboration et al., *Physical Review D* **99**, 122002 (2019).
- <sup>466</sup>M. A. Papa, J. Ming, E. V. Gotthelf, B. Allen, R. Prix, V. Dergachev, H.-B. Eggenstein, A. Singh, and S. J. Zhu, *The Astrophysical Journal* **897**, 22 (2020).
- <sup>467</sup>L. Fesik and M. A. Papa, *The Astrophysical Journal* **895**, 11 (2020).
- <sup>468</sup>L. Fesik and M. A. Papa, *The Astrophysical Journal* **897**, 185 (2020).
- <sup>469</sup>O. J. Piccinni, P. Astone, S. D’Antonio, S. Frasca, G. Intini, I. La Rosa, P. Leaci, S. Mastrogiovanni, A. Miller, and C. Palomba, *Physical Review D* **101**, 082004 (2020).
- <sup>470</sup>B. Steltner et al., *The Astrophysical Journal* **909**, 79 (2021).
- <sup>471</sup>V. Dergachev and M. A. Papa, *Physical Review D* **104**, 043003 (2021).
- <sup>472</sup>B. Rajbhandari, B. J. Owen, S. Caride, and R. Inta, *Physical Review D* **104**, 122008 (2021).
- <sup>473</sup>K. Wette, L. Dunn, P. Clearwater, and A. Melatos, *Physical Review D* **103**, 083020 (2021).
- <sup>474</sup>R. Abbott et al., *The Astrophysical Journal Letters* **913**, L27 (2021).
- <sup>475</sup>R. Abbott et al., *The Astrophysical Journal* **922**, 71 (2021).
- <sup>476</sup>V. C. LIGO Scientific Collaboration and KAGRA Collaboration et al., *Physical Review D* **104**, 082004 (2021).
- <sup>477</sup>A. Ashok, B. Beheshtipour, M. A. Papa, P. C. C. Freire, B. Steltner, B. Machenschalk, O. Behnke, B. Allen, and R. Prix, *The Astrophysical Journal* **923**, 85 (2021).
- <sup>478</sup>B. Abbott et al., *The Astrophysical Journal Letters* **683**, L45 (2008).
- <sup>479</sup>P. Casella, D. Altamirano, A. Patruno, R. Wijnands, and M. van der Klis, *The Astrophysical Journal Letters* **674**, L41 (2008).
- <sup>480</sup>D. Mata Sánchez, T. Muñoz-Darias, J. Casares, and F. Jiménez-Ibarra, *Monthly Notices of the Royal Astronomical Society* **464**, L41–L45 (2017).

- <sup>481</sup>A. Melatos and A. Mastrano, *The Astrophysical Journal* **818**, 49 (2016).
- <sup>482</sup>P. M. Bult, K. C. Gendreau, Z. Arzoumanian, D. Chakrabarty, P. S. Ray, S. Guillot, M. T. Wolff, S. Bogdanov, and R. M. Ludlam, *The Astronomer's Telegram* **3001** (2019).
- <sup>483</sup>P. Bult, D. Chakrabarty, Z. Arzoumanian, K. C. Gendreau, S. Guillot, C. Malacaria, P. S. Ray, and T. E. Strohmayer, *The Astrophysical Journal* **898**, 38 (2020).
- <sup>484</sup>A. J. Goodwin et al., *Monthly Notices of the Royal Astronomical Society* **498**, 3429–3439 (2020).
- <sup>485</sup>M. A. P. Torres et al., *The Astrophysical Journal* **672**, 1079–1090 (2008).
- <sup>486</sup>J. Homan, G. Sivakoff, D. Pooley, C. Heinke, J. Strader, V. Tudor, and J. Miller-Jones, *The Astronomer's Telegram* **8971** (2016).
- <sup>487</sup>A. Sanna, A. Papitto, L. Burderi, E. Bozzo, A. Riggio, T. Di Salvo, C. Ferrigno, N. Rea, and R. Iaria, *Astronomy and Astrophysics* **598**, A34 (2017).
- <sup>488</sup>D. K. Galloway, D. Chakrabarty, E. H. Morgan, and R. A. Remillard, *The Astrophysical Journal Letters* **576**, L137–L140 (2002).
- <sup>489</sup>A. B. Giles, J. G. Greenhill, K. M. Hill, and E. Sanders, *Monthly Notices of the Royal Astronomical Society* **361**, 1180–1186 (2005).
- <sup>490</sup>A. J. Tetarenko et al., *The Astrophysical Journal* **854**, 125 (2018).
- <sup>491</sup>A. Sanna et al., *Astronomy and Astrophysics* **610**, L2 (2018).
- <sup>492</sup>P. Bult, T. E. Strohmayer, C. Malacaria, M. Ng, and Z. Wadiasingh, *The Astrophysical Journal* **912**, 120 (2021).
- <sup>493</sup>A. Sanna, E. Bozzo, A. Papitto, A. Riggio, C. Ferrigno, T. Di Salvo, R. Iaria, S. M. Mazzola, N. D'Amico, and L. Burderi, *Astronomy and Astrophysics* **616**, L17 (2018).
- <sup>494</sup>P. Bult, C. B. Markwardt, D. Altamirano, Z. Arzoumanian, D. Chakrabarty, K. C. Gendreau, S. Guillot, G. K. Jaisawal, P. S. Ray, and T. E. Strohmayer, *The Astrophysical Journal* **877**, 70 (2019).
- <sup>495</sup>A. Sanna, L. Burderi, A. Riggio, F. Pintore, T. Di Salvo, A. F. Gambino, R. Iaria, M. Matranga, and F. Scarano, *Monthly Notices of the Royal Astronomical Society* **459**, 1340–1349 (2016).
- <sup>496</sup>C. O. Heinke et al., *The Astrophysical Journal* **714**, 894–903 (2010).
- <sup>497</sup>P. Bult, A. Patruno, and M. van der Klis, *The Astrophysical Journal* **814**, 138 (2015).
- <sup>498</sup>M. Ng et al., *The Astrophysical Journal Letters* **908**, L15 (2021).
- <sup>499</sup>P. G. Jonker, M. A. P. Torres, D. Steeghs, and D. Chakrabarty, *Monthly Notices of the Royal Astronomical Society* **429**, 523–528 (2013).
- <sup>500</sup>P. M. Bult, D. Altamirano, A. C. Albayati, T. E. Strohmayer, P. S. Ray, D. Chakrabarty, M. Ng, K. C. Gendreau, Z. Arzoumanian, and A. Sanna, *The Astronomer's Telegram* **4428** (2021).
- <sup>501</sup>A. Sanna et al., *Monthly Notices of the Royal Astronomical Society* **514**, 4385–4397 (2022).
- <sup>502</sup>A. Papitto, E. Bozzo, C. Ferrigno, T. Belloni, L. Burderi, T. di Salvo, A. Riggio, A. D'Aì, and R. Iaria, *Astronomy and Astrophysics* **535**, L4 (2011).

- <sup>503</sup>M. Falanga, L. Kuiper, J. Poutanen, D. K. Galloway, E. Bozzo, A. Goldwurm, W. Hermsen, and L. Stella, *Astronomy and Astrophysics* **545**, A26 (2012).
- <sup>504</sup>A. Paizis, M. A. Nowak, J. Rodriguez, J. Wilms, S. Chaty, M. Del Santo, and P. Ubertini, *The Astrophysical Journal* **755**, 52 (2012).
- <sup>505</sup>A. Riggio, A. Papitto, L. Burderi, T. di Salvo, M. Bachetti, R. Iaria, A. D'Aì, and M. T. Menna, *Astronomy and Astrophysics* **526**, A95 (2011).
- <sup>506</sup>C. B. Markwardt, J. H. Swank, T. E. Strohmayer, J. J. M. in 't Zand, and F. E. Marshall, *The Astrophysical Journal Letters* **575**, L21–L24 (2002).
- <sup>507</sup>A. Papitto, M. T. Menna, L. Burderi, T. di Salvo, and A. Riggio, *Monthly Notices of the Royal Astronomical Society* **383**, 411–416 (2008).
- <sup>508</sup>A. Sanna et al., *Monthly Notices of the Royal Astronomical Society* **481**, 1658–1666 (2018).
- <sup>509</sup>T. D. Russell, N. Degenaar, R. Wijnands, J. van den Eijnden, N. V. Gusinskaia, J. W. T. Hessels, and J. C. A. Miller-Jones, *The Astrophysical Journal Letters* **869**, L16 (2018).
- <sup>510</sup>A. Sanna et al., *Monthly Notices of the Royal Astronomical Society* **495**, 1641–1649 (2020).
- <sup>511</sup>C. B. Markwardt, M. Juda, and J. H. Swank, *International Astronomical Union Circular* **8095**, 2 (2003).
- <sup>512</sup>A. Patruno, J. M. Hartman, R. Wijnands, D. Chakrabarty, and M. van der Klis, *The Astrophysical Journal* **717**, 1253–1261 (2010).
- <sup>513</sup>M. I. Krauss, Z. Wang, A. Dullighan, A. M. Juett, D. L. Kaplan, D. Chakrabarty, M. H. van Kerkwijk, D. Steeghs, P. G. Jonker, and C. B. Markwardt, *The Astrophysical Journal* **627**, 910–914 (2005).
- <sup>514</sup>A. Papitto, T. di Salvo, L. Burderi, M. T. Menna, G. Lavagetto, and A. Riggio, *Monthly Notices of the Royal Astronomical Society* **375**, 971–976 (2007).
- <sup>515</sup>C. Pallanca, E. Dalessandro, F. R. Ferraro, B. Lanzoni, and G. Beccari, *The Astrophysical Journal* **773**, 122 (2013).
- <sup>516</sup>A. Papitto et al., *Nature* **501**, 517–520 (2013).
- <sup>517</sup>D. B. Fox, *The Astronomer's Telegram* **526** (2005).
- <sup>518</sup>P. Kaaret, E. H. Morgan, R. Vanderspek, and J. A. Tomsick, *The Astrophysical Journal* **638**, 963–967 (2006).
- <sup>519</sup>A. Patruno, *The Astrophysical Journal Letters* **753**, L12 (2012).
- <sup>520</sup>S. Yoshida and U. Lee, *The Astrophysical Journal* **546**, 1121–1125 (2001).
- <sup>521</sup>LIGO Scientific Collaboration and Virgo Collaboration et al., *Physical Review D* **96**, 122006 (2017).
- <sup>522</sup>C. Messenger et al., *Physical Review D* **92**, 023006 (2015).
- <sup>523</sup>LIGO Scientific Collaboration and Virgo Collaboration et al., *Physical Review D* **100**, 024004 (2019).
- <sup>524</sup>D. Davis et al., *Classical and Quantum Gravity* **38**, 135014 (2021).

- <sup>525</sup>J. Zweizig and K. Riles, *LIGO-T2000384-v4: Information on self-gating of  $h(t)$  used in O3 continuous-wave and stochastic searches.*
- <sup>526</sup>L. Sun et al., *Classical and Quantum Gravity* **37**, 225008 (2020).
- <sup>527</sup>L. Sun et al., *arXiv e-prints*, arXiv:2107.00129 (2021).
- <sup>528</sup>LSC Instrument Authors et al., *Physical Review D* **97**, 082002 (2018).
- <sup>529</sup>E. Goetz et al., *LIGO-T2100200-v1: O3 lines and combs in found in self-gated C01 data*.
- <sup>530</sup>M. M. Romanova, G. V. Ustyugova, A. V. Koldoba, and R. V. E. Lovelace, *The Astrophysical Journal* **610**, 920 (2004).
- <sup>531</sup>A. Sanna et al., *Monthly Notices of the Royal Astronomical Society* **466**, 2910–2917 (2017).
- <sup>532</sup>V. De Falco, L. Kuiper, E. Bozzo, D. K. Galloway, J. Poutanen, C. Ferrigno, L. Stella, and M. Falanga, *Astronomy and Astrophysics* **599**, A88 (2017).
- <sup>533</sup>A. Marino, T. Di Salvo, A. F. Gambino, R. Iaria, L. Burderi, M. Matranga, A. Sanna, and A. Riggio, *Astronomy and Astrophysics* **603**, A137 (2017).
- <sup>534</sup>L. Keek, W. Iwakiri, M. Serino, D. R. Ballantyne, J. J. M. in't Zand, and T. E. Strohmayer, *The Astrophysical Journal* **836**, 111 (2017).
- <sup>535</sup>J. van den Eijnden et al., *The Astronomer's Telegram* **1487** (2018).
- <sup>536</sup>H. Negoro et al., *The Astronomer's Telegram* **1447** (2018).
- <sup>537</sup>W. E. Harris, *arXiv e-prints*, arXiv:1012.3224 (2010).
- <sup>538</sup>R. Sharma, A. Beri, A. Sanna, and A. Dutta, *Monthly Notices of the Royal Astronomical Society* **492**, 4361–4368 (2020).
- <sup>539</sup>R. Wijnands, E. Rol, E. Cackett, R. L. C. Starling, and R. A. Remillard, *Monthly Notices of the Royal Astronomical Society* **393**, 126–132 (2009).
- <sup>540</sup>M. Linares et al., *The Astronomer's Telegram* **3568** (2011).
- <sup>541</sup>N. V. Gusinskaia, T. D. Russell, J. W. T. Hessels, S. Bogdanov, N. Degenaar, A. T. Deller, J. van den Eijnden, A. D. Jaodand, J. C. A. Miller-Jones, and R. Wijnands, *Monthly Notices of the Royal Astronomical Society* **492**, 1091–1101 (2020).
- <sup>542</sup>L. Kuiper, S. S. Tsygankov, M. Falanga, I. A. Mereminskiy, D. K. Galloway, J. Poutanen, and Z. Li, *Astronomy and Astrophysics* **641**, A37 (2020).
- <sup>543</sup>A. Riggio, T. Di Salvo, L. Burderi, M. T. Menna, A. Papitto, R. Iaria, and G. Lavagetto, *The Astrophysical Journal* **678**, 1273–1278 (2008).
- <sup>544</sup>D. K. Galloway and A. Cumming, *The Astrophysical Journal* **652**, 559–568 (2006).
- <sup>545</sup>A. J. Goodwin, D. K. Galloway, A. Heger, A. Cumming, and Z. Johnston, *Monthly Notices of the Royal Astronomical Society* **490**, 2228–2240 (2019).
- <sup>546</sup>P. D'Avanzo, S. Campana, J. Casares, S. Covino, G. L. Israel, and L. Stella, *Astronomy and Astrophysics* **508**, 297–308 (2009).
- <sup>547</sup>M. Suzuki et al., *Publications of the Astronomical Society of Japan* **59**, 263–268 (2007).
- <sup>548</sup>D. K. Galloway, M. P. Muno, J. M. Hartman, D. Psaltis, and D. Chakrabarty, *The Astrophysical Journal Supplement Series* **179**, 360 (2008).

- <sup>549</sup>D. I. Jones, *Monthly Notices of the Royal Astronomical Society* **453**, 53–66 (2015).
- <sup>550</sup>C. V. D. Broeck, *Classical and Quantum Gravity* **22**, 1825–1839 (2005).
- <sup>551</sup>G. Ashton and R. Prix, *Physical Review D* **97**, 103020 (2018).
- <sup>552</sup>P. B. Covas and A. M. Sintes, *Physical Review Letters* **124**, 191102 (2020).
- <sup>553</sup>R. Tenorio, D. Keitel, and A. M. Sintes, *Physical Review D* **104**, 084012 (2021).
- <sup>554</sup>D. Foreman-Mackey, D. W. Hogg, D. Lang, and J. Goodman, *Publications of the Astronomical Society of the Pacific* **125**, 306 (2013).
- <sup>555</sup>W. D. Vousden, W. M. Farr, and I. Mandel, *Monthly Notices of the Royal Astronomical Society* **455**, 1919–1937 (2016).
- <sup>556</sup>L. Dunn, A. Melatos, S. Suvorova, W. Moran, R. J. Evans, S. Osłowski, M. E. Lower, M. Bailes, C. Flynn, and V. Gupta, *Monthly Notices of the Royal Astronomical Society* **512**, 1469–1482 (2022).
- <sup>557</sup>L. Dunn, A. Melatos, C. M. Espinoza, D. Antonopoulou, and R. Dodson, *Monthly Notices of the Royal Astronomical Society* **in press**, 10.48550/arXiv.2304.13382 (2023).
- <sup>558</sup>A. Basu, B. C. Joshi, M. A. Krishnakumar, D. Bhattacharya, R. Nandi, D. Bandhopadhyay, P. Char, and P. K. Manoharan, *Monthly Notices of the Royal Astronomical Society* **491**, 3182–3191 (2020).
- <sup>559</sup>S. Johnston et al., *Monthly Notices of the Royal Astronomical Society* **493**, 3608–3615 (2020).
- <sup>560</sup>M. Amiri et al., *The Astrophysical Journal Supplement Series* **255**, 5 (2021).
- <sup>561</sup>A. Melatos and M. Millhouse, *The Astrophysical Journal* **948**, 106 (2023).
- <sup>562</sup>H. J. Kushner, *Journal of the Society for Industrial and Applied Mathematics Series A Control* **2**, 106–119 (1964).
- <sup>563</sup>M. Zakai, *Zeitschrift für Wahrscheinlichkeitstheorie und Verwandte Gebiete* **11**, 230–243 (1969).
- <sup>564</sup>Z. Schuss, “Nonlinear Filtering and Smoothing of Diffusions”, in *Nonlinear Filtering and Optimal Phase Tracking*, edited by Z. Schuss, *Applied Mathematical Sciences* (Springer US, Boston, MA, 2012), pp. 85–106.
- <sup>565</sup>A. Watts et al., in *Proceedings of Advancing Astrophysics with the Square Kilometre Array — PoS(AASKA14)*, Vol. 215 (May 2015), p. 043.
- <sup>566</sup>J. Singha, B. C. Joshi, D. Bandyopadhyay, H. Grover, S. Desai, P. Arumugam, and S. Banik, *Journal of Astrophysics and Astronomy* **43**, 81 (2022).
- <sup>567</sup>M. A. Ellison, *Quarterly Journal of the Royal Astronomical Society* **4**, 62 (1963).
- <sup>568</sup>E. N. Parker, *The Astrophysical Journal* **330**, 474 (1988).
- <sup>569</sup>D. H. Hathaway, *Living Reviews in Solar Physics* **12**, 4 (2015).
- <sup>570</sup>V. I. Abramenco, R. A. Suleymanova, and A. V. Zhukova, *Monthly Notices of the Royal Astronomical Society* **518**, 4746–4754 (2023).

- <sup>571</sup>V. I. Abramenko, O. I. Tikhonova, and A. S. Kutsenko, *Geomagnetism and Aeronomy* **57**, 792–797 (2017).
- <sup>572</sup>K. D. Leka et al., *The Astrophysical Journal Supplement Series* **243**, 36 (2019).
- <sup>573</sup>K. D. Leka et al., *The Astrophysical Journal* **881**, 101 (2019).
- <sup>574</sup>M. Vigelius and A. Melatos, *Monthly Notices of the Royal Astronomical Society* **395**, 1972–1984 (2009).
- <sup>575</sup>M. Priymak, A. Melatos, and D. J. B. Payne, *Monthly Notices of the Royal Astronomical Society* **417**, 2696–2713 (2011).
- <sup>576</sup>R. Bondarescu, S. A. Teukolsky, and I. Wasserman, *Physical Review D* **79**, 104003 (2009).
- <sup>577</sup>A. Buikema et al., *Physical Review D* **102**, 062003 (2020).
- <sup>578</sup>L. Sun, A. Melatos, S. Suvorova, W. Moran, and R. J. Evans, *Physical Review D* **97**, 043013 (2018).
- <sup>579</sup>K. J. Wagner, J. T. Whelan, J. K. Wofford, and K. Wette, *Classical and Quantum Gravity* **39**, 075013 (2022).
- <sup>580</sup>M. Punturo et al., *Classical and Quantum Gravity* **27**, 194002 (2010).
- <sup>581</sup>B. P. Abbott et al., *Classical and Quantum Gravity* **34**, 044001 (2017).